



**ELECTROANALYTICAL INVESTIGATIONS OF BISMUTH
ELECTRODES AND SILVER NANOPARTICLES**

Aondoakaa Steve Nomor

**School of Chemistry
Newcastle University
Newcastle upon Tyne, UK.**

**A thesis submitted for the degree of
Doctor of Philosophy**

October 2018

Abstract

Bismuth bulk electrodes (BiBEs) have been suggested as possible replacements for mercury electrodes in electroanalytical studies in part because they are simply prepared by melting bismuth powder in a glass capillary and also because of the relative lack of toxicity of Bi. The double layer of BiBEs in aqueous media was studied using electrochemical impedance spectroscopy (EIS). The differential capacitance of BiBEs was determined in three aqueous electrolytes: sodium nitrate (NaNO_3), sodium bromide (NaBr) and sodium chloride (NaCl) as well as the non-aqueous electrolyte LiClO_4 /acetonitrile (AN). Comparative measurements were made with a polycrystalline platinum electrode. Up to $43 \mu\text{F cm}^{-2}$ were recorded for the double layer capacitance at the BiBEs in the aqueous electrolytes, while more typical capacitance values of $<20 \mu\text{F cm}^{-2}$ were obtained for the Bi|AN/LiClO_4 interface. Combined investigations by EIS and x-ray photoelectron spectroscopy (XPS) suggest the high values of capacitance in the aqueous electrolytes are due to pseudocapacitance effects, owing to adsorptions of bromide and chloride ions as well as the formation/reduction of a bismuth(III) oxide film at the electrode surface. The capacitance values of the Bi|AN/LiClO_4 interface are consistent with the standard Gouy-Chapman-Stern model; ClO_4^- anions are thought to be weakly adsorbing in non-aqueous media. The EIS measurements also enabled the determination of the potential of zero charge PZC of -0.49 V versus Ag/AgCl at BiBEs in the aqueous electrolyte mixture of $\text{NaNO}_3/\text{NaCl}$.

The differential capacitance studies provided an understanding of the nature of the BiBE interfaces required to interpret electron transfer measurements. Several redox couples were investigated by slow scan cyclic voltammetry (CV): ruthenium hexaammine, methyl viologen, sodium anthraquinone-2-sulfonate monohydrate, methylene blue, toluidine blue, hexaamminecobalt(III) chloride and cobaltocenium hexafluorophosphate. Many of these couples showed complex behaviour at Bi; either due to Bi oxidation or a lack of chemical reversibility and possible complications due to adsorption. However, ruthenium hexaammine showed reversible, uncomplicated CVs at the BiBE/KCl(aq) interface and therefore was selected for detailed study of the electron transfer kinetics by EIS. The standard rate constant (k^0) and electron transfer coefficient (α) were determined for the outer-sphere one-electron transfer process for ruthenium hexaammine trichloride $\text{Ru(NH}_3)_6\text{Cl}_3$ at BiBEs in KCl(aq) as supporting electrolyte. In contrast to previous work on viologen derivatives in AN in the literature, there was a marked difference between the k^0 values at BiBEs and Pt electrodes- the voltammetry and impedance spectra were found to be reversible at Pt. We ascribe this difference to the presence of a thin oxide layer on the BiBE at potentials near the standard potential for ruthenium hexaammine. Despite the presence of such an oxide layer, repeatable impedance spectra could be obtained for the system and the expected linear dependence of the charge transfer resistance on $[\text{Ru(III)}]$ was observed. Further, the (dc) potential dependence of the EIS data allowed the determination of the potential dependence of the transfer coefficient. This data provided direct evidence of the importance of double layer corrections to k^0 because of the rapid variation of α observed near the potential of zero charge. In summary, BiBEs show somewhat complex behaviour in aqueous media; many redox couples cannot be easily studied because of the susceptibility of Bi to oxidation and complex adsorption effects, not well understood. However in the case of ruthenium hexaammine, precise voltammetric data can be obtained even though photoemission spectra and differential capacitance data indicates the presence of a thin oxide film.

The second part of the thesis concerns the detection of Ag(I) ions released by corrosion of silver nanoparticles (AgNPs) in aqueous media. Neither BiBEs nor Pt electrodes were found to be suitable for the detection of Ag(I), however straightforward anodic stripping voltammetry (ASV) at glassy carbon electrodes was successful. AgNPs were synthesized by the citrate reduction method and dialysed either in pure water, or different concentrations of chloride and sulphate to examine the effect of the medium on the release of Ag(I) ions. The importance of these studies relate to the fate of AgNPs in the environment; AgNPs are now widely employed for their antimicrobial activity, however it is not clear what their eventual fate is nor how much Ag(I), the putative agent is released. The experimental technique involved dialysis of the initial AgNP preparation against a particular aqueous medium and (i) analysis of the [Ag(I)] released from the dialysis membrane into the external medium and (ii) characterization of the aliquots of AgNPs remaining inside the dialysis membrane. Optical absorption spectra showed a redshift of the AgNP plasmon band throughout the dialysis, consistent with aggregation of the NPs. This is unexpected based on simple DLVO stabilization as the reduction in ionic strength against water should disfavour aggregation. However it was confirmed by dynamic light scattering (DLS) and atomic force microscopy (AFM) of drop-cast aliquots and probably arises from loss of citrate ligands.

Release of Ag(I) ions was monitored by anodic stripping voltammetry at glassy carbon electrodes. The ASV data was calibrated by standard addition and indicated the presence of about 90 μM of Ag(I) ions in the initial preparation. Over time, the [Ag(I)] decreased until it reached a steady-state value of the order of a few μM . Unexpectedly, a similar steady-state concentration was observed in chloride or sulphate containing media. The presence of chloride does indeed reduce the concentration of Ag(I) in the initial preparation (to a value controlled by the solubility product of AgCl), however in that case a strong decrease in [Ag(I)] throughout the dialysis was not observed. A concentration of about 4 μM was still detected after 73 h of dialysis. This effect is interpreted in terms of the decrease in the electrode potential for the Ag/Ag(I) couple in the presence of Cl^- ; we suggest that the steady-state concentration of Ag(I) is determined mainly by the corrosion of the AgNPs.

Dedication

To Professor Emmanuel Hemen Agba, a true friend of all ages.

Acknowledgements

This work will not be complete without my expression of sincere gratitude to God Almighty for the gift of life. I must not forget to thank immensely, my supervisors Prof. Andrew Houlton and Dr. Benjamin Richard Horrocks. I lack words with which to express special appreciation to Dr Ben Horrocks for being not just a supervisor but a tutor who not only took time to train me on the operation of electrochemical equipment but also put me through some data analyses. He also read through all the manuscripts of this thesis, making useful suggestions and inputs to make it a worthwhile piece of research material. I pray God to bless and sustain this goodwill in you.

William McCormack (now retired) and Robyn Hare of the Glass Blowing Unit, School of Chemistry, Newcastle University readily helped in the construction of the bismuth electrodes and the three-electrode electrochemical cells that are at the centre of this research. I really appreciate you.

I would also want to thank my wife and children as well as my old parents for enduring the period of my long absence away from home. It has really been a trying period for all of us. It will be unfair to forget my true friends who have given me moral support all along the pursuit of this programme. They include Prof. Moses Chiawa, Dr. Simon Ubwa, Messrs Patrick Anikpa, Sebastian Atia, Ronald Mnyim and Shimrumun Anngu. I specially appreciate Prof. Msugh Kembe, who as Dean of the Faculty of Science Benue State University, recommended me for this training.

These words of appreciation will be incomplete without the mention of my colleagues in the Chemical Nanoscience Laboratories of Newcastle University for their various assistances and moral support. They are Dr. Osama El-Zubir, who not only trained me on the operation of atomic force microscope (AFM) but was always willing to help resolve issues of AFM images. Others are Michael Bracchi, Shams Ali, Lamia Al-Mahamad, Barnabas Oshido and Hector Oyem. I will remain eternally grateful to Thompson Izuagie and Aondover Kajo who were readily available to help in resolving issues related with computer operation. Lastly, I wish to thank Benue State University Makurdi and the Nigerian Tertiary Education Trust Fund for partly funding this research.

Table of Contents

Abstract.....	ii
Dedication	iii
Acknowledgements	iii
Table of Contents	v
List of Figures.....	ix
List of Schemes.....	xviii
List of Tables	xix
Chapter 1. Introduction	1
1.1 Bismuth electrodes.....	1
1.1.1 <i>Measurement of differential capacitance.</i>	3
1.1.2 <i>Kinetic studies at Bi</i>	4
1.1.3 <i>Bismuth electrodes in stripping voltammetry</i>	4
1.1.4 <i>Application of bismuth electrodes in sensors</i>	5
1.2 Electrical double layer and capacitance	6
1.3 Frumkin Correction.....	13
1.4 Electron transfer reactions	14
1.4.1 <i>Methyl viologen</i>	18
1.4.2 <i>Sodium anthraquinone-2-sulfonate</i>	19
1.4.3 <i>Cobaltocenium hexafluorophosphate</i>	20
1.4.4 <i>Hexaammine cobalt(III) chloride</i>	23
1.4.5 <i>Hexaammine ruthenium(III) chloride</i>	25
1.5 Silver Nanoparticles: detection of Ag(I) release by electroanalysis.	26
Chapter 2. Experimental	29
2.1 Analyses at Bismuth Electrodes.....	29
2.2 Preparation of Reagents	30

2.2.1	<i>Ruthenium(III) hexaammine</i>	30
2.2.2	<i>Methyl viologen dichloride</i>	31
2.2.3	<i>Sodium anthraquinone-2-sulfonate monohydrate</i>	31
2.2.4	<i>Methylene blue hydrate</i>	31
2.2.5	<i>Toluidine blue</i>	31
2.2.6	<i>Hexaammine cobalt(III)chloride</i>	32
2.2.7	<i>Cobaltocenium hexafluorophosphate</i>	32
2.3	Preparation of Silver Nanoparticles	32
2.4.	Characterization of Silver Nanoparticles.....	35
2.5	Construction of Bismuth Electrodes.....	36
2.6	Double Layer Capacitance at Bismuth Electrodes.....	37
2.7	Standard Rate Constants.	38
2.8	Analytical and Characterisation Techniques.....	39
2.8.1	<i>Cyclic voltammetry</i>	39
2.8.2	<i>Electrochemical impedance spectroscopy</i>	41
2.8.3	<i>X-ray photoelectron spectroscopy</i>	46
2.8.4	<i>Dynamic light scattering</i>	48
2.8.5	<i>Atomic force microscopy</i>	49
2.8.6	<i>Dialysis</i>	52
2.8.7	<i>Stripping voltammetry</i>	52
Chapter 3.	Capacitance Measurements	55
3.1	Aims.....	55
3.2	Capacitance Measurements at Bismuth in Aqueous Solutions.....	55
3.2.1	<i>The double electrolyte effect</i>	70
3.3	Capacitance Measurements at Platinum in Aqueous Solutions.....	70
3.4	Capacitance Measurements at Bismuth in Non-aqueous Solvents	75
3.5	Capacitance Measurements at Platinum in Non-aqueous Solvents	77

3.6	Conclusions.....	78
Chapter 4. Electrochemical Behaviour of Selected Redox Couples at Bismuth Electrodes.....		
		81
4.1	Synopsis.....	81
4.2	Ruthenium(III) hexaammine	81
4.3	Methyl Viologen or Paraquat	83
4.4	Sodium Anthraquinone-2-sulfonate Monohydrate	88
4.5	Methylene Blue Hydrate	94
4.6	Toluidine Blue	97
4.7	Hexaammine Cobalt(III) Chloride	98
4.8	Cobaltocenium Hexafluorophosphate	99
4.9	Conclusion	104
Chapter 5. Kinetic Studies of Ruthenium(III) Hexaammine at Bulk Bismuth Electrodes.....		
		105
5.1	Introduction	105
5.2	Cyclic Voltammetry.....	106
5.3	Electrochemical Impedance Spectroscopy (EIS)	108
5.4	Data Analysis	113
5.4.1	<i>Charge transfer resistance and transfer coefficient</i>	113
5.4.2	<i>Differential capacitance</i>	117
5.4.3	<i>Double layer effects.....</i>	120
5.5	Conclusions.....	122
Chapter 6. Preparation and Characterization of Silver Nanoparticles (AgNPs)		
		125
6.1	Introduction	125
6.2	Preparation of Silver Nanoparticles.....	126
6.3	Characterization Techniques.....	128

6.3.1	<i>Ultraviolet-visible (UV-Vis) spectroscopy</i>	128
6.3.2	<i>Colloid stability and aggregation</i>	130
6.3.3	<i>Dynamic light scattering (DLS)</i>	133
6.3.4	<i>Atomic force microscopy (AFM)</i>	137
6.3.5	<i>Anodic stripping voltammetry (ASV)</i>	146
6.4	Conclusions	150
Chapter 7. Conclusions and Future Work.		151
7.1	Bismuth Electrodes.....	151
7.1.1	<i>Capacitance measurements</i>	151
7.1.2	<i>Anthraquinone-2-sulfonate (AQS)</i>	152
7.1.3	<i>Cobaltocenium</i>	152
7.1.4	<i>Methyl viologen</i>	153
7.1.5	<i>Ruthenium(III) hexaammine</i> ²⁰⁴	153
7.2	Silver Nanoparticles.....	154
7.3	Future Work.....	155
References.		156
APPENDIX I: Glossary of Abbreviations		175
APPENDIX II: Symbols		177

List of Figures

<i>Figure 1.1 Diagram to illustrate the variation in density of states near the Fermi level between metals and semi-metals. Filled states are shaded blue, while E_F indicates the energy corresponding to the Fermi-level. The areas under the rectangles of width AB and CD clearly show how the concentration of electrons in the valence band in metals is higher than that in semi-metals.</i>	<i>2</i>
<i>Figure.1.2 Sketch of the Helmholtz model of the double layer showing (a) rigid arrangement of ions, X_2 being the distance of closest approach of the charges to the electrode (b) variation of C_d with applied potential.</i>	<i>7</i>
<i>Figure 1.3. Sketch of the Gouy-Chapman model showing (a) diffuse arrangement of ions and (b) variation of differential capacitance (C_d) with potential.</i>	<i>8</i>
<i>Figure 1.4 Gouy-Chapman-Stern model showing variation of C_d with potential as concentration changes.</i>	<i>10</i>
<i>Figure 1.5. Potential profile illustrating electron transfer across the compact double layer at a plane distance x_2 from the electrode.....</i>	<i>13</i>
<i>Figure 1.6 Graphical representation of the Butler-Volmer equation showing the effects of changing the potential and the value of the transfer coefficient (α) on the current. The curve was constructed for one-electron transfer at 298 K, with a standard rate constant k_0 of 1 cm s^{-1}. The concentrations of the oxidized and reduced species were the same, with a value of $1 \times 10^{-6} \text{ mol cm}^{-3}$</i>	<i>16</i>
<i>Figure 2.1 Freshly prepared 10 mM AgNPs of (A) pure water and (B) NaCl(aq) contained in 250 mL conical flasks. The NaCl(aq)-AgNPs turned turbid after addition of NaCl crystals. The NPs were prepared by the citrate reduction method..</i>	<i>34</i>
<i>Figure 2.2 Apparatus showing dialysis of 10 mM NaCl(aq)-AgNPs contained in a 400 mL beaker</i>	<i>35</i>
<i>Figure 2.3 Sketch diagram of a bismuth bulk electrode.....</i>	<i>37</i>
<i>Figure 2.4 Structure of the three electrode cell. It has an external diameter of 3 cm with a height of 8 cm and takes 18-20 mL of analyte solution</i>	<i>38</i>
<i>Figure 2.5. Potential-time profile of a cyclic voltammogram</i>	<i>39</i>

Figure 2.6. A typical cyclic voltammogram showing peak currents (I_{pc} , I_{pa}) and peak potentials (E_{pc} , E_{pa}) for the reduction of species present as the oxidized form in bulk solution and under conditions where the voltammetry is reversible.....	40
Figure 2.7(a) A Randles circuit for mixed – kinetics diffusion. R_U is for uncompensated resistance, CPE stands for constant phase element which represents the non-ideality of the double layer capacitance in solution and RCT is for charge transfer resistance. The Warburg impedance which enables calculation of diffusion coefficients is indicated by W . (b) A Nyquist plot showing the real part of impedance as Z' while the imaginary part is denoted by $-Z''$	45
Figure 2.8 Image of an atomic force microscope showing a sample placed on the AFM piezoelectric stage.....	51
Figure 3.1. Combined capacitance at Bi in aq. $NaNO_3$ at (A) 500 Hz (B) 1 kHz (C) 2 kHz.....	56
Figure 3.2 Sketch for an impedance plane plot to illustrate a CPE	57
Figure 3.3. Capacitance data at Bi in aq. $NaBr$ at (A) 500 Hz (B) 1 kHz (C) 2 kHz...	59
Figure 3.4. Capacitance data at Bi in aq. $NaCl$ at frequencies of (A) 500 Hz (B) 1 kHz (C) 2 kHz.....	60
Figure 3.5. Capacitance data at Bi in $NaNO_3$ at (A) 500 Hz (B) 1 kHz (C) 2 kHz with Ag wire RE	62
Figure 3.6. XPS (A) survey and (B) resolution spectra of the Bi $NaNO_3$ interface....	64
Figure 3.7. Sketch illustrating XPS data showing pseudocapacitance owing to presence of bismuth oxide layer	66
Figure 3.8. XPS (A) survey and (B) Cl-2p resolution spectra of the Bi $NaCl$ interface.....	67
Figure 3.9. (A) XPS survey (B) Br-3d resolution spectrum of the Bi $NaBr$ interface..	69
Figure 3.10. Capacitance data at Bi at in the $NaNO_3/NaCl$ electrolyte mixture at frequency of 1 kHz showing the pzc of -0.49 V.....	70
Figure 3.11. Capacitance data at Pt in aq. $NaBr$ at (A) 500 Hz (B) 1 kHz (C) 2 kHz.	71
Figure 3.12. Capacitance data at Pt in aq. $NaCl$ at (A) 500 HZ (B) 1 kHz (C) 2 kHz frequencies	73

<i>Figure 3.13. Capacitance data at Pt in the NaNO₃/NaCl electrolyte mixture at frequencies of (A) 500 Hz (B) 1 kHz and (C) 2 kHz.....</i>	<i>74</i>
<i>Figure 3.14 Capacitance data at Bi in the non-aqueous AN/LiClO₄ at (A) 500 Hz (B) 1 kHz (C) 2 kHz</i>	<i>76</i>
<i>Figure 3.15. Capacitance data at Pt in AN/LiClO₄ at (A) 500 Hz (B) 1 kHz (C) 2 kHz.....</i>	<i>77</i>
<i>Figure 4.1. CV of 5 mM ruthenium(III) hexaammine at scan rate of 25 mV/s at bismuth in 0.1 M KCl. The potentials were measured against an Ag/AgCl (1 M KCl) reference electrode</i>	<i>82</i>
<i>Figure 4.2. Variation of peak currents with scan rate for 5 mM ruthenium(III) hexaammine in 0.1 M KCl at Bi</i>	<i>83</i>
<i>Figure 4.3. CV of 2 mM methyl viologen at Bi at scan rate of 25 mV/s in 0.1 M KCl(aq). The reference electrode was Ag/AgCl (1 M KCl).....</i>	<i>84</i>
<i>Figure 4.4. CV of 5 mM methyl viologen at Bi at scan rate of 25 mV/s in 0.1 M KCl(aq). The smaller peak is indicated in red.....</i>	<i>85</i>
<i>Figure 4.5. Nyquist plot of 2 mM methyl viologen at bismuth at -0.58 V in 0.1 M KCl(aq). The reference electrode was Ag/AgCl (1 M KCl).....</i>	<i>86</i>
<i>Figure 4.6. Nyquist plot of 2 mM methyl viologen at bismuth at -0.67 V in 0.1 M KCl versus Ag/AgCl (1 M KCl)</i>	<i>86</i>
<i>Figure 4.7 Nyquist plot of 10 mM methyl viologen at bismuth at -0.56 V in 0.1 M KCl versus Ag/AgCl (1 M KCl)</i>	<i>87</i>
<i>Figure 4.8. Variation of charge transfer resistance with potential for methyl viologen at bismuth in 0.1 M KCl(aq).....</i>	<i>87</i>
<i>Figure 4.9. Variation of differential capacitance with potential for methyl viologen at bismuth in 0.1 M KCl(aq).....</i>	<i>88</i>
<i>Figure 4.10 CV of 2 mM AQS at Bi at scan rate of 200 mV/s in argon- purged 0.1 M KCl solution. An Ag/AgCl (1 M KCl) reference electrode was used.....</i>	<i>89</i>
<i>Figure 4.11 Variation of peak currents with scan rate for 10 mM AQS at Bi.....</i>	<i>89</i>
<i>Figure 4.12. AC voltammogram of 10 mM AQS at bismuth in 0.1 M KCl solution. An Ag/AgCl (1 M KCl) reference electrode was used. The scan rate was 25 mV/s</i>	

<i>with amplitude of 10 mV at frequency of 1000 Hz. The green and red arrows point to the 1st and 2nd peaks respectively.....</i>	<i>90</i>
<i>Figure 4.13 Nyquist plot of 2 mM AQS at bismuth at -0.78 V Vs Ag/AgCl (1 M KCl) in 0.1 M KCl.....</i>	<i>91</i>
<i>Figure 4.14 Nyquist plot of 2 mM AQS at bismuth at -0.89 V Vs Ag/AgCl (1 M KCl) in 0.1 M KCl.....</i>	<i>91</i>
<i>Figure 4.15. Charge transfer profile of AQS at Bi in 0.1 M KCl as supporting electrolyte</i>	<i>92</i>
<i>Figure 4.16. Overlay of impedance spectra at various dc potentials for 2 mM AQS at Bi in 0.1 M KCl solution as supporting electrolyte. The frequency range of 101 Hz -105 Hz (41 frequencies per spectrum) and the dc potential range was -0.66 V to -0.90 V in steps of 20 mV.....</i>	<i>93</i>
<i>Figure 4.17. CV of 2 mM AQS at a bismuth electrode at scan rate of 2500 mV s⁻¹ in 0.1 M KCl. The reference electrode was Ag/AgCl (1 M KCl).....</i>	<i>94</i>
<i>Figure 4.18. CV of 5 mM methylene blue at Bi at scan rate of 25 mV/s in 0.1 M aq. H₂SO₄.....</i>	<i>95</i>
<i>Figure 4.19. CV of 5 mM methylene blue at Pt at the scan rate of 25 mV/s in 0.1 M aq. H₂SO₄ against the potential of an Ag/AgCl reference electrode</i>	<i>95</i>
<i>Figure 4.20 Variation of peak currents with scan rate for 5 mM methylene blue at Bi in 0.1 M aq. H₂SO₄.....</i>	<i>96</i>
<i>Figure 4.21. Variation of peak currents with scan rate for 5 mM methylene blue at Pt in 0.1 M aq. H₂SO₄.....</i>	<i>96</i>
<i>Figure 4.22. AC voltammogram of 5 mM methylene blue at Pt in 0.1 M aq. H₂SO₄. The scan rate was 25 mV/s with amplitude of 10 mV at frequency of 1000 Hz.</i>	<i>97</i>
<i>Figure 4.23. CV of 5 mM toluidine blue in 0.1 M KCl at scan rate of 25 mV/s at Bi against the potential of an Ag/AgCl (1 M KCl) reference electrode.....</i>	<i>98</i>
<i>Figure 4.24. CV of 5 mM toluidine blue in 0.1 M KCl at scan rate of 25 mV/s at Pt against the potential of an Ag/AgCl (1 M KCl) reference electrode.....</i>	<i>98</i>

Figure 4.25. CV of 5 mM hexaammine cobalt(III) chloride at bismuth. The scan rate was 20 mV/s in 0.1 M HClO ₄ as electrolyte against an Ag/AgCl (1 M KCl) reference electrode	99
Figure 4.26. Variation of peak current with scan rate for 5 mM hexaammine cobalt(III) at Bi in 0.1 M aq. HClO ₄	99
Figure 4.27. CV of 2 mM cobaltocenium at Bi at scan rate of 10 mV/s in 0.1 M TBAPF ₆ /AN. The non-aqueous Ag/Ag ⁺ reference electrode was used here	100
Figure 4.28. CV of 2 mM cobaltocenium at Pt at scan rate of 10 mV/s in 0.1 M TBAPF ₆ /AN against the potential of an Ag/Ag ⁺ reference electrode	101
Figure 4.29. Impedance spectra at different dc potentials for 5 mM cobaltocenium hexafluorophosphate at Bi. The potential range was -0.72 to -0.92 V in steps of 20 mV. The analyte solution which was prepared in 0.1 M TBAPF ₆ /AN was purged with argon gas for 15 minutes prior to scanning.....	102
Figure 4.30. EIS fitted spectrum of 2 mM cobaltocenium hexafluorophosphate at Bi at -0.89 V. The green line is the simulated data while the red points are the experimental data.....	102
Figure 4.31. EIS fitted spectrum of 8 mM cobaltocenium hexafluorophosphate at Bi at -0.87 V. The red points are the experimental data fitted into the simulated green line.....	103
Figure 4.32. Variation of charge transfer resistance with potential for 2 mM to 10 mM cobaltocenium hexafluorophosphate at bismuth	104
Figure 5.1. Cyclic voltammograms at Pt (blue) and Bi (orange) electrodes of Ru(NH ₃) ₆ Cl ₃ in 0.1 M KCl(aq). (a) The scan rate was 50 mV s ⁻¹ , [Ru(NH ₃) ₆ Cl ₃] = 10 mM and the reference electrode was Ag/AgCl in 1M KCl(aq). (b) Cathodic peak current (absolute value) against square root of scan rate for 2 mM Ru(NH ₃) ₆ Cl ₃ in 0.1 M KCl(aq) at a Bi electrode	107
Figure 5.2. Slow scan cyclic voltammetric peak potential data for 2 mM Ru(NH ₃) ₆ Cl ₃ in 0.1 M KCl(aq) at a Bi electrode. (a) Cathodic peak potential against ln(scan rate) and (b) Peak separation against ln(scan rate).....	108
Figure 5.3. Nyquist plot of the impedance spectrum at a Bi electrode (symbols) and complex least squares fit (solid line) of the modified Randles circuit. The electrolyte	

contained 2 mM Ru(NH₃)₆Cl₃ in 0.1 M KCl(aq). Applied dc potential = -0.21 V vs Ag/AgCl (1M KCl). Frequency range 101 – 105 Hz. Statistical uncertainties on the values of RCT obtained from the fit were about 0.2%..... 109

Figure 5.4. Diagram of a Randles circuit for mixed kinetics-diffusion behaviour showing: uncompensated or solution resistance (R_u), constant phase element (CPE) in place of a perfect capacitor for values of differential capacitance, charge transfer resistance (RCT) and the Warburg impedance (W) which depends on the concentration and the diffusion coefficient..... 110

Figure 5.5. RCT-1 against [Ru(NH₃)₆Cl₃] in 0.1 M KCl(aq). The values of charge transfer resistance plotted are those at a dc potential equal to the formal potential 111

Figure 5.6. Charge transfer resistance against dc potential at a Bi electrode with 2 mM Ru(NH₃)₆Cl₃ in 0.1 M KCl(aq). The difference between data and fit measured as $SSR = \sqrt{\sum(R^{expt}-R^{theory})^2}$ was (a) SSR = 3.4 kΩ; (b) SSR = 2.6 kΩ and (c) SSR = 2.7 mΩ. The RCT versus E data was obtained using the instrument software to record a sequence of impedance spectra at different values of E automatically and we found a statistical uncertainty of about 0.2% on each value of RCT 112

Figure 5.7. Variation of apparent transfer coefficient α(E) at Bi with dc potential E. The data was obtained by the regularized least squares procedure defined by equations (5.6) and (5.8). The electrolyte contained 2 mM Ru(NH₃)₆Cl₃ in various concentrations of KCl(aq). The statistical uncertainties on each value of transfer coefficient are of order 1% or less 115

Figure 5.8. Effective differential capacitance at 1 kHz for a Bi electrode in 10 mM NaCl(aq) against dc potential..... 117

Figure 5.9. Contribution of (Δα) to the measured transfer coefficient α(E) (Fig.5.7) arising from the reduction of the anodic film. The data was calculated according to equation (5.16) using the experimental differential capacitance of Fig.5.8 120

Figure 5.10. Values of relative φ₂ estimated from the variation of charge transfer resistance with ionic strength according to equation (5.12). The data was obtained for a Bi electrode in 2 mM Ru(NH₃)₆Cl₃ (aq). The reference ionic strength was chosen to be the highest employed (electrolyte = 0.2 M KCl(aq)) at which φ₂ is expected to be small..... 120

<i>Figure 5.11. Ex-situ photoemission spectra of Bi electrodes emersed from 0.1 M NaCl(aq) electrolyte. (a) Bi 4f spectra and (b) Cl 2p spectra</i>	<i>121</i>
<i>Figure 6.1. UV-Vis absorption spectrum of pure water AgNPs before dialysis</i>	<i>129</i>
<i>Figure 6.2. UV-Vis absorption spectrum of AgNPs after dialysis against pure water for 73 h</i>	<i>130</i>
<i>Figure 6.3. UV-Vis absorption spectrum of 10 mM Na₂SO₄-AgNPs before dialysis run 1 with a peak wavelength of 420 nm and a peak absorbance of 1.06</i>	<i>130</i>
<i>Figure 6.4. Interparticle interaction potential according to the DLVO theory for two identical spherical particles</i>	<i>132</i>
<i>Figure 6.5. DLS analysis of pure water AgNPs before dialysis showing particles with a mean diameter of 31.1 nm and a PDI of 0.26. The peak for particles at size 1-10 nm is probably an artefact resulting from impurities or other extraneous scattering sources, while the lower intensity of 30 % is for particles of sizes ranging from 10-100 nm</i>	<i>134</i>
<i>Figure 6.6. DLS analysis histogram of pure water AgNPs before dialysis showing the size ranges of the isolated and aggregate particles</i>	<i>134</i>
<i>Figure 6.7. DLS analysis of pure water AgNPs after dialysis. They are more populated with particles about 100 nm in size with a light scattering intensity of 79%</i>	<i>135</i>
<i>Figure 6.8. DLS analysis histogram of pure water AgNPs after dialysis with a PDI value of 0.72 indicating that the particles are highly polydisperse</i>	<i>135</i>
<i>Figure 6.9. DLS analysis of 10 mM NaCl-AgNPs particles before dialysis with diameter of 102 nm and polydispersity index of 0.50</i>	<i>136</i>
<i>Figure 6.10. DLS analysis histogram of 10 mM NaCl-AgNPs before dialysis</i>	<i>136</i>
<i>Figure 6.11. Schematic diagram of the AFM measurement of AgNPs. The blue circles represent individual AgNPs and the curves with arrows indicate the path of the AFM tip as it passes over the sample (ignoring the tapping motion for simplicity). (a) Samples comprising well-separated AgNPs give roughly the same particle size whether it is obtained from the height of the feature or its lateral dimension (denoted diameter). (b) If monolayer islands of AgNPs form on the surface, the feature height will roughly match the diameter from DLS, but the feature diameter will be much</i>	

larger. (c) The formation of clusters of AgNPs is also possible and this will result in feature heights larger than individual particle diameters and possibly larger than DLS sizes..... 137

Figure 6.12. (A) AFM image of 10 mM NaCl-AgNps before dialysis showing the line profile of 03 particles (B) 10 mM NaCl-AgNPs after dialysis with a line profile of 02 particles. The scale bars are as indicated on the images. The sample aliquot was drop cast on Si wafer that had been cleaned with acid piranha solution, properly rinsed with nanopure water and dried with a stream of nitrogen gas 139

Figure 6.13. (A) Diameter histogram of 10 mM NaCl(aq)-AgNPs before dialysis showing 19 particles with a mean size of 451 nm and standard deviation of 385 nm. (B) Diameter histogram of 10 mM NaCl(aq)-AgNPs after dialysis showing 126 particles with a mean size of 199 nm and standard deviation of 102 nm. 140

Figure 6.14. AFM images of 30 mM NaCl(aq)-AgNPs (A) showing single particles before dialysis and (B) aggregates after dialysis. The sample aliquot was drop cast on Si wafer that had been cleaned with acid piranha solution, properly rinsed with nanopure water and dried with a stream of nitrogen gas 141

Figure 6.15. (A) Height histogram of 30 mM NaCl(aq)-AgNPs before dialysis showing 43 particles with a mean size 10.9 nm and a standard deviation of 2.7 nm. (B) Height histogram of 30 mM NaCl(aq)-AgNPs after dialysis showing 09 particles with mean size of 135 nm and a standard deviation of 81.7 nm 142

Figure 6.16. AFM images of 10 mM Na₂SO₄(aq)-AgNPs (A) before dialysis and (B) after dialysis; all with scan size of 4 μm and scale bars as indicated on the images. . The sample aliquot was drop cast on Si wafer that had been cleaned with acid piranha solution, properly rinsed with nanopure water and dried with a stream of nitrogen gas 144

Figure 6.17. (A) Diameter histogram of 10 mM Na₂SO₄(aq)-AgNPs before dialysis showing 30 particles with a mean size of 254 nm and a standard deviation of 121 nm. (B) Diameter histogram of 10 mM Na₂SO₄(aq)-AgNPs after dialysis showing 42 particles with a mean size of 100 nm and a standard deviation of 25.1 nm..... 145

Figure 6.18. Baseline corrected calibration curve for stripping at AgNO₃(aq) 147

Figure 6.19. Variation of [Ag(I)] with time of dialysis for four different sets of experiments to show the composition of the medium against which the sample was dialysed..... 148

Figure 6.20. Anodic stripping voltammogram for 20 μM $\text{AgNO}_3(\text{aq})$ in 0.1 M $\text{NaNO}_3(\text{aq})$. The data is presented as was acquired, before baseline correction. The Ag stripping peak is observed just below 0.1 V and the scan rate was 1 V s⁻¹ 148

Figure 6.21. (A) Anodic stripping voltammogram for 1st fraction of 50 mM $\text{NaCl}(\text{aq})$ -AgNPs dialysate at glassy carbon. (B) Anodic stripping voltammogram for 5th fraction of 50 mM $\text{NaCl}(\text{aq})$ -AgNPs dialysate at glassy carbon. The data is presented as was acquired, before baseline correction. The Ag stripping peaks are observed just below 0.2 V and the scan rate was 1 V s⁻¹ 149

List of Schemes

<i>Scheme 1.1 The electron transfer process between MV^{2+} and MV^+</i>	<i>18</i>
<i>Scheme 1.2. The redox couple of AQS and its dianion AQS^{2-}</i>	<i>19</i>
<i>Scheme 1.3. Structure of cobaltocenium hexafluorophosphate.....</i>	<i>21</i>
<i>Scheme 1.4. The cobaltocenium/cobaltocene redox couple showing a one-electron transfer.....</i>	<i>21</i>
<i>Scheme 1.5. Structure of hexaammine cobalt(III) chloride.</i>	<i>23</i>
<i>Scheme 1.6. Structure of bonding in hexaammine cobalt(III) complex.....</i>	<i>23</i>
<i>Scheme 1.7. d-orbital splitting in hexaammine cobalt(III).....</i>	<i>24</i>
<i>Scheme 1.8. Electron transfer in hexaammine cobalt (III)</i>	<i>24</i>
<i>Scheme 1.9. The structure of ruthenium hexaamine (hexaamine ruthenium (III) chloride).....</i>	<i>25</i>

List of Tables

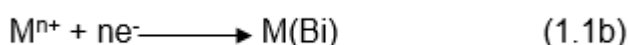
<i>Table 4.1. Mean values of standard rate constants for $\text{CoCp}_2^{+3/+2}$ at bismuth.....</i>	<i>103</i>
<i>Table 6.1. Summary of DLS data on particle sizes for pure water and NaCl-AgNPs.....</i>	<i>136</i>
<i>Table 6.2. Summary of AFM data obtained for NaCl-AgNPs. SD is the standard deviation of the feature height (Ht) or of the feature lateral diameter (dia) in nm.....</i>	<i>143</i>
<i>Table 6.3. Summary of AFM data for 10 mM $\text{Na}_2\text{SO}_4(\text{aq})$-AgNPs. SD is the standard deviation of the feature height (Ht) or of the feature lateral diameter (Dia) in nm.....</i>	<i>146</i>

Chapter 1. Introduction

1.1 Bismuth electrodes.

In the search for an electrode material that will replace mercury in electroanalysis, research has centred on bismuth owing largely to its reputation as benign to the environment and to many species.¹⁻⁸ A number of factors account for the environmental friendliness of bismuth. These include its extremely low toxicity compared to mercury and widespread pharmaceutical use. It can also form multicomponent, low melting temperature alloys with numerous heavy metals.^{1,4,6,8} Other features of bismuth electrodes that are favourable for its use as an electrode material include low cost and ease of fabrication because of the relatively low melting point of the semi-metal as well as relative insensitivity to dissolved oxygen in aqueous solutions by comparison with mercury.^{2,6,9,10}

Bismuth electrodes can be broadly classified into bismuth bulk electrodes (BiBEs)¹¹⁻¹³ and bismuth film electrodes (BiFEs).¹⁴⁻¹⁶ Factors that are responsible for the differences between bismuth bulk and film electrodes include surface roughness or morphology¹² and the substrate¹ that forms the support for the electrode material. Whereas bismuth bulk electrodes are essentially made of polycrystalline bismuth, bismuth film electrodes constitute of a thin film of Bi(III) ions; by their *in situ* reduction and deposition over a substrate such as glassy carbon or carbon paste^{1,7,10} as illustrated in equation 1.1.



Other carbon substrates used in bismuth film electrodes include pencil-lead, wax impregnated graphite and screen-printed carbon ink.¹⁷ The conductivity of polycrystalline bismuth is lower than that of glassy carbon used as substrate in BiFEs.¹² Consequently, BiBEs may exhibit lower responses than BiFEs. Bismuth film electrodes are often employed in stripping analysis and the use of a thin film increases sensitivity of the measurement. The low activity of BiBEs in electrochemical processes has also been attributed to their relatively low density of states (DOS); the carrier density is of the order of $3 \times 10^{17} \text{ cm}^{-3} \text{ eV}^{-1}$ while that of

platinum, a typical metal is $1.2 \times 10^{23} \text{ cm}^{-3} \text{ eV}^{-1}$.¹⁸⁻²⁰ This carrier density is typical of a semi-metal.²⁰ In a semi-metal, one band is almost filled and another almost empty, e.g., as a result of the conduction edge being slightly lower than the valence band edge. The small overlap of the conduction and valence bands leads to a small density of states near the Fermi level and a small carrier density. Another implication of the small overlap of the conduction and valence bands is that, high energy electrons in the valence band can enter into the conduction band without excitation. If energy is supplied in the form of heat, more valence electrons will move to the conduction band, hence increase in conductivity. A diagram to illustrate the difference between a metal and a semi-metal in terms of density of states is shown in *figure 1.1*.

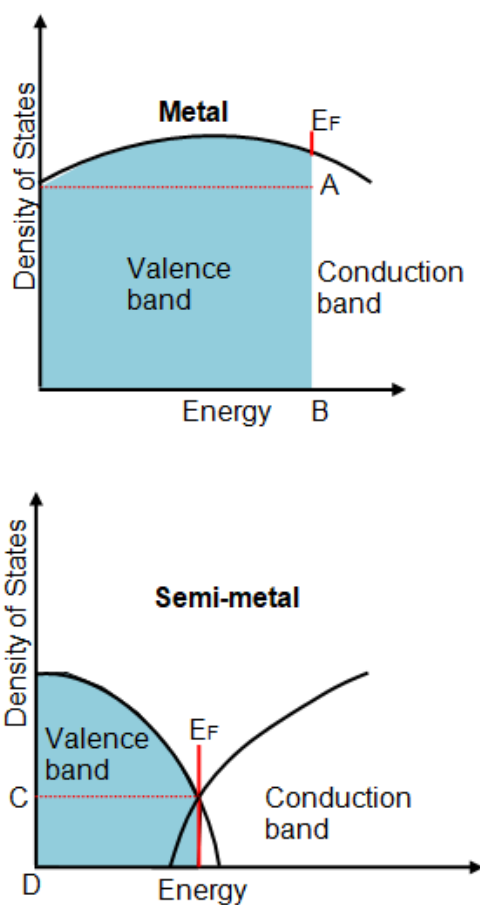


Figure 1.1 Diagram to illustrate the variation in density of states near the Fermi level between metals and semi-metals. Filled states are shaded blue, while E_F indicates the energy corresponding to the Fermi-level. The areas under the rectangles of width AB and CD clearly show how the concentration of electrons in the valence band in metals is higher than that in semi-metals.

This partly explains the lower electroactivity of bismuth bulk electrodes compared to the noble metal electrodes and to bismuth film electrodes with glassy carbon as substrate. However, it should be noted that the surface of elemental Bi has different

properties from the bulk and there is evidence that the carrier density at the surface of BiBEs is comparable to metal electrodes.¹⁹

Bismuth bulk electrodes also have a very wide potential window in alkaline media: as large as -0.47 V to -1.70 V in 0.1 M NaOH has been reported.¹² The smooth surface of BiBEs can also be easily regenerated by polishing.¹

One major shortcoming of BiBEs however lies in their oxidation at high positive potentials^{10,12}, although in compensation, their operational potential window usually extends towards more negative potentials than common electrode materials such as Pt, Au and C.

The use of bismuth electrodes has covered measurements of differential capacitance, kinetic studies of reactions, monitoring of trace metal concentrations through different forms of stripping voltammetry, and applications in sensors.^{4,7,8,19,21} In the rest of the chapter, some of the theoretical background to these aspects will be reviewed, focusing on those concepts of importance for the discussion of the results in Chapters 3-5. The known properties of various redox couples employed in Chapters 4-5 will also be discussed. Finally, there is a section on silver nanoparticles as preparation for chapter 6. This part of the work did not involve Bi electrodes (Ag(I) oxidises Bi), however electroanalytical techniques are employed in Chapter 6 to study the release of Ag(I) from nanoparticles although carbon-based electrodes were found to be superior for the purpose.

1.1.1 Measurement of differential capacitance.

The differential capacitance of bismuth bulk and film electrodes has been measured in aqueous²¹⁻²³, ethanol²⁴⁻²⁶, methanol and propanol²² as well as in acetonitrile^{13,19} electrolytes. As observed in this work as reported in chapter 3, the $C_d - E$ curves for Bi in aqueous solutions yielded data with maxima rather than the minima expected on the basis of simple double layer theories. The maxima have been attributed to adsorption of the various halide ions of Cl^- , Br^- , and I^- on the electrode surface. The irregular variation of differential capacitance with concentration presented in this work has also been reported elsewhere²³, where it decreased with increasing concentration of 1,6-hexanediol (HD) in aqueous Na_2SO_4 but started to rise as the concentration of the HD exceeded 0.5 M.

Comparisons of the findings of this research with the works cited above indicate similar trends as regards the performance of the bismuth electrode in acetonitrile solutions. The C_d-E curves had minimum values, and their small sizes was explained to be due to weak adsorptions of the ClO_4^- on the electrode surface as well as the relatively low dielectric constant of acetonitrile.

In this work, the potential of zero charge, PZC at bismuth has been estimated to be -0.49 V vs aqueous Ag/AgCl in the electrolyte mixture of $\text{NaNO}_3/\text{NaCl}$. This value compares favourably with the -0.5 ± 0.01 V vs aqueous saturated calomel electrode in LiClO_4/AN reported by Vaartnou and Lust¹³ for the Bi(III) crystal plane.

The similarity in the findings of this work with that of other researchers is an indication that electrochemical analyses at Bi could be reproducible, despite the different environments and reaction conditions.

1.1.2 Kinetic studies at Bi

Electron transfer rates of various analytes at the Bi electrode surface have been reported.^{19,27-29} Standard rate constants for stripping of Zn^{2+} , Cd^{2+} , and Pb^{2+} at bismuth film electrodes as reported by Mirceski *et al*²⁹ indicate reproducibility as they range from 1 to 3 cm s^{-1} for solutions of all the three metal analytes. A detailed study of the reduction kinetics of cobalt hexaammine by rotating disc methods has been reported and the rate constants interpreted in terms of inner layer effects.³⁰ Similarly, standard rate constants (k^0) and transfer coefficients (α) for the first one-electron reduction of methyl viologen and five derivatives at a bismuth bulk electrode as reported by Cook and Horrocks¹⁹ do not show marked differences compared to Pt electrodes, but do show strong double layer effects on the rates. While the values of transfer coefficient obtained by these authors are about 0.5 as expected for outer sphere reactions, a lower value of 0.34 for diazepam²⁷ at a bismuth-pencil graphite electrode could be a result of the absence of a supporting electrolyte in the diazepam solutions. It is however worthy of note that bismuth electrodes have been successfully used in the measurement of rates of reactions.³⁰

1.1.3 Bismuth electrodes in stripping voltammetry

Reports abound in the literature on the use of the various forms of bismuth based electrodes in the determination of trace metals. The different voltammetric techniques

employed include anodic stripping voltammetry (ASV)^{4,10,12,14,31-34} and its variants of adsorptive stripping voltammetry (AdSV)^{9,35,36} which have been used in the determination of *Co*, *Ni* and *Se(IV)*. Square wave anodic stripping voltammetry (SWASV)^{37,38} has been utilized for the determination of *Cd(II)* and *Pb(II)*. Trace metal concentrations that have been monitored with bismuth electrodes include those of *Cd*, *Pb*, *Zn*, *Tl*, *Ni*, *Cu*, *Co*, *Al*, *Fe*, *In*, *Cr*¹, while differential pulse voltammetry (DPV) has been used in the detection of organic compounds using bismuth film electrodes. As at the 10th anniversary of the use of bismuth electrodes in electroanalysis, about 200 reports of analyses were published using the various voltammetric techniques.² This allows for a projection of more than double this value by the year 2020 when these electrodes would have been under investigation for 20 years.

It is interesting to note that BiBEs which make up the main study of this work have also been used in trace analysis of *Zn*, *Cd* and *Pb*. However, they could not be utilized in the estimation of *Ag(I)* from dialysates of silver nanoparticles because of the high electrode potential of this noble metal (Chapter 6). In general, the anodic oxidation of bismuth appears to be an important limitation on its use in electroanalysis.

1.1.4 Application of bismuth electrodes in sensors

The environmentally benign characteristics of bismuth which include ease of handling, low toxicity hence safe disposal and low cost have been exploited in the production of sensors^{5,8,16,39,40} for sampling and monitoring of various products. An example is the bismuth-based sensor for the detection of hydrogen sulphide gas. This sensor with a wet, porous, paper-like substrate coated with Bi(OH)_3 is said to be suitable for testing human bad breath⁴¹ and its sensitivity is at least 2 orders of magnitude more than the commercial lead(II) acetate test paper.

While many of these bismuth-based sensors use the technique of stripping voltammetry, it has become expedient to group these electrodes differently because of the precision and speed with which determinations are made. Worthy of note is the report by Jothimuthu *et al*⁵ who affirm the precision of the low-cost based bismuth sensor that needs only about 2 drops of blood and provides results on the level of heavy metal in 10 minutes, compared to the mercury-based sensor which uses 5 mL of blood to deliver results in 48 h. With this relatively short time of operation, this

device has an additional advantage that it can be used to assess a large population of patients especially in rural but high risk areas that have limited access to analytical laboratories.

In addition, the extended cathodic potential window of -0.3 to -1.9 V enabled the detection of electronegative manganese (Mn) with a stripping peak at -1.47 V vs Ag/AgCl(3 M KCl).⁵

1.2 Electrical double layer and capacitance

The electrical double layer is a term used to describe the ionic environment in the vicinity of an electrode|electrolyte interface. It may also be described as the array of charged particles and/or oriented dipoles present at a material interface.⁴²

Helmholtz was the first scientist who in 1853 proposed the existence of a defined order of negative and positive charges at interfaces.⁴³ He likened the behaviour of the interface between a metallic electrode and an electrolyte solution to that of a parallel plate capacitor, a device that can store electric charge. This means that the stored charge density will vary with potential across the plates according to equation 1.2 where ϵ is the dielectric constant (now more commonly referred to as the relative permittivity) and ϵ_0 , the vacuum permittivity, while d is distance between the plates.

□

$$\frac{\partial \sigma}{\partial V} = C_d = \frac{\epsilon \epsilon_0}{d} \quad (1.2)$$

σ is the charge density ($C\ m^{-2}$), E the applied potential (V) and C_d is the differential capacitance per unit area ($F\ m^{-2}$). This equation predicts the differential capacitance of the system to be independent of concentration and also of potential as neither the concentration of the medium nor the dc potential appear in equation 1.2.

In this model, Helmholtz assumed that the electrode holds a charge (q^m) which arises from either an excess or deficiency of electrons at the electrode surface and that this charge is balanced by an amount of equal but oppositely charged ions at a plane a fixed distance from the metal in solution (q^s) so that the electrical neutrality of the interface is maintained. This means $q^m = -q^s$ or $q^m + q^s = 0$.

The solution side of the double layer is assumed to be made of several distinct parts.^{42,44} The inner layer closest to the electrode, known as the inner Helmholtz plane (IHP) contains solvent molecules and specifically adsorbed ions, which are not fully solvated. The next closest layer, the outer Helmholtz plane (OHP) is characteristic of solvated ions at their closest approach to the electrode surface. These solvated ions are non-specifically adsorbed hence are attracted to the metal surface by long-range electrostatic forces. The IHP and OHP together make up the compact layer.

A sketch of the Helmholtz model is shown in figure 1.2 below. Figure.1

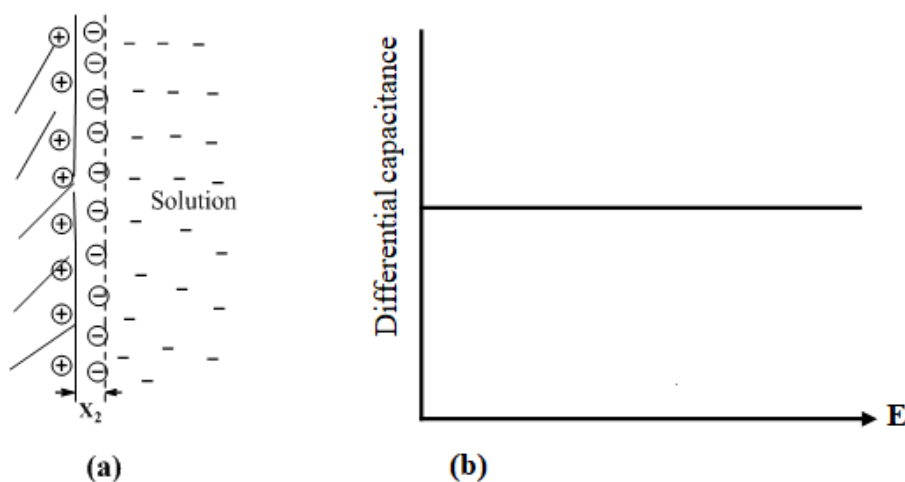


Figure. 1.2 Sketch of the Helmholtz model of the double layer showing (a) rigid arrangement of ions, X_2 being the distance of closest approach of the charges to the electrode (b) variation of C_d with applied potential.

The shortcomings of this model are that (i) it assumes the electrode - electrolyte interface to be static, especially for ions further away from the electrode than the first layer as these solvated ions would have to approach the electrode through a distance limited by a monolayer of solvent molecules assumed to exist between them and the electrode (ii) it does not account for electrolyte concentration effects on the capacitance. (iii) it does not incorporate presence of a diffuse layer, i.e., counter charges not rigidly bound to the OHP.

Gouy-Chapman Model

Within the period of 1910-1913, Gouy and Chapman developed the double layer model which predicted the dependence of double layer capacitance on applied potential and electrolyte concentration. According to these authors, the double layer

would not be compact as in Helmholtz model⁴³ but would be of variable thickness, with the ions being free to move. This *diffuse double layer* therefore allows for a distribution of counterions to extend from the OHP into the bulk solution due to thermal agitation, owing largely to the fact that the solvated ions are non-specifically adsorbed.^{42,44} The total charge of the compact and diffuse layers would be equal (but opposite in sign) to the net charge on the electrode side.

Although a significant contribution, the Gouy-Chapman model failed to explain the experimental variations of the capacitance-potential curves for potentials far from PZC and at high electrolyte concentrations.⁴⁴ Furthermore, measured capacitance values were found to be much lower than calculated values. In essence, the capacitance|potential curves could be said to be incorrect as the predicted dependence on concentration and potential was not completely observed. The source of these issues is the lack of accounting for the finite sizes of the ions which allows them to approach the electrode arbitrarily closely in the Gouy-Chapman model. The result is an overestimation of the capacitance at potentials far from that at which the electrode is uncharged (PZC, potential of zero charge). However, the model does provide a mechanism for concentration and potential dependence of C_d that is absent in the earlier Helmholtz model.

A sketch of the Gouy-Chapman model is presented in the *figure* below.

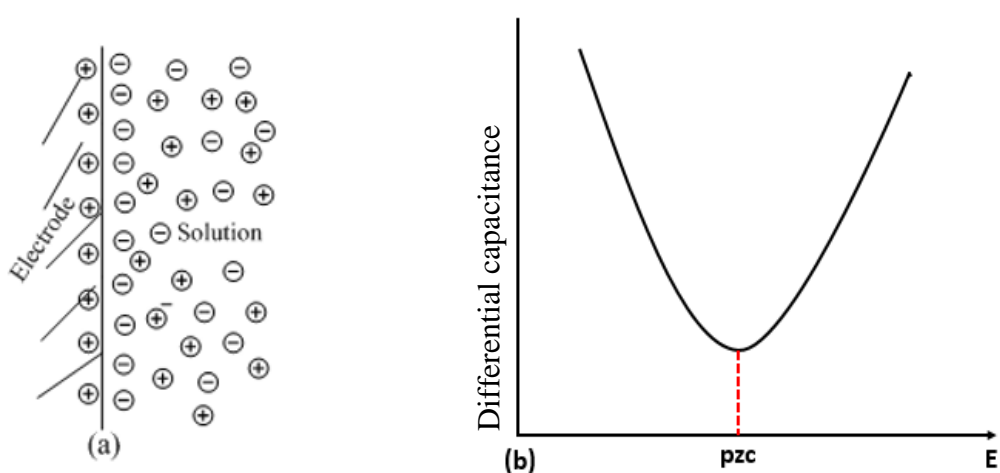


Figure 1.3. Sketch of the Gouy-Chapman model showing (a) diffuse arrangement of ions and (b) variation of differential capacitance (C_d) with potential.

The Stern Model

A further input into the nature of the double layer was made by Stern.⁴⁵ He combined the two previous models of Helmholtz and Gouy-Chapman, by suggesting that the double layer was formed by a compact layer of ions next to the electrode, followed by a diffuse layer extending into the bulk solution. By identifying two distinct layers of the electrical double layer, Stern was able to account for the main experimental findings regarding metal electrode capacitance. The dependence of the double layer capacitance on electrode potential is caused by the compression of the diffuse layer as the charge on the electrode is increased in the manner described by Gouy and Chapman. However, the finite sizes of the ions are partly accounted for by including a distance of closest approach, the OHP.

Another implication of the two distinct layers is that two capacitors must be operational in determining the total capacitance of the double layer interface. Stern was able to explain the experimental capacitance-potential curves in terms of the series combination of the Helmholtz and Gouy-Chapman capacitances and the applied potential with respect to the potential of zero charge, *PZC*. Far from the *PZC*, the electrode exerts a strong attraction towards the ions, which are attached rigidly to the surface, with the potential drop being restricted to the compact layer. Close to *PZC* however, there is diffuse distribution of ions - the diffuse layer.⁴³

The foregoing analysis can be summed up in a statement that the capacitance of the double layer consists of a combination of the capacitance of the compact layer in series with that of the diffuse layer. For two capacitors in series, the total capacitance is given by equation 1.3 in which C_H and C_G represent the capacitance of the compact and diffuse layers after Helmholtz and Gouy-Chapman respectively.

$$\frac{1}{C} = \frac{1}{C_H} + \frac{1}{C_G} \quad (1.3)$$

This finding proved to be significant since it indicates that the smaller of the two capacitances determines the observed or total capacitance.^{42,43} The value of C_G is greatly affected by the electrolyte concentration whereas the compact layer is largely independent of concentration. This model predicts that, at high electrolyte concentrations, or at potentials far from *PZC*, most of the charge is accumulated near

the outer Helmholtz plane with little scattered diffusely into the solution. Under such conditions, $1/C_H \gg \gg 1/C_G$ hence from equation (1.3),

$$1/C \approx 1/C_H \text{ or } C \approx C_H \quad (1.4)$$

Conversely, for dilute solutions (close to *PZC* according to Stern), there is diffuse distribution of ions and C_G is very small compared to C_H so $1/C_G \gg \gg 1/C_H$ hence $C \approx C_G$.

A sketch of the differential capacitance predicted by Stern model is shown in figure 1.4.

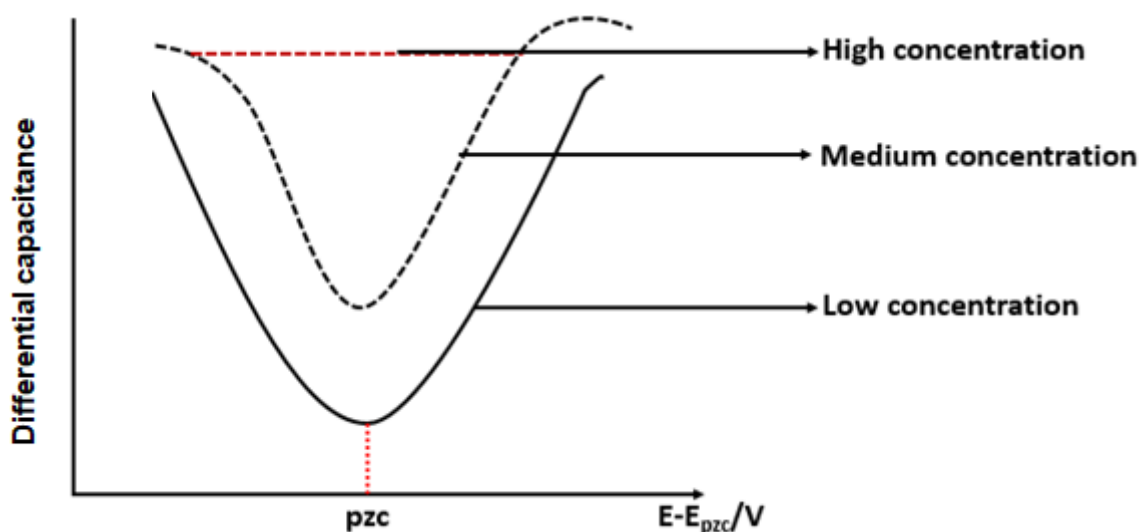


Figure 1.4 Gouy-Chapman-Stern model showing variation of C_d with potential as concentration changes.

The Grahame Model

In 1947, Grahame⁴⁶ after agreeing with Stern that some ions were adsorbed at the electrode surface and others diffusely dispersed in solution went further to identify the existence of specifically adsorbed ions. Specific adsorption is the adsorption of ions at the electrode surface after they have lost their solvation completely or partially⁴³. These ions can have the same charge as the electrode or the opposite charge, yet chemical bonding of the ions with the electrode can still be very strong. This affects the capacitance because any change in the distance of closest approach (d in equation 1.2) affects the capacitance of the Helmholtz part.

The Bockris, Devanathan and Muller Model

In 1963, Bockris *et al*⁴⁷ proposed a double layer model which takes into account, the role of the solvent. All the other models have considered the effect of electrolyte in terms of the ionic solutes. The fact that solvent concentration is always much higher than that of the solute underscores the significance of the contribution of Bockris and his co-workers.

Double Layer Capacitance

From the foregoing discussions, it can be summarised that the electrical double layer is made up of two layers of charge and a potential drop which varies across the Helmholtz plane into the bulk solution. The double layer therefore behaves much like a parallel plate capacitor.^{43,44} For such an ideal capacitor, the charge is directly proportional to applied potential in accordance with the equation,

$$\sigma = C_d E \quad (1.5)$$

The charge on the capacitor arises due to an excess of electrons on one plate and a deficit of electrons on the other. The electrode|solution interface is no less different, for at any given potential, there exists a charge q^m on the metal electrode and a charge q^s in solution. The sign of the charge on the metal electrode with respect to the solution however depends on the potential across the interface and the solution composition. In any case, at every material time, $q^m + q^s = 0$ for overall electrical neutrality of the solution.

The charge on the metal, q^m resides in a very thin layer on the metal surface whereas the charge, q^s of the solution comprises of either an excess or deficiency of cations or anions in the vicinity of the electrode surface. To be able to account for the actual regions where these charges reside, they are often divided by the electrode area and expressed as charge densities such as $\sigma^m = \frac{q^m}{A}$ for the metal electrode, with units of $\mu\text{C cm}^{-2}$. Therefore, at any given potential, the electrode -solution interface is characterized by a double layer capacitance C_d whose experimental values have been found to typically lie between 10 to 40 $\mu\text{F cm}^{-2}$.^{42,44}

Unlike real capacitors whose capacitances are independent of potential, double layer capacitance C_d varies with both applied potential and concentration as earlier

discussed under the Gouy-Chapman model. The capacitance of the interface is characterized by its ability to store charge in response to a change in applied potential. Therefore as the electrode becomes more highly charged due to an increase in potential, the diffuse layer would become more compact and C_d would increase.

Furthermore, the electrostatic potential which gives rise to C_d varies linearly with distance from the electrode to the OHP then decreases exponentially into the bulk solution. Dependence of double layer capacitance on electrolyte concentration can likewise be explained in the light of the compression of the diffuse layer. With an increase in electrolyte concentration, the rate of diffusion will increase resulting into high adsorption (both specific and non-specific) onto the electrode surface with an overall increase in capacitance.

Potential of Zero Charge

The potential of zero charge *PZC*, also known as point of zero charge may be regarded as where the sign of the electrode charge is reversed and no net charge exists on the electrode.⁴² *PZC* is the value of potential at which an electrode surface will not acquire an electrical charge when in contact with an electrolyte.

When determined in relation to pH of an electrolyte, the *PZC* is the pH value at which a solid submerged in an electrolyte exhibits an electrical charge of zero on the surface⁴⁸. The pH value is however used to describe *PZC* for systems in which $H^+|OH^-$ are the only ions that determine the potential. According to IUPAC⁴⁹, *PZC* is the value of electric potential of an electrode (measured against a stated reference electrode) at which one of the charges defined is zero. In terms of *PZC* therefore, IUPAC defines the electrode potential difference as

$$\Delta E = E - E_{\sigma=0} \quad (1.6)$$

where E is the potential of the electrode against a stated reference electrode and $E_{\sigma=0}$ or *PZC* is the potential of the electrode when the surface charge is zero. For systems characteristic of an excess in surface charge like the electrical double layer, the best way to identify the point of zero charge is the existence of a maximum in the surface tension of the metal|solution interface.^{44,48} The potential at which the surface tension is a maximum is called the electrocapillary maximum (ECM). The slope of the

curve of surface tension (γ) versus potential (E) at this point is zero; hence it's the potential of zero charge (PZC). Therefore, at the PZC , the surface tension is a maximum while the electrical capacitance at the boundary is a minimum. Of course the electrocapillary curves are not usually experimentally accessible for solid electrodes and the capacitance measurements are preferred in these cases.

Another significance of PZC is that, it serves a source for further information as to the orientation of dipoles in a metal|solution interface. The metal surface is positively charged at potentials more positive than the PZC ⁵⁰ and water (or solvent molecules in general) will adsorb with a preferred orientation of the electronegative O atom directed towards the metal. If on the other hand, the electrode potential is negative with respect to PZC , then positive ions will be attracted to the metal surface. This knowledge is important in environmental studies as it helps determine how easily a substrate is able to adsorb potentially harmful ions such as Cd , Pb and Hg .

PZC is also vital in the study of colloidal systems. At zero zeta potential, the colloidal particles of the system will remain stationary under an applied electric field, giving rise to maximum coagulation of particles in the solid phase and a high viscosity of the dispersion medium.

1.3 Frumkin Correction

Owing to the structure of the double layer, the concentration of ions taking part in charge transfer reactions is different from their concentration in the bulk solution. Only those close to the electrode surface can take part in the reaction.

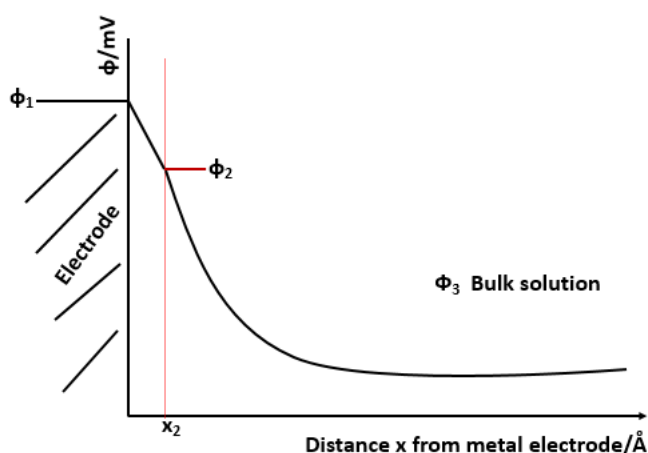


Figure 1.5. Potential profile illustrating electron transfer across the compact double layer at a plane distance x_2 from the electrode.

In the *Figure 1.*, the concentration of analyte at x_2 where electron transfer is assumed to actually take place can be estimated from the Boltzmann distribution using equation 1.7 in which z is the charge on the species and F is Faraday constant. The plane of electron transfer x_2 is considered in principle to be the same as the OHP but it may not be exactly so in practice.

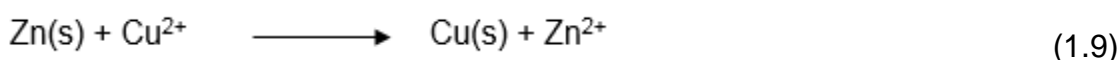
$$C_x = C_o \exp\left(\frac{-zF}{RT}\right) \quad (1.7)$$

The second factor affecting the rate of charge transfer because of double layer structure is the electrostatic potential (ϕ) which in general varies with distance away from the electrode surface. This means that in the figure 1.5, ϕ_1 at the metal electrode will be different from ϕ_2 at the outer Helmholtz plane (OHP). The value of electrostatic potential ϕ_3 in the bulk solution will similarly be different from ϕ_1 and ϕ_2 because of potential drop through the diffuse layer as well as adsorption of some ions.^{44,51} The effective driving force or potential difference at the site of electron transfer would be $\Delta\phi = \phi_1 - \phi_2$ instead of the whole potential drop between the electrode surface and the bulk solution ($\phi_1 - \phi_3$). The observed heterogeneous electron transfer constant has to be corrected to take into account the effects of these two factors of concentration and potential to give the true standard rate constant using equation 1.8. This is known as the Frumkin correction.^{44,51}

$$k_{FC}^o = k^o \exp\left(\frac{-(\alpha - z)F\phi_2}{RT}\right) \quad (1.8)$$

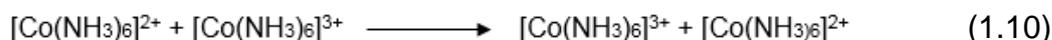
1.4 Electron transfer reactions

An electron transfer reaction may be defined as a reaction in which one or more electrons relocate from one species to another. An elementary reaction that is often used to illustrate electron transfer in the laboratory is that between a strip of Zn metal and Cu^{2+} ions as presented in equation 1.9 in which two electrons are transferred from



Zn metal to copper(II) ions, leading to an increase in the oxidation state of the former and a decrease in the oxidation state of the latter. Marcus⁵² describes such an

electron transfer reaction between two different redox systems as electron transfer “cross sections” to distinguish between self-exchange electron transfer reactions, an example of the $\text{Co}^{3+/2+}$ redox couple illustrated in equation 1.10



Two things are evident in the self-exchange reaction⁵² (i) the products and reactants are identical and (ii) chemical bonds are neither broken nor formed in the electron transfer process, a characteristic property of outer-sphere electron transfer reactions.

Electron transfer reactions may be broadly classified into inner-sphere and outer-sphere transfer reactions.⁵³ The inner-sphere mechanism is characterized by electron transfer via a covalently bonded bridging ligand while electron transfer by the outer-sphere mechanism does not require a covalent linkage between the reactants.

Pioneers in the area of electrode kinetics i.e., rates of reactions at an electrode in solution, John Alfred Butler and Max Volmer, in 1924⁵⁴ formulated the model of equation 1.11 which predicts the exponential dependence of current on potential as well as its linear dependence on concentration.

$$i = F A k^o \left\{ C_O e^{-\alpha F(E-E^o)/RT} - C_R e^{(1-\alpha)F(E-E^o)/RT} \right\} \quad (1.11)$$

It also brought to the fore, concepts of exchange current, charge transfer resistance and transfer coefficient. It is also consistent with thermodynamics for at equilibrium when the rates of forward and backward reaction are equal and there is no current ($i = 0$), it reduces to the Nernst equation (1.12) which links the electrode potential with bulk concentrations⁴⁴.

$$E = E^o + \frac{RT}{nF} \ln \left(\frac{C_O}{C_R} \right) \quad (1.12)$$

Although the Butler-Volmer equation is useful in the treatment of a majority of the problems relating to heterogeneous kinetics, it has some shortcomings e.g., is unable to predict the exact value of the charge transfer coefficient (α) but only assumes it to lie between $0 < \alpha < 1$. The transfer coefficient may be defined from the current-overpotential plot of *figure* 1.6 as a measure of the symmetry of the energy barrier;

and stands for the reductive symmetry factor. The oxidative symmetry factor associated with the backward reaction would therefore be $1-\alpha$.

The standard rate constant k^o may be defined here in terms of the Faradaic current, the passage of which through a potential difference E results in the oxidation/reduction of material in accordance with Faraday's laws. It is the value of the rate constant when the applied potential E is equal to the formal potential E^o . C_O and C_R stand for the concentrations of the oxidized species or reactant and of the reduced species or product respectively. These values are understood to be the concentrations near the electrode surface at the plane at which electron transfer occurs and are not in general equal to the values in the bulk solution.

A plot illustrating the Butler-Volmer equation is shown in the *figure* below.

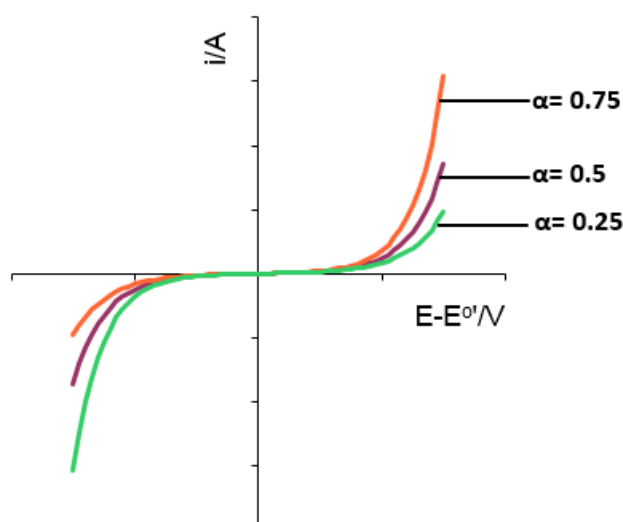


Figure 1.6 Graphical representation of the Butler-Volmer equation showing the effects of changing the potential and the value of the transfer coefficient (α) on the current. The curve was constructed for one-electron transfer at 298 K, with a standard rate constant k_o of 1 cm s^{-1} . The concentrations of the oxidized and reduced species were the same, with a value of $1 \times 10^{-6} \text{ mol cm}^{-3}$.

If the effect of changing the potential is identical on both sides of the energy barrier, then $\alpha = 0.5 = 1 - \alpha$. This current-overpotential plot also enables the estimation of the charge transfer coefficient R_{CT} ; the negative reciprocal of the slope⁴⁴ of the curve at low overpotential ($\eta < 10 \text{ mV}$) where the curve passes through the origin. It is the far right end of equation 1.13 for a one-electron transfer process. Overpotential (η) as indicated in the x-axis of the figure 1.6 is the difference between the potential at zero current (equilibrium) and the potential required to drive a current.

$$R_{CT} = \frac{-1}{\partial i / \partial E} = \frac{RT}{n^2 F^2 k^0 AC} = \frac{RT}{Fi_o} \quad (1.13)$$

The exchange current i_o may be taken to have the same magnitude as either the anodic or cathodic current, as these currents cancel each other to give the net current at equilibrium of zero.

Marcus⁵⁵ in the course of continuing investigations went further to quantify the rate of electron transfer in terms of a rate constant

$$k = Ze^{-\Delta F^*/RT} \quad (1.14)$$

$$\text{where } \Delta F^* = w + m^2 \lambda \quad (1.15)$$

$$\text{and } \alpha = -\left(1/2 + \frac{\Delta F^o + w^p - w}{2\lambda}\right) \quad (1.16)$$

The parameter Z stands for the collision frequency of the particles in solution (or of a particle with the electrode) and w is the work done in bringing the two reactants (or reactant and electrode) together while w^p is the work term for the products. ΔF^o stands for the standard Gibbs free energy of the electron transfer step in the reaction medium while its value for electron transfer at the electrode surface is $-nF\eta_a$ where n is the number of electrons transferred, while m is their mean mass and η_a is the activation overpotential. λ , the reorganization energy, defines the effects of changes in the bond lengths and bond angles in the coordination sphere of the reactants. Marcus' quantitative model was therefore able to predict a value of about 0.5 for the transfer coefficient as well as give insights for the estimation of the energy costs in bringing two reactants (or a reactant and electrode) together.

Chapters 4 and 5 are primarily concerned with the study of redox couples in which electron transfer follows the heterogeneous outer-sphere mechanism in which electron(s) are exchanged between an analyte solution and the electrode surface. A few of those redox couples are therefore reviewed hereunder.

1.4.1 Methyl viologen

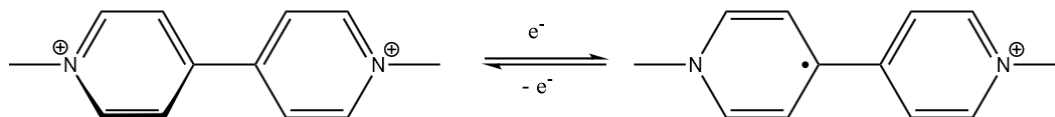
Methyl viologen or paraquat, also known by the trade names of Gramoxone or Herboxone⁵⁶ belongs to a class of 1, 1'- disubstituted- 4- 4'-bipyridinium salts known as viologens. Its IUPAC name is 1, 1 –dimethyl-4-4' –bipyridinium dichloride. The loss of the two chloride ions results in a dication (MV^{2+}) which undergoes a two-step reduction, first to give the monocation radical (MV^+) and then the neutral compound as the final product. The simple 2-step reduction process of the methyl viologen complex is illustrated below:



This monocation complex is oxygen sensitive^{57,58} hence the solution has to be purged with either argon or nitrogen gas to get rid of oxygen in the reaction vessel for consistent results to be achieved.



The neutral compound is of low solubility hence can adsorb on the electrode surface.⁵⁹⁻⁶¹ The structure of the methyl viologen dication and its reduction to the monocation is also shown in *scheme 1.1*



Scheme 1.1 The electron transfer process between MV^{2+} and MV^+

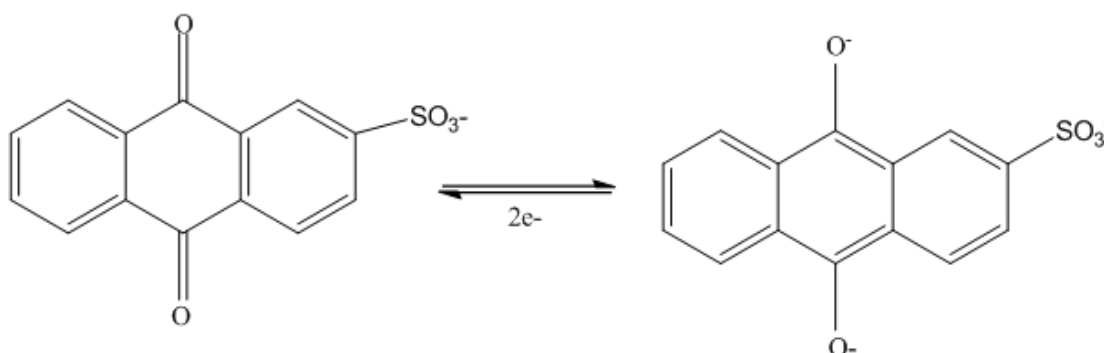
Continuing electrochemical investigations of the reduction of the monocation to the neutral compound are however limited because of dimerization^{19,62,63} of the monovalent compound.

Paraquat is an interesting compound to study because of its toxicity and persistence in the environment^{56,62,64} occasioned by world-wide use as herbicide on a variety of crops. The very high solubility of MV^{2+} in water which facilitates its spray over crops lends credence to why water is a solvent of choice for this compound in electrochemical studies. However, because it is non-biodegradable, continued application of paraquat on food crops increases the health risk of the consumers due

to bioaccumulation. This partly explains why the use of this herbicide is banned in so many countries including the UK.

1.4.2 Sodium anthraquinone-2-sulfonate

Sodium anthraquinone-2-sulfonate (AQS) is a member of the homologous series of substituted 9,10-anthraquinones that form a group of compounds that are used for the indirect cathodic reduction of vat dyes where they act as mediators.^{65,66} The structures of AQS and its reduction product, the dianion are shown in *scheme1.2*



Scheme 1.2. The redox couple of AQS and its dianion AQS²⁻.

It might appear from the redox equation that 2 electrons are transferred simultaneously but the product is actually formed as a result of 2 fast 1-electron transfers, in tune with the current IUPAC definition of the transfer coefficient in electrochemistry⁶⁷ and explanation of associated terms.

The search for mediators or electron shuttlers⁶⁸, soluble and electrochemically active redox couples, arose from the behaviour of some redox systems that undergo very slow heterogeneous electron transfer at electrodes, occasioned by adsorption on the electrode surface. This often led to irreversible electrochemical behavior. Some reducing agents used to aid reduction also showed irreversible behavior. An ideal mediator should be stable in both oxidation states of the oxidized and reduced forms and its formal potential should be in close proximity with that of the redox system under study.^{68,69}

Reductants such as Na₂S₂O₄ and glucose used on dyes as it applies to anthraquinones could not be regenerated as their oxidized forms could not be reversed to the reduced state, resulting in high costs of the dyeing process. To be used efficiently as a mediator for indirect cathodic dye reduction, a redox couple

should possess the desirable quality of being able to undergo regeneration several times without decomposition.⁶⁵ The reduction potential of the mediator system should also be far more negative than that of the dye.^{70,71} For this reason, potential values of < -950 mV vs Ag/AgCl (3 M KCl) are recommended for reduction of vat dyes.⁷² For the indirect reduction of indigo and sulfur dyes, recommended potentials of < -750 mV and < -600 mV respectively are required for optimum dye reduction.^{70,72-74}

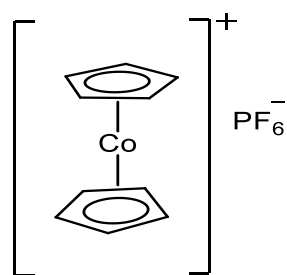
Another important consideration is adsorption on the cellulose fabric during dyeing. A good mediator should exhibit very low substantivity or attachment on the fabric to avoid the shade of dyeing. Bailey and Ritchie⁷¹ have however confirmed that anthraquinone-2-sulfonate was not observed to undergo decomposition over the entire pH range of 0-14 of its investigation.

In this work, cyclic voltammetry (CV), a good technique to use in assessing the viability of a redox couple to serve as a mediator for indirect cathodic reduction was used to study sodium anthraquinone-2-sulfonate in aq. KCl. The data which is presented in Chapter 4 shows good CVs within the cathodic potential range of -0.2 V to -1.0 V for all the concentrations of 2 to 10 mM investigated. In terms of the cathodic potential criterion therefore, AQS can be said to qualify to be used as a mediator for indirect reduction of dyes.

In addition, the compound is completely soluble in the aqueous supporting electrolyte solution of KCl; and because it has been confirmed to work well without decomposition in both acidic and alkaline media, it is safe to conclude that AQS can serve as a mediator for indirect reduction of vat dyes.

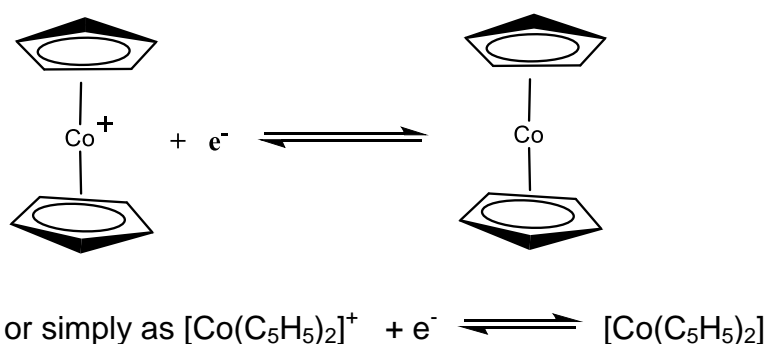
1.4.3 Cobaltocenium hexafluorophosphate

Also known by the IUPAC name of bis(cyclopentadienyl)cobalt(III) hexafluorophosphate, this compound has the condensed formula of C₁₀H₁₀CoF₆P. Its structural formula is shown in *scheme 1.3*.



Scheme 1.3. Structure of cobaltocenium hexafluorophosphate.

The redox couple can be represented in either of the ways of *scheme 1.4*.



Scheme 1.4. The cobaltocenium/cobaltocene redox couple showing a one-electron transfer.

The inclusion of cobaltocenium cation|cobaltocene in the search for reference redox couples followed the IUPAC recommendation⁷⁵ that another metallocene, the ferrocene|ferricenium redox couple be used as a reference redox system for non-aqueous solvents.

In their investigations, Stojanovic and Bond⁷⁶ studied the voltammetric behaviour of cobaltocenium cation (CoCp_2^+) reduction in the aprotic solvents of acetonitrile (AN) and dichloromethane as well as the protic solvents of ethanol and water, using a variety of supporting electrolytes. The conventionally sized working electrodes they employed are hanging mercury drop electrode (HMDE), gold (Au), platinum (Pt) and glassy carbon (GC); as well as their microelectrodes. The voltammetric reduction behaviour of CoCp_2^+ was not similar in the solvents and at the electrodes of investigation. Whereas the peak current ratios approximated to unity at the scan rate of 100 mV s^{-1} for all the electrodes in acetonitrile, dichloromethane and ethanol, values far less than one were recorded for water. In all cases of their investigation, the potential peak separation was in excess of the 59 mV expected of a one-electron

reversible process at 298 K. Unlike the measurements carried out in other solvents, much lower concentrations of CoCp_2^+ and slow scan rates of the order of 10 mV s^{-1} are to be used if the $\text{CoCp}_2^+/\text{CoCp}_2$ is to be used as a reference system for water. In spite of some identified shortcomings, the workers recommended the use of $\text{CoCp}_2^+/\text{CoCp}_2$ as a redox reference system “under certain specified conditions”.

Other researchers⁷⁷⁻⁸⁰ have studied the voltammetric reduction of CoCp_2^+ in ionic liquids, salts that exist in the liquid phase at and around 298 K. Because the room temperature of most laboratory working environments is about 298 K, these compounds are popularly referred to as room temperature ionic liquids (RTILs). Rogers and co-workers⁷⁷ are particularly interested in RTILs because of their very low volatility which makes their working environment relatively safe due to absence of organic vapours, and of their high conductivity which does not necessitate the use of supporting electrolytes, among others. Their main focus in the study of the $\text{CoCp}_2^+/\text{CoCp}_2$ is on diffusion coefficients and viscosity variations in RTILs in line with Stokes –Einstein equation (1.17) in which the diffusion coefficient D varies inversely as the viscosity η .

$$D = \frac{k_B T}{6\pi\eta\alpha} \quad (1.17)$$

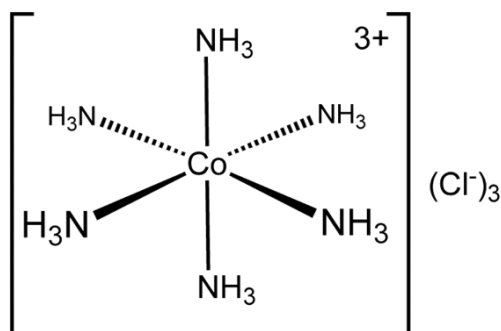
All these researchers recommended $\text{CoCp}_2^+/\text{CoCp}_2$ as a redox reference system based on the results of their investigations.

In this work, cyclic voltammetry was used to study the $\text{CoCp}_2^+/\text{CoCp}_2$ couple in AN/TBAPF₆ and the best voltammograms were obtained at scan rate of 10 mV s^{-1} at both Bi and Pt electrodes, as beyond this it became impossible to locate the cathodic and anodic peaks as the peaks disappeared. The peak current ratio was found to be far less than unity just as the potential peak separation was about 130 mV.

Interestingly, TBAPF₆ which was used as supporting electrolyte here did not feature in any of the research works cited, for a favourable comparison to be made. From these findings therefore, the $\text{CoCp}_2^+/\text{CoCp}_2$ redox couple falls short of being recommended as a reference system at Bi based on the conditions for a one-electron transfer process. In exceptional cases where there is no other reference electrode, the $\text{CoCp}_2^+/\text{CoCp}_2$ redox couple could be used as reference system at slow scan rate of 10 mV s^{-1} for electron transfer at bismuth.

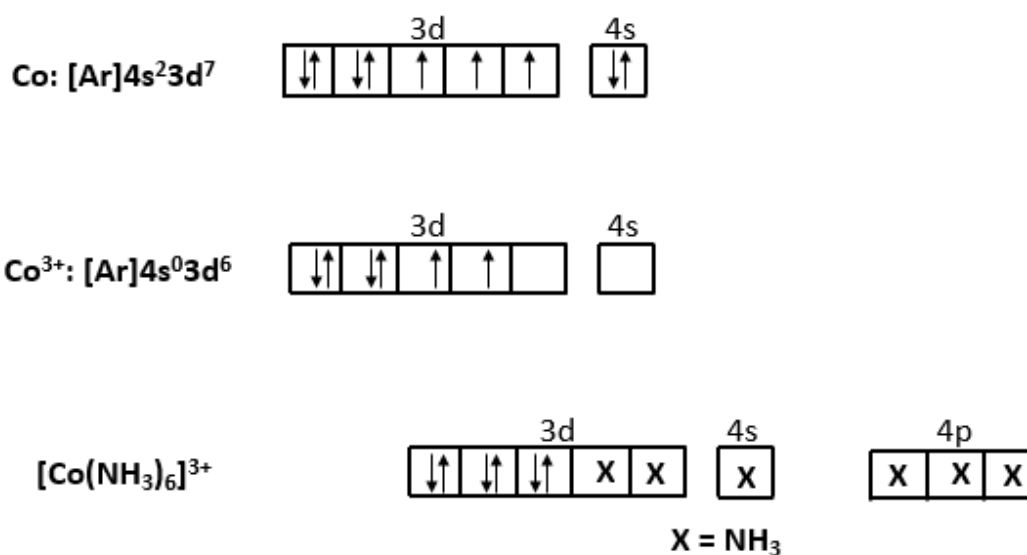
1.4.4 Hexaammine cobalt(III) chloride

Hexaammine cobalt(III) chloride whose structural formula is presented in *scheme 1.5* is an inorganic complex that contains six monodentate ammonia ligands attached to the central cobalt(III) ion with a configuration of $[\text{Ar}]4s^03d^6$.



Scheme 1.5. Structure of hexaammine cobalt(III) chloride.

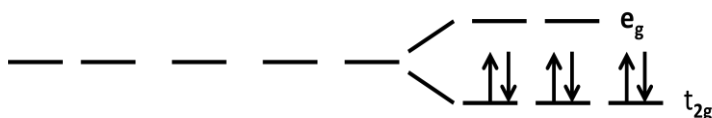
From the spectrochemical series, ammonia (NH_3) is a strong field ligand and their approach forces the unpaired electrons in the Co^{3+} together, resulting in a diamagnetic, low spin inner octahedral complex of d^2sp^3 hybridization. The interaction of the central metal ion with the ligands is illustrated in *scheme 1.6*.



Scheme 1.6. Structure of bonding in hexaammine cobalt(III) complex

Furthermore, the central metal cation is said to obey the 18-electron rule⁸¹ which postulates that the valence shell of the metal consists of nine valence orbitals (1-s, 3-p and 5-d orbitals) which all together can accommodate 18 electrons as either

bonding or antibonding pairs. It is these 9 atomic orbitals that combine with ligands to form 9 molecular orbitals. By obeying the 18- electron rule, $[\text{Co}(\text{NH}_3)_6]^{3+}$ is considered as an 'exchange inert' metal complex more so that the strong field due to NH_3 results in the d-orbital splitting whereby all the six (6) electrons occupy the three t_{2g} subset which are of lower energy for octahedral complexes. When the $[\text{Co}(\text{NH}_3)_6]^{3+}$ complex is to gain an electron, the electron enters in the higher energy e_g which requires extra energy hence the relative inertness of the complex. The d-orbital splitting in the complex is illustrated in *scheme 1.7*.



Scheme 1.7. d-orbital splitting in hexaammine cobalt(III).

The electron transfer process is therefore often irreversible, even though it is a simple outer sphere reaction as indicated in *scheme 1.8*.



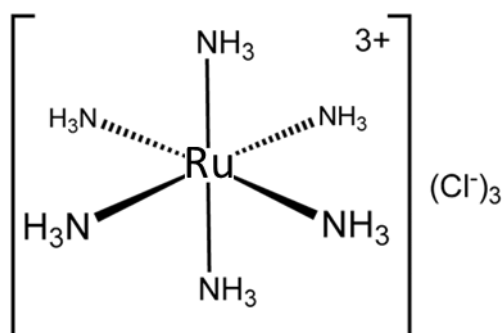
Scheme 1.8. Electron transfer in hexaammine cobalt (III).

The electrochemical behaviour of hexaammine cobalt (III) has been investigated both at gold⁸²⁻⁸⁴ and bismuth^{11,30} electrodes in aqueous HClO_4 solutions and in all these, the irreversible nature of electron transfer in the complex cation has been confirmed. Jager *et al*³⁰ however went further to study the electroreduction kinetics of the complex at Bi(001), Bi(111) and Bi(011) crystal planes using cyclic voltammetry and rotating disc electrode techniques. However, the values of corrected standard rate constants, k_{corr}^0 clearly varied with concentration which is not expected. This suggests that adsorption or other complications were present in the system. Apart from the evidence in the table of results, the authors also admit that "for more concentrated $[\text{Co}(\text{NH}_3)_6]^{3+}$ solutions of the order of 1×10^{-3} M, the value of k_{corr}^0 for the Bi(hkl) is somewhat lower and the weak adsorption of the $[\text{Co}(\text{NH}_3)_6]^{3+}$ seems to be possible". The value of experimental charge transfer coefficient α_{exp} for the most active Bi(001) plane was found to be less than 0.5 and they admit this to be "a noticeable deviation of this interfacial process from classical outer-sphere charge transfer model".

Two years later, Hark and Lust¹¹ which had been part of the team that worked on the electroreduction of $[\text{Co}(\text{NH}_3)_6]^{3+}$ at polished bismuth planes published another report but on Bi(hkl) electrodes in LiClO_4 acidified with $1 \times 10^{-3} \text{ M HClO}_4$. The techniques of cyclic voltammetry and rotating disc electrodes were used. The report on the value of k_{corr}^0 at the concentration of $[\text{Co}(\text{NH}_3)_6]^{3+}$ around $1 \times 10^{-3} \text{ M}$ and at lower values, as well as its adsorption, is not different from the earlier one just as the irreversible electroreduction of the complex cation was confirmed. There is however an improvement in this data in the sense that the value of transfer coefficient α_{exp} was reported to be "slightly higher" than 0.5, even as it depends on the crystallographic structure of the Bi plane.

In this work, the electroactivity of hexaammine cobalt(III) was investigated by CV at both bismuth and platinum electrodes but there were however great signs of adsorption at the bismuth electrode surface. These experimental findings are presented in Chapter 4.

1.4.5 Hexaammine ruthenium(III) chloride



Scheme 1.9. The structure of ruthenium hexaamine (hexaamine ruthenium (III) chloride).

Hexaammine ruthenium(III) chloride whose structural formula is presented in *scheme 1.9* is an inorganic complex that contains six monodentate ammonia ligands attached to the central ruthenium(III) ion with a configuration of $[\text{Kr}]5s^04d^5$. In the same group as Fe, Ru(III) shares a preference for octahedral coordination geometry. In contrast to Co, the t_{2g} orbitals are fully occupied in the Ru(II) or Fe(II) oxidation state and e_g are empty (see *scheme 1.7*). The ligand exchange kinetics, as indicated by the rates of water ligand exchange are much slower in Ru: 10^{-2} s^{-1} for Ru(II) versus 10^6 s^{-1} for Fe(II); this is a typical result for second row transition elements and can be explained on the basis of the crystal field stabilisation energy.⁸⁵

The importance of the Ru(III) electronic structure and ligand exchange kinetics lies in the fact that $\text{Ru}(\text{NH}_3)_6^{3+}$ and $\text{Ru}(\text{NH}_3)_6^{2+}$ are both fairly stable species in aqueous media at neutral pH and the reduction involves addition of an electron to complete the t_{2g} orbitals rather than to the higher energy e_g orbitals. The aqueous $\text{Ru}(\text{NH}_3)_6^{3+/2+}$ couple is therefore widely used as a simple one-electron outer sphere test couple in electrochemistry.^{86,87} This behaviour was observed also at bismuth electrodes and in chapter 5 its voltammetry and electrode kinetics are investigated in detail.

1.5 Silver Nanoparticles: detection of Ag(I) release by electroanalysis.

A substance is considered to be “nano” if it has one dimension in the range 1 – 100 nm. This size range is significant because it accounts for the many changes in the chemical and physical properties of the substance. Silver nanoparticles (AgNPs) may therefore be defined as nanoparticles of silver that are between 1 nm and 100 nm in diameter. They are typically prepared by the reduction of silver salts.

There has been a growing interest in the study of silver nanoparticles because of their very wide applications in almost all spheres of life. Silver nanoparticles (AgNPs) are applied in a variety of products such as socks^{88,89}, sports wears and wound dressings⁹⁰⁻⁹³ to serve as antibacterials and to inhibit unwanted odours. Silver nanoparticles are also incorporated in such consumer products as toothpastes and washing machines and refrigerators.^{94,95} They are also adsorbed on the cellulose fibres of filter paper to work as antibacterial water filter in water and waste water treatment.⁹⁶⁻⁹⁸ Their antimicrobial effects have been demonstrated to work against *S. aureus* at a minimum inhibitory concentration (MIC) range of 0.2 nM to 3.3 nM while MIC of AgNPs against *E. coli* was estimated between 3.3 nM to 6.6 nM.⁹⁹ Suchomel *et al*¹⁰⁰ have been able to compare the efficacy of AgNPs and Ag(I) ion against certain bacteria and fungi. For most cases of bacteria that were tested including *staphylococcus epidermidis* (+) and *staphylococcus aureus* (+), AgNPs were more effective than Ag(I) ions. Silver ions were however observed to be more effective against the fungi of *candida albicans* I and *candida tropicalis* than silver nanoparticles.

Studies have also been conducted on the toxicity of AgNPs against a variety of aquatic organisms including fish.¹⁰¹⁻¹⁰⁹ However in all these, the controversy of whether the toxic effect is mainly due to AgNPs or to Ag^+ ions has not been resolved.

A comparison has however been made¹⁰² with the assertion that Ag^+ exhibited higher toxicity than AgNPs by the inhibition of photosynthesis in *Euglena gracilis*.

Nonetheless, this assertion is questionable as the alga was exposed to unequal concentrations (400 nM Ag^+ and 40 μM AgNPs) of the reacting species.

Toxicity effects of AgNPs to human health^{110,111} have also been investigated in which DNA damage has been prominently featured. DNA damage is characterized by an alteration in the chemical structure of DNA such as a break in its strand or helix. Damage could also be due to a missing base in the backbone of the DNA.¹¹²⁻¹¹⁵

The various products of sports wears, socks, washing machines, cosmetics etc serve as entry routes of AgNPs into humans by absorption into the skin through sweat. As these products are washed or get into water bodies through disposal, the silver nanoparticles leach out, dispersing in water where they may release Ag(I) ions.¹¹⁶

In this work, attempts have been made to estimate the amount of Ag(I) ions released into water bodies based on their sources of discharge. Details of the findings which are presented in Chapter 6 indicate that the final concentration of Ag^+ in simulated aquatic systems is fairly constant, irrespective of the product from which the AgNPs have been released.

Chapter 2. Experimental

2.1 Analyses at Bismuth Electrodes

Bismuth powder (>99.999%) of particle size 150 μm was obtained from Goodfellow Cambridge Limited, England. Sodium nitrate (NaNO_3) and sodium bromide (NaBr) were purchased from BDH Limited Poole, England while sodium chloride (NaCl) was obtained from Alfa Aesar, Lancaster, UK.

Acetonitrile, CH_3CN (AN) and lithium perchlorate, LiClO_4 used in this research are products of Sigma Aldrich, Gillingham, UK. AnaLAR grade ruthenium hexaammine trichloride ($\text{Ru}(\text{NH}_3)_6\text{Cl}_3$), product of Strem Chemicals, Newburyport, USA was purchased from Sigma Aldrich, UK. Similarly, potassium chloride, KCl ($\geq 99.5\%$ purity) used as supporting electrolyte for this complex was obtained from Sigma Aldrich.

Electrochemical grade tetrabutyl ammonium hexafluorophosphate, TBAPF_6 ($\geq 99.0\%$ purity) also used as a solution in AN for an electrolyte as well as the redox couple, cobaltocenium hexafluorophosphate (98% purity), were purchased from Sigma Aldrich, UK and used as received.

Bismuth electrodes were used as working electrodes (WE) in most of the electrochemical measurements carried out in chapters 3 to 5 of this work. Platinum (Pt) was also used as WE when it was desired to compare output of results at such a noble metal electrode with that of bismuth, in which case, gold disc electrode of outer diameter (OD) 6 mm and internal diameter (ID) 3 mm was used as the counter electrode (CE). Platinum disc electrodes, also of OD 6 mm and ID 3 mm and platinum wire were however mainly used as counter electrodes. The surface area of the 3 mm gold and platinum electrodes was 0.071 cm^2 . An Ag/AgCl (1 M KCl) electrode (IJ Cambria, UK) served as the standard reference for aqueous electrolytes. In cases where the presence of excess chloride in the electrolyte was undesirable (Chapter 6), a $\text{Hg}/\text{Hg}_2\text{SO}_4$ (sat K_2SO_4) reference (IJ Cambria, UK) electrode was employed.

In an experiment to trace the sources of peaks observed in the capacitance-potential curves at bismuth, high purity (99.99%) Ag wire of diameter 0.5 mm, purchased from Goodfellow Limited, Cambridge, England was used as reference. The non-aqueous Ag/AgNO_3 (0.01 M) reference (IJ Cambria, UK) was accordingly used for analysis in

the AN/LiClO₄ and TBAPF₆/ electrolyte mixtures. The sources of the peaks were further confirmed by X-ray photoelectron spectroscopy (XPS) and this was done by NEXUS, Newcastle University.

2.2 Preparation of Reagents

Capacitance measurements were conducted separately in pure aq. NaNO₃ solutions and in NaCl as supporting electrolyte. In each case, 100 mM concentration of the salt (molar mass 84.99 g mol⁻¹) was prepared by dissolving 2.1248 g in 250 mL of solution. Nanopure water was used as electrolyte in one case while 0.1 M NaCl was used as supporting electrolyte in the other. The lower concentrations of 50 mM, 30 mM and 10 mM were obtained by dilution.

Similarly, 100 mM NaCl was prepared by dissolving 5.844 g of the salt (molar mass 58.44 g) in enough of nanopure water to give 1000 mL of solution. Lower concentrations of 50 mM, 30 mM and 10 mM were obtained by dilution to 250 mL volumes.

A similar approach was adopted for the preparation of NaBr electrolyte solutions. 2.5725 g of the salt whose molar mass is 102.9 g mol⁻¹ was dissolved in enough of nanopure water in a 250 mL volumetric flask to give a 100 mM solution. Lower concentrations of 50 mM, 30 mm and 10 mM were obtained by serial dilution in flasks of the same capacity.

For lithium perchlorate LiClO₄, 2.6597 g of the salt of molar mass 106.39 g mol⁻¹ was dissolved in enough of acetonitrile CH₃CN (AN), to give a 100 mM concentration in 250 mL of solution. Lower concentrations of 50 mM, 30 mM and 10 mM were equally obtained by dilution using AN as supporting electrolyte.

2.2.1 Ruthenium(III) hexaammine

This compound has a molar mass of 309.61 g mol⁻¹ so 0.3096 g of the complex was measured and dissolved in enough quantity of 0.1 M KCl to give a 10 mM stock solution of the redox couple of 100 mL volume. The lower concentrations of 8 mM, 5 mM and 2 mM were obtained by dilution. In the experiment to determine the effect of ionic strength on electron transfer, 2 mM concentration was prepared in different KCl concentrations of 0.1 M, 0.5 M, 0.1 M, 0.05 M, 0.02 M and 0.01 M.

2.2.2 Methyl viologen dichloride

Methyl viologen dichloride, also known as gramoxone or paraquat dichloride $C_{12}H_{14}Cl_2N_2$, with IUPAC name of 1, 1'-dimethyl-4, 4'-bipyridinium dichloride, and of 98% purity was purchased from Sigma Aldrich, UK. It has molar mass of $257.16 \text{ g mol}^{-1}$ and so to prepare 100 mL of a 10 mM solution, 0.2572 g of the compound was measured and dissolved in enough of 0.1 M KCl. As usual, the lower concentrations of 8 mM, 5 mM and 2 mM were obtained by dilution of the 10 mM stock solution. Experimental surveys revealed the H_2O/CH_3CN mixture as well as aq. NaCl to be good supporting electrolytes for this redox couple but KCl was given preference for purpose of comparison of kinetic data with those of other redox couples studied in the same electrolyte.

2.2.3 Sodium anthraquinone-2-sulfonate monohydrate

This sodium salt of anthraquinone-2-sulfonic acid $C_{14}H_7NaO_5 \cdot H_2O$, of 97% purity was purchased from Sigma Aldrich, UK. It has a molar mass of $328.27 \text{ g mol}^{-1}$ hence to prepare 100 mL of its 10 mM concentration, 0.3283 g was weighed and dissolved in enough of 0.1 M KCl.

2.2.4 Methylene blue hydrate

AnaLAR grade methylene blue hydrate (97% purity), also called methylthionium chloride hydrate $C_{16}H_{18}ClN_3S \cdot xH_2O$ was purchased from Sigma Aldrich, UK. It has molar mass of 319.85 g (anhydrous basis). For a 5 mM solution, 0.0799 g was weighed and dissolved in enough quantity of 0.1 M H_2SO_4 as supporting electrolyte. 10 mL of the 1 M H_2SO_4 present on the bench was taken and added slowly to 50 mL of nanopure water in a 100 mL volumetric flask. After thorough mixing, the flask was made up to the mark with nanopure water.

2.2.5 Toluidine blue

AnaLAR grade toluidine blue dye ($C_{15}H_{16}ClN_3S \cdot 0.5ZnCl_2$) of Sigma Aldrich, UK has molar mass of $373.97 \text{ g mol}^{-1}$. To prepare a 5 mM solution, 0.0935 g of the powder was measured and dissolved in enough quantity of ethanol to give a 50 mL solution.

2.2.6 Hexaammine cobalt(III)chloride

This amine complex with formula $\text{Co}(\text{NH}_3)_6\text{Cl}_3$ has a molar mass of $267.84 \text{ g mol}^{-1}$. A 5 mM solution was prepared by dissolving 0.0669 g of the substance in 50 mL of 0.1 M HClO_4 as electrolyte. The complex powder (of 99% purity) and density of 1.71 g mL^{-1} at $25 \text{ }^\circ\text{C}$ was purchased from Sigma Aldrich, UK.

The assay of perchloric acid indicates a specific gravity of 1.664, implying a density of 1.664 g cm^{-3} , and molar mass of $100.46 \text{ g mol}^{-1}$. The concentration of the pure product was given as 70% w/w which means the stock acid is 11.595 M. To prepare 100 mL of a 0.1 M solution, 0.862 mL was taken and added to 25 mL of nanopure water and mixed thoroughly. The volume was then adjusted to the 100 mL mark by addition of more nanopure water.

2.2.7 Cobaltocenium hexafluorophosphate

Bis(cyclopentadienyl)cobalt(III) hexafluorophosphate $\text{C}_{10}\text{H}_{10}\text{CoF}_6\text{P}$, has a molar mass of $334.04 \text{ g mol}^{-1}$. The supporting electrolyte for this redox couple is the AN/TBAPF₆ mixture. 3.8743 g of TBAPF₆ (molar mass of $387.43 \text{ g mol}^{-1}$) was dissolved in 100 mL of AN to give a 0.1 M solution.

Enough of this stock solution was used to dissolve 0.0835 g of cobaltocenium hexafluorophosphate to give 50 mL of a 5 mM solution.

2.3 Preparation of Silver Nanoparticles

ACS grade silver nitrate, AgNO_3 ($\geq 99.0\%$ purity) and AnaLAR grade sodium borohydride (NaBH_4) were both purchased from Sigma Aldrich, UK while AnaLaR grade tri-sodium citrate dihydrate, $\text{Na}_3\text{C}_6\text{H}_5\text{O}_7 \cdot 2\text{H}_2\text{O}$ (99.0%) was purchased from BDH Chemicals Limited Poole, England.

The various concentrations of AgNO_3 used in stripping analyses for calibration were prepared in 0.1 M NaNO_3 as supporting electrolyte. 1 mM AgNO_3 was prepared as stock solution by dissolving 0.0085 g of the salt in enough of 0.1 M NaNO_3 in a 50 mL volumetric flask. This stock solution was diluted to give the lower micromolar (μM) and nanomolar (nM) concentrations as was desired.

Silver nanoparticles (AgNPs) studied in this research were synthesised by two main methods. In the Creighton method of borohydride reduction¹¹⁷, 30 mL of 2 mM NaBH₄, (molar mass 37.83 g) was prepared in a 50 mL conical flask by dissolving 0.0023 g of the salt in enough of nanopure water to give the 30 mL solution. To this was added a magnetic stirrer after which the flask was placed in an ice bath that had already been placed on a magnetic stir plate. This reducing agent was stirred as it was being cooled in ice for about 20 minutes. 2 mL of 1 mM AgNO₃ (molar mass 169.87 g mol⁻¹), prepared by weighing 0.0034 g/20 mL of solution was then dripped into the stirring NaBH₄ at approximately one drop per second. Stirring was stopped as soon as all the AgNO₃ was added. Upon complete addition of the 2 mL of silver nitrate, a yellow colouration was obtained, indicating the formation of silver nanoparticles (AgNPs). The equation for the borohydride reduction of silver nitrate is



However, it should be noted that the oxidation of borohydride is complex and other reduction products of boron (oxyhydrides, borates) are likely. In order to ensure the efficiency of the reduction process, the initial concentrations of sodium borohydride and silver nitrate were maintained in the ratio of 2:1 for the AgNPs to remain stable as the investigators¹¹⁷ confirmed a decrease in stability with alteration of the concentration ratio. The amount of sodium borohydride was also in a large excess of AgNO₃ so that the nitrate was completely reduced as soon as it was added to the borohydride. AgNPs synthesised by borohydride reduction were characterised for stability by UV-Vis spectrophotometry. In spite of the precautionary measures put in place, the AgNPs soon lost their stability and began to aggregate shortly after commencement of dialysis.

In another synthetic technique, the citrate reduction method of Lee-Meisel¹¹⁸ was adopted with modification by scaling it down by a factor of 5. Here, 18 mg or 0.018 g of AgNO₃ was dissolved in 100 mL of nanopure water to give a 1.06 mM solution and brought to the boil. 2 mL of 1% tri-sodium citrate dihydrate, prepared by dissolving 0.1 g of the salt in 10 mL of nanopure water was added to the boiling mixture. Greenish-yellow AgNPs were formed (photo in *figure 2.1A*) after about seven minutes of addition of the sodium citrate. The equation for the citrate reduction of silver nitrate is



In the equation, $\text{C}_5\text{H}_4\text{O}_5^{2-}$ is the conjugate base of acetone dicarboxylic acid.¹¹⁹ AgNPs prepared by the citrate reduction of silver nitrate were relatively stable as they showed neither aggregation nor colour change on standing after about three months.

Silver nanoparticles were further incorporated with Cl^- and SO_4^{2-} in varying concentrations to see the effect of the ions and their concentrations on the release of Ag(I) ions from the nanoparticles. Pictures of freshly prepared AgNPs and of the apparatus for dialysis are shown in *figure 2.1* and *figure 2.2* respectively.

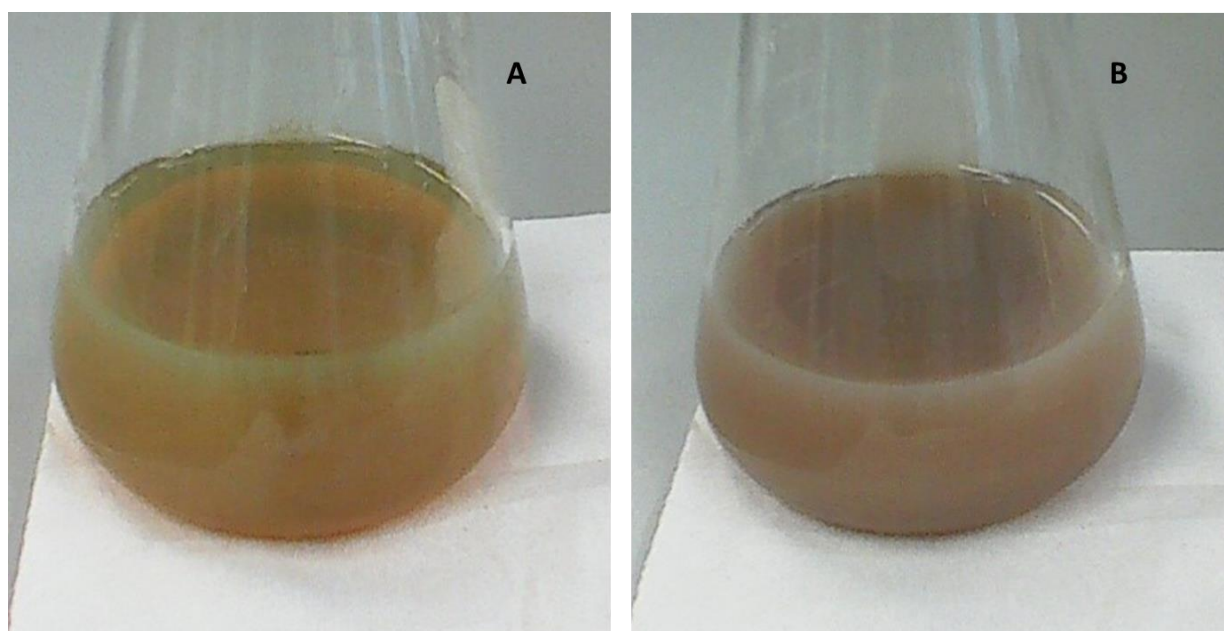


Figure 2.1 Freshly prepared 10 mM AgNPs of (A) pure water and (B) NaCl(aq) contained in 250 mL conical flasks. The NaCl(aq)-AgNPs turned turbid after addition of NaCl crystals. The NPs were prepared by the citrate reduction method.

In NaCl(aq)-AgNPs, three different concentrations of 10 mM, 30 mM and 50 mM were used. For the 10 mM NaCl(aq)-AgNPs, 0.0584 g of sodium chloride (molecular mass 58.44 g mol^{-1}) was measured and infused into 100 mL of the AgNPs while 0.5844 g/L of the solution was used as dialysate. In case of the 30 mM concentration, 0.1753 g of the salt was infused into 100 mL of AgNPs while 1.7532 g/L of solution served as the dialysate. In a similar vein, 0.2922 g of NaCl was weighed and incorporated into 100 mL of AgNPs to give the 50 mM NaCl(aq)-AgNPs and 2.922 g/L was prepared and used as the dialysate.

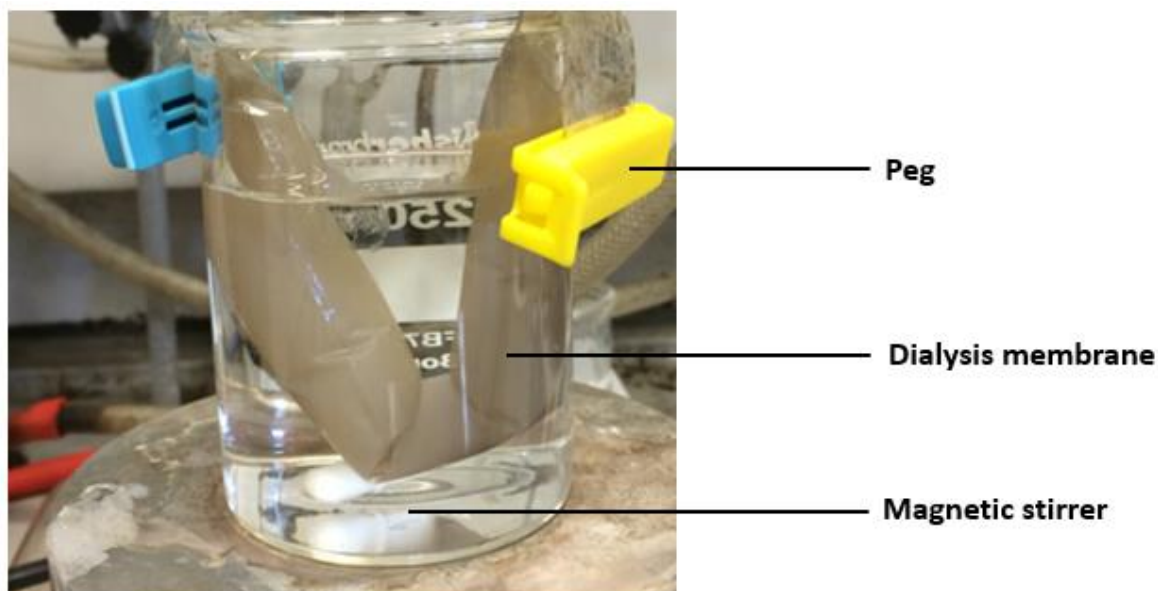


Figure 2.2 Apparatus showing dialysis of 10 mM NaCl(aq)-AgNPs contained in a 400 mL beaker.

Only the 10 mM concentration of sodium sulphate, Na_2SO_4 was used to monitor the effect of sulphate ion on the release of Ag(I) ions from silver nanoparticles. This is because stripping peaks for Ag(I) ions could not be obtained even at this low concentration beyond the 2nd fraction of dialysate in spite of increased deposition time to 300 s.

0.142 g of the anhydrous salt, an ACS reagent of $\geq 99\%$ purity and molar mass $142.04 \text{ g mol}^{-1}$, purchased from Sigma Aldrich UK, was weighed and incorporated into 100 mL of silver nanoparticles. The dialysate was prepared by dissolving 1.4204 g of the salt in enough of nanopure water to give a one-litre solution.

2.4. Characterization of Silver Nanoparticles.

Stability tests on silver nanoparticles (AgNPs) synthesised by both the Creighton and Turkevich (or citrate reduction) methods were done with the aid of Cary 100 Bio UV-Vis spectrophotometer of Agilent Technologies, USA while their particle sizes were estimated by dynamic light scattering (DLS) and atomic force microscopy (AFM).

It is worthwhile to note that XPS was not used to characterize silver nanoparticles because by virtue of their preparation under atmospheric conditions, the presence of oxygen is obvious. In addition, the main aim of the research was to observe the

properties of AgNPs with respect to release of Ag(I) in solution, and not in the dry state.

In the stripping voltammetric analyses of the silver nanoparticles (AgNPs) discussed in detail in Chapter 6, a glassy carbon microelectrode of outer diameter (OD) 3.0 mm and internal diameter (ID) 1.0 mm was used as the WE while platinum wire served as the CE and mercurous sulphate in saturated potassium sulphate worked as the reference electrode (RE) for pure water and sulphate AgNPs dialysates. The aqueous Ag/AgCl reference electrode was used in the stripping analyses of the NaCl(aq)-AgNPs dialysates.

Dialysis cellulose membranes of average width diameter 35 mm (1.4 in), used in the purification of prepared metal nanoparticles were purchased from Sigma Aldrich, UK. The membranes which have an inflated diameter of approximately 21 mm (0.83 in) and length of 30 cm (12 in) have a pore size of 12,000 Da MWCO (molecular weight cut-off). This means that the membranes will retain particles with $M.W > 12,000$ Da.

Water used for preparation of electrolyte solutions, rinsing of electrodes and glassware as well as soaking of dialysis membranes was collected directly from the purifying source, NANOpure RO operating at a resistivity of 18.2 M Ω .cm, model DH 931 of Barnstead International, Dubuque, Iowa, USA.

All the reagents were used as purchased without further treatments.

2.5 Construction of Bismuth Electrodes.

A soda-lime glass capillary of length 13 cm, 6 mm outer diameter and 1.92 mm bore (internal diameter) was sealed at one end in a blue flame. The cooled capillary was then filled with pure bismuth powder to about 3 cm of the glass length through the open end by means of an injection needle. Copper wire of diameter 1.13 mm was inserted into the soda-lime glass and made to penetrate 1 cm into the bismuth powder. The powder was then melted under vacuum by heating the sealed end of the capillary tube as the open end was connected to a vacuum pump. The aim of melting under vacuum was to avoid oxidation of the bismuth, after which the glass was cooled to room temperature.

The sealed end of the glass capillary was finally ground to provide a smooth surface, extreme care being taken to ensure that the copper wire was not exposed at the surface. The open end was glued with epoxy resin to prevent the copper wire from becoming loose due to mechanical stress when the electrode is connected to an external circuit. From the dimensions of the soda-lime glass, the surface area of the bismuth electrode was calculated to be 0.029 cm^2 . The surface areas of the working electrodes of bismuth and platinum have been used in computing the capacitance values. The set-up of the bismuth electrode is shown in the *figure 2.3* below.

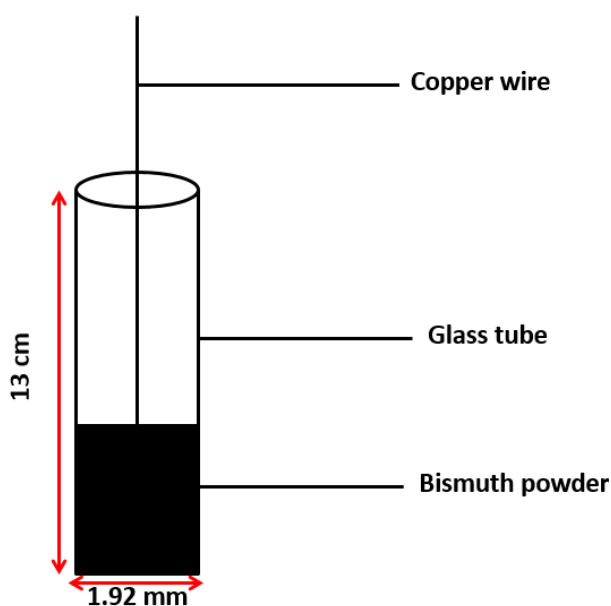


Figure 2.3 Sketch diagram of a bismuth bulk electrode.

2.6 Double Layer Capacitance at Bismuth Electrodes.

Capacitance data were obtained at the Bi|solution interface for the aqueous electrolyte solutions of NaBr, NaCl and NaNO_3 as well as the non-aqueous electrolyte solution AN/ LiClO_4 (AN denotes acetonitrile). Impedance (potential scan) measurements were made at various dc potential ranges in the concentration range of 10 mM to 100 mM but at fixed frequencies of 500 Hz, 1000 Hz and 2000 Hz for each concentration of analyte. The measurements were made using an Ivium compactstat model e 1030 ($\pm 10 \text{ V}/\pm 30 \text{ mA}$) (Ivium Technologies, The Netherlands) connected to a Dell Precision workstation.

All the experiments were performed in a standard three-electrode cell containing 18-20 mL of sample solution. The Bi electrode served as the WE and except

otherwise stated, the Pt and Ag/AgCl electrodes were used as counter and reference electrodes respectively.

The electrochemical cell was purged with a stream of nitrogen gas for about 8-10 minutes prior to every experimental run to remove traces of oxygen that may otherwise interfere with the electrode reactions.⁴²⁻⁴⁴ After each analysis, the working electrode was polished with a slurry of 0.05 μm alumina powder of Banner Scientific Ltd., Coventry, UK spread over an 8 inch Buehler microcloth surface and thereafter, rinsed with nanopure water.

The structure of the three-electrode cell used for the experiments is shown in *figure 2.4*.

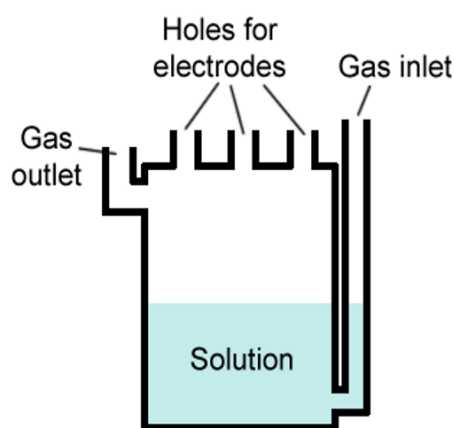


Figure 2.4 Structure of the three electrode cell. It has an external diameter of 3 cm with a height of 8 cm and takes 18-20 mL of analyte solution.

2.7 Standard Rate Constants.

Standard rate constants for electron transfers in ruthenium hexaamine trichloride and cobaltocenium hexafluorophosphate at bismuth were estimated using electrochemical impedance spectroscopy (EIS) measurements. Even though the waveshapes of cyclic voltammograms of these complexes obtained at bismuth closely resembled those obtained at Pt, a noble metal electrode, the electrode kinetics were sufficiently slow to be determined at Bi. The rates were too fast to measure by cyclic voltammetry (CV) because the reactions were affected by uncompensated resistance, but impedance spectroscopy over the frequency range of $10^1 - 10^5$ Hz was sufficient. Voltammetric data that gave rise to this decision will be fully discussed in Chapters 4 and 5.

Some alternating current (AC) voltammetric measurements were conducted on these redox couples and the reversible potentials of the voltammograms therefrom formed the constant potentials for the impedance measurements; results of which have been presented and fully discussed in Chapters 4 and 5.

2.8 Analytical and Characterisation Techniques.

2.8.1 Cyclic voltammetry

Cyclic voltammetry (CV) is a technique in which the potential of the working electrode is linearly scanned between two values in a triangular waveform.¹²⁰ The voltage or potential is swept forth and back between two values, say from E_1 where there is no reaction to E_2 where reduction or oxidation of the analyte occurs, at a fixed rate. Due to its relative simplicity and richness in information content, cyclic voltammetry is widely used as to elucidate the mechanisms of reactions at the electrode|solution interface.

The potential –time profile of cyclic voltammetry is shown in *figure 2.5*.

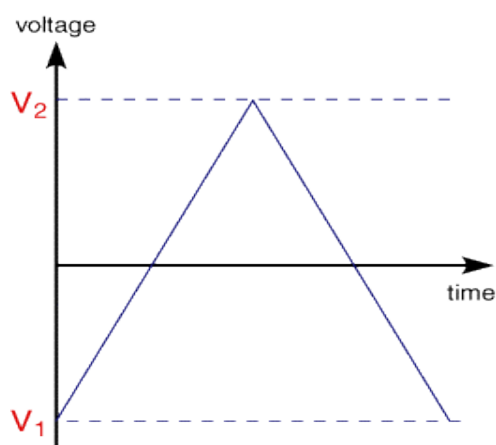


Figure 2.5. Potential-time profile of a cyclic voltammogram.

During the potential sweep, current that is generated because of the applied potential is recorded by the potentiostat. The plot of this current (I) versus potential (E) is called a cyclic voltammogram, CV. Such a current –potential ($I - E$) curve is shown in *figure 2.6*.

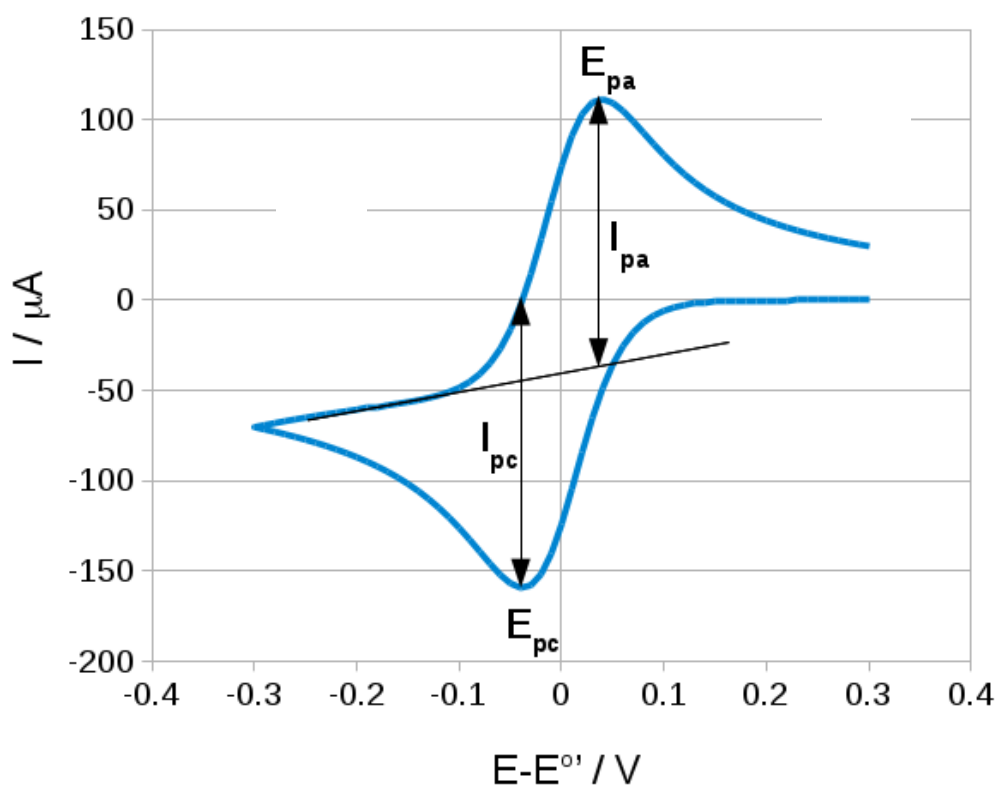


Figure 2.6. A typical cyclic voltammogram showing peak currents (I_{pc} , I_{pa}) and peak potentials (E_{pc} , E_{pa}) for the reduction of species present as the oxidized form in bulk solution and under conditions where the voltammetry is reversible.

A typical cyclic voltammetric experiment is carried out in a three – electrode cell (figure 2.4) containing the working, reference and counter electrodes as well as the analyte solution and a supporting electrolyte^{121,122}. The supporting electrolyte which should neither react with the analyte nor the electrode serves three main functions.¹²¹⁻¹²⁴ Firstly, to increase the conductivity (or decrease the resistance) of the solution, second to maintain a high and constant ionic strength and thirdly to eliminate electromigration effects. Massive movement of charged reactants and products could also lead to complex and to adsorption on the electrode surface.

A cyclic voltammogram has many parameters which could be used to characterize the reversibility or otherwise of an electrochemical process. These include the cathodic (E_{pc}) and anodic (E_{pa}) peak potentials as well as the cathodic (i_{pc}) and anodic (i_{pa}) peak currents which are in direct proportion to the square root of scan rate. The positions of peak potential do not alter with change in scan rate for a reversible process.

At 25°C, the peak current for a redox process is given by the Randles – Sevcik equation as

$$i_p = (2.69 \times 10^5) n^{3/2} A C D^{1/2} \nu^{1/2} \quad (2.3)$$

where n = number of electrons transferred

A = area of electrode in cm²

C = concentration of analyte in mol cm⁻³

ν = scan rate in Vs⁻¹

D = diffusion coefficient in cm²s⁻¹

Other tests for reversibility include³ a peak current ratio $\frac{i_{pa}}{i_{pc}}$ of unity while the potential peak separation is defined by

$$\Delta E_p = |E_{pa} - E_{pc}| = \frac{0.059}{n} V \quad (2.4)$$

For a one–electron transfer process, the value of equation 2.4 simplifies to 59 mV at 298 K. Furthermore, the formal potential of a redox couple is expected to lie half-way between the cathodic and anodic peak potentials and is given by

$$E^o = \frac{E_{pa} + E_{pc}}{2} \quad (2.5)$$

2.8.2 Electrochemical impedance spectroscopy

Electrochemical impedance spectroscopy (EIS) is an alternating current (AC) technique in which the impedance of an electrochemical system is measured as a function of frequency⁵⁴. When a sinusoidal potential is applied to an electrochemical cell, a current is caused to flow through it, perhaps resulting in the formation of new chemical species owing to the faradaic reaction at the electrode.¹²³ Because the potential is sinusoidal, it is time dependent and its value is given by

$$E_t = E_o \sin (\omega t) \quad (2.6)$$

The current flowing as a result of the applied potential will also be sinusoidal and is defined by

$$I_t = I_o \sin (\omega t + \phi) \quad (2.7)$$

where $\omega = 2\pi f$ expresses the relationship between angular frequency ω in radians s^{-1} and linear frequency f , in Hertz while ϕ is the phase angle and represents the observation that the current response is not always in phase with the applied potential.

From equations (2.6) and (2.7) above,

$$Z = \frac{E_t}{I_t} = \frac{E_o \sin \omega t}{I_o \sin(\omega t + \phi)} \quad (2.8)$$

This can be simplified to read

$$Z = \frac{Z_o \sin \omega t}{\sin(\omega t + \phi)} \quad (2.9)$$

Equation (2.7) gives the relationship between the applied potential and the current flow, known as impedance, which is analogous to the current–potential relationship of a d.c circuit defined by Ohm’s law $E = IR$.^{125,126} It also serves to explain that the impedance has a magnitude Z_o whose components of potential and current are separated by a phase angle ϕ . For a sinusoidal potential applied across a pure resistor R , the magnitude of the impedance will equal the resistance ($Z = R$) and the phase angle $\phi = 0$ at all frequencies.

Impedance is therefore the proportionality factor between applied potential and current which expresses the ability of a circuit to resist the flow of current, but unlike resistance, it is applicable to more systems than those that obey the simple Ohms’ law and is generally frequency dependent.

In the absence of a faradaic process, the electrode|solution interface in an electrochemical cell behaves like a capacitor, a device that stores charge according to the potential applied to it i.e.

$$q = KE \quad (2.10a)$$

where q is the stored charge in Coulombs, K the integral capacitance in Farads and E is the applied voltage or potential in volts (with respect to the potential of zero charge).

In general, the capacitance of an electrode is potential-dependent and therefore another, more general definition can be given in terms of small changes in charge and potential (dq , dE) which describes the differential capacitance C (also in Farads). Unless otherwise stated, capacitance in this thesis will refer to differential capacitance, C .

$$dq = CdE \quad (2.10b)$$

The flow of current is the change of charge with time,

$$I = \frac{dq}{dt} \quad (2.11)$$

Hence from equation (2.10b) by differentiation,

$$I = C \frac{dE}{dt} \quad (2.12)$$

If we substitute the value of potential from equation 2.6 here and differentiate, we obtain the relation

$$I = \omega CE \cos \omega t = 2\pi fCE \cos (2\pi ft) \quad (2.13)$$

On application of Euler's relationship, $\exp(j\phi) = \cos\phi + j \sin\phi$ and by combining sines and cosines together and with $j = \sqrt{-1}$, equation (2.13) becomes

$$I = 2\pi fCE.j \quad (2.14)$$

By analogy with Ohm's law, the ratio of potential to current yields

$$Z = \frac{E}{I} = \frac{1}{2\pi fC.j} = \frac{-j}{\omega C} \quad (2.15)$$

This means that the impedance of a circuit in which the resistor and capacitor are in series will contain real and imaginary parts and can be expressed as

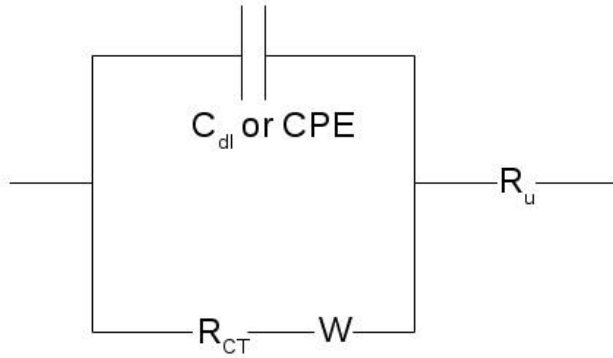
$$Z = R - \frac{j}{\omega C} \quad (2.16)$$

The real part Z' or $\text{Re}Z = R$ while the imaginary part Z'' or $\text{Im}Z = \frac{-1}{\omega C}$

There are various ways of presenting impedance data, the two most common are (i) the Bode plot of magnitude Z_0 and phase ϕ against frequency f and (ii) the Nyquist plot in which $-Z''$ is plotted against Z' in the complex plane. The Nyquist plot suffers the disadvantage that it hides the frequency dependence of the data; however it is often easier to read important values directly from the plot. For example, equation 2.16 appears as a series of points parallel to the imaginary axis which accumulate at high frequency on the real axis at $Z'=R$. In an electrochemical impedance spectrum, this value is usually the uncompensated resistance.

In this work, a Randles circuit for mixed-kinetics diffusion including a constant phase element (CPE), shown in *figure 2.7(a)* was simulated to enable measurement of precise values of charge transfer resistance. *Figure 2.7(b)* is an impedance plot typical of the circuit, known as a Nyquist plot in which the imaginary and real parts of the impedance are displayed on the complex plane.

(a) Randles circuit



(b) Nyquist plot

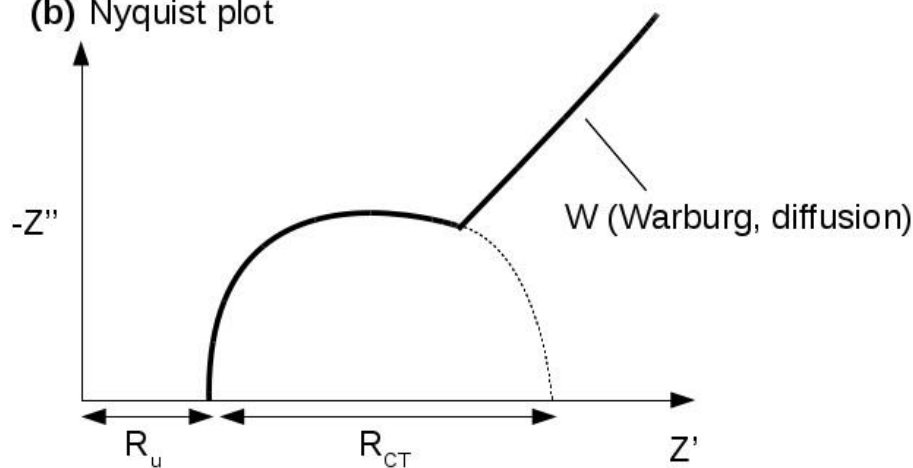


Figure 2.7(a) A Randles circuit for mixed – kinetics diffusion. R_u is for uncompensated resistance, CPE stands for constant phase element which represents the non-ideality of the double layer capacitance in solution and R_{CT} is for charge transfer resistance. The Warburg impedance which enables calculation of diffusion coefficients is indicated by W . (b) A Nyquist plot showing the real part of impedance as Z' while the imaginary part is denoted by $-Z''$.

It is worthwhile to note that each point on the Nyquist plot corresponds to the impedance at a given frequency, with high frequency data on the left and low frequency data on the right-hand side of the plot – the magnitude of impedance decreases with frequency. The Warburg impedance dominates at low frequencies. The Warburg impedance is given by

$$Z_w = \sigma(\omega)^{-1/2}(1 - j) \quad (2.17a)$$

The Warburg coefficient can be estimated from equation 2.17b

$$\sigma = \frac{RT}{n^2 F^2 A \sqrt{2}} \left(\frac{1}{C^{*O} \sqrt{D_O}} + \frac{1}{C^{*R} \sqrt{D_R}} \right) \quad (2.17b)$$

The parameters have their usual meanings of:

ω = radial frequency

D_O = diffusion coefficient of oxidized species

D_R = diffusion coefficient of reduced species

A = surface area of the electrode

n = number of electrons transferred

2.8.3 X-ray photoelectron spectroscopy

X-ray photoelectron spectroscopy (XPS) also known as electron spectroscopy for chemical analysis (ESCA) is a surface analysis technique that can be applied to a wide range of materials because of its ability to provide valuable quantitative and chemical state information from the surface of the material under investigation.¹²⁷ The surface of the material can be analysed into about 5 nm of its depth by this technique.

XPS is essentially achieved by exciting the surface of a sample with mono-energetic X-rays, e.g., Al $K\alpha$, causing photoelectrons to be emitted from the core orbitals of near-surface atoms of the sample into the vacuum.¹²⁸ The Einstein relation developed below allows the binding energy of the photoelectrons to be determined from measurements of their kinetic energy. From the values of binding energy and intensity of the photoelectron peaks or counts per second (cps), the elemental identity as well as chemical state and quantity of a detected element can be obtained.

The intensity of the peaks is related to the concentration of the element in the sampled region hence XPS also provides a quantitative analysis of the sample composition.

Theoretical Framework

The energy of a photon emitted from all types of electromagnetic radiation is defined by Max Plank's equation as

$$E = h\nu \quad (2.18)$$

The parameter h stands for Planck's constant with a value of 6.62×10^{-34} J.s. and ν represents the frequency of the radiation in Hertz (Hz). In XPS, the photon is absorbed by an atom in a molecule or solid which results in ionisation and emission of a core electron. The kinetic energy distribution of the emitted photoelectron particles i.e. their number as function of kinetic energy can be measured with an appropriate electron energy analyser to record a photoelectron spectrum.

The process of photo-ionisation of a metallic surface say A may be seen to follow the process



By the principle of conservation of energy

$$E(A) + h\nu = E(A^+) + E(e^-) \quad (2.20)$$

Equation 2.19 can also be written as

$$E(e^-) = h\nu - E(A^+) + E(A) \quad (2.21)$$

The main energy of the electron in this instance is kinetic energy, K. E hence equation 2.21 can be re-arranged to read

$$K. E. = h\nu - [E(A^+) - E(A)] \quad (2.22)$$

Equation 2.22 can be further simplified to read

$$K. E. = h\nu - B. E. \quad (2.23)$$

The difference between the ionized and neutral atom is called the binding energy (B.E.) of the electron hence equation 2.23 serves to also explain why XPS spectra could be analysed either in terms of kinetic energy (K.E.) or binding energy (B.E.) of the emitted photons with respect to intensity.

XPS is useful for elemental analysis because the major determinant of the core electron energies is the atomic number of the atom. Information on oxidation state may also be obtained, because although core electrons are not involved in bonding, their binding energies will be shifted to slightly larger values as the oxidation state

increases. This effect can be rationalised as a simple electrostatic effect based on the partial charge of the atom. Large reference databases of atomic binding energies exist¹²⁹ which aid in the assignment of XPS spectra.

Finally, XPS is also 'surface sensitive', which means that it provides information only on atoms within a few nanometres (nm) of the sample surface. Although the X-rays typically used (Al $k\alpha = 1.486$ keV) may penetrate deeply into the sample, the photoelectrons generated at depths greater than a few nm are scattered before they reach the sample surface and are therefore not usually detected. Those at the surface also have very high probability to escape.

2.8.4 Dynamic light scattering

Dynamic light scattering (DLS) also known as quasi-elastic light scattering (QELS) and photon correlation spectroscopy (PCS) is a technique that measures the changes in the intensity of light scattered from a suspension or solution due to random (Brownian) motion of particles therein.¹³⁰ The working principle of DLS involves the illumination of a sample by a laser beam whence the fluctuations of the scattered light are detected at a known scattering angle θ by a fast photon detector.¹³¹ The raw data collected by the instrument (intensity fluctuations versus time) is processed by the software to produce a correlogram (the correlation function of the intensity against lag time). A model for the intensity fluctuations produced by diffusing particles is then fitted to the correlogram to deduce the particle size distribution. In brief, rapid fluctuations of the intensity correspond to rapid movement of the scattering particles and therefore to large values of diffusion coefficient. Particle size for a sphere is determined from the diffusion coefficient a combination of the Einstein-Smoluchowski equation and Stokes' equation which includes the viscosity of the medium as

$$D_h = \frac{k_B T}{3\pi\eta D_t} \quad (2.24)$$

The symbols take their usual meanings of:

- D_h is the hydrodynamic diameter
- D_t is the translational diffusion coefficient
- k_B is the Boltzmann's constant

- T is the absolute temperature
- η is the dynamic viscosity of the medium

It is important to note here that this principle assumes diffusion to be the predominant motion of particles in the sample and the size measured is the diameter of a sphere. In general the analysis of the raw data is also complicated by sample heterogeneity; samples containing particles of different sizes produce a mixture of rapid and slow fluctuations that are analysed by the software to produce distributions of particles size rather than a single value.

Another important parameter to be considered in the analysis of a sample by DLS is the polydispersity index (PDI) which is a measure of how wide the particle sizes are distributed.¹³¹ It is defined by the formula

$$PDI = \left(\frac{\delta}{d} \right)^2 \quad (2.25)$$

where the symbols δ and d stand for standard deviation and mean diameter respectively. Samples with PDI values less than 0.1 are generally said to be monodisperse while those with values higher than 0.7 have a very wide size distribution, i.e., are polydisperse.¹³²

Dynamic light scattering (DLS) measurements were made using a Malvern high performance particle sizer (HPPS) incorporated with a non-invasive back scatter (NIBS) technology of Malvern Instruments Limited, Worcs, UK. This technology allows for high sensitivity measurement of samples as dilute as 0.1 ppm in disposable plastic or glass cuvettes while the back-scatter optics enables concentrated samples of the order of 100,000 ppm and particle size up to 10,000 nm to be measured.

2.8.5 Atomic force microscopy

Atomic force microscopy (AFM) is a scanning probe microscope (SPM) technique that is designed to measure sample properties such as height, friction, elastic modulus and magnetism, with a sharp probe.¹³³ To acquire an image, the SPM scans the probe over a small area of the sample, measuring several properties at a time.

Atomic force microscopes (AFM) work by measuring the force between a probe and sample. The microscope uses a cantilever which has a very sharp tip fixed at one end to scan over a sample surface. As the tip approaches the surface, van der Waals attractive forces between the surface and the tip cause the cantilever to deflect towards the surface.¹³⁴ However, a closer approach of the cantilever whence the tip makes contact with the surface results in repulsive forces which cause the cantilever to deflect away from the surface. These deflection of the cantilever and these forces on the tip are governed by Hooke's law

$$F = -k.z \quad (2.26)$$

where F = the force measured

k = the cantilever spring constant

z = the cantilever deflection in the direction normal to the sample surface.

The deflection is monitored by a laser beam which is focused on the back of the cantilever; as the cantilever bends, the position of the laser beam also changes. The reflections from the laser beam are focused on a 4-quadrant position-sensitive photo detector. The instrument software compiles the deflections and the current lateral position as the tip is rastered across the surface. In this way, images of the topography of a sample surface are recorded as the cantilever is scanned over its selected areas of interest and based on the nature of the tip/sample interaction, other properties can be mapped across the image too.

There are three basic modes of operation of the AFM. In the **contact mode**, the probe tip which senses surface properties and causes the cantilever to deflect is in contact with the surface. This mode operates better for solid surfaces which are not susceptible to damage by the large tip/sample force. In the **non-contact mode**, the tip vibrates at a constant frequency over the surface while in the **tapping mode**; the tip is closer to the surface than obtains in the non-contact mode but vibrates at high amplitude.

The contact mode of imaging is susceptible to influences of adhesion and friction. Because the tip makes contact with the surface of sample, this scanning mode can lead to sample damage hence alter the image data.¹³⁴ The non-contact scanning

mode has the demerit of low resolution as the probe tip vibrates at a relatively far distance away from the sample surface. The tapping mode resolves the problems of the contact and non-contact modes in that the tip makes contact with the surface at irregular intervals and the high amplitude of vibration does not allow for influences of adhesive forces from a possible contaminant layer. The intermittent contact of tip with sample also reduces sample damage. Tapping mode is therefore now the preferred technique for routine AFM imaging. It is especially suited to soft samples which often cannot be reliably imaged in contact mode. This mode is now employed almost as the standard method and is used in this thesis in Chapter 6.

Samples for Atomic force microscopy (AFM) imaging were prepared by drop casting 2 μL of aliquot on Si wafer that had been cleaned with acid piranha solution (3:1 solution of concentrated sulphuric acid and hydrogen peroxide), rinsed with nanopure water and dried in a stream of nitrogen gas. The drop was allowed to dry after which AFM images were obtained in the tapping mode TM with a Dimension Nanoscope V atomic force microscope of Veeco Inc. Metrology group Brussels, Belgium using NanoProbe tips model TAP300 AI-G of Budget Sensors USA. The cantilever was of resonant frequency 300 kHz with a force constant of 40 N/m and length of 125 μm .

Essential parts of an atomic force microscope are shown in *Figur 2.8*.

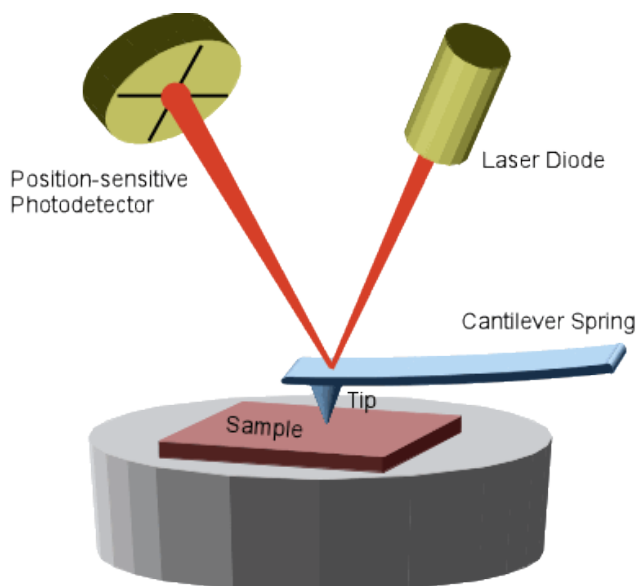


Figure 2.8 Image of an atomic force microscope showing a sample placed on the AFM piezoelectric stage.

Source: <https://physik.uni-greifswald.de/en/biophysics-and-soft-matter-prof-christiane-helm/methods/afm-atomic-force-microscope/> Accessed on 28th June, 2017.

2.8.6 Dialysis.

Dialysis is a process that uses semi-permeable membranes in the separation of small and large particles in solution.¹³⁵ In this technique, the sample is contained inside a dialysis membrane that is surrounded by a dialysate whose volume is usually a large multiple of the volume of the sample. This arrangement creates a concentration gradient that allows particles to diffuse into and out of the dialysis membrane until equilibrium is established.

The dialysis time may be decreased by stirring and to maintain a high concentration gradient of diffusible particles across the membrane. The dialysate is also changed from time to time to re-create the concentration gradient that is necessary for the efficiency of the dialysis process. In Chapter 6 a dialysis experiment is used to allow the electrochemical measurement of Ag(I) produced by the corrosion of AgNPs without complications from oxidation of AgNPs at the electrode or of oxidation of the reducing agents used to prepare the nanoparticles.

2.8.7 Stripping voltammetry

Stripping voltammetry is an electroanalytical method that embraces all the techniques that incorporate deposition or pre-concentration of analyte onto or into the working electrode followed by their stripping or removal.^{42-44,136,137} In the deposition step, metal ions in the analyte solution are accumulated on the surface of the electrode. This process can be represented by the equation



The stripping or measurement step involves the reduction or re-oxidation of the metal in solution as applicable to the stripping technique. The re-oxidation step could be indicated as



The resulting stripping peak area or charge, $\int i dt$, is proportional to the amount of the analyte on the electrode hence the concentration present in the solution. Stripping analysis has found wide application because it is extremely cheap as minute

quantities of materials are used and it has very low detection limits^{42-44,136} in the order of 10^{-10} M.

In addition, several metals in their various oxidation states can be determined at the same time. The instrumentation is simpler and of lower cost than ICP-MS or AAS as well. Anodic stripping voltammetry (ASV) is the technique employed to determine Ag(I) present in preparations of AgNPs in Chapter 6.

Chapter 3. Capacitance Measurements

3.1 Aims

The main objective of the research study is to establish the use of bismuth electrodes as a potential replacement for mercury in electroanalysis. One of the steps taken to achieve this was to carry out impedance measurements in selected aqueous and non-aqueous solvents at bismuth. The results of differential capacitance obtained from the measurements were compared with those obtained at platinum, a noble metal electrode, since neither the dropping mercury electrode (DME) nor the hanging mercury drop electrode (HMDE) was used in the investigation.

3.2 Capacitance Measurements at Bismuth in Aqueous Solutions

Electrochemical impedance spectroscopy (EIS) measurements were carried out in different concentrations of the reagent but at fixed frequencies to check the effects of these parameters on the charge storage capacity of the bismuth electrode. Potentials were measured against the Ag/AgCl reference electrode in solutions of concentration ranging from 10 mM to 100 mM at fixed frequencies of 500 Hz, 1 kHz and 2 kHz.

As these analyte solutions are not redox couples, the absence of electron transfer reactions across the electrode|solution interface was assumed. Values of differential capacitance, plotted against potential were obtained from the relation in equation 3.1 in which f stands for the frequency of measurement and Z'' is the imaginary part of the electrochemical impedance.

$$C = \frac{-1}{2\pi f Z''} \quad (3.1)$$

For capacitive systems, the imaginary part of impedance, Z'' is less than zero because the phase of the voltage lags the phase of the ac current by 90 degrees. Therefore, the value of capacitance described by equation 3.1 is real and positive. The real part of the impedance Z' contains information about factors such as solution resistance and charge transfer resistance, i.e., components in-phase with the applied ac signal.

The results of capacitance measurements as shown in *Figure 3.1* clearly indicate that the capacitance-potential ($C_d - E$) curves for the Bi|NaNO₃ interface had maximum

values at all the frequencies (500 Hz, 1 kHz and 2 kHz) and electrolyte concentrations (10, 30, 50 and 100 mM) investigated.

The measured differential capacitances are not quite in line with the frequency-independence expected from equation 3.1. In fact, they decrease slightly with applied frequency (compare *figure 3.1a, b and c*).

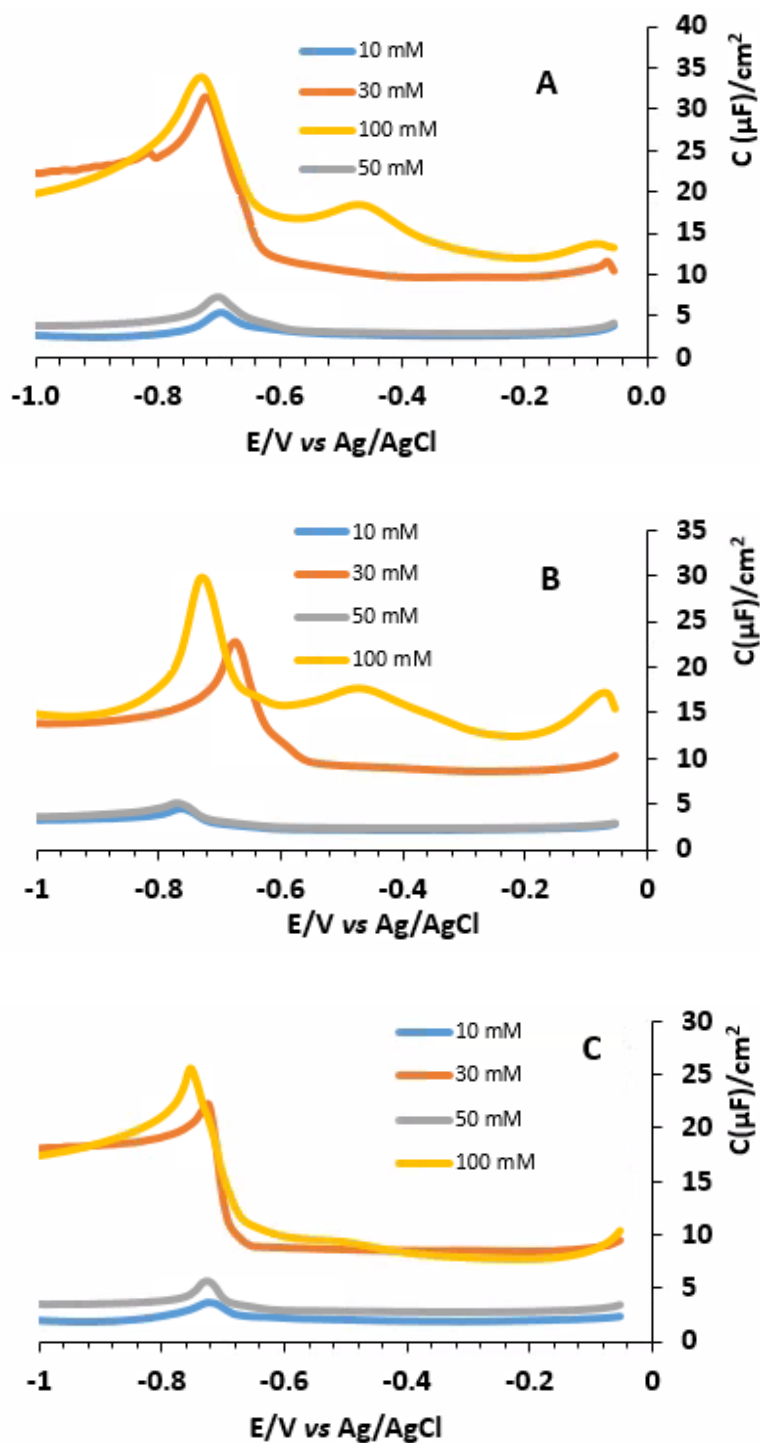


Figure 3.1. Combined capacitance at Bi in aq. NaNO₃ at (A) 500 Hz (B) 1 kHz (C) 2 kHz

This is typical constant phase element behaviour as described by equation 3.2. A constant phase element (CPE) is an electronic circuit that is characterised by a phase angle that is not changing with frequency hence the name ‘constant phase element’^{54,137}. The size of this phase angle is usually less than 90° but greater than zero as can be observed in the angle the red straight line makes with the Z' axis in the plane impedance plot of *figure 3.2*.

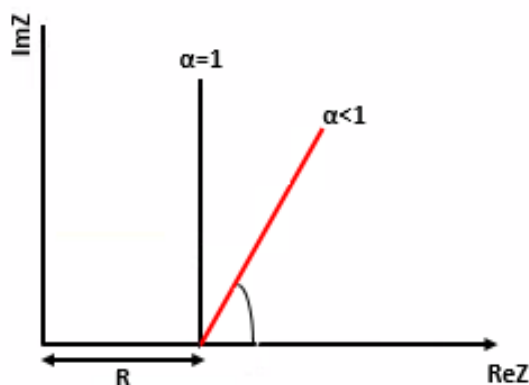


Figure 3.2 Sketch for an impedance plane plot to illustrate a CPE

The impedance of a CPE is defined by equation 3.2 in which at $\alpha = 1$, the constant phase element Q becomes an ideal capacitor.^{19,54,137}

$$Z = \frac{1}{(i\omega)^\alpha Q} \quad (3.2)$$

Constant phase elements are characteristic of solid electrodes, often ascribed to surface roughness and adsorption effects. In general $0 < \alpha < 1$ and Q is strictly only a simple (frequency-independent) capacitance for $\alpha = 1$. One can however define an *effective* capacitance at a given frequency using equation 3.1 even for a CPE and this is followed throughout the chapter.

The maxima in the capacitance-potential curves of *figure 3.1* indicate the failure of the Gouy-Chapman model for Bi|aqueous electrolyte, which predicts a minimum in the dependence of capacitance on applied potential. Electrocapillary maxima (ECM) are characteristic of surface tension-potential plots⁴²⁻⁴⁴ in which the potential of zero charge, *PZC* is estimated from the gradient of the slope. Estimation of *PZC* at the bismuth electrode surface therefore becomes difficult in this instance.

Capacitance measurements were also carried out in aqueous electrolyte solutions of sodium bromide (NaBr) and sodium chloride (NaCl). The capacitance-potential data obtained showed similarities to that obtained at bismuth in sodium nitrate, with maximum values of capacitance. Apart from a few cases of irregular behaviour, the variation of capacitance with concentration follows theoretical prediction as values generally increase with increase in concentration of the analyte solution. The mathematical expression for this prediction is

$$C_d = 228zC^{\frac{1}{2}} \cosh(19.5z\phi_0) \quad (3.3)$$

In equation 3.3, C_d is the differential capacitance in $\mu\text{F cm}^{-2}$, C is the bulk concentration in mol dm^{-3} , z is the charge of the ions and ϕ_0 is the total potential drop across the solution side of the double layer. In essence, the capacitance of the diffuse layer increases with concentration of ions because the average distance, as measured by the Debye length, between the counter charges and the electrodes decreases. The results of the capacitance measurements at the bismuth electrode surface can therefore be said to consistent with general expectations (see also section 1.2 and equation 1.3).

The capacitance-potential data in NaBr is presented in *Figure 3.3* while that obtained in NaCl is presented in *figure 3.4*.

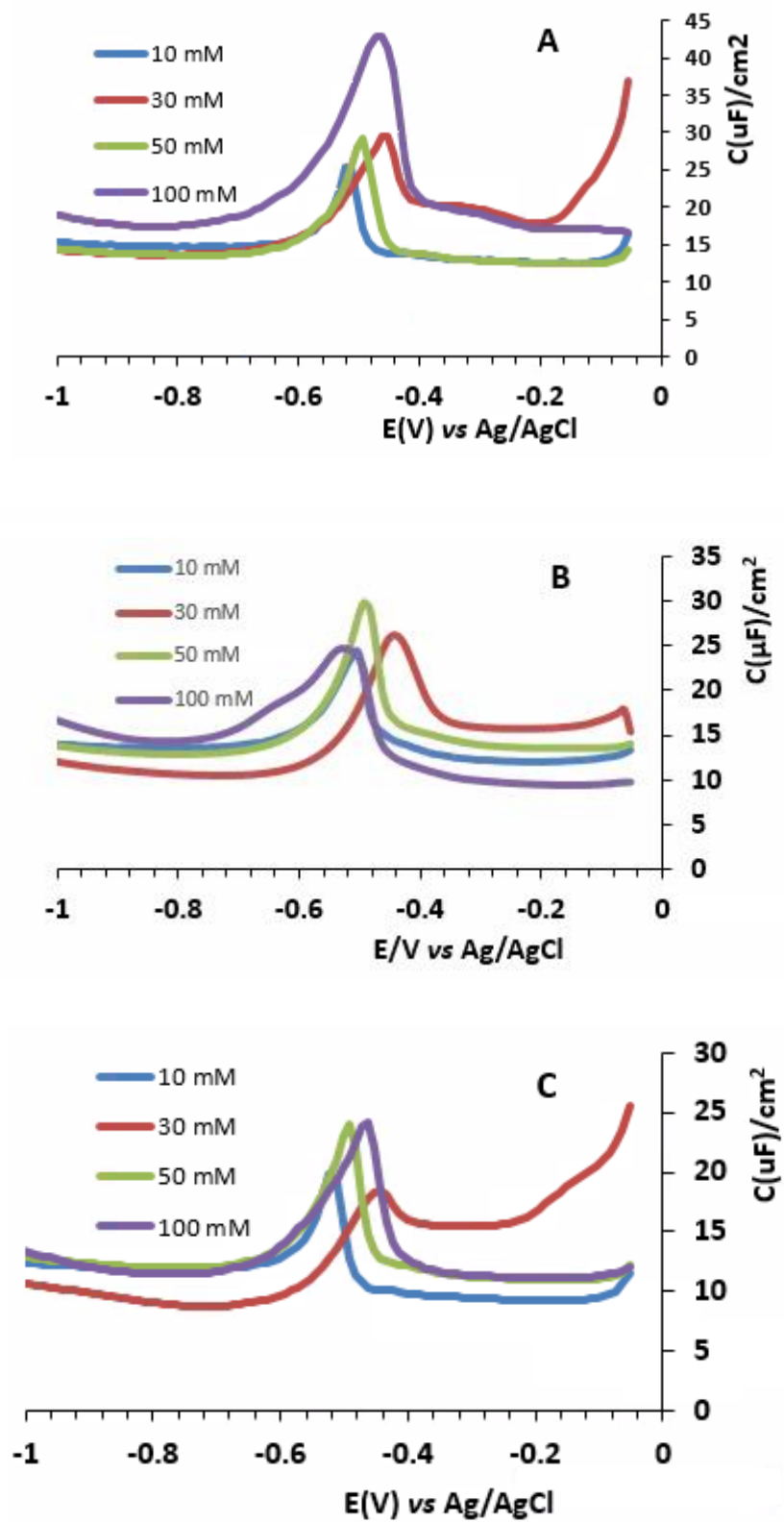


Figure 3.3. Capacitance data at Bi in aq. NaBr at (A) 500 Hz (B) 1 kHz (C) 2 kHz

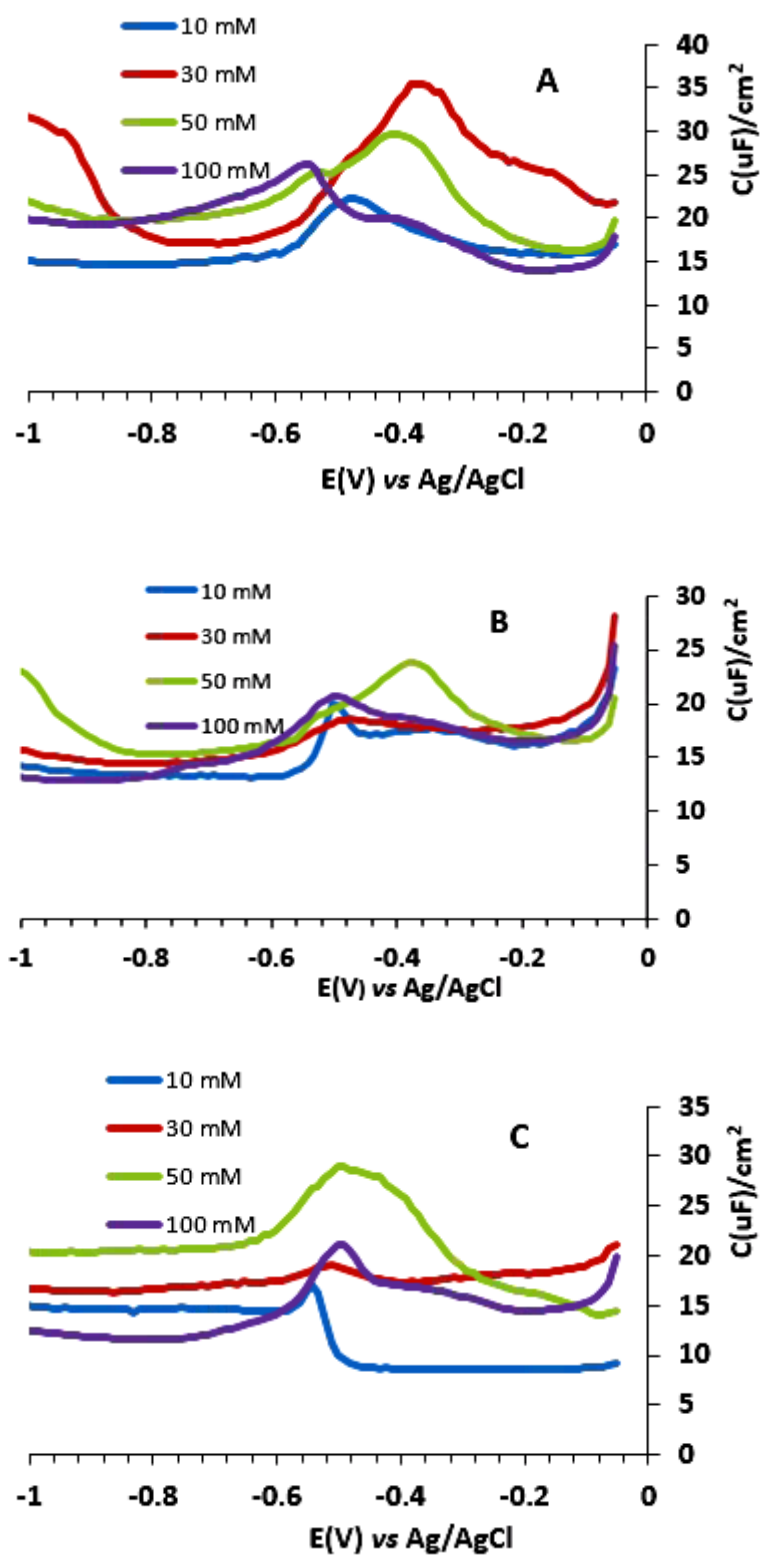


Figure 3.4. Capacitance data at Bi in aq. NaCl at frequencies of (A) 500 Hz (B) 1 kHz (C) 2 kHz

The maxima in the capacitance-potential curves in the Bi|NaBr and Bi|NaCl interfaces have been attributed to adsorptions of bromide and chloride ions at the bismuth electrode surface.^{13,21,22} While the source of high values of differential

capacitance could be traced to adsorptions of the halide anions on the electrode surface, the peaks characteristic of the Bi|NaNO₃ could not be easily accounted for.

To eliminate the possibility of chloride ion Cl^- interference by leaching into the NaNO₃ from the Ag/AgCl reference electrode, separate experiments were conducted, but with pure Ag wire as the reference electrode. Capacitance-potential data obtained at bismuth in aqueous NaNO₃ with Ag wire as reference is presented in *Figure 3.5*.

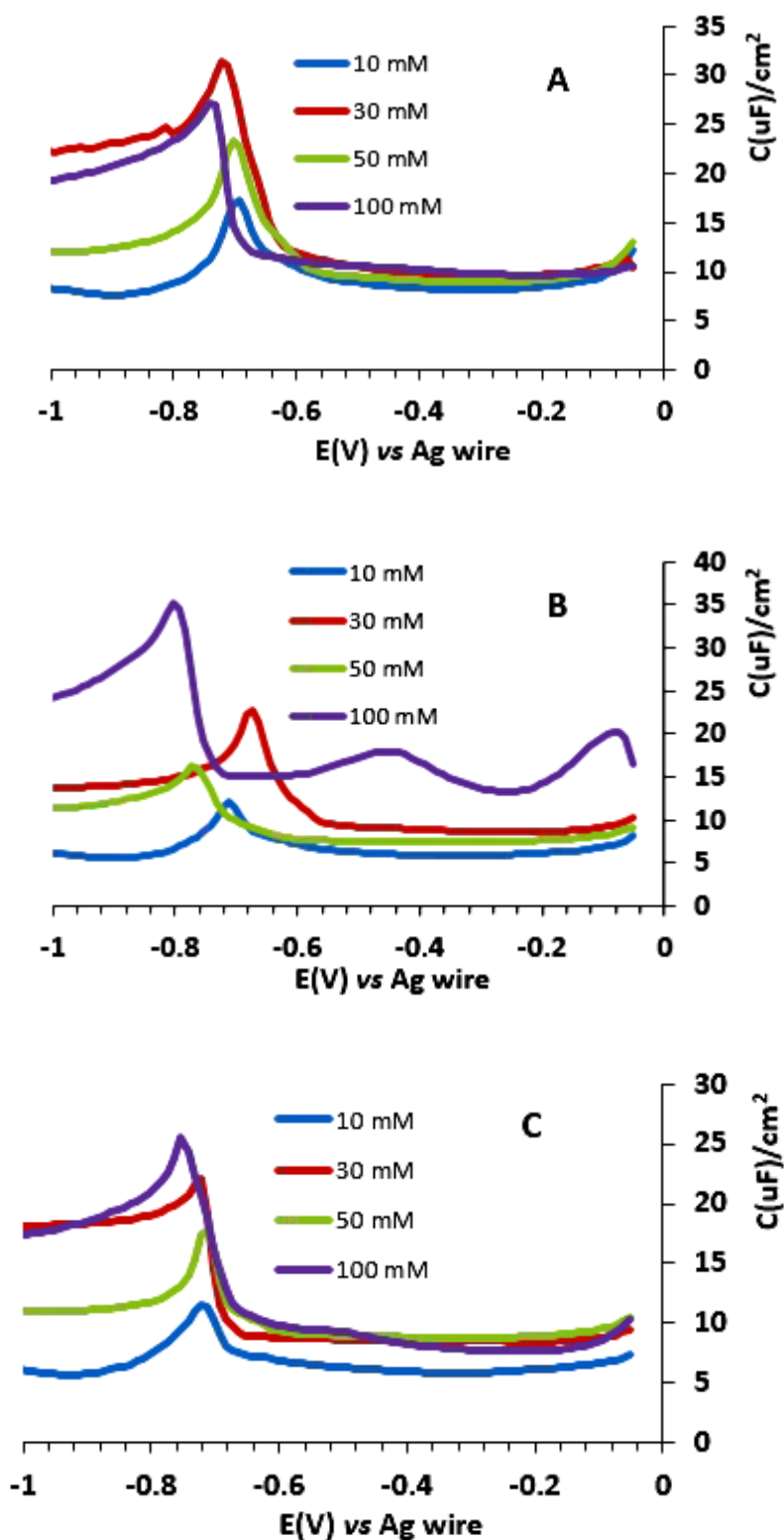


Figure 3.5. Capacitance data at Bi in NaNO_3 at (A) 500 Hz (B) 1 kHz (C) 2 kHz with Ag wire RE

The result was a shift in the capacitance maxima at potentials of about -0.5 V to more negative values of about -0.7 V vs Ag wire, but no other substantial change – this indicates a simple shift of the potential scale on changing the reference and not an effect on the Cl^- . The influence of negative potential was exerted more on the 100

mM concentration of the analyte where a value of -0.793 V was recorded at the frequency of 1 kHz. Interestingly, the second round of measurements at bismuth in aq. NaNO₃ with the Ag/AgCl reference at 2 kHz yielded the same results when Ag wire was used as reference at the same frequency.

Differential capacitance measurements alone were not sufficient to probe the Bi|electrolyte interface, therefore X-ray photoelectron spectroscopy (XPS) measurements were carried out to ascertain the source of the capacitance peaks. This data is presented in *figure 3.6*.

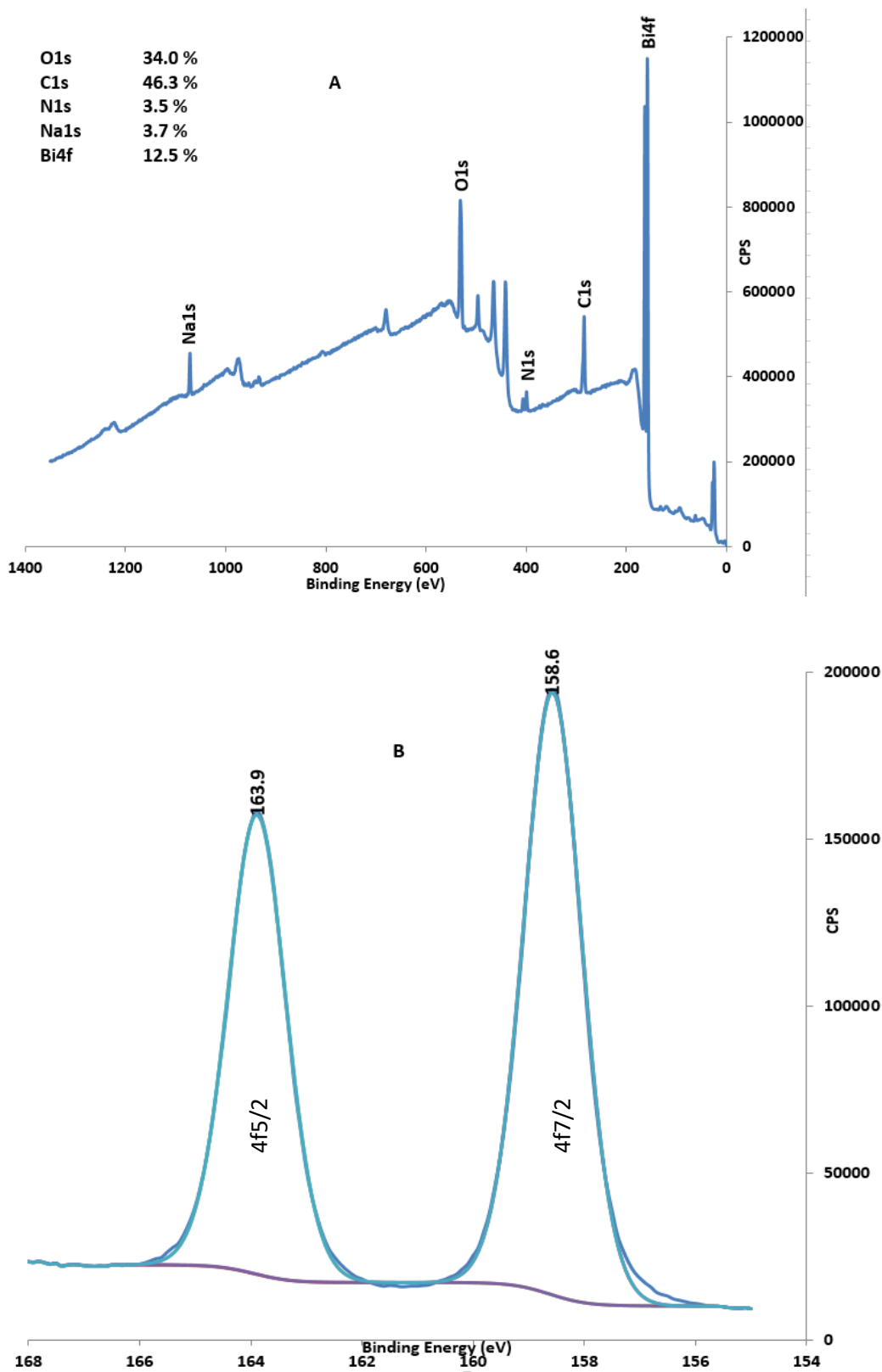


Figure 3.6. XPS (A) survey and (B) resolution spectra of the Bi|NaNO₃ interface.

The XPS survey and resolution spectra of all the analyte solutions of NaNO₃, NaBr and NaCl indicate an abundance of bismuth in the 4f spectral line. The experimental values of lower binding energy (B.E) of 158.6 eV but higher stability for 4f_{7/2} has

been found to be due to bismuth metal¹³⁸⁻¹⁴⁶ while the higher B.E of 159.3 eV also of the 4f7/2 spectral line and 163.9 eV for 4f5/2 are characteristic of bismuth(III) oxide (Bi₂O₃) and O₂/Bi adsorption¹⁴⁶⁻¹⁵¹, respectively. The spin-orbit splitting of these bismuth peaks is in the intensity ratio of 4:3. This ratio is found as follows:

For any electron with an orbital angular momentum, there is coupling between field of magnetic spin (*s*) and angular momentum (*l*). The total angular momentum (*j*) is defined by $j = |l \pm s|$; which provides for two energy states of $l+s$ and $l-s$. For the Bi 4f orbital, the principal quantum number (*n*) is 4 while $l = 3$ and $s = \pm 1/2$. The values of total angular momentum are therefore $3+1/2$ and $3-1/2$. This gives the energy states of 4f $3\frac{1}{2}$ or (4f 7/2) and 4f $2\frac{1}{2}$ or (4f5/2) respectively. The intensity ratios therefore simplify to $2(7/2) + 1$ and $2(5/2) + 1$ which is 4:3.

The ratio of the Bi(III) to the Bi(0) peak as revealed by the fitting programmes is 97.2: 2.8 or 97:3. The thickness *L* of the bismuth oxide film was therefore estimated to be about 9 nm, using the equation 3.4 in which *f* stands for the electron inelastic mean free path (IMFP) of the oxide and *r* is the metal: oxide ratio of 97:3.

$$L = f \times \ln \left(1 + \frac{1}{r} \right) \quad (3.4)$$

In the absence of standard data for the IMFP of bismuth(III) oxide in the literature, its value of 2.6 nm was estimated from the curve of TPP-2M equation at five (5) valence electrons for bismuth¹⁵² and on the assumption that the inelastic mean free path of these electrons will not be too different from those of the metal. Other parameters used in the calculation are as reported elsewhere¹⁵³ by the same authors. The value of 9 nm for the oxide film thickness is probably an overestimate as it would effectively block electron transfer to redox couples. It is noticeable that the dependence of the capacitance data on electrolyte concentration is somewhat irregular (see Figure 3.1) and in many cases very low ($< 5 \mu\text{F cm}^{-2}$) differential capacitances are observed. The most likely explanation is that the oxide film thickness depends on exposure time of the electrode to the atmosphere – XPS is an ex-situ technique. In Chapter 5 an alternative estimate of film thickness is made using the capacitance data directly which is more consistent with the observation of electron transfer at such electrodes.

However, the XPS data does establish the presence of a thin oxide film on the bismuth electrode. At more negative potentials, this oxide will be reduced to elemental bismuth and, in general, the differential capacitance increases at the most negative potentials.^{154,155} The unusually high values of capacitance at the peak near -0.7 V (*figure 3.1* and *figure 3.5*) or near -0.5 V (*figure 3.3* and *figure 3.4*) reflect pseudocapacitance related to the charge stored in the form of faradaic processes involved in reduction of the oxide. A sketch to illustrate the effect of the oxide layer and its reduction back to the metal is shown in *figure 3.7*.

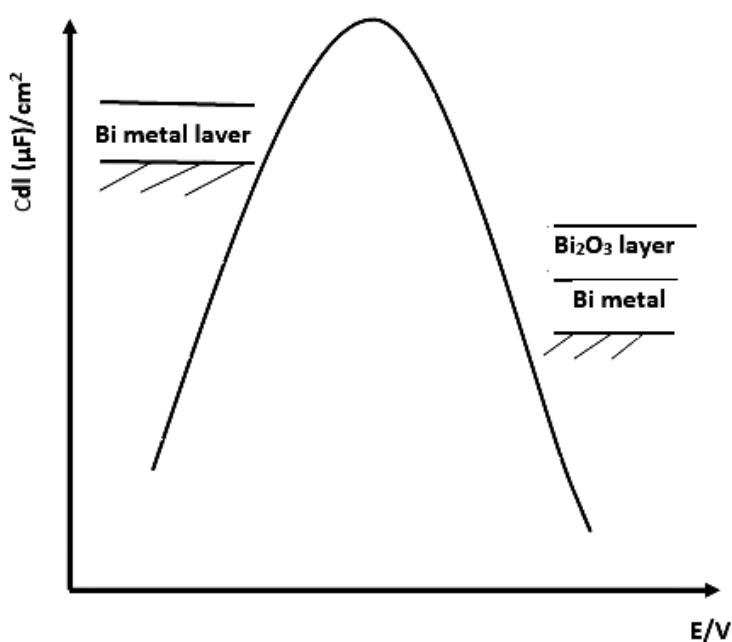


Figure 3.7. Sketch illustrating XPS data showing pseudocapacitance owing to presence of bismuth oxide layer.

Adsorption of halide ions on the electrode surface also appear to contribute to the effect because of the difference observed between NaBr, NaCl and NaNO₃ electrolytes.

XPS measurements were also conducted on the bismuth electrode in aqueous NaCl to evaluate the extent of adsorption of chloride ions at the bulk bismuth electrode surface. The bulk bismuth electrode differs from the bismuth film and the bismuth crystal plane surfaces owing to their Fermi-level density of states.¹⁵⁶ The XPS data obtained at bismuth in aq. NaCl is shown in *figure 3.8*.

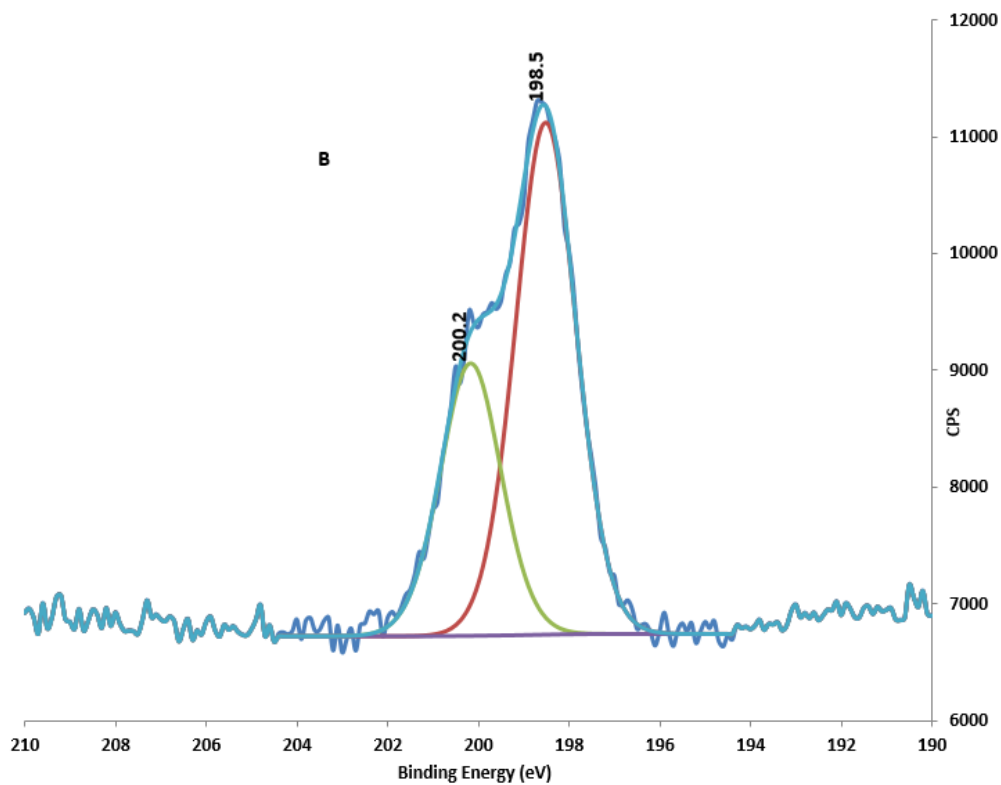
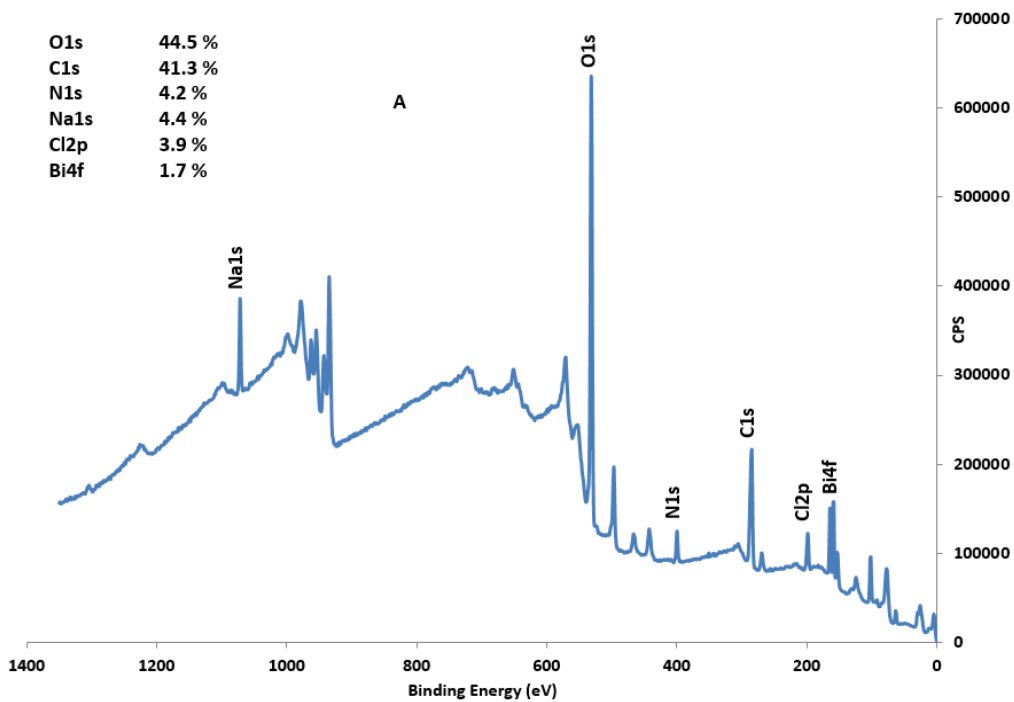


Figure 3.8. XPS (A) survey and (B) Cl-2p resolution spectra of the Bi|NaCl interface.

The photoemission spectrum of the Cl-2p region shows a doublet of closely spaced peaks which result from spin-orbit splitting, with values of binding energy 198.5 eV

and 200.2 eV in the spectral lines of 2p_{3/2} and 2p_{1/2} respectively, with an intensity ratio of 2:1 and are assigned to chloride anions. These binding energies and experimental findings are in agreement with other researchers¹⁵⁷⁻¹⁶⁰ in the field.

Similarly, XPS data generated of bromide anion adsorption at bismuth in aqueous sodium bromide, shown in *figure 3.9* indicate weak and strong adsorptions with binding energies of 68.2 eV in the 3d_{5/2} and 69.3 eV in the 3d_{3/2} spectral lines, with intensity ratio of 3:2. This finding is also not too far from what other workers^{140,161,162} have found in their investigations and confirm bromide anion adsorption.

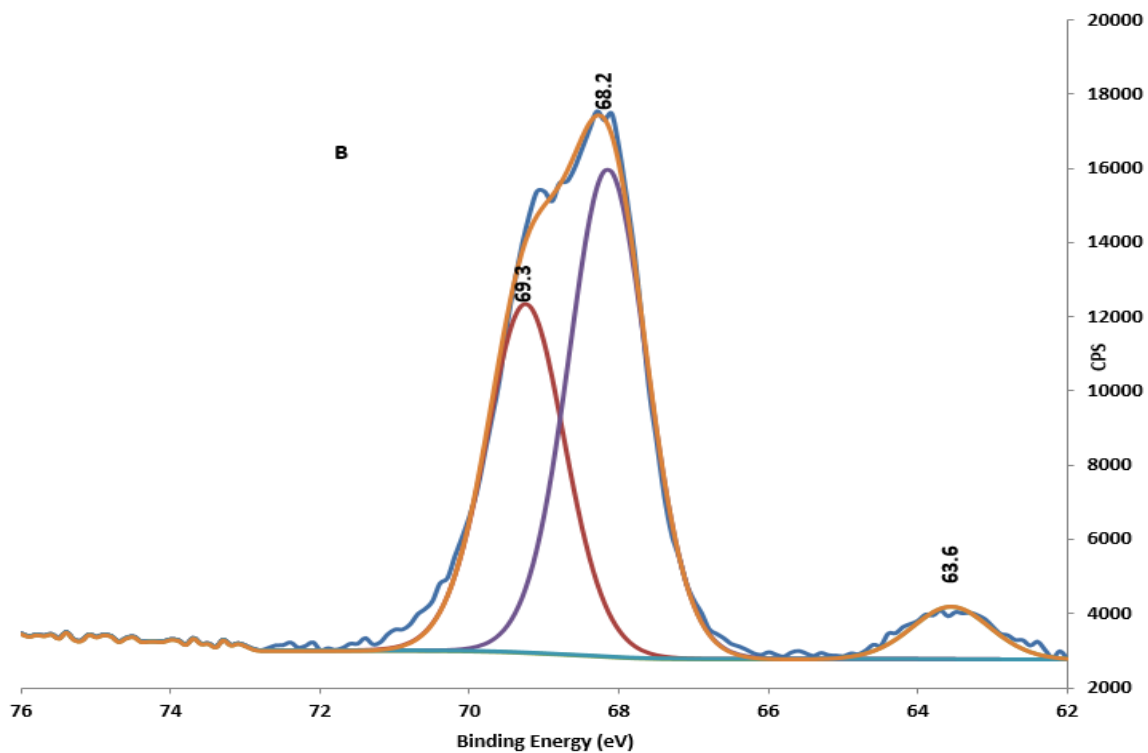
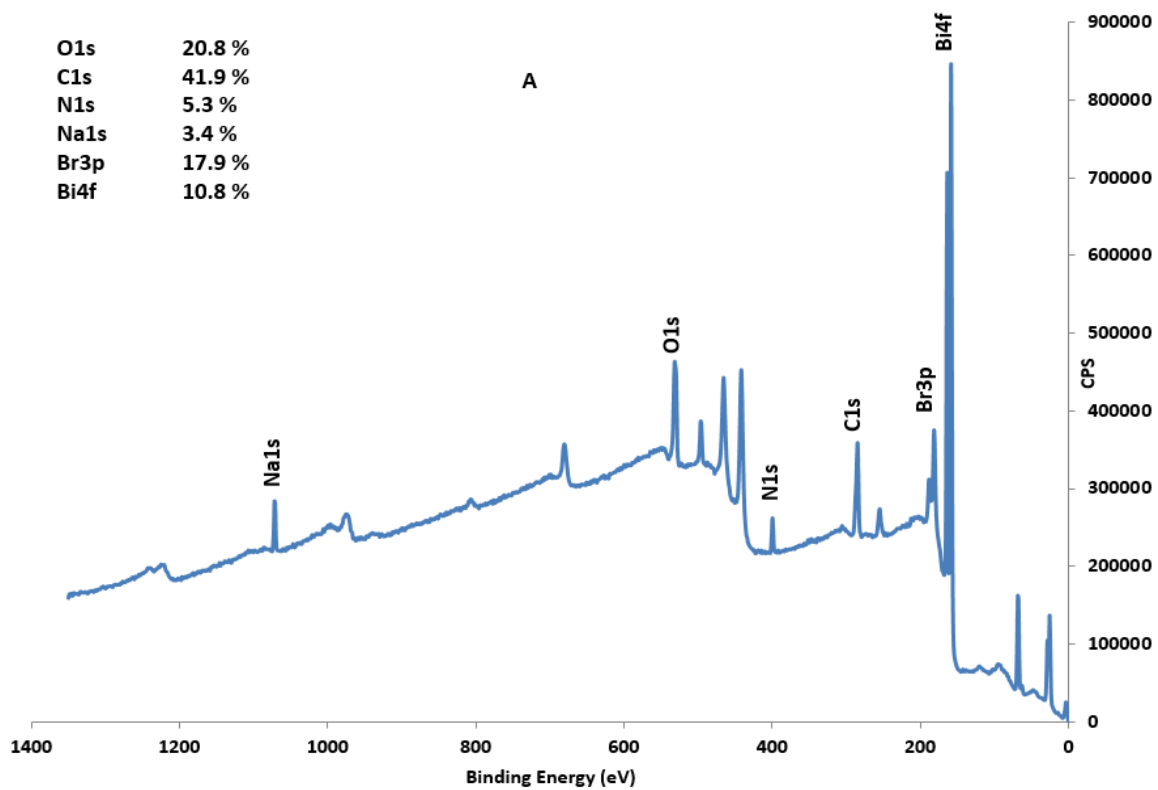


Figure3.9. (A) XPS survey (B) Br-3d resolution spectrum of the Bi|NaBr interface.

3.2.1 The double electrolyte effect

Sodium nitrate is itself an electrolyte, but to further investigate into the adsorption behaviour of the nitrate ion, the salt was prepared in aqueous sodium chloride solution as supporting electrolyte. The output of data presented in *figure 3.10* yielded curves with minimum values from which the potential of zero charge, PZC was estimated to have a value of -0.49 V. Herein lies the significance of the $\text{NaNO}_3/\text{NaCl}$ electrolyte mixture.

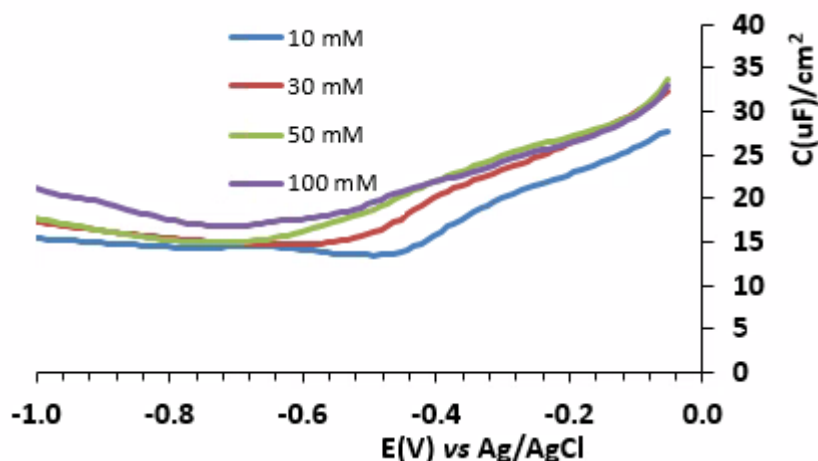


Figure 3.10. Capacitance data at Bi at in the $\text{NaNO}_3/\text{NaCl}$ electrolyte mixture at frequency of 1 kHz showing the pzc of -0.49 V.

3.3 Capacitance Measurements at Platinum in Aqueous Solutions

Electrochemical impedance spectroscopy measurements were also performed at the disc platinum electrode of dimensions as described in chapter 2 in the aqueous solutions of NaBr , NaNO_3 and NaCl , with the Ag/AgCl electrode as reference. In contrast to the data obtained at bismuth, the capacitance-potential curves resulting from these experiments had minimum values at all analyte concentrations and frequencies of measurement, i.e., they behave much more in line with expectations from the double layer theories discussed earlier in the introductory chapter. The set of data acquired in $\text{NaBr}(\text{aq})$ has been captured in *figure 3.11*.

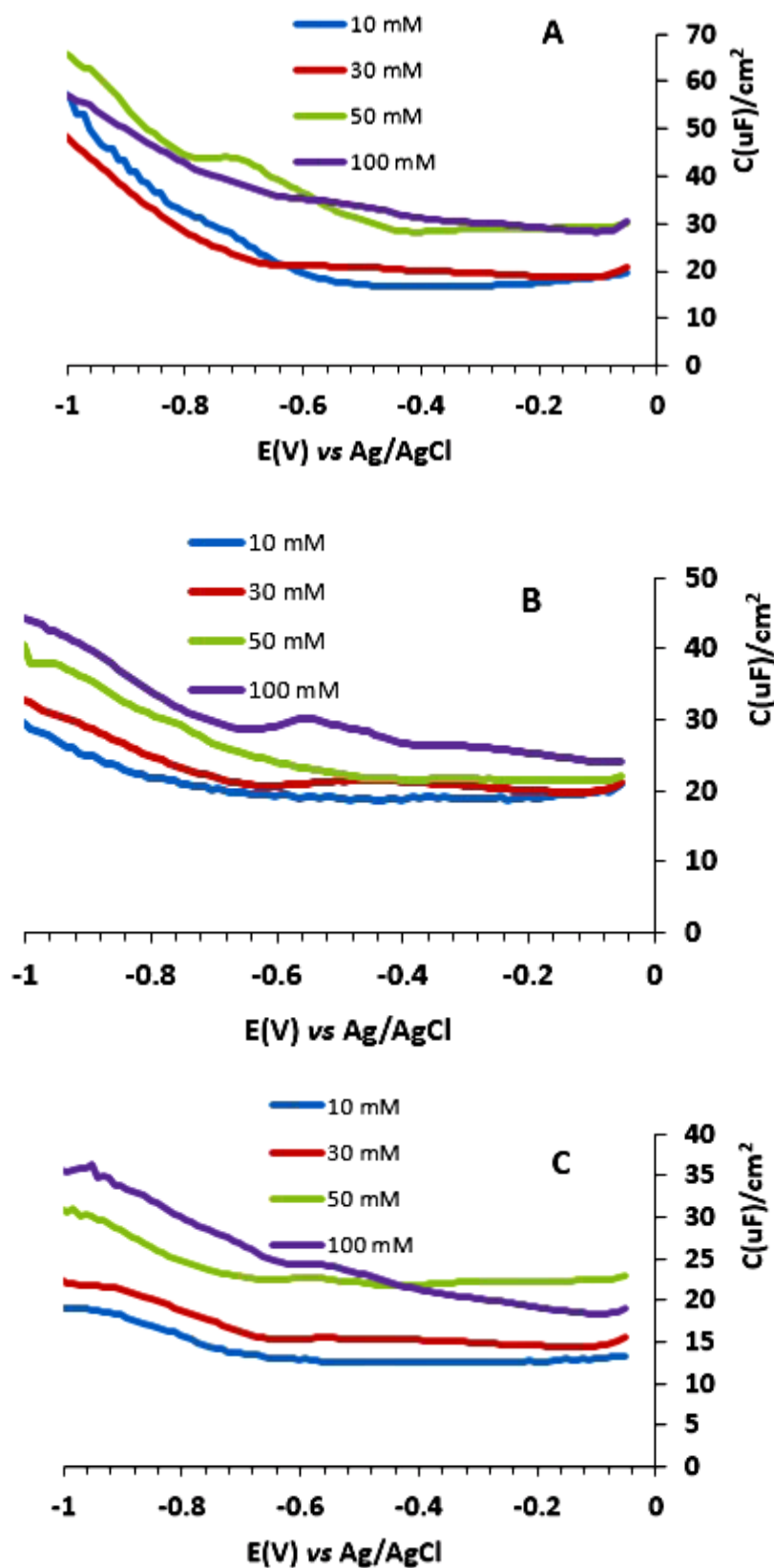


Figure 3.11. Capacitance data at Pt in aq. NaBr at (A) 500 Hz (B) 1 kHz (C) 2 kHz

As observed from the data, values of double layer capacitance decrease with increase in frequency as predicted by equations 3.1 and 3.2. The potential of zero

charge, *PZC* at Pt could be estimated from the mean of the minimum values at all the frequencies to be -0.32 V with respect to the Pt|NaBr interface.

The capacitance-potential data curves of Pt in aqueous NaCl show semblance with those obtained in NaBr solution in terms of decrease with frequency as is observable in *figure 3.12*. In addition, increase in capacitance with concentration is reflected in this electrolyte.

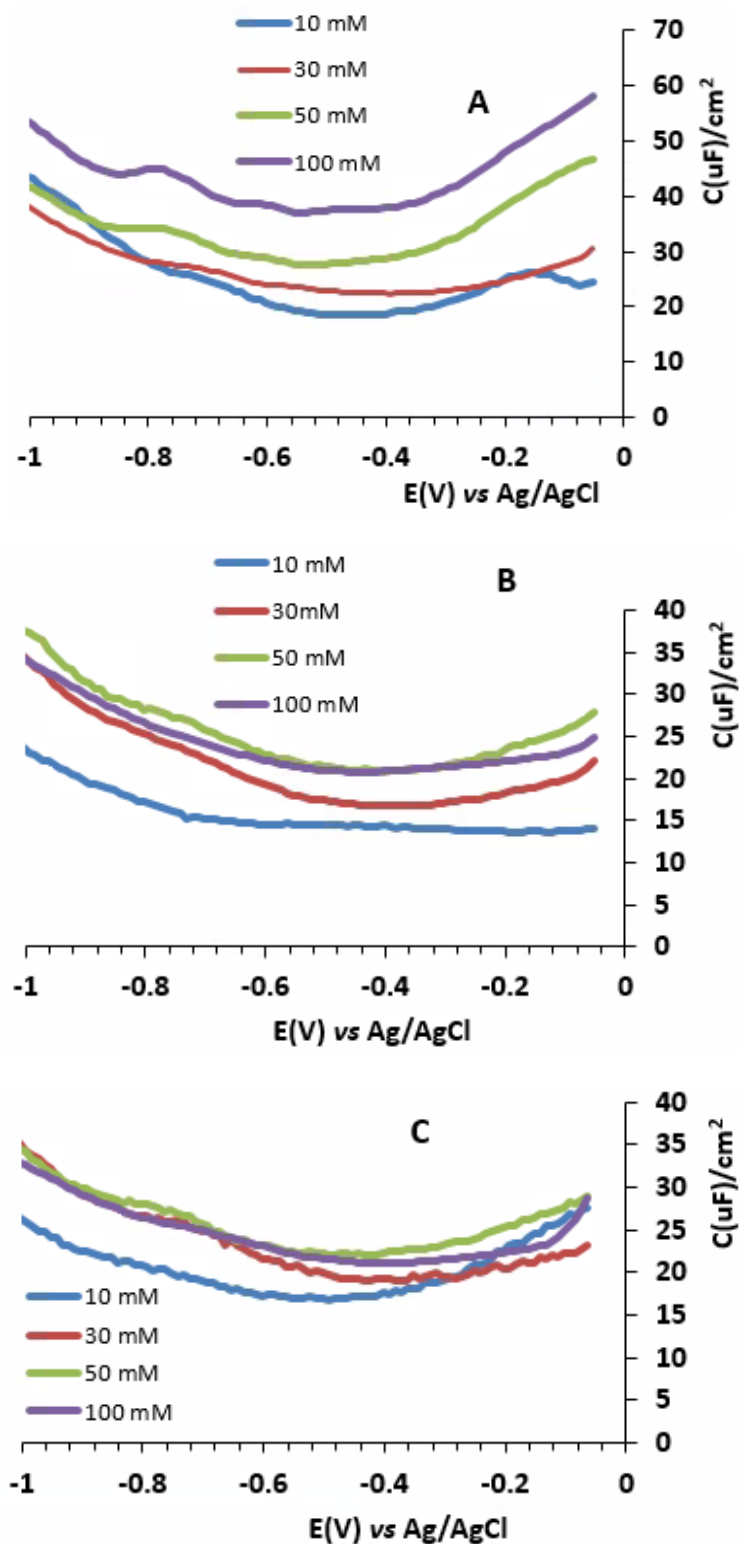


Figure 3.12. Capacitance data at Pt in aq. NaCl at (A) 500 HZ (B) 1 kHz (C) 2 kHz frequencies.

The capacitance-potential curves of platinum in aqueous $\text{NaNO}_3/\text{NaCl}$ electrolyte mixture however do not show a definite pattern at the three frequencies of measurement especially with respect to variation with concentration of analyte. The data, presented in figure 3.13 clearly shows that the electrolyte mixture has no

significant influence on the electrochemical activity of the platinum electrode. This could be one way to distinguish a noble metal electrode from that of a semimetal.

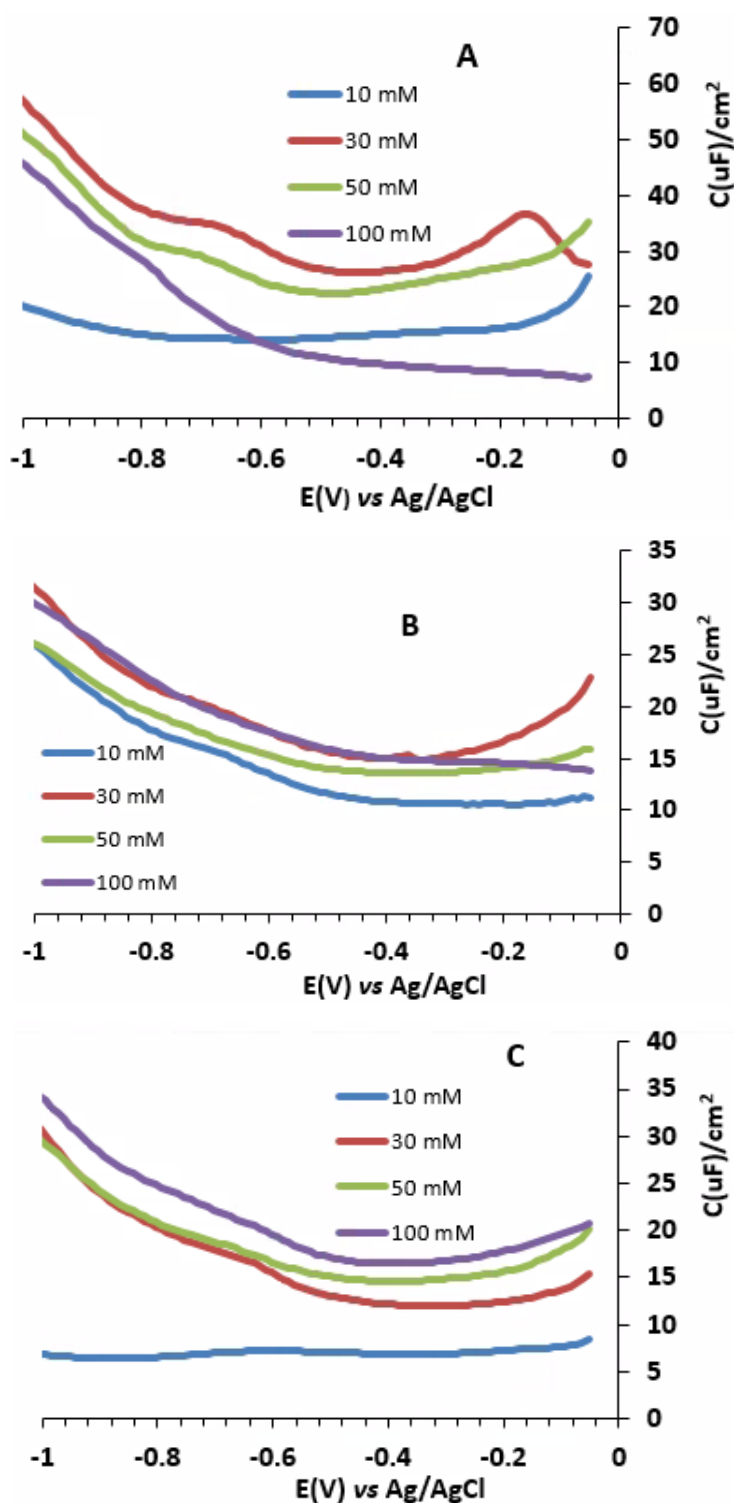


Figure 3.13. Capacitance data at Pt in the $\text{NaNO}_3/\text{NaCl}$ electrolyte mixture at frequencies of (A) 500 Hz (B) 1 kHz and (C) 2 kHz.

3.4 Capacitance Measurements at Bismuth in Non-aqueous Solvents

The charge storage capacity of the bismuth electrode surface was also investigated in the non-aqueous electrolyte mixture of acetonitrile (AN) and lithium perchlorate. While the former is adjudged to be an excellent polar organic solvent and ideal for analysis owing to its relatively high dielectric constant and dipole moment, the latter is a very good inorganic electrolyte that ionizes completely in solution. Acetonitrile has a dipole moment of 3.44 D and a dielectric constant of 37.5 at 20 °C.¹⁶³ This value of dielectric constant, considered to be high in some circumstances is still lower than that of water which is 80.1 at the same temperature of 20 °C.

Values of double layer capacitance of the Bi | acetonitrile (AN) interface are presented in Figure and as can be clearly observed, all lie below 20 $\mu\text{F cm}^{-2}$ at the three frequencies of measurement. The very low capacitance of the Bi | AN interface could be attributable to the relatively low dielectric constant of acetonitrile¹³ as well as the weak adsorption of the ClO_4^- at the bismuth electrode surface in ethanol.²⁶ Lithium perchlorate LiClO_4 is believed to exhibit low surface activity in non-aqueous solutions. An un-usual behaviour of the bismuth electrode in these non-aqueous solvents is the steady decrease of stored charge as the concentration of analyte increases. This could be due to increased surface activity of lithium perchlorate as the concentration increases.

Apart from the 100 mM concentration with about 43 $\mu\text{F cm}^{-2}$ effective capacity at 500 Hz, values of double layer capacitance at bismuth for all the other interfaces of NaBr, NaCl and NaNO_3 generally fell within the standard range^{42,44} of 10-40 $\mu\text{F cm}^{-2}$. This implies that the bismuth electrodes can safely replace noble metal electrodes in the measurement of differential capacitance. The high values of differential capacitance recorded in the 100 mM concentration could be attributed to adsorption at the surface associated with high analyte concentrations.

The capacitance values however increased in the order of electrolyte solutions $\text{LiClO}_4 < \text{NaNO}_3 < \text{NaCl} < \text{NaBr}$. In principle the capacitance is expected to increase as the solvated ionic radius decreases. However anions, such as Br^- , which have a strong tendency to specifically adsorb (i.e., lose part of their solvation shell) may not follow this simple trend.

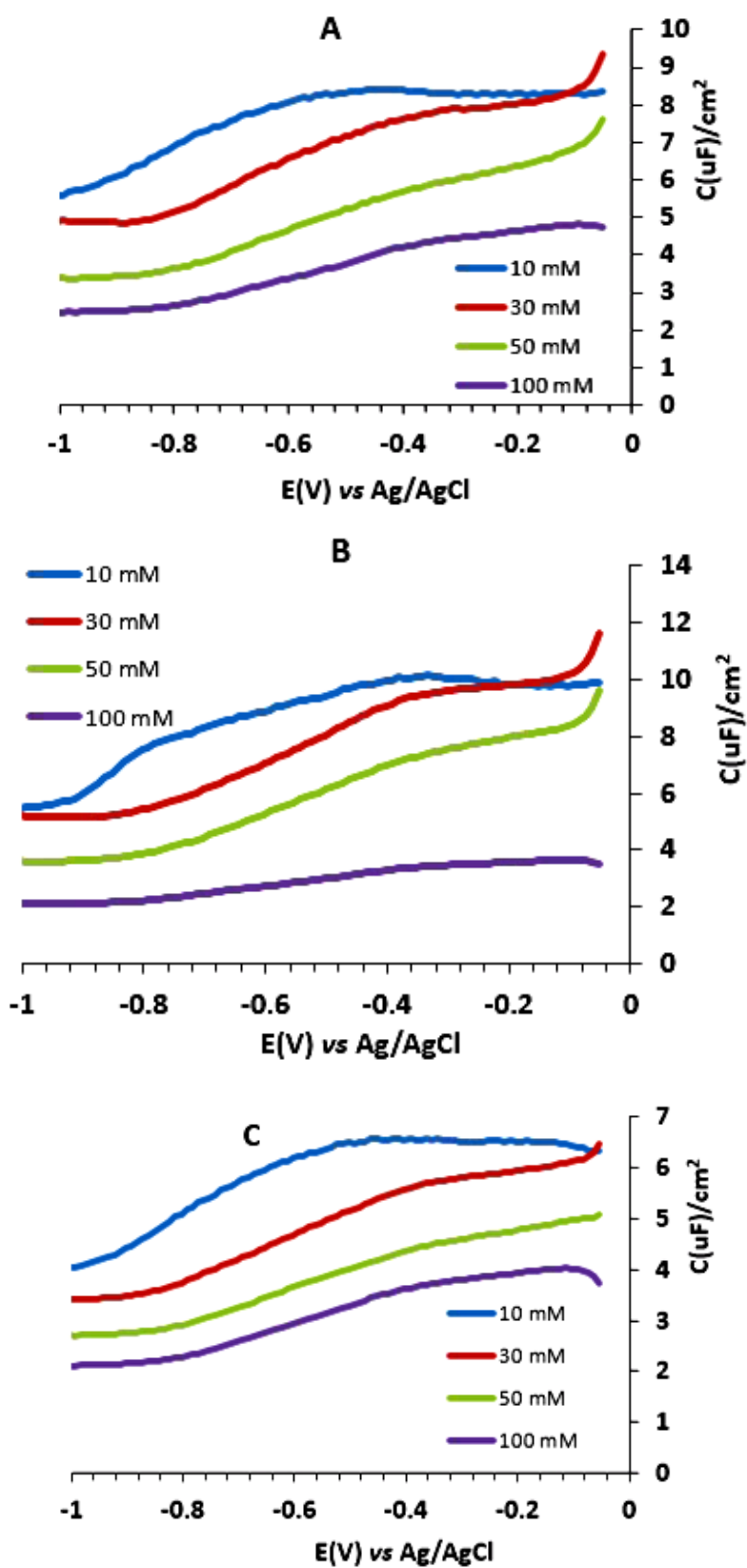


Figure 3.14 Capacitance data at Bi in the non-aqueous AN/LiClO₄ at (A) 500 Hz (B) 1 kHz (C) 2 kHz

3.5 Capacitance Measurements at Platinum in Non-aqueous Solvents

By way of comparison, impedance measurements were also carried out with platinum as the working electrode in the non-aqueous electrolyte of acetonitrile/lithium perchlorate. Data obtained from the investigation is presented in *Figure 3.15* below.

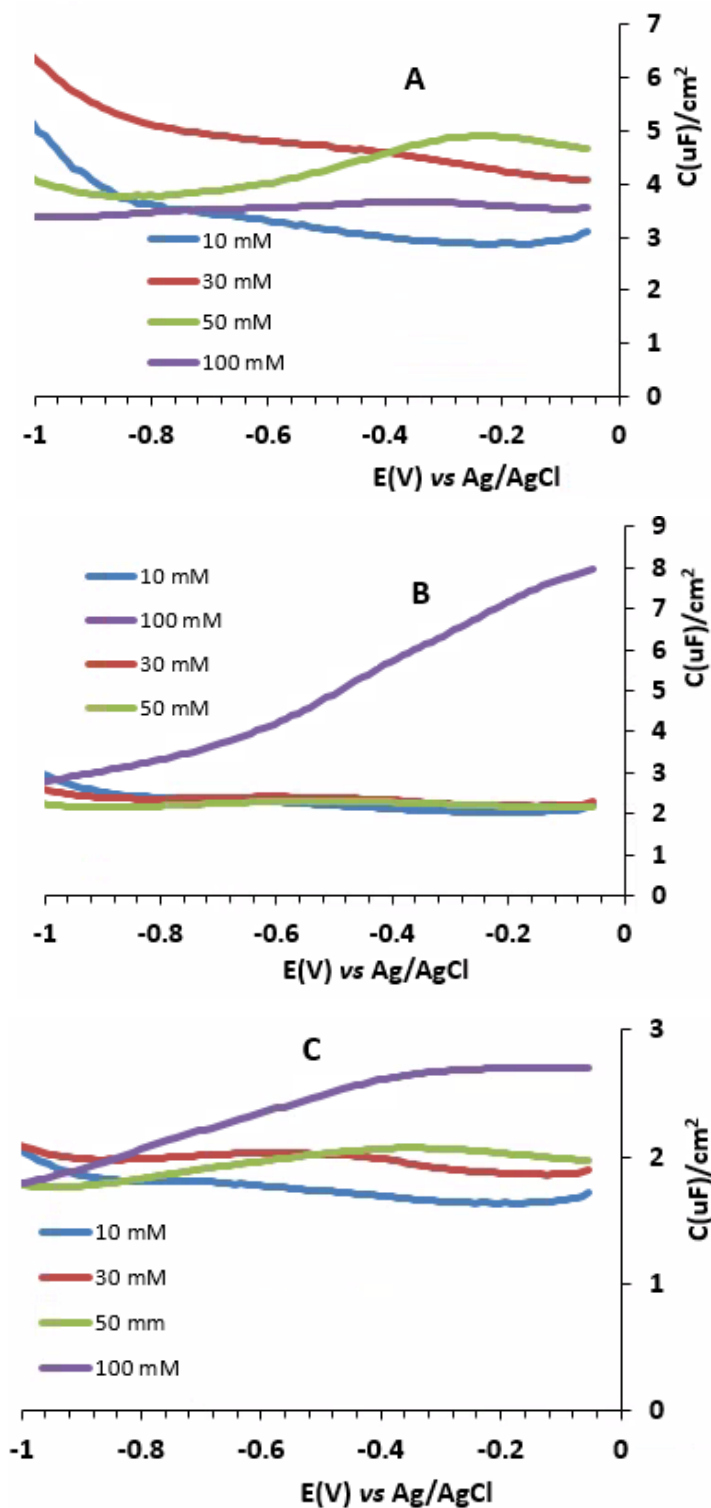


Figure 3.15. Capacitance data at Pt in AN/LiClO₄ at (A) 500 Hz (B) 1 kHz (C) 2 kHz

Values of differential capacitance recorded at the platinum electrode surface in the non-aqueous medium are lower than at the bismuth electrode surface in aqueous media. This is due to the lower relative permittivity of the non-aqueous electrolyte and the much greater tendency for halides to specifically adsorb than perchlorate. This can be further explained in terms of constant phase element behaviour. The physical roughness of the Bi electrode allows for more adsorption of charges than the relatively smoother surface of the platinum electrode.

The sizes of the capacitance values however show a general decrease with increasing magnitude of frequency of measurement, and this is in agreement with theoretical prediction.

3.6 Conclusions

Bismuth electrodes show complex differential capacitance-potential curves in aqueous electrolytes which are not in line with expectations of the standard double layer theories. The curves generally show a sharp maximum which is suggested to result from pseudocapacitance effects related to the presence of an oxide film at potentials positive of the maximum and its reduction to elemental bismuth at potentials negative of the maximum. Electrochemical impedance spectroscopy (EIS) measurements performed as described in the foregoing sections enabled the determination of potential of zero charge PZC, at the bismuth and platinum electrodes surfaces in two cases. A value of -0.49 V was obtained at bismuth in the aqueous NaNO₃/NaCl electrolyte mixture while -0.32 V was the determination made at platinum in aqueous NaBr.

Findings from EIS and XPS experiments put together indicate that the capacitance peaks at bismuth in aqueous solutions are due to adsorption of anions as well as pseudocapacitance contributions of the redox processes of the bismuth oxide film and the metal at this electrode surface. On the other hand, the low values of double layer capacitance ($<20 \mu\text{F cm}^{-2}$) in the non-aqueous electrolyte of AN/LiClO₄ is as a result of the relatively low dielectric constant of AN as well as the weak adsorption capacity of the ClO₄⁻ anion. This finding is broadly consistent with the Gouy-Chapman-Stern theory.

Bismuth electrodes have also been used to study the electron transfer process of the redox couple of ruthenium hexaamine trichloride (Chapter 5) and this has at a formal potential of $-0.217\text{ V vs Ag/AgCl (1 M KCl)}$. The significance of the differential capacitance measurements in this chapter is that they show electron transfer reaction for this couple takes place at an oxide-covered electrode.

The irregular variation of capacitance with concentration and frequency only goes to confirm that the bismuth and platinum electrode surfaces are not ideal capacitors. These surfaces should therefore be seen to be behaving as constant phase elements (CPEs) or non-ideal capacitors.

Chapter 4. Electrochemical Behaviour of Selected Redox Couples at Bismuth Electrodes

4.1 Synopsis

A series of redox couples were chosen and their electrochemical behavior at bismuth electrodes was investigated in a qualitative manner. Attempts were also made to compare the electroactivity of the redox couples at the semi-metallic bismuth bulk electrodes with that of platinum, a noble metal electrode more commonly used in electroanalytical chemistry. The redox couples chosen include: ruthenium(III) hexaammine, methyl viologen, anthraquinone-2-sulfonate, methylene blue, toluidine blue, hexaammine cobalt(III) and cobaltocenium. This large array of redox couples was chosen to establish the suitability of bismuth electrodes as potential replacements in electroanalysis and to determine a suitable test case for detailed electrode kinetics. These couples were selected because they are known to show straightforward voltammetry at noble metal electrodes under appropriate conditions. The aim of the present chapter is to investigate the redox reactions of the couples and establish which show simple, uncomplicated voltammetry that is suited for a deeper study of the electrode kinetics in Chapter 5.

4.2 Ruthenium(III) hexaammine

Preliminary investigations on this complex were carried out in analyte solutions prepared in 0.1 M KCl as supporting electrolyte. Cyclic voltammetric measurements performed with different concentrations of 10 mM, 8 mM, 5 mM and 2 mM to check the effect of concentration on the shape of the voltammograms showed reproducibility. A CV of the 5 mM concentration is shown in *figure 4.1* for illustration.

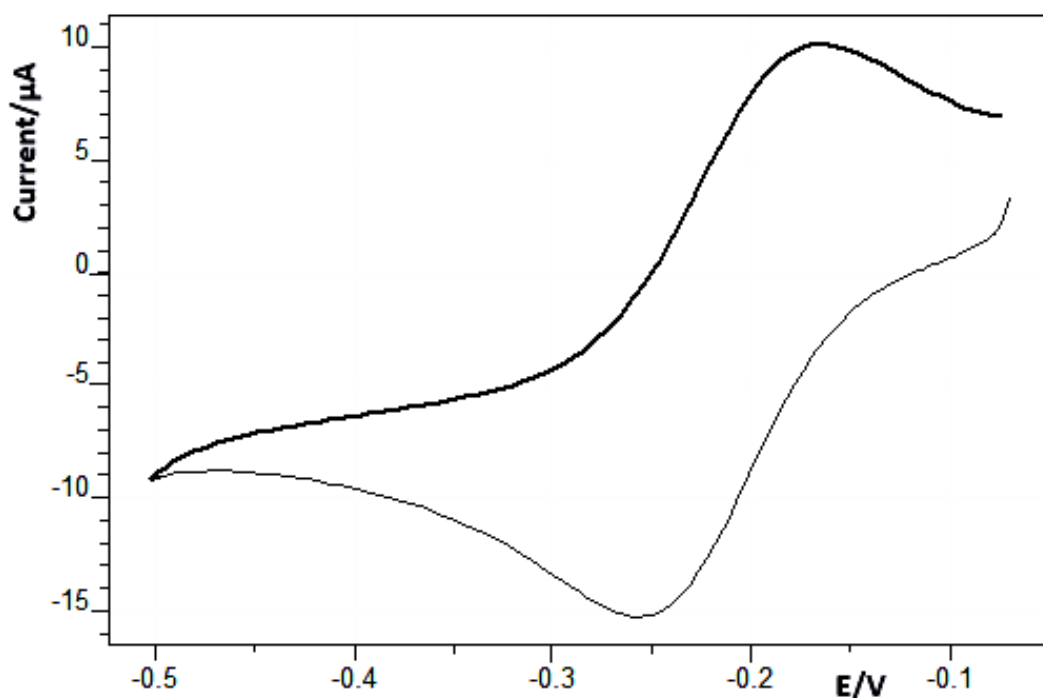


Figure 4.1. CV of 5 mM ruthenium(III) hexaammine at scan rate of 25 mV/s at bismuth in 0.1 M KCl. The potentials were measured against an Ag/AgCl (1 M KCl) reference electrode.

The peak potential differences ranged from 80 mV for the lower concentrations to 88 mV for the 10 mM concentration. Although the CV of *figure 4.1* shows a peak separation greater than the 60 mV for a reversible process, the peak potential is linear with square root of scan rate. The unusually high value of peak separation is not expected for a quasi-reversible process. Instead it is more likely that the voltammetry is reversible but that uncompensated resistance effects increase the peak separation. This is consistent with the observation of larger ΔE_p at higher concentrations of ruthenium hexaammine. A plot of peak currents against scan rate showed a near 100% correlation as can be seen in the *figure 4.2*. The absence of deviations from the regression line also shows that adsorption effects (peak current proportional to scan rate) are negligible.

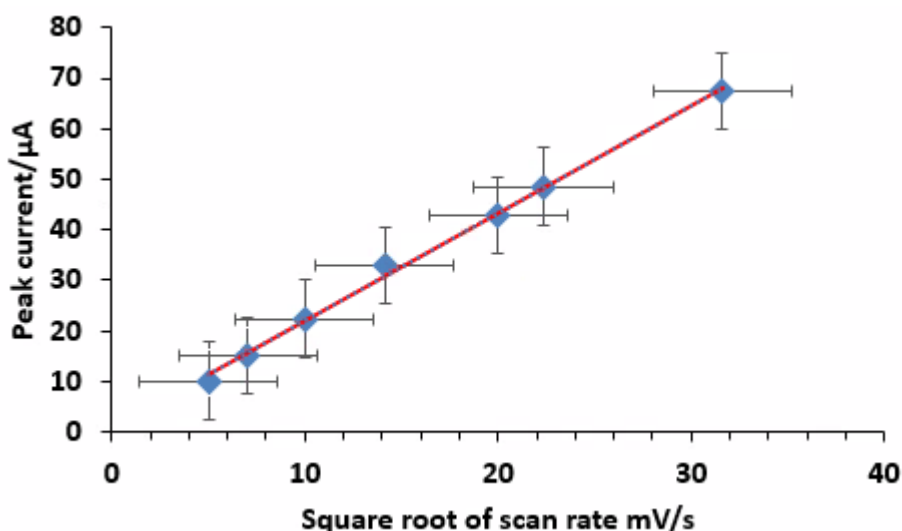


Figure 4.2. Variation of peak currents with scan rate for 5 mM ruthenium(III) hexaammine in 0.1 M KCl at Bi.

An electrochemical process is reversible if the electron transfer at the electrode surface is so fast that the local concentrations immediately adjust to establish local equilibrium in response to changes in potential. Precisely, the surface concentrations (not the bulk values) obey the Nernst equation at all points in the experiment.

Ruthenium hexaammine showed electrochemical behaviour that is close to that of a reversible process; with a peak potential difference of 88 mV at scan rate of 5 mVs^{-1} , a peak current ratio of unity and a symmetrical shape for the cyclic voltammograms. The electrode kinetics of the redox couple was therefore investigated in detail and the results are presented in chapter 5.

4.3 Methyl Viologen or Paraquat

Paraquat is an interesting compound to study because of its toxicity and persistence in the environment^{56,62,64} occasioned by world-wide use as herbicide on a variety of crops. Because it is non-biodegradable, continued application on food crops increases the health risk of the consumers due to bioaccumulation. It is known to undergo two one-electron reductions to the radical cation and then to the neutral species.

The first step in the kinetic studies of the compound was to run cyclic voltammograms of its samples to check if they satisfy the conditions of a reversible electron transfer process. Cyclic voltammograms (CVs) were run with analyte concentrations of 10 mM, 5 mM and 2 mM, prepared in 0.1 M KCl(aq) as supporting electrolyte but the characteristic two-step-two-electron voltammogram was not achieved. A CV of the

2 mM concentration is presented in *figure 4.3* for illustration. The solid line indicates increase in the cathodic currents, occasioned by accumulation of adsorbed material; hence the reduction peaks suggest adsorption.

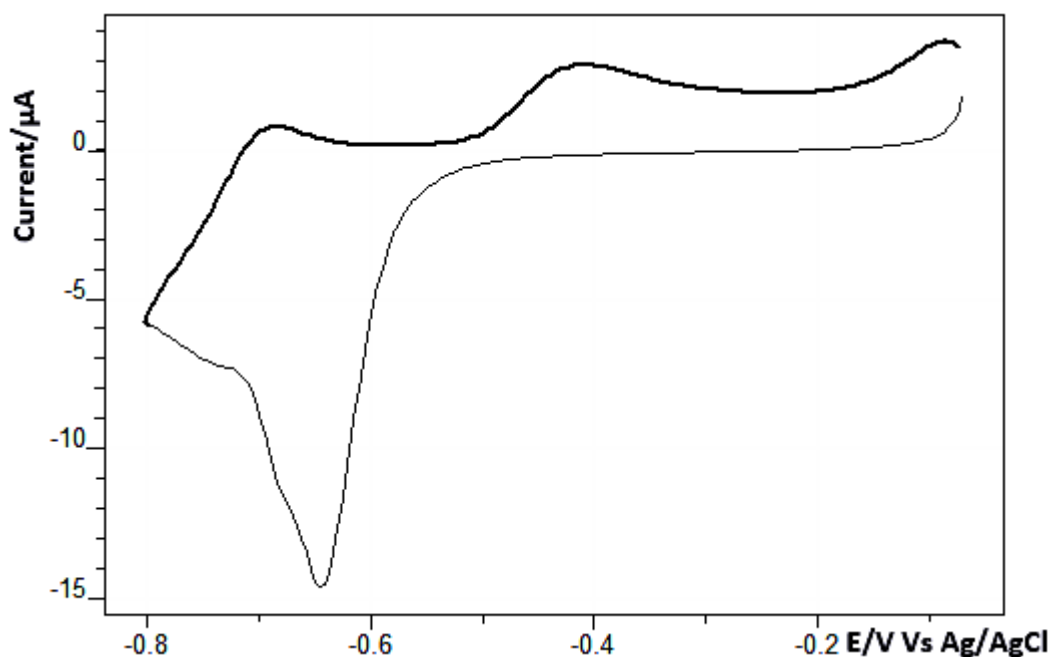


Figure 4.3. CV of 2 mM methyl viologen at Bi at scan rate of 25 mV/s in 0.1 M KCl(aq). The reference electrode was Ag/AgCl (1 M KCl).

Methyl viologen undergoes a 2-step reduction process:



This monocation complex is oxygen sensitive^{57,58} hence the solution was argon purged.



The neutral compound has low solubility and may adsorb on the electrode surface.⁵⁹⁻⁶¹

Two reduction peaks were obtained in the cyclic voltammogram of the 5 mM concentration, at scan rate of 25 mV s⁻¹; shown in *figure 4.4*.

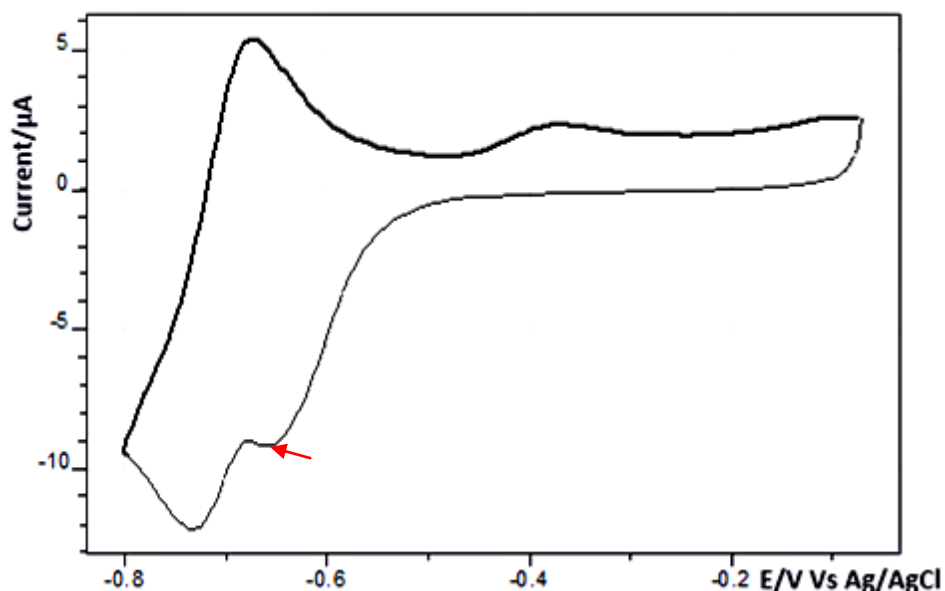
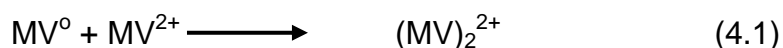


Figure 4.4. CV of 5 mM methyl viologen at Bi at scan rate of 25 mV/s in 0.1 M KCl(aq). The smaller peak is indicated in red.

The smaller peak disappeared as the scan rate was increased, suggesting dimerization^{19,62,63} of the monovalent compound. The dimer is believed to result from an interaction of the neutral molecule MV^0 at the electrode with the divalent complex MV^{2+} from the bulk solution



This radical-cation dimer is spin-coupled¹⁶⁴ and is electro-inactive^{164,165} therefore the voltammetry is irreversible and interpretations of its electrochemical behaviour become complicated.

Electrochemical impedance spectroscopy (EIS) measurements were made at various concentrations; the semi-circular Nyquist plots (*figure 4.5* and *figure 4.6*) point to kinetic control and the Warburg impedance (*figure 4.6*) to diffusion control^{60,166} at lower frequencies and larger overpotentials. Selected data for the 2 mM concentration are presented in *figure 4.5* and *figure 4.6* below which indicate kinetic behavior at potential of -0.58 V but a Warburg impedance at the more negative potential of -0.67 V. This is quite expected, but it should be noted that the data at -0.67 V show almost purely diffusion control and we could not extract the charge transfer resistance from the data.

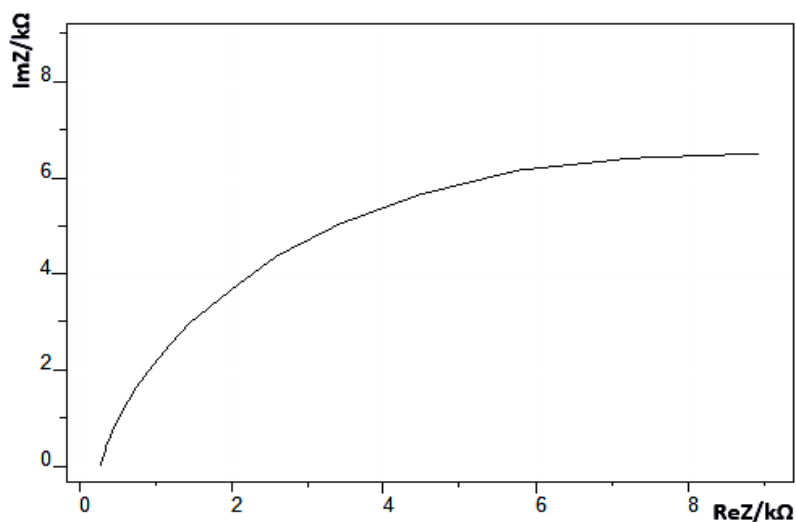


Figure 4.5. Nyquist plot of 2 mM methyl viologen at bismuth at -0.58 V in 0.1 M KCl(aq). The reference electrode was Ag/AgCl (1 M KCl).

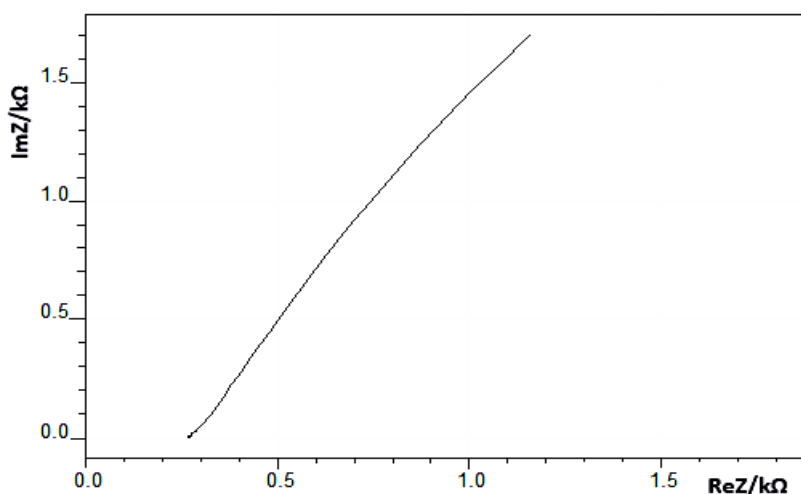


Figure 4.6. Nyquist plot of 2 mM methyl viologen at bismuth at -0.67 V in 0.1 M KCl versus Ag/AgCl (1 M KCl).

Upon comparison of the curves of *figure 4.5* and *figure 4.7* however, the data is seen not to be so clear. Both datasets show semi-circular Nyquist plots and were generated at very close potentials, however the impedance is observed to increase with concentration. This is unexpected and is likely a result of electrode fouling by the reduction products noted in the cyclic voltammetric data.

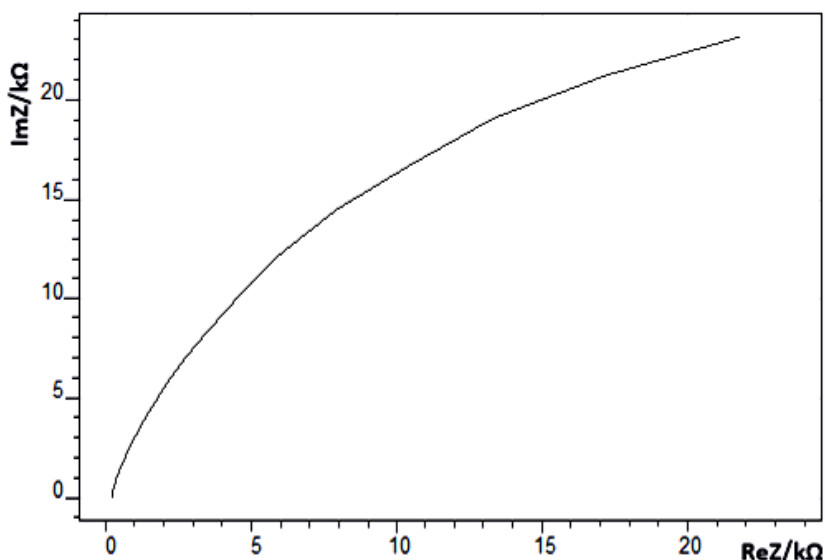


Figure 4.7 Nyquist plot of 10 mM methyl viologen at bismuth at -0.56 V in 0.1 M KCl versus Ag/AgCl (1 M KCl).

Some kinetic information was obtained by fitting the data to a Randles equivalent circuit. Figure 4.8 shows the variation of the charge transfer (R_{CT}) with dc potential for 2 mM and 10 mM methyl viologen in 0.1 M KCl(aq). Normally the $R_{CT} - E$ plot is U-shaped as the increase in electron transfer rate with overpotential is opposed by the decrease in surface concentration of reactant according to the Nernst equation. This is not observed in the 10 mM data, although the 2 mM data shows approximately normal behaviour. Such a concentration dependence is typical of second order processes such as dimerization or adsorption. In addition, R_{CT} should decrease with increase in concentration (they are inversely proportional) but the reverse is the case here.

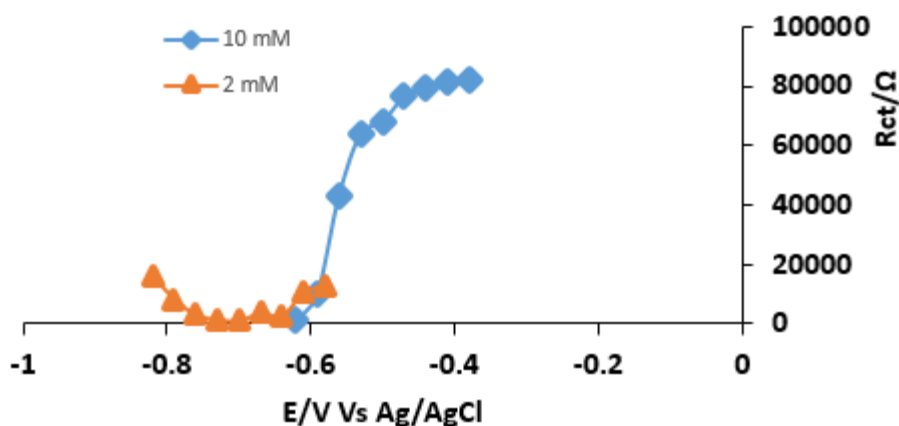


Figure 4.8. Variation of charge transfer resistance with potential for methyl viologen at bismuth in 0.1 M KCl(aq).

The differential capacitance was also extracted from the fitted equivalent circuit and the C_d-E profile presented in *figure 4.9* shows even more complex behaviour. There is no correspondence between the two datasets and this argues that adsorption phenomena are significant.

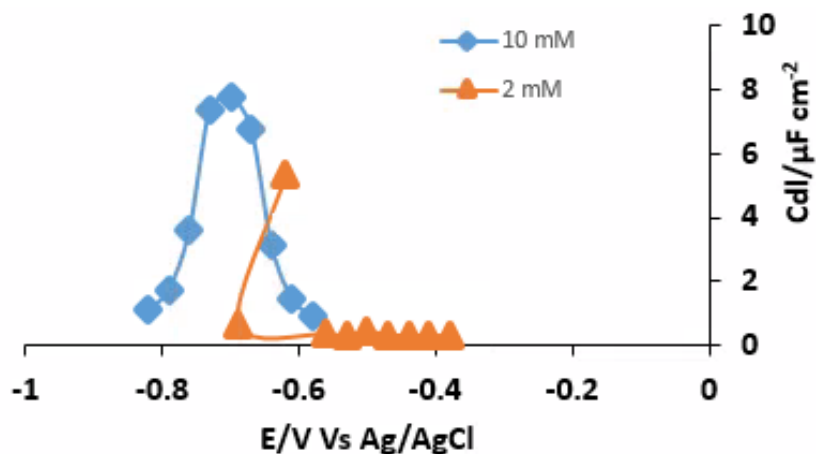


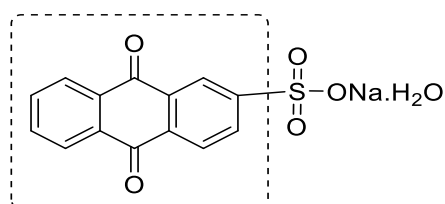
Figure 4.9. Variation of differential capacitance with potential for methyl viologen at bismuth in 0.1 M KCl(aq).

Further work on methyl viologen was therefore suspended on account of the following: (i) possible dimerization of the monocation MV^+ as the product is irreversible and therefore electro-inactive.

(ii) Bold solid lines in the reduction peaks and the dependence of the impedance spectroscopy on concentration suggest strong adsorption of the products at Bi.

4.4 Sodium Anthraquinone-2-sulfonate Monohydrate

An enormous amount of data has been generated on this compound. The reduction occurs by a two electron mechanism to the phenolate or, with addition of two protons, to the corresponding phenols. The structure of the compound is shown in *scheme 4.1* in which the anthraquinone part is enclosed in the dotted rectangle.



Scheme 4.1 Structure of sodium anthraquinone-2-sulfonate monohydrate

Good CVs of samples of the compound were obtained from solutions purged with nitrogen and later with argon gas. The best shape of a reduction CV was obtained at scan rate of 200 mV s^{-1} . Good CVs were obtained for all the concentrations of analyte. An example of a voltammogram for the 2 mM concentration is shown in *figure 4.10* below. Below, the compound is denoted as AQS.

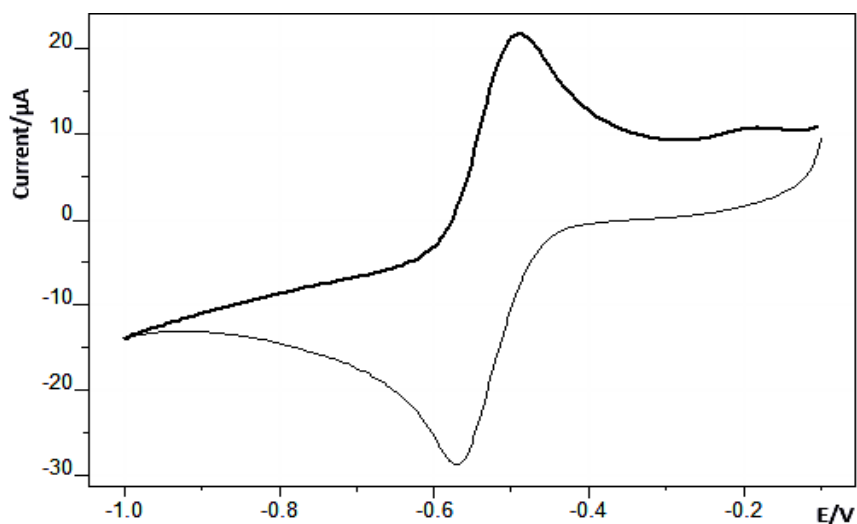


Figure 4.10 CV of 2 mM AQS at Bi at scan rate of 200 mV/s in argon-purged 0.1 M KCl solution. An Ag/AgCl (1 M KCl) reference electrode was used.

A plot of peak currents against square root of scan rates shown in *figure 4.11* yielded a perfect straight line, an indication that the redox process is diffusion controlled.⁴⁴

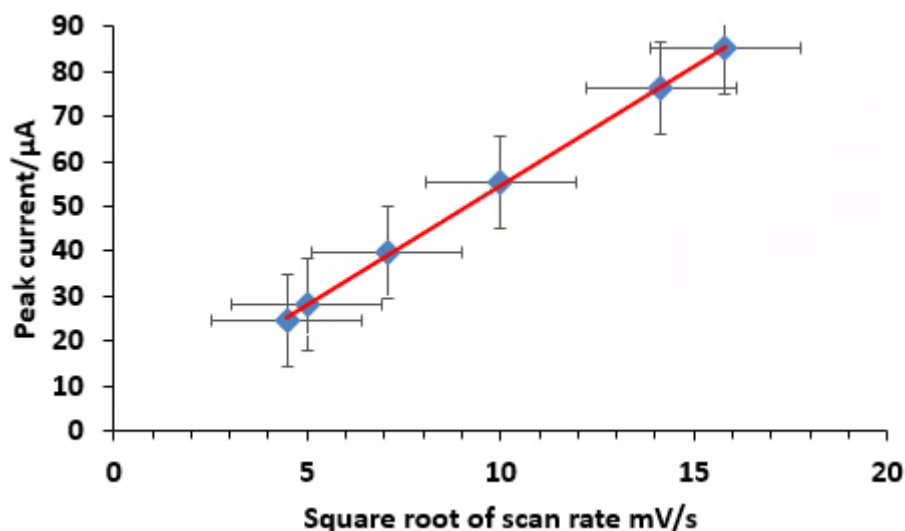
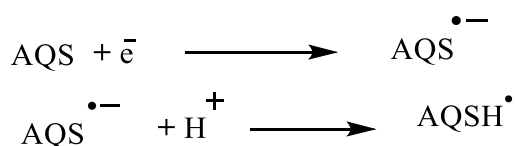


Figure 4.11 Variation of peak currents with scan rate for 10 mM AQS at Bi.

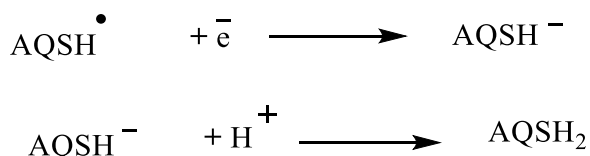
This plot satisfies one condition for a simple reversible electrochemical process even though the least value of potential peak separation is 88 mV. Following the nature of

the CVs and plot of peak currents against square root of scan rates, AC voltammetry was carried out to obtain the formal potential E° that would serve as the reversible potential for *EIS* measurements and because simple CV is often not able to distinguish closely overlapping redox processes.

The AC voltammogram of the 10 mM concentration is also shown in the *figure 4.12* and it reveals an incomplete curve as well as presence of two peaks which creates uncertainties as to which peak parameters would be used as guide for further investigations. We suggest the following mechanism takes place at the first cathodic peak:



And at the second peak,



Previous workers suggested the formation of a charge transfer complex¹⁶⁷ that arises because of the electron-withdrawing nature of the sulfonate group. Different positions of the sulfonate group on the complex can give rise to multiple peaks.

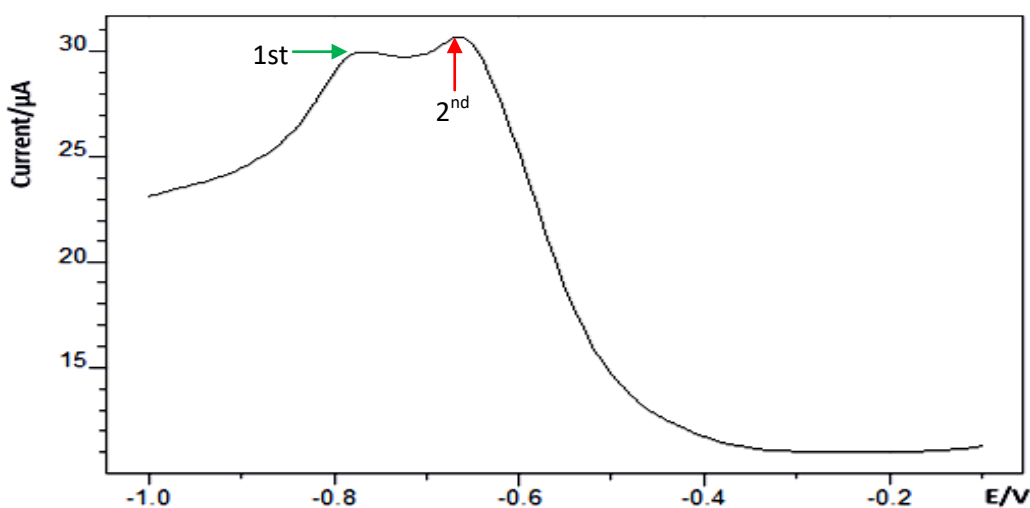


Figure 4.12. AC voltammogram of 10 mM AQS at bismuth in 0.1 M KCl solution. An Ag/AgCl (1 M KCl) reference electrode was used. The scan rate was 25 mV/s with amplitude of 10 mV at frequency of 1000 Hz. The green and red arrows point to the 1st and 2nd peaks respectively.

Impedance measurements at various dc potentials were subsequently made at potentials of ± 30 , ± 60 , ± 90 and ± 120 mV with respect to the formal potential to give a total of nine (9) spectra for each concentration. The frequency range was $10^1 - 10^5$ Hz. Most of the spectra showed Warburg impedance and for these, no values of R_{CT} were obtained. Some spectra presented evidence of kinetic limitations and values of R_{CT} were extracted by fitting a Randles equivalent circuit. Sample impedance spectra are shown in *figure 4.13* and *figure 4.14*.

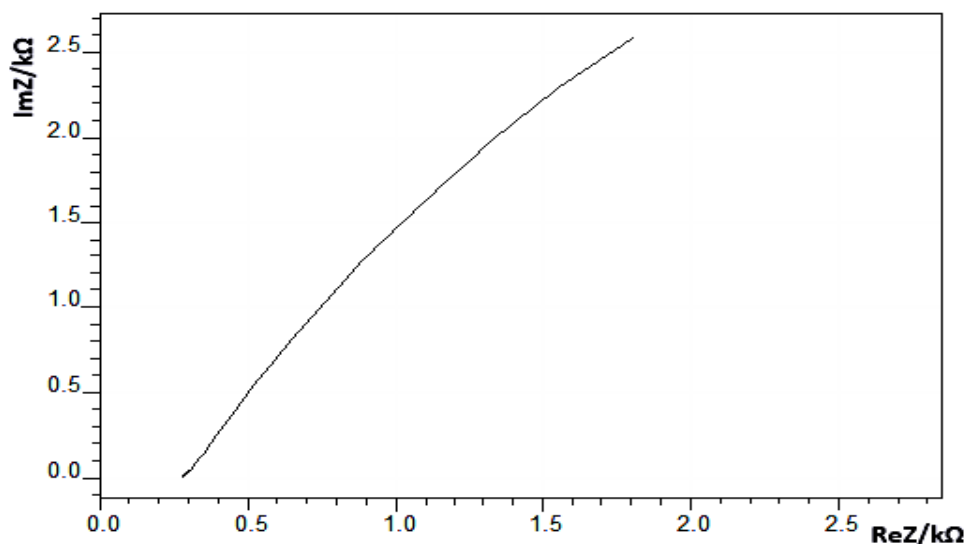


Figure 4.13 Nyquist plot of 2 mM AQS at bismuth at -0.78 V Vs Ag/AgCl (1 M KCl) in 0.1 M KCl.

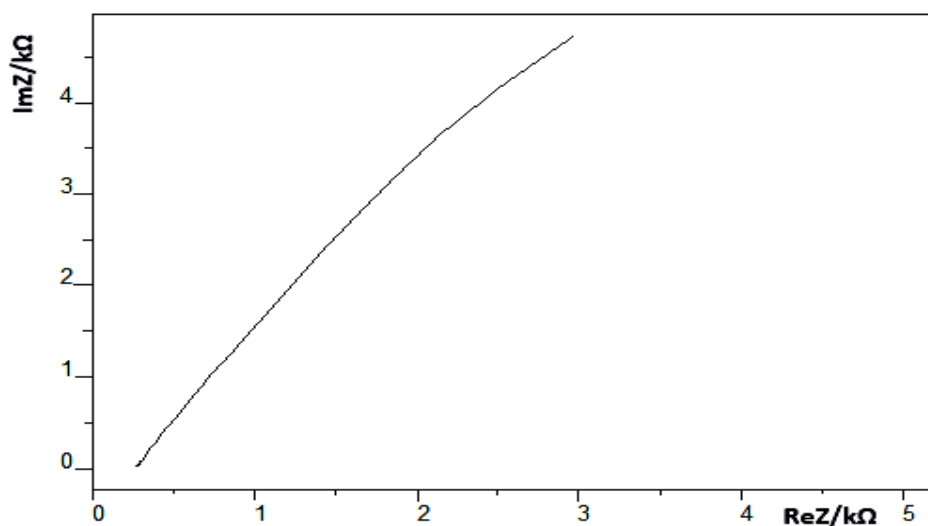


Figure 4.14 Nyquist plot of 2 mM AQS at bismuth at -0.89 V Vs Ag/AgCl (1 M KCl) in 0.1 M KCl.

The kinetic data generated from the impedance spectra are as presented in *figure 4.15* below.

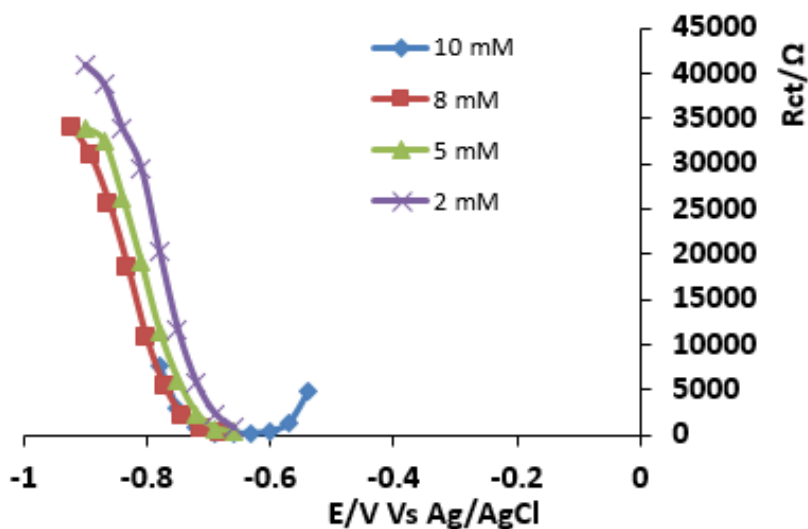


Figure 4.15. Charge transfer profile of AQS at Bi in 0.1 M KCl as supporting electrolyte.

The quality of the impedance data was adjudged to be insufficient for a detailed kinetic analysis because the charge transfer resistance profile did not yield the U-shape characteristic of a simple redox process and the variation of R_{CT} with concentration is complex.

A potential scan was also performed at values of the potential gap with a potential step of 20 mV, after the electrodes had been cleaned and the analyte solution purged again with argon gas for a minimum of 10 minutes. The overlaid impedance spectra of the 2 mM concentration are shown in *figure 4.15*. Spectra near the formal potential are dominated by the Warburg impedance and measurable charge transfer resistances are only obtained at large overpotentials.

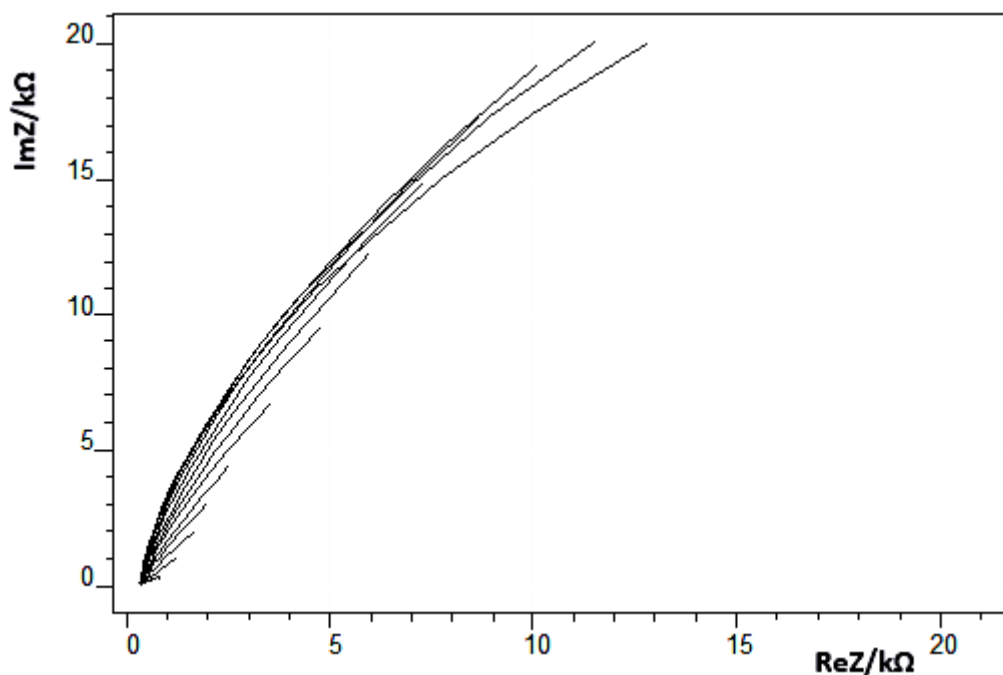


Figure 4.16. Overlay of impedance spectra at various dc potentials for 2 mM AQS at Bi in 0.1 M KCl solution as supporting electrolyte. The frequency range of 10^1 Hz - 10^5 Hz (41 frequencies per spectrum) and the dc potential range was -0.66 V to -0.90 V in steps of 20 mV.

Evidence for adsorption effects was obtained when recording voltammograms at rates of 200 mV s^{-1} as in figure 4.17. The data of figure 4.17 at scan rate of 2500 mV s^{-1} shows an unusual-shaped reduction peak more characteristic of a surface-bound reactant. For such an adsorbed species, the peak current is directly proportional to the scan rate, and it will therefore dominate at the higher scan rate over contributions from freely diffusing AQS which vary with the square root of scan rate.

Although AQS satisfies some of the criteria necessary to obtain good quality kinetic data, it is a much less favourable case than ruthenium hexaammine and suffers from some of the same complications as methyl viologen.

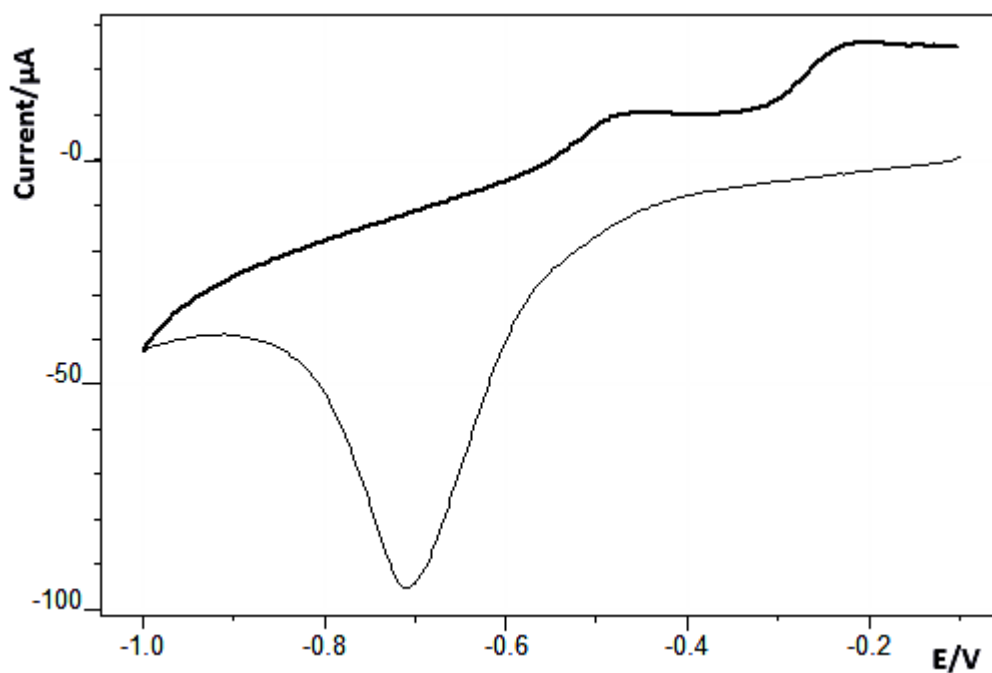


Figure 4.17. CV of 2 mM AQS at a bismuth electrode at scan rate of 2500 mV s⁻¹ in 0.1 M KCl. The reference electrode was Ag/AgCl (1 M KCl).

4.5 Methylene Blue Hydrate

Methylene blue (MB) hydrate is also known as methylthioninium chloride hydrate (C₁₆H₁₈ClN₃S.XH₂O). Solutions of the compound were prepared in 0.1 M aqueous sulphuric acid as supporting electrolyte. The shapes of CVs of methylene blue at bismuth were not as good as those at platinum electrodes. Examples are given in *figure 4.18* and *figure 4.19*.

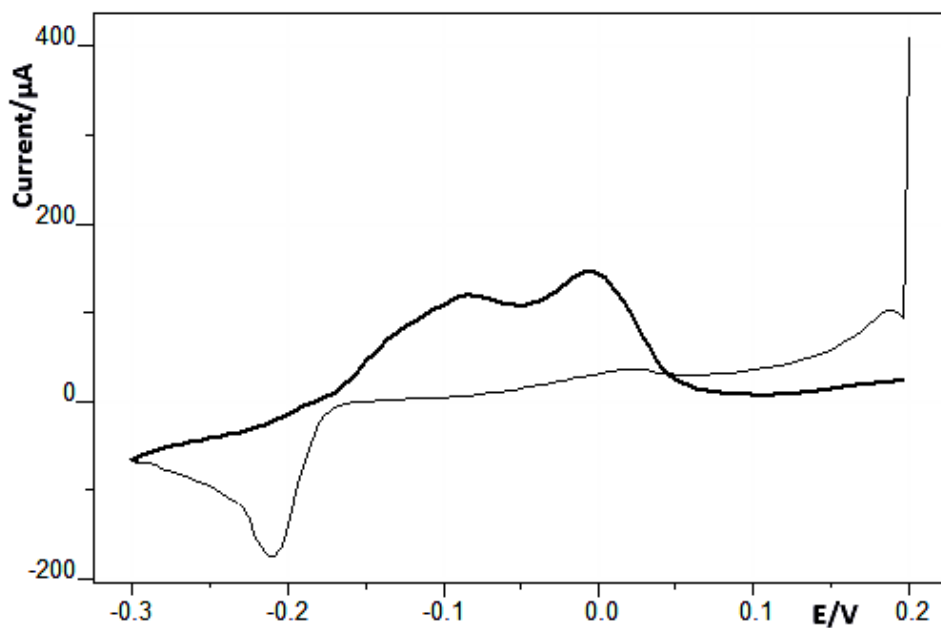


Figure 4.18. CV of 5 mM methylene blue at Bi at scan rate of 25 mV/s in 0.1 M aq. H_2SO_4

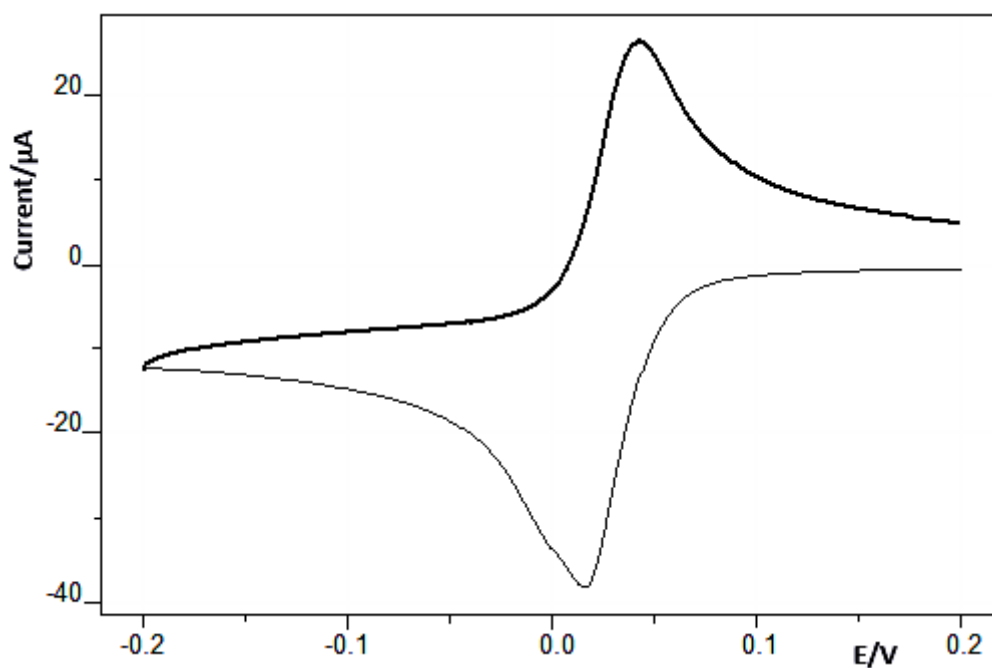


Figure 4.19. CV of 5 mM methylene blue at Pt at the scan rate of 25 mV/s in 0.1 M aq. H_2SO_4 against the potential of an Ag/AgCl reference electrode.

The voltammetry at platinum is consistent with a simple, reversible two-electron couple, however the peak potential is much more negative at bismuth and the reverse waves are complex. Plots of cathodic peak current against square root of scan rate were however made (Figure 4.20 and Figure 4.21) and showed the

expected linear trend, although the data is rather scattered about the regression line for the bismuth electrode (Figure 4.20).

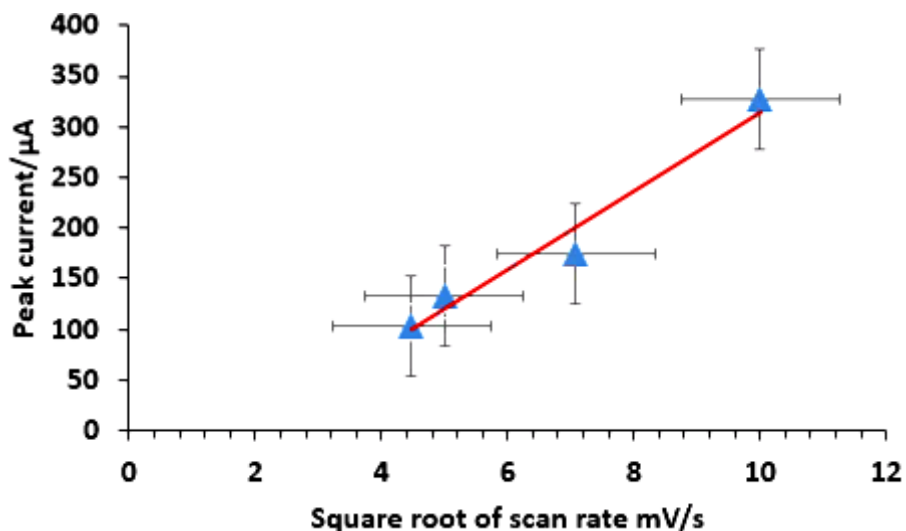


Figure 4.20 Variation of peak currents with scan rate for 5 mM methylene blue at Bi in 0.1 M aq. H_2SO_4

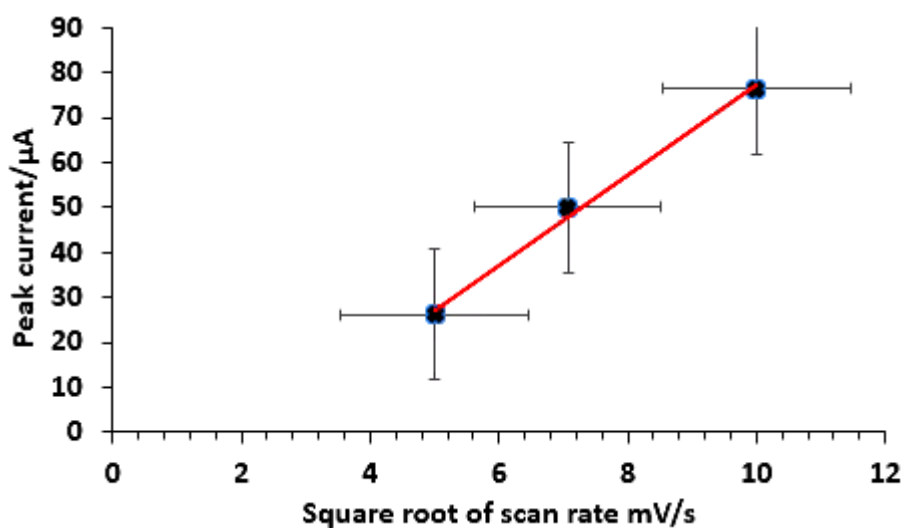


Figure 4.21. Variation of peak currents with scan rate for 5 mM methylene blue at Pt in 0.1 M aq. H_2SO_4

The linearity in the data of *figure 4.21* confirms that even at platinum metal electrode surface, electron transfer from the dye molecules is diffusion controlled; the plot of peak current against scan rate is a near perfect straight line.

AC voltammetry was also run for methylene blue at Pt and the curve had peak parameters of 0.002 V and 66.9 μA . This voltammogram is shown in Figure 4.22.

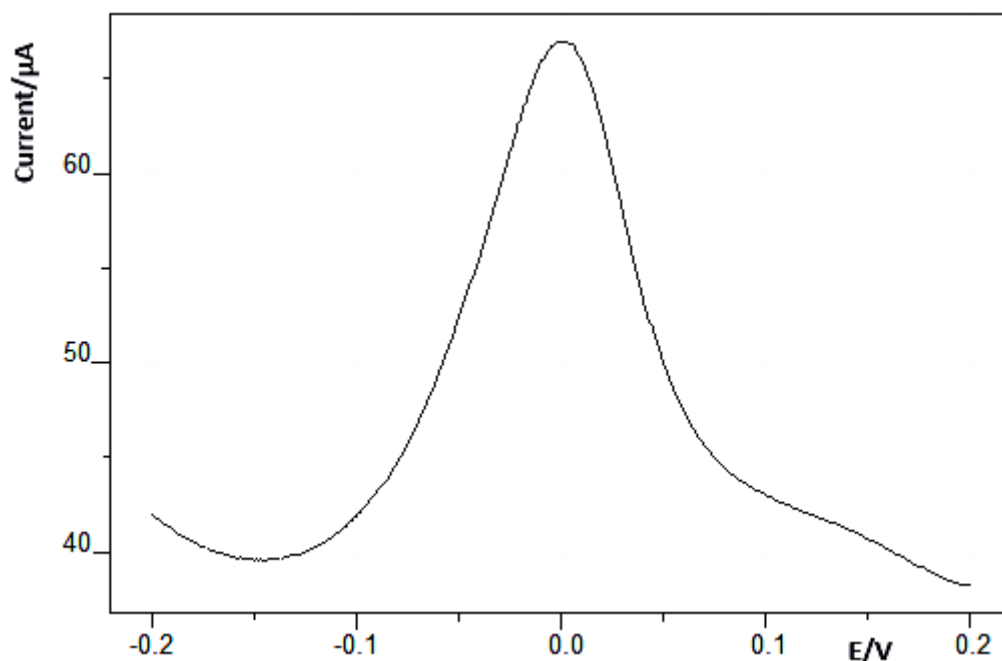


Figure 4.22. AC voltammogram of 5 mM methylene blue at Pt in 0.1 M aq. H_2SO_4 . The scan rate was 25 mV/s with amplitude of 10 mV at frequency of 1000 Hz.

However, a good ACV could not be obtained at Bi even with the parameters of AC voltammetry obtained with the Pt electrode. In summary, the voltammetry of MB at bismuth is entirely unsuited for a kinetic study. The reason for the difference in behavior at bismuth is not certain, but in view of the more positive formal potential of this couple compared to others in this chapter, the reason is likely to be due to anodic oxidation of the bismuth electrode.

4.6 Toluidine Blue

5 mM solutions of the sample were prepared separately in 0.1 M NaCl and 0.1 M KCl, both identified as good supporting electrolytes for the compound. Cyclic voltammetric measurements were carried out with these analyte solutions, with both bismuth and platinum electrodes. These however gave data (see *figure 4.23* and *figure 4.24*) that had no analytical significance and work on toluidine blue was halted.

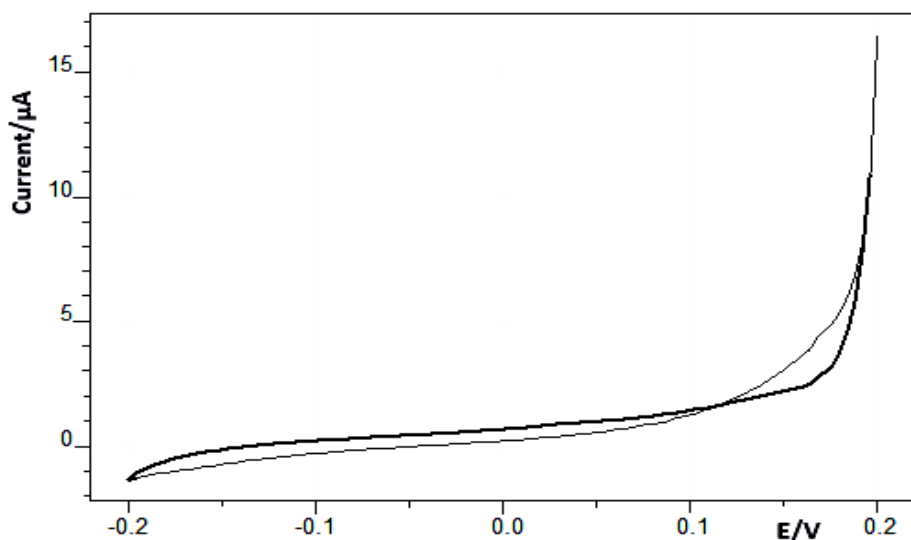


Figure 4.23. CV of 5 mM toluidine blue in 0.1 M KCl at scan rate of 25 mV/s at Bi against the potential of an Ag/AgCl (1 M KCl) reference electrode.

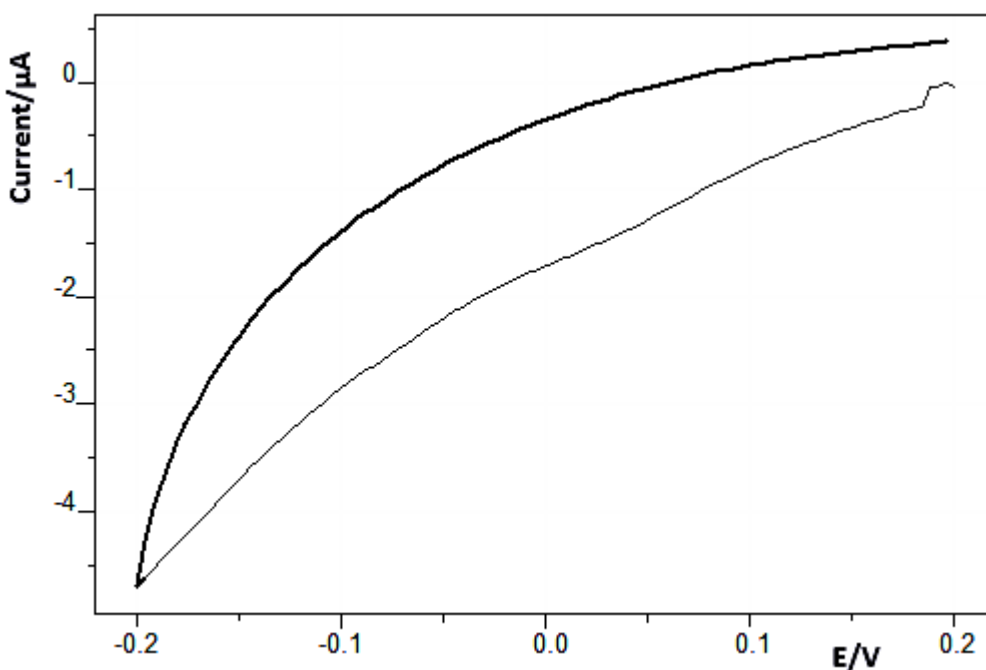


Figure 4.24. CV of 5 mM toluidine blue in 0.1 M KCl at scan rate of 25 mV/s at Pt against the potential of an Ag/AgCl (1 M KCl) reference electrode.

4.7 Hexaammine Cobalt(III) Chloride

CV experiments were carried out at both bismuth and platinum electrodes. The bismuth electrode had to be polished after each change of scan rate because there were visible signs of adsorption at the surface. The shape of the voltammetric waves were imperfect, an example is given in *figure 4.25*.

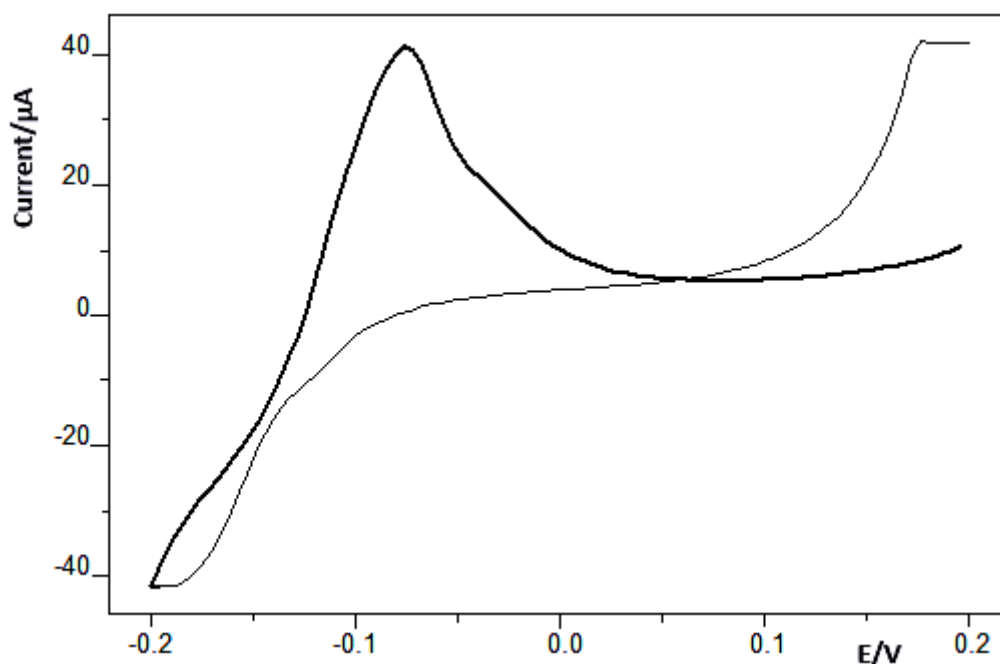


Figure 4.25. CV of 5 mM hexaammine cobalt(III) chloride at bismuth. The scan rate was 20 mV/s in 0.1 M HClO₄ as electrolyte against an Ag/AgCl (1 M KCl) reference electrode.

A plot of peak currents against scan rate shown in figure 4.25 further shows the complexity of the electron transfer process as there is no correlation between faradaic current and scan rate. Work on hexaammine cobalt(III) was therefore halted.

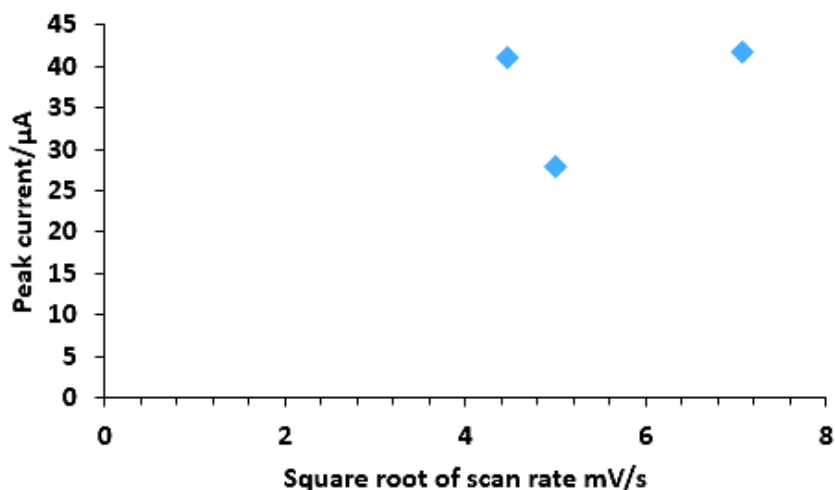
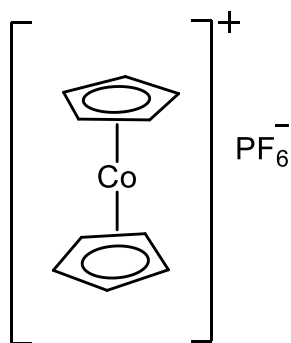


Figure 4.26. Variation of peak current with scan rate for 5 mM hexaammine cobalt(III) at Bi in 0.1 M aq. HClO₄.

4.8 Cobaltocenium Hexafluorophosphate

Known by the IUPAC name of bis(cyclopentadienyl)cobalt(III) hexafluorophosphate, this compound has the structure shown in scheme 4.2 and a condensed formula of C₁₀H₁₀CoF₆P with a molar mass of 334.08 g mol⁻¹. The cation is denoted CoCp₂⁺.



Scheme 4.2 Structure of cobaltocenium hexafluorophosphate.

Solutions of the compound were prepared with tetrabutylammonium hexafluorophosphate in acetonitrile (0.1 M TBAPF₆/AN) as supporting electrolyte. Experimental investigations revealed that the best cyclic voltammograms at both bismuth and platinum electrodes could be obtained at the scan rate of 10 mV s⁻¹ in the potential range of -0.6 V to -1.1 V as can be observed in *figure 4.27* and *figure 4.28* respectively. The non-aqueous reference electrode Ag/Ag⁺ (0.01 M AgNO₃ in AN) was used instead of Ag/AgCl because AgCl is soluble in AN.

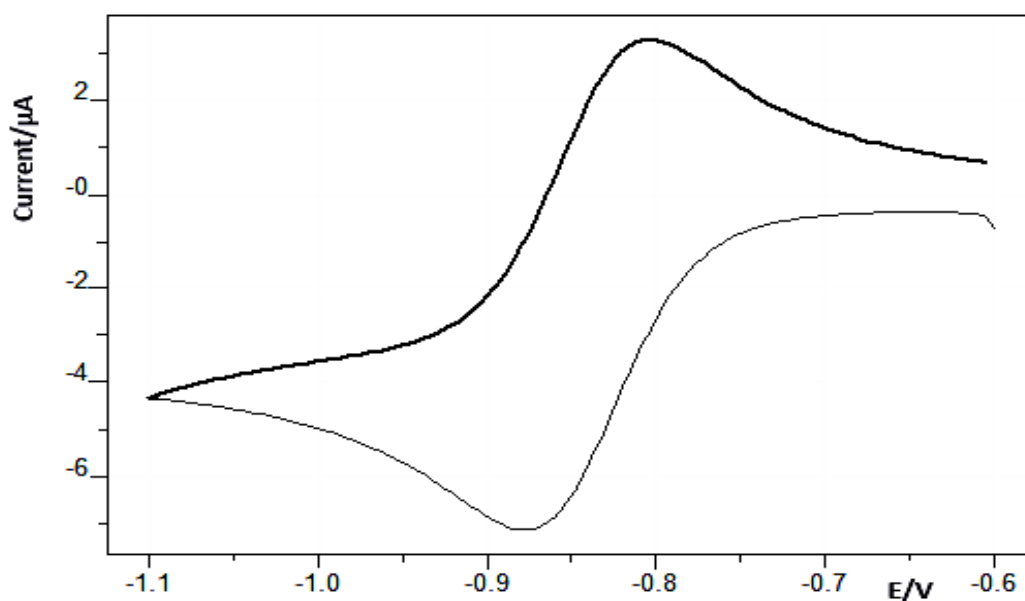


Figure 4.27. CV of 2 mM cobaltocenium at Bi at scan rate of 10 mV/s in 0.1 M TBAPF₆/AN. The non-aqueous Ag/Ag⁺ reference electrode was used here.

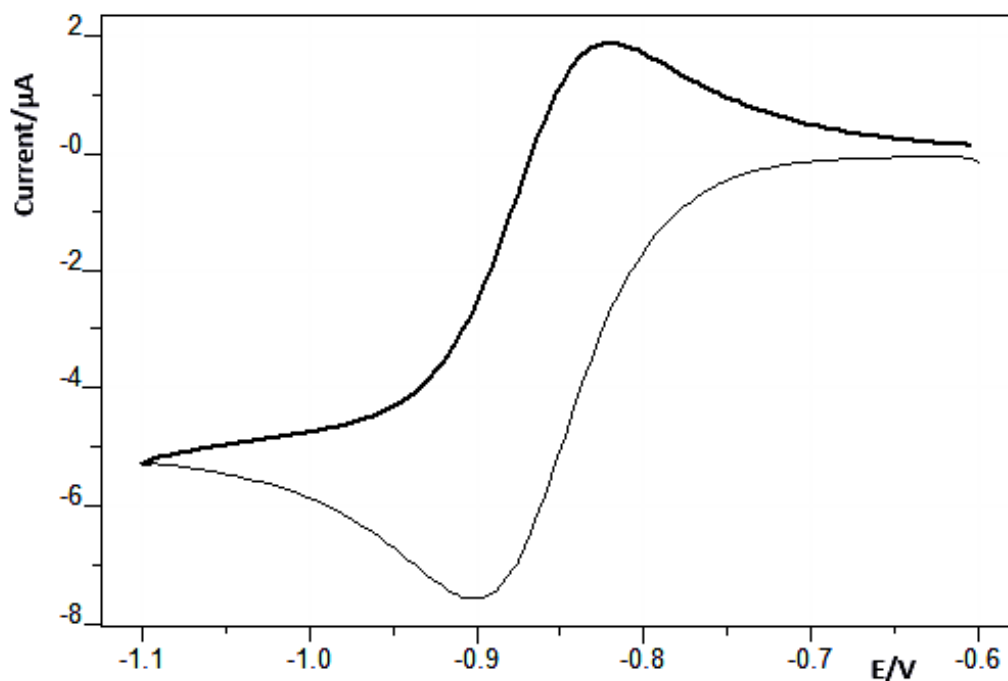


Figure 4.28. CV of 2 mM cobaltocenium at Pt at scan rate of 10 mV/s in 0.1 M TBAPF6/AN against the potential of an Ag/Ag⁺ reference electrode.

A lot of data was generated using different concentrations of the analyte, ranging from 2 mM to 10 mM. The CVs clearly confirm the CoCp₂(III/II) couple to be quasi-reversible in agreement with previous reports.^{168,169} As the CV results were promising, with no evidence of electrode fouling/absorption, we attempted to determine the electrode kinetics by impedance spectroscopy. Impedance measurements at constant dc potentials were carried out at potential values of 0, ±30, ±60, ±90 and ±120 mV away from the formal potential obtained of each analyte concentration.

Some consistent impedance spectra datasets as a function of potential were obtained at the various concentrations. These spectra are shown in *figure 4.29*.

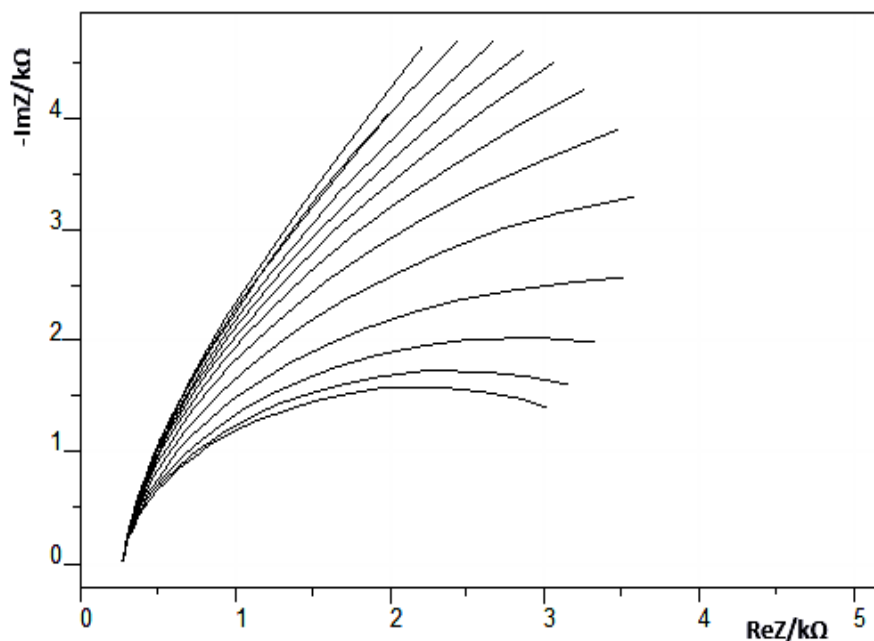


Figure 4.29. Impedance spectra at different dc potentials for 5 mM cobaltocenium hexafluorophosphate at Bi. The potential range was -0.72 to -0.92 V in steps of 20 mV. The analyte solution which was prepared in 0.1 M TBAPF6/AN was purged with argon gas for 15 minutes prior to scanning.

Impedance spectra fitting by complex non-linear least squares was carried out using EISanalyzer.¹⁷⁰ In general, a good fit of the simulated Randles impedance to the experimental data was seen. Examples are given in the spectra of *figure 4.30* and *figure 4.31*.

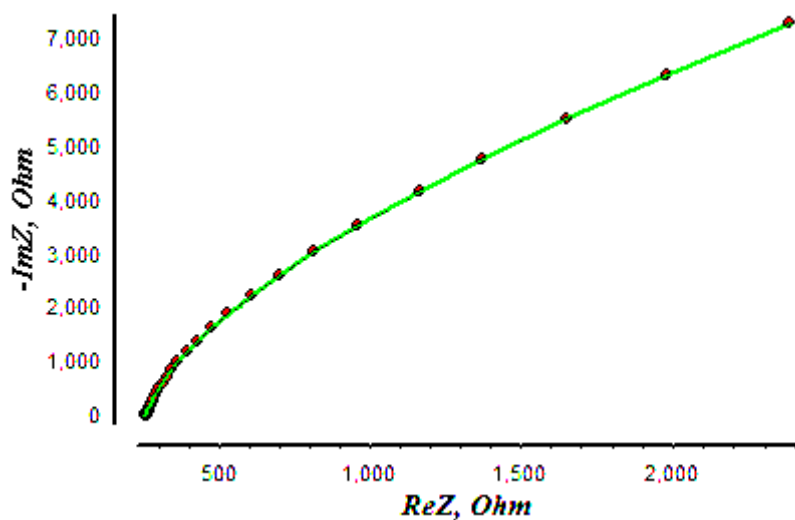


Figure 4.30. EIS fitted spectrum of 2 mM cobaltocenium hexafluorophosphate at Bi at -0.89 V. The green line is the simulated data while the red points are the experimental data.

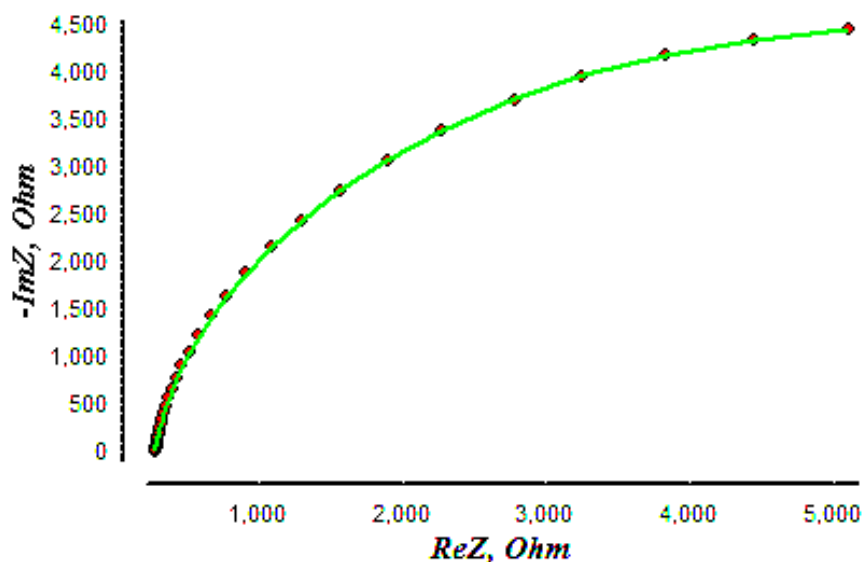


Figure 4.31. EIS fitted spectrum of 8 mM cobaltocenium hexafluorophosphate at Bi at -0.87 V. The red points are the experimental data fitted into the simulated green line.

Ultimately, a total of nine estimates for values of standard rate constants (k^0) were obtained for each of the analyte concentrations, the mean of which is presented in *table 4.1*. Ideally, k^0 values should not vary with concentration but the data presented in the table clearly indicates that electron transfer does not reflect a simple electrode process. Although the CV data shows no evidence of complications, the impedance data is not as consistent, especially when compared to ruthenium hexaammine (Chapter 5).

Concentration/mM	Standard rate constant k^0/cms^{-1}
10	$2.59 \times 10^{-4} \pm 5.81 \times 10^{-6}$
8	$3.96 \times 10^{-3} \pm 1.98 \times 10^{-3}$
5	$6.79 \times 10^{-4} \pm 1.83 \times 10^{-5}$
2	$1.39 \times 10^{-3} \pm 1.64 \times 10^{-4}$

Table 4.1 Mean values of standard rate constants for $\text{CoCp}_2^{+3/+2}$ at bismuth.

In spite of the good quality of individual spectra, the charge transfer resistance profile of the compound was too complex to analyse as seen in *figure 4.32* and this led to stoppage of further work on cobaltocenium hexafluorophosphate.

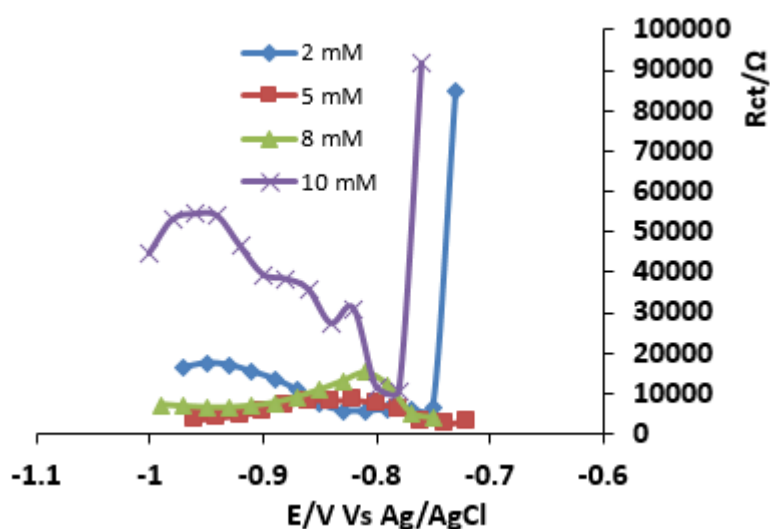


Figure 4.32. Variation of charge transfer resistance with potential for 2 mM to 10 mM cobaltocenium hexafluorophosphate at bismuth.

It is however worthwhile to conclude that bismuth electrodes have been successfully tested to confirm the quasi-reversible behavior of cobaltocenium hexafluorophosphate.

4.9 Conclusion

In summary, a range of redox couples were tested at bismuth electrodes in the search for a suitable candidate for a detailed electrode kinetic investigation. The four most promising (on the basis of simple cyclic voltammetry) were ruthenium hexaammine, methyl viologen, anthraquinone-2-sulfonate and cobaltocenium. However, a more stringent test is whether the couple remains stable, i.e. show no electrode fouling during the time taken to collect a series of impedance spectra. From this point of view, ruthenium hexaammine was clearly the most promising and was studied in detail in the work presented in Chapter 5. Methyl viologen has been studied previously¹⁹ at bismuth, but only in acetonitrile and the compound is much less well-behaved in aqueous media. AQS and cobaltocenium are sufficiently stable to allow collection of impedance spectra, but the data quality is not sufficient to reveal anything about the potential dependence of the rate analogous to the analysis possible for ruthenium hexaammine.

Chapter 5. Kinetic Studies of Ruthenium(III) Hexaammine at Bulk Bismuth Electrodes.

5.1 Introduction

Bismuth bulk¹¹⁻¹³ and film¹⁴⁻¹⁶ electrodes have been investigated as alternatives to Hg and noble metal electrodes for electroanalytical applications. Stripping voltammetry at bismuth electrodes has been reviewed.⁷ Their favourable characteristics compared to other solid metal electrodes include a low melting point, which facilitates electrode fabrication, and a lower cost than noble metals. Bismuth also has much lower toxicity than mercury hence is environmental friendly.² Bismuth electrodes are also of interest for fundamental studies of heterogeneous electron transfer because of the unusual electronic properties of bismuth. In particular, the electronic properties of bulk bismuth are those of a semi-metal with a carrier density in the order of $3 \times 10^{17} \text{ cm}^{-3}$ ^{18,20}, much lower when compared to Pt, Au or Hg. Electron transfer at materials with low densities of states is of current interest because of attempts to test the adiabaticity of outer-sphere electrode reactions. In the nonadiabatic case, the reaction rate should depend on the density of states at the Fermi energy and in the adiabatic case the rate should be independent of the density of states.¹⁷¹

In this chapter, we study the reduction of ruthenium(III) hexaammine at bismuth bulk electrodes in aqueous KCl electrolytes as a typical example of an outer sphere reaction uncomplicated by adsorption or coupled chemical processes. Despite the fact that the formal potential lies in a region where the Bi is partially oxidised, we show that electrochemical impedance spectroscopy provides precise electron transfer resistance data as a function of the dc potential. Fitting a nonlinear regression model to the potential dependence of the charge transfer resistance allowed estimation of the transfer coefficient at each dc electrode potential without making any assumption about the inherent potential dependence of the transfer coefficient. Finally, we show that the measured potential dependence of the transfer coefficient arises mainly from double layer effects as postulated in the classical Frumkin correction.

5.2 Cyclic Voltammetry

Cyclic voltammograms of $\text{Ru}(\text{NH}_3)_6^{3+}$ at Pt electrodes in aqueous KCl under Ar showed uncomplicated one-electron behaviour with a formal potential of -0.217 V vs Ag/AgCl (1 M $\text{KCl}(\text{aq})$) (*figure 5.1 a*). At Bi electrodes, the voltammogram is very similar and can be superimposed on the Pt voltammogram, though a small additional current at more positive potentials can be seen in *figure 5.1a*. We attribute the extra anodic current to oxidation of the Bi surface. The peak current at Bi electrodes varied approximately linearly with scan rate (*figure 5.1b*) and the anodic and cathodic peak currents were equal. The peak separation is slightly greater than expected for a reversible one-electron process (about 80 mV at 50 mV s^{-1} ; *figure 5.2*). The behaviour is that of a reversible system with some influence of uncompensated solution resistance. Slow scan cyclic voltammetry is not a suitable method for investigating the electrode kinetics, but it is an important check on the nature of the redox process; it demonstrates that adsorption and coupled chemical processes do not affect the measured currents.

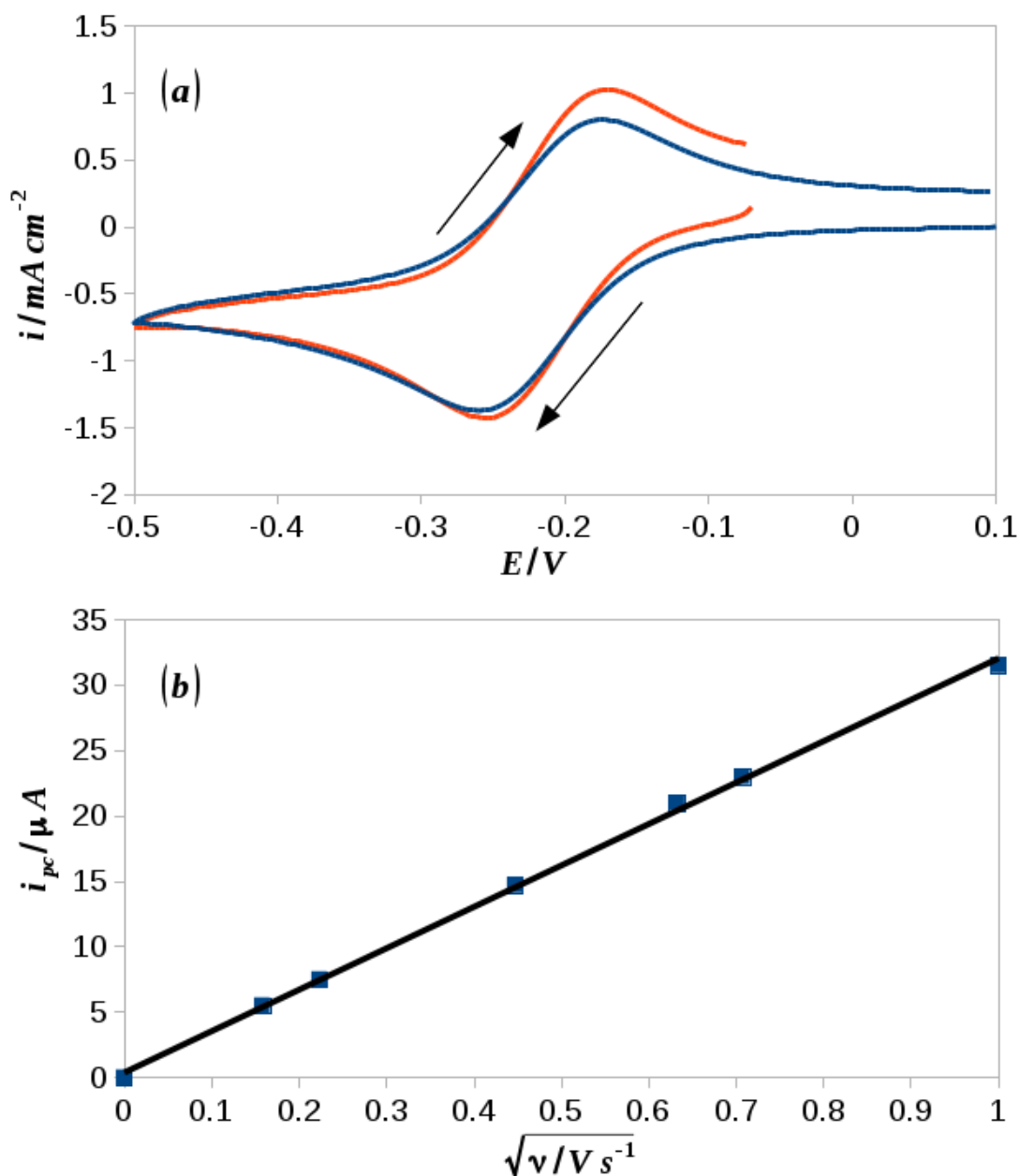


Figure 5.1. Cyclic voltammograms at Pt (blue) and Bi (orange) electrodes of $\text{Ru}(\text{NH}_3)_6\text{Cl}_3$ in 0.1 M $\text{KCl}(\text{aq})$. (a) The scan rate was 50 mV s^{-1} , $[\text{Ru}(\text{NH}_3)_6\text{Cl}_3] = 10 \text{ mM}$ and the reference electrode was Ag/AgCl in 1M $\text{KCl}(\text{aq})$. (b) Cathodic peak current (absolute value) against square root of scan rate for 2 mM $\text{Ru}(\text{NH}_3)_6\text{Cl}_3$ in 0.1 M $\text{KCl}(\text{aq})$ at a Bi electrode. The precision of the current values was better than 1% and y-error bars are not plotted, because they are not visible on the graph.

Figure 5.2 shows the variation of cathodic peak potential and the peak separation with scan rate. Above about 200 mV s^{-1} the cathodic peak potential starts to change to more negative values. This suggests that electrode kinetic limitations become important at these scan rates, however at the mm-size electrodes employed, uncompensated resistance effects will also contribute.

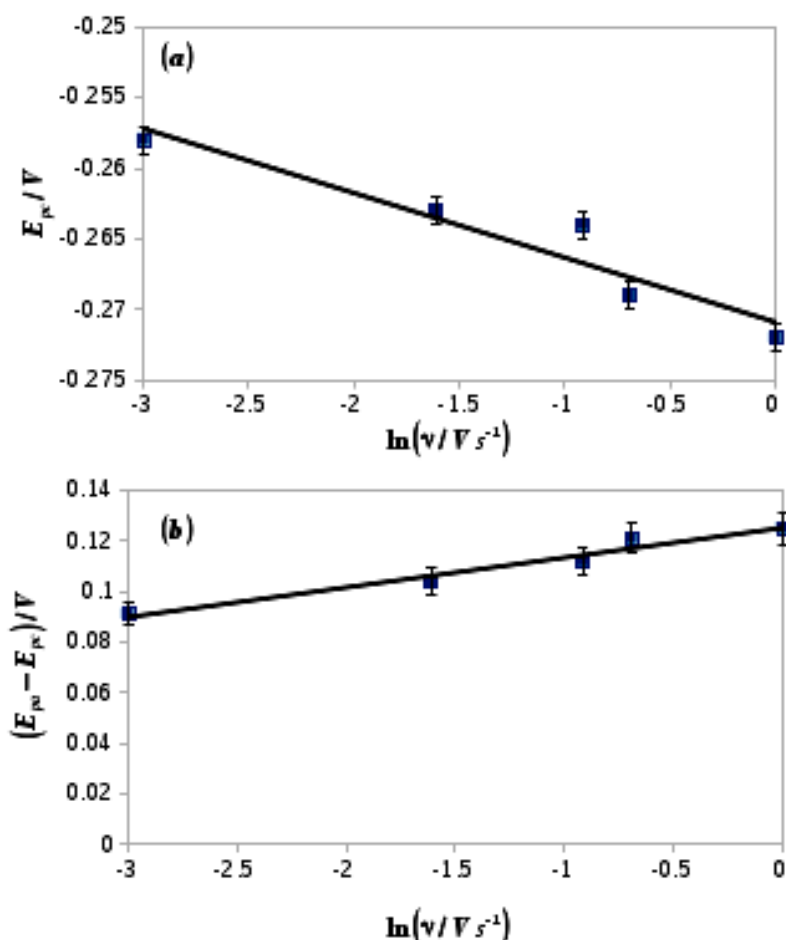


Figure 5.2. Slow scan cyclic voltammetric peak potential data for 2 mM $Ru(NH_3)_6Cl_3$ in 0.1 M $KCl(aq)$ at a Bi electrode. (a) Cathodic peak potential against $\ln(\text{scan rate})$ and (b) Peak separation against $\ln(\text{scan rate})$.

5.3 Electrochemical Impedance Spectroscopy (EIS)

Impedance spectroscopy was chosen as a tool with which to evaluate the kinetics of ruthenium(III) hexaammine because the electrochemistry of the redox couple was observed to be stable; without adsorption nor fouling effects over the times required to collect a complete spectrum at each dc potential chosen. When this is possible, impedance spectroscopy can produce higher precision data than large amplitude techniques such as fast scan voltammetry. It also enabled a simultaneous determination of the differential capacitance of the Bi | $KCl(aq)$ interface. EIS has the additional advantage that the estimation of uncompensated resistance and double layer charging contributions is straightforward and the integration of the signal over many cycles of the ac perturbation improves the signal-to-noise ratio.

The $Ru(NH_3)_6^{3+/2+}$ redox couple showed fast electrode kinetics at Pt and we observed reversible behaviour – a Warburg impedance – at frequencies up to the maximum of

10^5 Hz. However, the impedance spectra at Bi showed clear evidence of charge-transfer limitations. A typical impedance spectrum for 2 mM $\text{Ru}(\text{NH}_3)_6\text{Cl}_3$ in 0.1 M $\text{KCl}(\text{aq})$ at a Bi electrode is presented in *figure 5.3*.

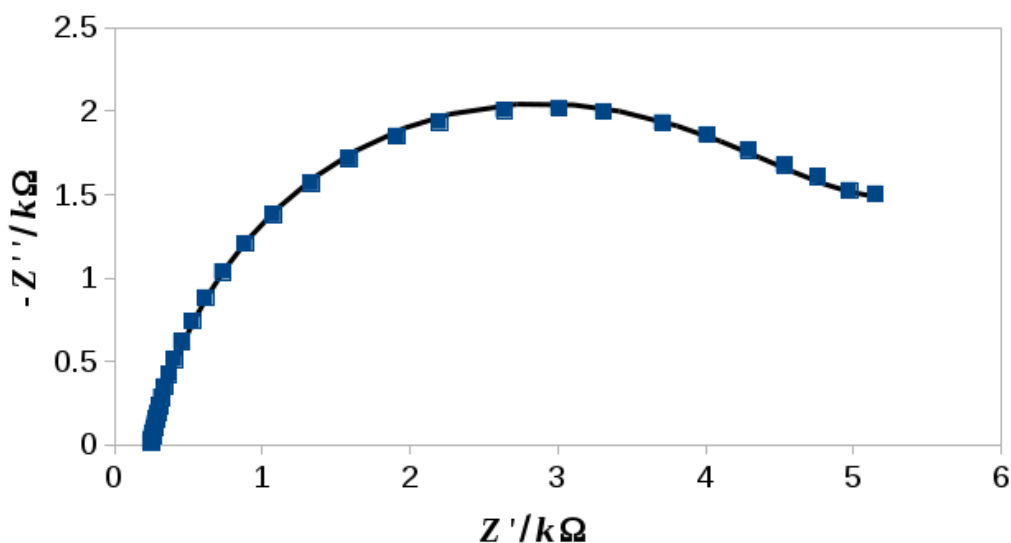


Figure 5.3. Nyquist plot of the impedance spectrum at a Bi electrode (symbols) and complex least squares fit (solid line) of the modified Randles circuit. The electrolyte contained 2 mM $\text{Ru}(\text{NH}_3)_6\text{Cl}_3$ in 0.1 M $\text{KCl}(\text{aq})$. Applied dc potential = -0.21 V vs Ag/AgCl (1M KCl). Frequency range 101 – 105 Hz. Statistical uncertainties on the values of RCT obtained from the fit were about 0.2%.

Although bulk Bi has a much lower density of states than Pt, comparable rates for electron transfer to a series of viologen derivatives from Pt and Bi electrodes in acetonitrile after application of the Frumkin correction have been reported.¹⁹

Differential capacitance measurements indicated that the density of states at the Bi surface is greater than in bulk Bi and closer to that of Pt. It is also possible that the electron transfer process is in the adiabatic regime where the density of states effect is absent.¹⁷¹ The large difference observed between Pt and Bi in the present case therefore suggests an additional barrier to electron transfer at Bi is present for aqueous electrolytes; we ascribe the origin of this barrier to the formation of a thin anodic film at Bi and provide some evidence for it using ex-situ X-ray photoelectron spectroscopy and differential capacitance measurements (*figure 5.8* and *figure 5.10*).

In all cases reported, the impedance spectrum at Bi was well-fitted by the model represented by a Randles equivalent circuit, but allowing for constant - phase element (CPE) behaviour of the interface instead of a pure capacitance. The Randles circuit on which the data is based is illustrated in *figure 5.4*.

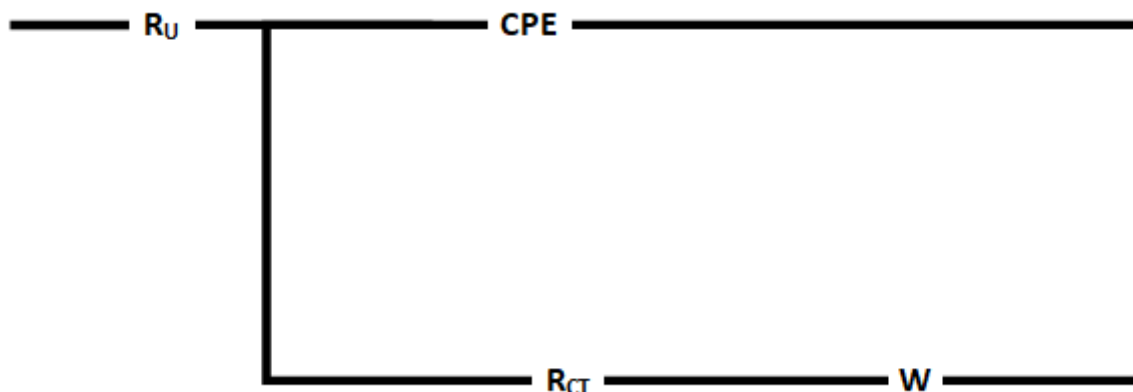


Figure 5.4. Diagram of a Randles circuit for mixed kinetics-diffusion behaviour showing: uncompensated or solution resistance (R_u), constant phase element (CPE) in place of a perfect capacitor for values of differential capacitance, charge transfer resistance (R_{CT}) and the Warburg impedance (W) which depends on the concentration and the diffusion coefficient.

The constant phase element has impedance given by equation (5.1):

$$Z_{CPE} = \frac{1}{(i\omega)^n Q} \quad (5.1)$$

When $n = 1$, the impedance of the CPE reduces to that of a simple capacitor and the equivalent circuit reduces to the original Randles model. For an electrolyte comprising between 2 - 10 mM RuHex and 0.1 M KCl we found $0.87 < n < 0.90$ and n was independent of potential over the range $-0.37 \text{ V} < E < -0.11 \text{ V}$ which spans the formal potential of -0.217 V . The Bi | KCl(aq) interface therefore approximates a capacitor quite closely.

The dependence of charge transfer resistance R_{CT} at the formal potential on the concentration of $\text{Ru}(\text{NH}_3)_6\text{Cl}_3$ is shown in Figure 5.5. The expected linearity is roughly observed; this rules out possible complications in the data arising from a rate determining step in which electrons are transferred to a surface state in an anodic film rather than directly to the $\text{Ru}(\text{NH}_3)_6^{3+}$ ions. Some scatter about the line is observed, which could be due to small changes in the condition of the electrode as it was emersed from one solution, washed and immersed in the next solution. This scatter was not observed when the charge transfer resistance was recorded as a function of potential in the same solution. The potential dependence of R_{CT} in 2 mM $\text{Ru}(\text{NH}_3)_6^{3+}$ is therefore analysed in more detail.

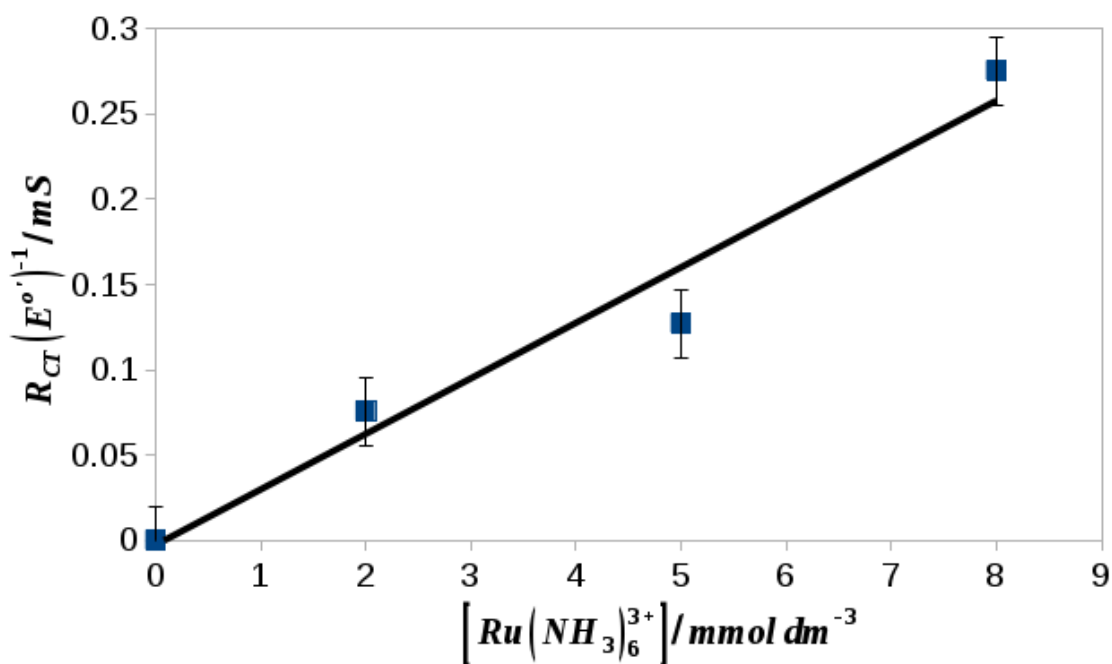


Figure 5.5. R_{CT}^{-1} against $[Ru(NH_3)_6Cl_3]$ in 0.1 M KCl(aq). The values of charge transfer resistance plotted are those at a dc potential equal to the formal potential.

Figure 5.6 shows typical plots of charge transfer resistance R_{CT} against the dc potential E and three different regression models. Values of R_{CT} were extracted from the fit of the modified Randles equivalent circuit to the data. The plots show the characteristic U-shape produced by two factors: the increase in heterogeneous rate constant with increasing overpotential and the decrease in surface concentration of the reactant with overpotential. However, it can clearly be seen that the data is not precisely symmetric about the minimum of the U as it would be for a constant value of transfer coefficient $\alpha = 0.5$. In fact, the data cannot be fitted satisfactorily by any constant value of the charge transfer coefficient (figure 5.6a, regression model appropriate to standard Butler-Volmer theory) nor by a linear variation of transfer coefficient with potential (figure 5.6b, regression model appropriate to Marcus-Hush theory). In both cases (figure 5.6a and figure 5.6b) there are small, but systematic deviations of the fits from the data and the residuals, $SSR = \sqrt{\sum(R^{expt} - R^{theory})^2}$ are of the order of k Ω . The fit shown in figure 5.6c is much superior ($\times 10^6$); the SSR is of order m Ω . The regression model of figure 5.6c makes no a priori assumption regarding the potential dependence of the transfer coefficient, except that it is regular in a sense described below. Instead, the potential dependence was obtained directly from the regression and then interpreted in terms of the properties of the Bi | KCl(aq) interface.

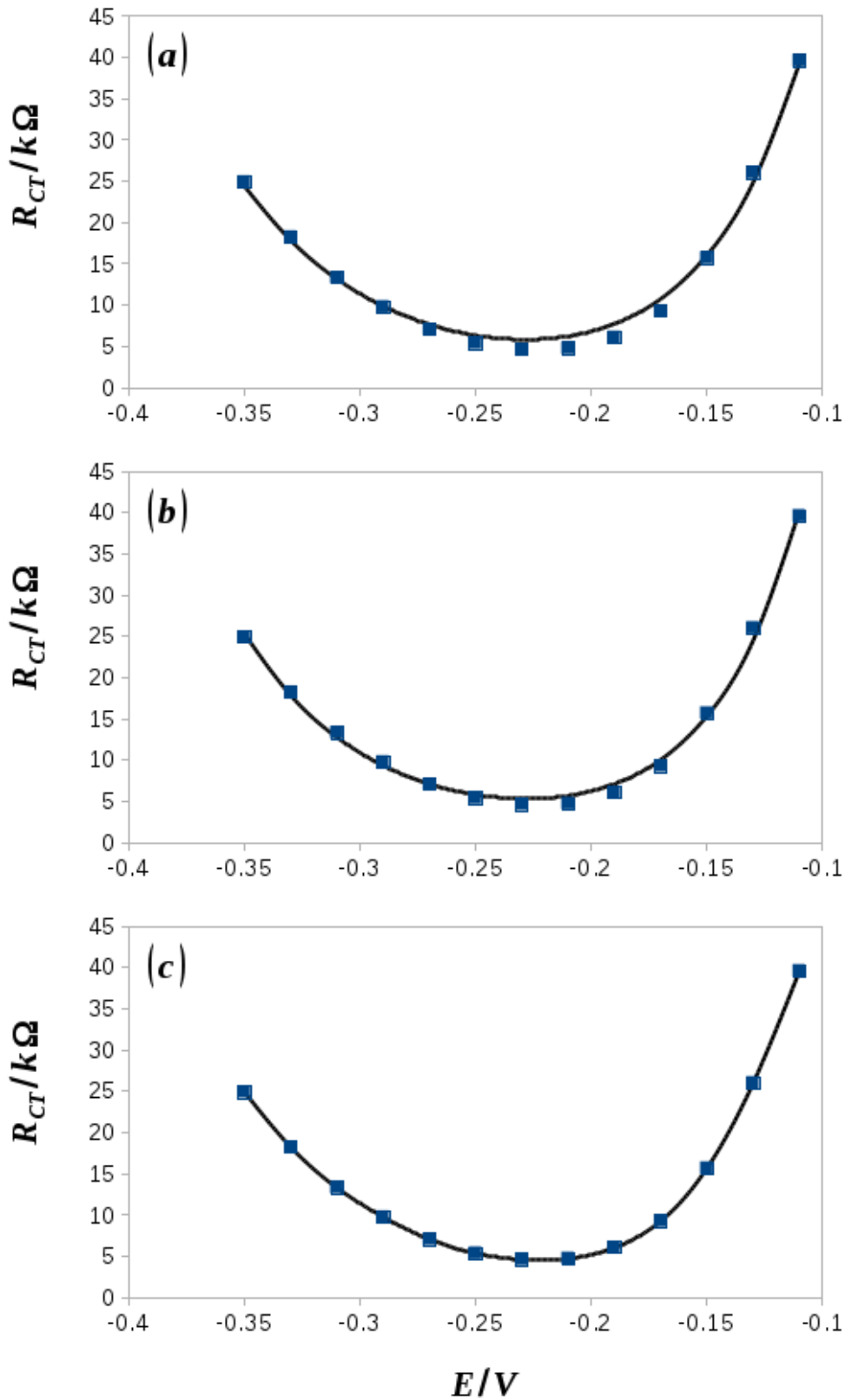


Figure 5.6. Charge transfer resistance against dc potential at a Bi electrode with 2 mM $Ru(NH_3)_6Cl_3$ in 0.1 M $KCl(aq)$. The difference between data and fit measured as $SSR = \sqrt{\sum (R^{expt} - R^{theory})^2}$ was (a) $SSR = 3.4 k\Omega$; (b) $SSR = 2.6 k\Omega$ and (c) $SSR = 2.7 m\Omega$. The R_{CT} versus E data was obtained using the instrument software to record a sequence of impedance spectra at different values of E automatically and we found a statistical uncertainty of about 0.2% on each value of R_{CT} .

5.4 Data Analysis

5.4.1 Charge transfer resistance and transfer coefficient

Below we developed the equations for charge transfer resistance for an arbitrary potential-dependence of the transfer coefficient and show that the observed potential-dependence can be interpreted in terms of a combination of two effects: the double-layer effect on the charge transfer coefficient predicted by the Frumkin correction and the presence of a thin anodic film which is reduced at sufficiently negative potentials.

For a one-electron outer sphere redox couple:



In our experiments, the bulk O concentration is C^* and the bulk R concentration is zero. In order to make the notation used for the transfer coefficients clear, the well-known Butler-Volmer equation is quoted in the form:

$$\frac{i}{FA} = k^o [C_O e^{-\alpha f(E-E^{o'})} - C_R e^{(1-\alpha)f(E-E^{o'})}] \quad (5.3)$$

where $f = F/RT$ and C_O and C_R are the concentrations of the oxidised (O) and reduced (R) forms of the couple at the outer Helmholtz plane – assumed in the standard treatment of double-layer effects to also be the plane at which electron transfer occurs. The values of C_O and C_R are fixed by the dc potential and change according to the Nernst equation (ignoring activity coefficients):

$$E = E^{o'} + \frac{RT}{nF} \ln \frac{C_O}{C_R} \quad (5.4)$$

The Butler-Volmer equation can be rewritten in terms of the deviation from equilibrium (overpotential, η):

$$\frac{i}{i_0} = e^{-\alpha f\eta} - e^{(1-\alpha)f\eta} \quad (5.5)$$

Finally, the charge-transfer resistance is obtained from the slope of the Butler Volmer equation (5.5) at the origin as $\left|\frac{\partial E}{\partial i}\right|_{\eta=0} = R_{CT} = \frac{1}{fi_0}$ and C_O and C_R are related by the Nernst equation to the bulk O concentration, C^* .

$$R_{CT} = \frac{RT}{F^2 A k^0 C^*} \frac{1 + e^{f(E-E^{o'})}}{e^{(1-\alpha)f(E-E^{o'})}} \quad (5.6)$$

This derivation is quite standard⁴⁴, but it is repeated here to illustrate that it does not make any assumption about the potential-dependence of the transfer coefficient, α because the derivative is evaluated at $\eta=0$. A potential-dependent transfer coefficient can be simply accommodated by writing $\alpha(E)$ in the final expression for R_{CT} given in equation (5.6).

The formal potential $E^{o'}$ was estimated from slow scan cyclic voltammetry at Pt and Bi electrodes as -0.217 V. Equation (5.6) was then fitted to the charge transfer resistance data as a function of dc potential using a least squares method in which k^0 and the values of α at each dc potential were floated. This procedure includes too many floated parameters to be carried out directly. To avoid the appearance of badly-behaved terms of the form expressed in equation 5.7, a regularization was employed with ε as a small constant.

$$\alpha(E) \propto \frac{E - E^{o'}}{(E - E^{o'})^2 + \varepsilon^2} \quad (5.7)$$

These terms are associated with arbitrary constant factors multiplying the effective value of k^0 . The regularization chosen was to minimize simultaneously the sum of squares of the second order finite differences $\Delta^2 \alpha(E)$. i.e., to bias $\alpha(E)$ to functions that are piecewise linear.

$$\min \left(\sum (R_{CT,i}^{expt} - R_{CT,i}^{theory}[k^0; \alpha_i])^2 + \lambda \sum (\Delta^2 \alpha_i)^2 \right) \quad (5.8)$$

A suitable starting guess of $\alpha(E) = 0.5$ was made and it was useful to enforce piecewise linearity on the optimized solution with a large initial value of $\lambda = 10^6$ and then re-optimize with a reduced value of $\lambda = 10$. The optimization procedure was conveniently carried out using the generalised reduced gradient method for nonlinear programming available as part of the 'Solver' add-in of MSExcel™ 2013.

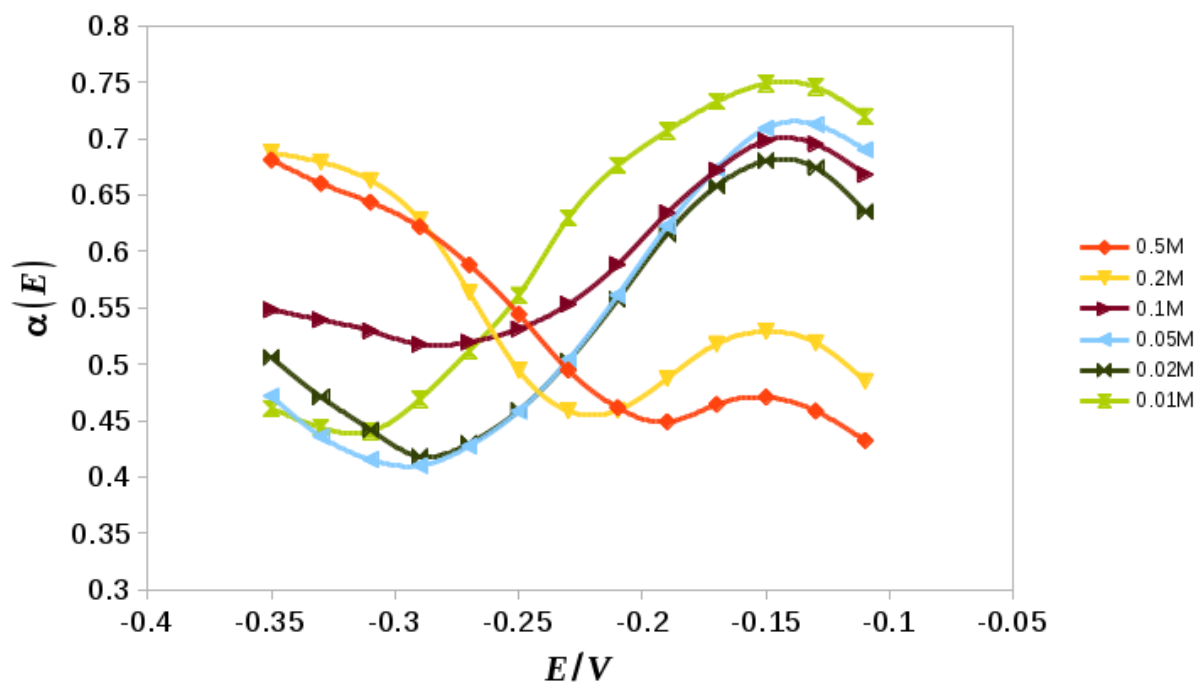


Figure 5.7. Variation of apparent transfer coefficient $\alpha(E)$ at Bi with with dc potential E . The data was obtained by the regularized least squares procedure defined by equations (5.6) and (5.8). The electrolyte contained 2 mM $\text{Ru}(\text{NH}_3)_6\text{Cl}_3$ in various concentrations of $\text{KCl}(\text{aq})$. The statistical uncertainties on each value of transfer coefficient are of order 1% or less.

Figure 5.7 shows the apparent transfer coefficients $\alpha(E)$ for the reduction of 2 mM $\text{Ru}(\text{NH}_3)_6\text{Cl}_3$ in various concentrations of $\text{KCl}(\text{aq})$. The uncertainties on each value of α was estimated by repeating the minimization of equation (5.8) with values of R_{CT} varying by random amounts consistent with the 0.2% uncertainties estimated from the fit of the Randles circuit to the experimental data. In general the uncertainties on α computed in this way were very low, <1% in all cases. This represents the precision of our estimates of α from the minimization and indicates that trends in α with potential E are sufficiently reliable to be analysed. The increase in apparent transfer coefficient at the most negative potentials in figure 5.7 is more prominent at high ionic strength. We suggest that its origin is related to the anodic film on the Bi electrode surface. Comparisons of different ionic strengths involve experiments in which the electrode was emersed from the solution between measurements and only qualitative differences are considered below because the variability in measurements of R_{CT} is greater in those cases.

The potential dependence $\alpha(E)$ is quite complex; in low ionic strength electrolytes, the transfer coefficient decreases as the potential becomes more negative, however at $[\text{KCl}]$ higher than about 0.1 M it increases as the potential becomes more negative.

This increase is also evident at low ionic strength at the most negative potentials. We suggest that the behaviour can be understood in terms of two competing factors: the Frumkin effect⁴⁴, which dominates at the lowest ionic strengths and the properties of the Bi/Bi₂O₃ film which are responsible for the increase in transfer coefficient at the most negative potentials.

A potential-dependent transfer coefficient can arise in several ways. Simple applications of Marcus theory predict a linear dependence of α on E . However, double-layer effects (known variously as the Frumkin correction, ϕ_2 -effect or Ψ -effect) are clearly also potential-dependent and therefore appear as a variation in α with potential when the voltammetric data is analysed in the standard Butler-Volmer framework.¹⁹

If ϕ_2 is the potential dropped between the outer Helmholtz plane and the bulk solution, then the corrected, k_{FC} , and conventional, k^o , standard rate constants are related by:

$$k^o = k_{FC} e^{(\alpha' - z_+) f \phi_2} \quad (5.9)$$

where z_+ is the charge on the reactant. This can be absorbed into equation (5.5) by defining.^{51,172}

$$\alpha(E) = -\frac{1}{f} \frac{\partial \ln k}{\partial \eta} = \alpha' - (\alpha' - z_+) \frac{\partial \phi_2}{\partial \eta} \quad (5.10)$$

where α' is a constant denoting the “true” transfer coefficient and η is the overpotential. When the Gouy-Chapman-Stern model of the double layer applies, the variation of ϕ_2 with overpotential may be written:

$$\frac{\partial \phi_2}{\partial \eta} = \frac{c_H}{c_H + c_{DL}} \quad (5.11)$$

where c_H and c_{DL} are the differential capacitances of the compact and the diffuse layers. The Frumkin correction⁴⁴ assumes that the electron transfer occurs at a plane, often taken to be the outer Helmholtz plane, but several authors have considered how this is modified when account is taken of the possibility of tunnelling from distances further away from the electrode surface.¹⁷³⁻¹⁷⁷ We have considered this possibility, but our data appears to be in the regime where the reactant

accumulates weakly at the interface and the classical Frumkin correction applies.¹⁷⁴ Evidence for this has been provided from the ionic strength effect on the charge transfer resistance in *figure 5.9*.

The model could be easily modified to describe Bi electrodes covered with a thin, insulating oxide layer by including the differential capacitance of the oxide in series with the compact layer as part of c_H . The diffuse layer effect on the apparent transfer coefficient is always positive in this model for reduction of a cation such as $\text{Ru}(\text{NH}_3)_6^{3+}$. The magnitude of the effect may increase or decrease with potential depending on whether the potential of zero charge is more positive or negative than the formal potential of the couple.

5.4.2 Differential capacitance

A typical measurement of the potential-dependence of the differential capacitance of the Bi | KCl(aq) interface is shown in *figure 5.8* (more details are given in Chapter 3).

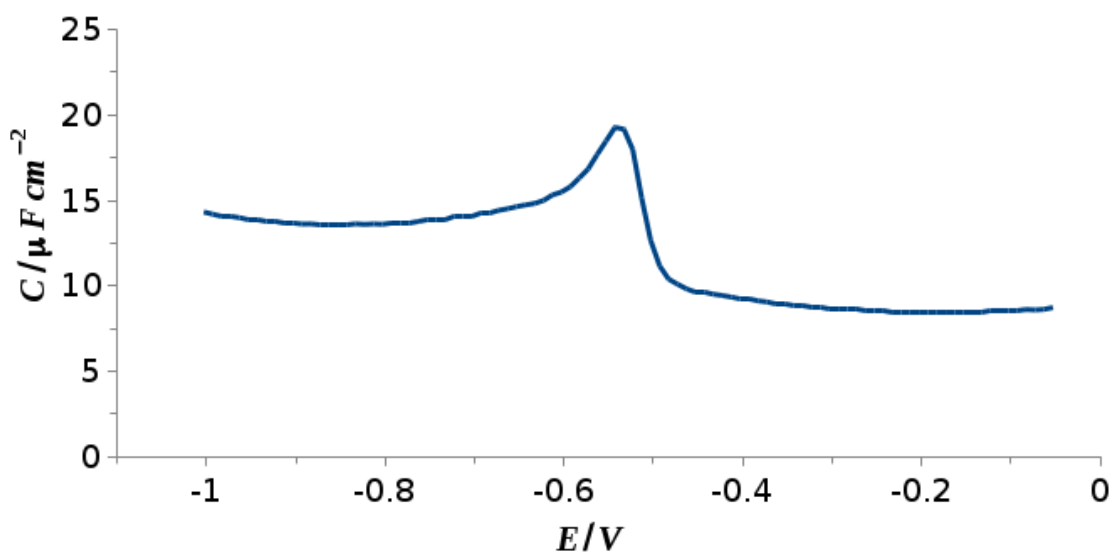


Figure 5.8. Effective differential capacitance at 1 kHz for a Bi electrode in 10 mM NaCl(aq) against dc potential.

The differential capacitance plotted is actually an effective value at the given frequency ($-1/\omega Z'$), because the interface shows constant phase element behaviour and is close to ($n \sim 0.9$), but not exactly described by a pure capacitor. Nevertheless it is clear that the potential dependence of this effective differential capacitance is much more complex than the Stern model and the potential of zero charge cannot be reliably determined from the data.

The sharp peak at about -0.6 V indicates a sudden change in the state of the Bi surface at more negative potentials which may be due to reduction of an oxide film and possibly desorption of adsorbed Cl⁻. On either side of the peak, the differential capacitance of Bi electrodes in the aqueous chloride is much more weakly dependent on potential, but it is higher at negative potentials and lower at potentials positive of the peak. We interpret this change as the reduction of a thin anodic film; the potential at which it occurs is similar to previous reports of the reduction of anodic films on Bi.^{154,155} At potentials <-0.6 V the electrode surface is elemental bismuth, but at potentials >-0.6 V the electrode is covered by an anodic film of thickness L which contributes an additional series capacitance per unit area of $\epsilon_r \epsilon_0 / L$. The film thickness may be estimated from the change in potential-independent capacitance on either side of the peak. Using a relative permittivity of 40 for the oxide film¹⁷⁸, we estimated its thickness to be about 1.5 nm based on a simple parallel plate capacitor model for the oxide.

The approximately potential-independent value of capacitance at strongly negative potentials is clearly substantially larger than that at potentials positive of the differential capacitance peak; this is also consistent with the formation of a thin oxide layer at $E > -0.6$ V. The standard potential of the $[\text{Ru}(\text{NH}_3)_6]^{3+/2+}$ couple is much more positive than the peak in the differential capacitance data and therefore the slow electrode kinetics at Bi compared to Pt are simply explained by the presence of a tunnelling barrier due to the thin oxide film.

Although the differential capacitance-potential curve is complex, values of charge transfer resistance can be used to estimate ϕ_2 in a relative sense from measurements of impedance spectra as a function of ionic strength. For example, if ϕ_2 is negative at the formal potential, the rate of reduction will increase at lower ionic strength because of accumulation of $\text{Ru}(\text{NH}_3)_6^{3+}$ at the interface and the charge transfer resistance will decrease at low ionic strength. Impedance spectroscopy is particularly advantageous for this purpose because the uncompensated resistance, which also varies with $[\text{KCl}]$, is easily distinguished from the charge transfer resistance as a simple shift of the data along the real axis in the Nyquist plot. At a given dc potential the ratio of charge transfer resistance to the value at a chosen reference ionic strength gives the change in ϕ_2 potential:

$$\ln\left(\frac{R_{CT}}{R_{CT}^0}\right) = (z_+ - \alpha)f(\phi_2 - \phi_2^0) \quad (5.12)$$

Since the diffuse layer capacitance increases with ionic strength, we chose the reference ionic strength to be 2 mM Ru(NH₃)₆Cl₃ + 0.2 M KCl.

The potential range of direct relevance to our electrode kinetics is positive of the capacitance peak, $-0.4 \text{ V} < E < -0.1 \text{ V}$. In this range the electrode is covered by a thin oxide film, but very close to the foot of the capacitance peak there is a small increase in capacitance which suggests incipient reduction of the oxide. We suggest that the rate of reduction of Ru(NH₃)₆³⁺ is sensitive to the changing oxide thickness and that this causes an increase in the apparent transfer coefficient in this region as the oxide becomes thinner at more negative potentials. A crude model of the effect can be obtained by writing the electron transfer rate constant as a function of layer thickness L :

$$k = k' e^{-\beta L(\eta)} \quad (5.13)$$

where we ignore the term related to the potential dropped across the barrier because of the small potential range involved and because the potential of zero charge is not known. We also neglect possible band-bending effects on the grounds that the oxide thickness is very small. The contribution to the apparent transfer coefficient is then obtained by differentiation.

$$\Delta\alpha = -\frac{1}{f} \frac{\partial \ln k}{\partial \eta} = \frac{\beta}{f} \frac{\partial L}{\partial \eta} \quad (5.14)$$

If we treat the oxide as a uniform thin film capacitor in series with the Helmholtz capacitance,

$$c^{-1} = \frac{L(\eta)}{\epsilon_r \epsilon_0} + c_{DL}^{-1} + c_H^{-1} \quad (5.15)$$

we obtain:

$$\Delta\alpha = -\frac{\beta \epsilon_r \epsilon_0}{f c^2} \frac{\partial c}{\partial \eta} \quad (5.16)$$

where c is the overall differential capacitance of the interface and we have neglected the contribution from the potential dependence of the diffuse layer. Equation (5.16) can be applied to estimate roughly the effect of the film reduction on the apparent

transfer coefficient using the experimental differential capacitance in *figure 5.8*. This effect is illustrated in *figure 5.9* below.

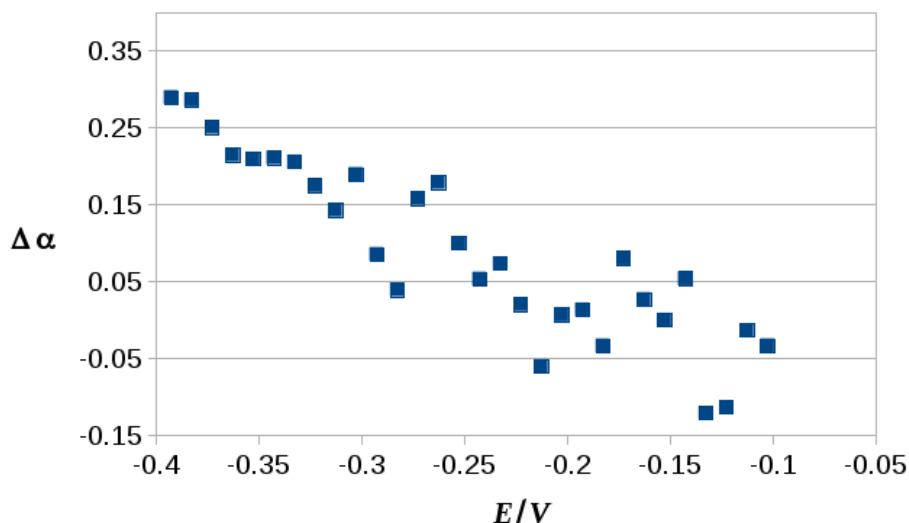


Figure 5.9. Contribution of $(\Delta\alpha)$ to the measured transfer coefficient $\alpha(E)$ (Fig.5.7) arising from the reduction of the anodic film. The data was calculated according to equation (5.16) using the experimental differential capacitance of Fig.5.8.

5.4.3 Double layer effects.

Figure 5.10 shows estimates of the ϕ_2 potential from a series of impedance spectra for 2 mM $\text{Ru}(\text{NH}_3)_6\text{Cl}_3$ in various $[\text{KCl}]$.

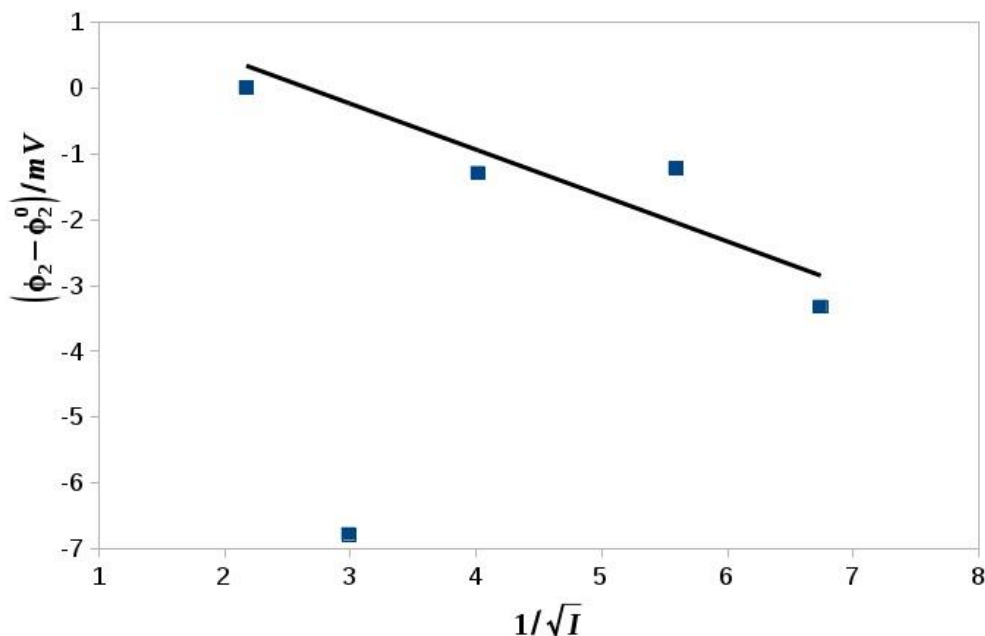


Figure 5.10. Values of relative ϕ_2 estimated from the variation of charge transfer resistance with ionic strength according to equation (5.12). The data was obtained for a Bi electrode in 2 mM $\text{Ru}(\text{NH}_3)_6\text{Cl}_3$ (aq). The reference ionic strength was chosen to be the highest employed (electrolyte = 0.2 M $\text{KCl}(\text{aq})$) at which ϕ_2 is expected to be small.

There is considerable scatter on the plot and one obvious outlier because the values are all only a few mV. However, it is also clear that ϕ_2 is negative; there is a definite trend to lower R_{CT} at lower ionic strength. This data suggests the potential of zero charge is more positive than the formal potential of -0.217 V. This is unexpected for a bare Bi surface where much more negative potentials of zero charge have been reported³⁰. However near the formal potential for $\text{Ru}(\text{NH}_3)_6^{3+}$, the Bi surface is covered with a thin oxide film. Ex-situ photoemission spectra show direct evidence for the oxide (*figure 5.11a*) and for the presence of adsorbed Cl^- (*figure 5.11b*).

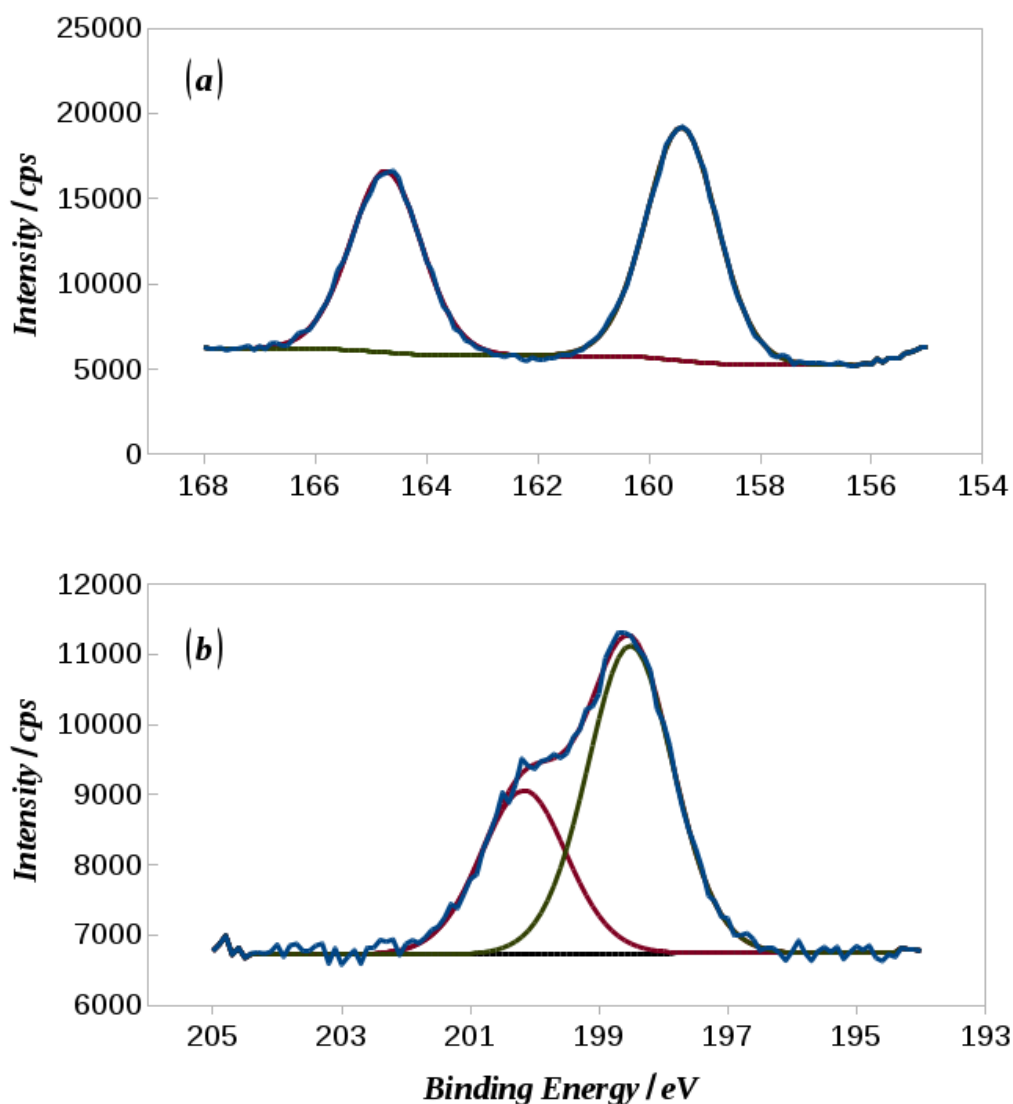


Figure 5.11. Ex-situ photoemission spectra of Bi electrodes emersed from 0.1 M NaCl(aq) electrolyte. (a) Bi 4f spectra and (b) Cl 2p spectra.

The Cl2p binding energies of 198.5 eV ($2p_{3/2}$) and 200.2 eV ($2p_{1/2}$) are assigned to the -1 oxidation state, i.e., chloride, and are consistent with the $2p_{3/2}$ data for NaCl (198.3eV)¹⁵⁸. The Bi 4f binding energies of 159.4 eV ($4f_{7/2}$) and 164.7 eV ($4f_{5/2}$) are

much closer to those observed for pure Bi_2O_3 and Bi_2O_3 films on Bi (160.1 eV, 165.4 eV) than they are to elemental Bi (156.9 eV, 162.2 eV).¹⁴⁶ Adsorbed Cl^- anions explain the negative values of ϕ_2 and are consistent with the discussion of the impedance data at varying ionic strength.

5.5 Conclusions

The electrode kinetics of the reduction of $\text{Ru}(\text{NH}_3)_6^{3+}$ at polycrystalline Bi electrodes in aqueous solution have been analysed by impedance spectroscopy. The rates were much slower than at Pt electrodes because of the presence of a thin oxide film at potentials in the vicinity of the formal potential of the couple. Differential capacitance and ex-situ photoemission spectra provide evidence for the presence of the thin oxide layer, in the order of 1.5 nm on the Bi surface near the formal potential of -0.217 V vs Ag/AgCl/1 M KCl(aq). Despite the presence of this oxide, reproducible impedance spectra near the formal potential were obtained for Bi/ $\text{Ru}(\text{NH}_3)_6^{3+}$ that could be analysed using a Randles circuit modified to incorporate a constant phase element.

The value of standard rate constant corrected for diffuse layer effects was $1.47 \pm 0.44 \times 10^{-3} \text{ cm s}^{-1}$. Under the same conditions, impedance spectra for Pt/ $\text{Ru}(\text{NH}_3)_6^{3+}$ were reversible up to the highest frequencies (10^5 Hz) employed. It is therefore safe to state that the voltammetric behaviour of $\text{Ru}(\text{NH}_3)_6^{3+}$ at Bi is that of an uncomplicated outer-sphere electron transfer and impedance spectra were obtained over a range of dc potentials from -0.1 to about -0.35 V and at electrolyte concentrations from 0.01 M KCl to 0.5 M KCl(aq).

The charge transfer resistances obtained from the impedance spectra were fitted by a new method in which the regression model allowed estimation of the transfer coefficients at each dc potential without any a priori assumption about the potential dependence of the transfer coefficient. This procedure may be generally useful for heterogeneous electrode kinetics investigations, because precise values of transfer coefficient (uncertainty 1% or better) are obtained as long as the electrode remains immersed in the electrolyte during the experiment.

The measured transfer coefficients showed clear evidence of diffuse layer effects, but in addition an increase in transfer coefficient at the most negative potentials studied

was observed and interpreted in terms of the reduction and thinning of the anodic oxide. In the particular case of $\text{Ru}(\text{NH}_3)_6^{3+}$ reduction at Bi, the potential dependence of the transfer coefficient can be interpreted in terms of two factors: (i) the well-known diffuse layer contribution arising from the Frumkin correction and (ii) the thinning of the tunnelling barrier due to reduction of the anodic oxide at negative potentials.

Chapter 6. Preparation and Characterization of Silver Nanoparticles (AgNPs)

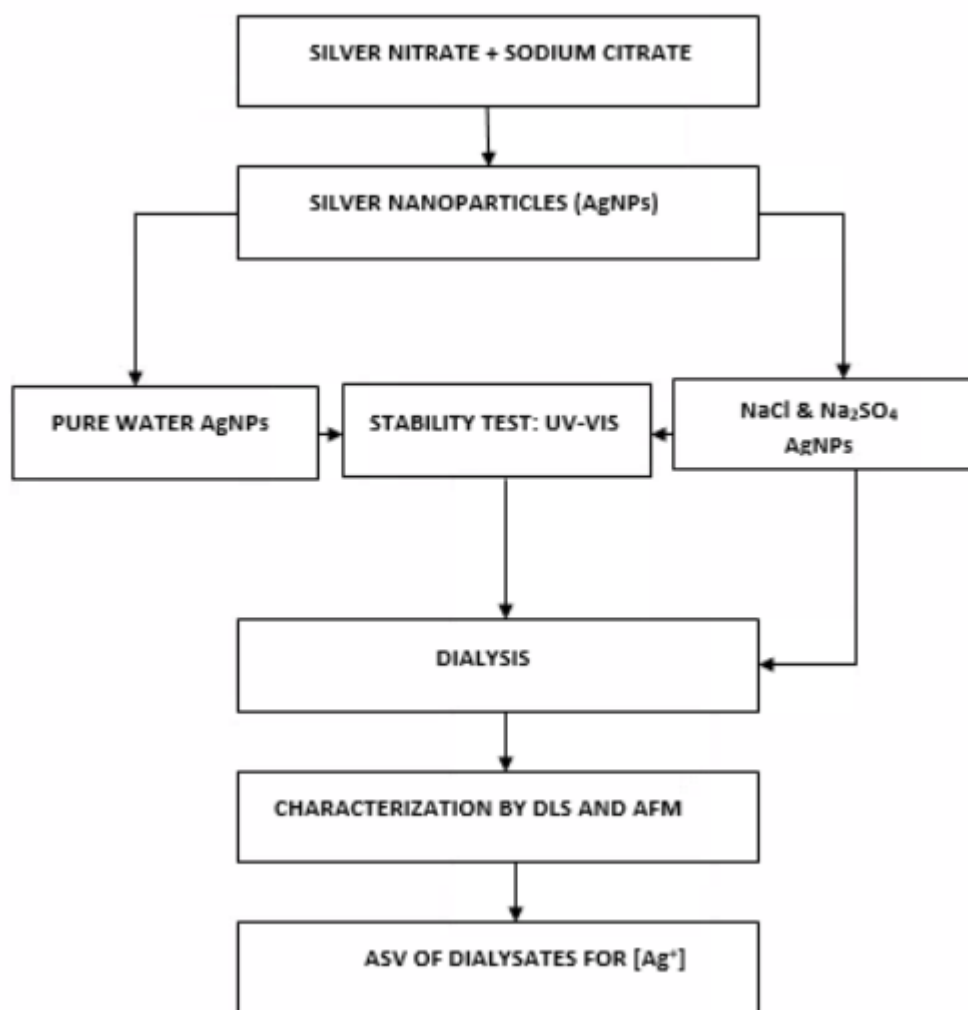
6.1 Introduction

Silver nanoparticles (AgNPs) have found wide applications in a variety of products such as socks^{88,89}, sports wears and wound dressings⁹⁰⁻⁹³ where they serve as antibacterials and inhibit unwanted odours. Silver nanoparticles have been incorporated in such consumer products as toothpastes and washing machine detergents.⁹⁴ AgNPs are also adsorbed on the cellulose fibres of blotting paper to work as antibacterial water filters in water and waste water treatment.⁹⁶⁻⁹⁸ When these products are washed, the silver nanoparticles leach out and disperse in the waste water where they can release silver(I) ions.¹¹⁶ Although the only contraindication of high levels of silver in humans is argyria¹⁷⁹, it is known to be very toxic to aquatic organisms that constitute the base of a series of food chains.^{180,181}

The action of AgNPs is partially related to the release of Ag(I) ions, therefore it is important to understand the factors that control the rate and extent of release of Ag(I). Although the electrode potential of the Ag/Ag(I) half-cell is high, about +0.8 V¹⁸² it may be very substantially reduced by the complexation of Ag(I) or the precipitation of AgX salts. This can affect the release of Ag(I) ions in two ways: by facilitating the oxidation of AgNPs by dissolved O₂ or by suppressing the Ag(I) concentration via solubility equilibria. Electroanalytical methods can determine low levels of Ag(I) in a straightforward manner, but in the present case care must be taken because the standard preparations of AgNPs may contain either excess Ag(I) reagents or traces of the reducing agent before any corrosion or release of Ag(I) from the NPs themselves. In this chapter a simple dialysis experiment is employed in order to resolve some of these issues. AgNPs were dialysed against a variety of electrolytes and pure water; Ag(I) was determined in the dialysate and aliquots of the sample were taken for analysis of the remaining AgNPs.

Silver nanoparticles were synthesized by the method of Lee and Meisel¹¹⁸, infused with and dialysed against various concentrations of chloride and sulphate salts to determine the effect of the medium on the release of Ag(I). The AgNPs were characterised by UV-Vis spectrometry, dynamic light scattering (DLS) and atomic force microscopy (AFM) while the concentration of Ag(I) ions released was monitored

by anodic stripping voltammetry (ASV). The chapter is organised in the following way: first the preparation of the various AgNP samples is described, followed by a brief overview of colloid stability. Next the changes in the AgNP optical spectra and particle size as a result of aggregation or corrosion during dialysis are discussed and finally we analyse the electrochemical data for the release of Ag(I) in the dialysate. A flow chart that summarizes the procedure of the experiment is shown in *scheme 6.1*.



Scheme 6.1. Schematic diagram of the dialysis experiment with silver nanoparticles. The NaCl-AgNPs did not however undergo absorption spectroscopic characterization.

6.2 Preparation of Silver Nanoparticles

The Creighton or sodium borohydride reduction method after Solomon *et al*¹¹⁷ as well as the citrate reduction method of Lee and Meisel¹¹⁸ were both used in the preparation of silver nanoparticles. However, because of the relative instability of the AgNPs prepared by the Creighton method, the nanoparticles studied here were

synthesized by the citrate reduction and stabilization method fully described in chapter 2.

Briefly, 18 mg or 0.018 g of AgNO₃ was dissolved in 100 mL of nanopure water to give a 1.06 mM solution and brought to the boil. 2 mL of 1% tri-sodium citrate dihydrate, prepared by dissolving 0.1 g of the salt in 10 mL of nanopure water was added to the boiling mixture. A greenish-yellow sol was formed about seven minutes after the addition of the sodium citrate. The equation for the citrate reduction of silver nitrate is



where C₅H₄O₅²⁻ is the conjugate base of acetone dicarboxylic acid.¹¹⁹ Depending on the temperature, the oxidation may proceed further to acetone, or to formaldehyde and formic acid. The essential steps of the process are a Kolbe-type electrolytic decarboxylation (RCOO⁻ → R[·] + CO₂ + e⁻) and oxidation of the radical R[·] to form the carbonyl group. AgNPs prepared by the citrate reduction of silver nitrate were relatively stable: they showed neither obvious aggregation nor colour change upon standing for about three months.

Different electrolytes were added to the as-prepared dispersions of AgNPs in order to study the effect of the anions and their concentrations on the release of Ag(I) ions from the nanoparticles. In NaCl-AgNPs, three different concentrations of aqueous NaCl; 10 mM, 30 mM and 50 mM were used.

For the 10 mM NaCl-AgNPs, 0.0584 g of sodium chloride (molecular mass 58.44 g mol⁻¹) was measured and infused into 100 mL of the AgNPs while 0.5844 g/L of the NaCl(aq) solution was used as dialysate. In case of the 30 mM concentration, 0.1753 g of the salt was infused into 100 mL of AgNPs while 1.7532 g/L of solution served as the dialysate. In a similar vein, 0.2922 g of NaCl was weighed and incorporated into 100 mL of AgNPs to give the 50 mM NaCl-AgNPs and 2.922 g/L of the NaCl(aq) solution was prepared and used as the dialysate.

Only a 10 mM concentration of sodium sulphate, Na₂SO₄ was used to monitor the effect of sulphate ion on the release of Ag(I) ions from silver nanoparticles. This is because stripping peaks for Ag(I) ions could not be obtained even at this low

concentration beyond the 2nd fraction of dialysate in spite of increasing the deposition time to 300 s.

Anhydrous Na₂SO₄, an ACS reagent of ≥99% purity and molar mass 142.04 g mol⁻¹ was purchased from Sigma Aldrich UK. 0.142 g of the salt was weighed and incorporated into 100 mL of silver nanoparticles. The dialysate was prepared by dissolving 1.4204 g of the salt in enough of nanopure water to give a one-litre solution.

Stability tests on the AgNPs were made with optical spectroscopy using a Cary 100 Bio UV-Vis spectrophotometer from Agilent Technologies, USA while their particle sizes were estimated by dynamic light scattering (DLS) and atomic force microscopy (AFM).

It is to be noted that where applicable, the AgNPs were not washed prior to dialysis as cleaning would give a false picture of the concentration of Ag(I) released from the preparation into the environment. The dialysis process itself removes the free Ag⁺ remaining after the preparation. A simple wash would not suffice. It is also worth noting that Ag(I) is continually released by the AgNPs and therefore the dialysis process must be carried out continuously and the dialysate monitored for the [Ag(I)].

6.3 Characterization Techniques

6.3.1 *Ultraviolet-visible (UV-Vis) spectroscopy.*

UV-Vis spectroscopy is concerned with the difference in electronic energy states of molecules/nanoparticles upon excitation. When a molecule absorbs sufficient energy, an excited electron from an occupied orbital will jump to an unoccupied orbital. This transition often takes place between the highest occupied molecular orbital (HOMO) and the lowest unoccupied molecular orbital (LUMO) which correspond to the ultraviolet (UV) or visible (VIS) regions of the electromagnetic spectrum. The nature of the transition in metallic nanoparticles is different: the excited state responsible for the intense absorbance of AgNPs is a plasmon. The plasmon corresponds to the motion of the valence electrons with respect to the ion cores (Ag⁺). The displacement of the valence electrons results in a restoring force arising from the electrostatic interaction of the displaced electron density and the positive ions cores. Adsorption of light in metal particles sets up an oscillation that is often compared to the tidal motion

of the earth's oceans induced by the moon. In this analogy, the water of the oceans correspond to the valence electrons of the metal. The surface plasmon is the quantum of energy associated with the motion. Unlike the molecular case, where the absorbed photon causes a large change in the motion of a *single* electron by promoting an electron from HOMO to LUMO with minor effects on other electrons, the plasmon corresponds to the small displacement of *all* the valence electrons. The plasmon energy is sensitive to particle size; smaller particles give a blue-shift of the plasmon peak and larger particles or aggregates of smaller particles produce a red-shift.

The surface plasmon resonance (SPR) peak of the pure water AgNP preparation was observed at 445 nm and a peak absorbance of 0.76. This spectrum is presented in *figure 6.1*.

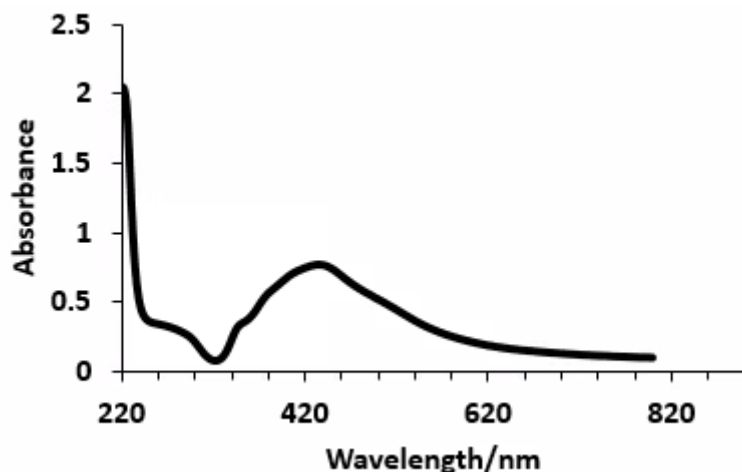


Figure 6.1. UV-Vis absorption spectrum of pure water AgNPs before dialysis.

After dialysis however, the surface plasmon peak wavelength was observed to decrease to 423 nm but the absorbance increased to 1.28. This is clearly observable in the spectrum of *figure 6.2*.

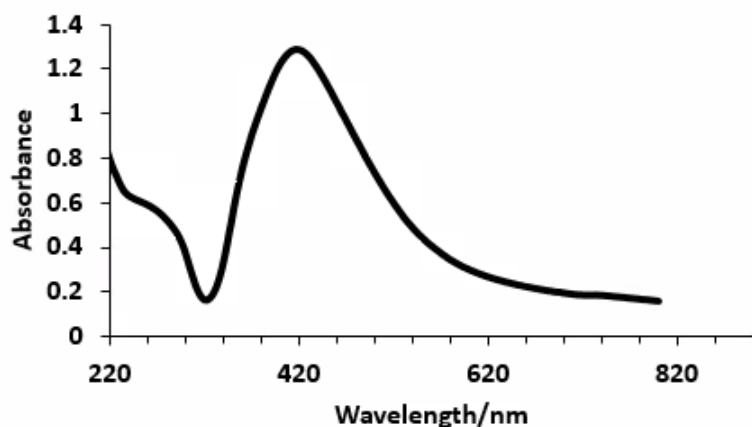


Figure 6.2. UV-Vis absorption spectrum of AgNPs after dialysis against pure water for 73 h.

This hypsochromic effect (blue-shift) can be explained on the basis of a reduction in particle size due to corrosion of the AgNPs by dissolved O_2 . In a similar manner to quantum confinement, the plasmon energy increases with decreasing size.¹⁸³

The optical absorption spectra of the sodium chloride and Na_2SO_4 -AgNPs however showed a red-shift in the surface plasmon band, indicating aggregation^{94,100,117,184-191} of the nanoparticles and an increase in their effective size by interparticle coupling of the plasmons. This effect that is due to the sulphate ions is shown in figure 6.3.

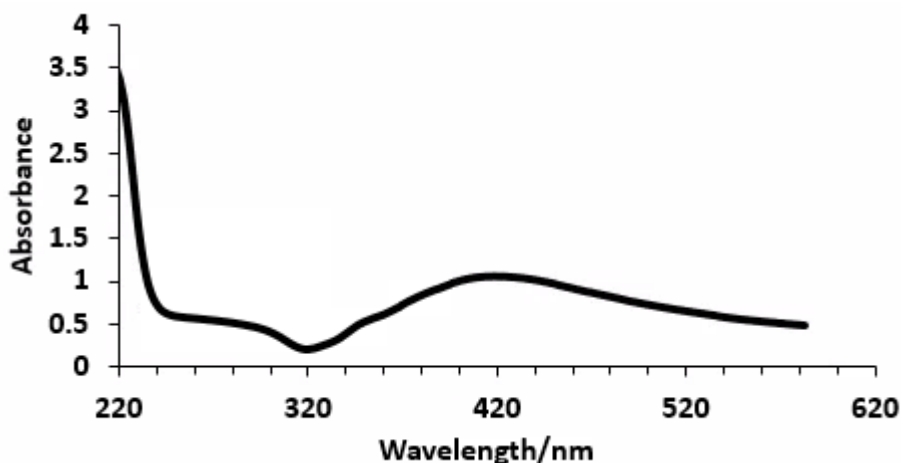


Figure 6.3. UV-Vis absorption spectrum of 10 mM Na_2SO_4 -AgNPs before dialysis run 1 with a peak wavelength of 420 nm and a peak absorbance of 1.06.

6.3.2 Colloid stability and aggregation

Aggregation of AgNPs may be understood on the basis of the DLVO theory of colloid stability.¹⁹² Essentially, the DLVO theory presupposes that the total potential energy of interaction of charged colloidal particles in an electrolyte is the sum of an attractive

van der Waals force and the repulsive electrostatic force arising from the overlap of double layers between them. For agglomeration to take place, the maximum energy barrier called the primary maximum must be overcome. The DLVO potential $V(s)$ ¹⁹⁰ comprises an attractive van-der Waal's interaction and a repulsive electrostatic interaction which arises from the double layers of the two particles (or a particle and a surface). In general $V(s)$ is complex and geometry-dependent, but for the purposes of this chapter it is enough to represent it as the sum of these two terms:

$$V_{(s)} = -v dW + V_{elec} \quad (6.2)$$

In which the separation s is the distance between the points of closest approach of the particles ($s = r - 2a$), r is the centre-centre distance and a is the particle radius. The van-der Waal's interaction depends inversely on separation ($-A_H \frac{a}{12s}$) and the Hamaker constant A_H . The dependence on separation is weaker than for interactions between atoms because the interaction is summed over pairs of atoms in the volume of each particle. The Hamaker constant A_H can be evaluated from equation 6.3 in which C is the coefficient appearing in the atom-atom interaction, e.g., for the van der Waal's interaction potential, $V(r) = -\frac{C}{r^6}$ and ρ is the atomic number density.

$$A_H = \pi^2 C \rho^2 \quad (6.3)$$

Its value is a characteristic property of the material comprising the colloidal particles. For AgNPs, the Hamaker constant for Ag in water has been estimated to be 3.35×10^{-19} J.¹⁹³ The electrostatic term V_{elec} depends on the inverse of the Debye-Huckel screening function κ which in turn depends on the ionic strength, I of the solution. This part of the theory accounts for the effect of inert salts on the aggregation of the colloids. k is given by equation 6.4 in which ϵ stands for the permittivity of the medium which in this case is NaCl(aq) and may be taken as that of water, i.e., $78.5 \times \epsilon_0$ where $\epsilon_0 = 8.854 \times 10^{-12}$ F m⁻¹, the vacuum permittivity. k is the Boltzmann constant.

$$k^2 = \frac{2000e^2 N_A I c^o}{\epsilon \kappa T} \quad (6.4)$$

The ionic strength is nowadays defined in a dimensionless manner as $I = \frac{1}{2} \sum_i \frac{c_i z_i^2}{c^o}$

where z_i is the charge number of ion i , c_i is the concentration of ion i in mol dm^{-3} and the standard concentration $c^o = 1 \text{ mol kg}^{-1}$. In aqueous media at 298 K, where the density is close to 1 g cm^{-3} , $c^o = 1 \text{ mol dm}^{-3}$. The factor of 1000 arises from a unit conversion between dm^3 and m^3 . Depending on the value of κa , there are two cases illustrated in *figure 6.4*. $\kappa a \ll 1$ corresponds to relatively thick double layers around the particles and a large potential barrier that maintains the separation of the particles. In the contrary case, the double layers are relatively thin compared to the particle radius a and a new feature appears – the shallow secondary minimum into which aggregation is reversible (known as flocculation).

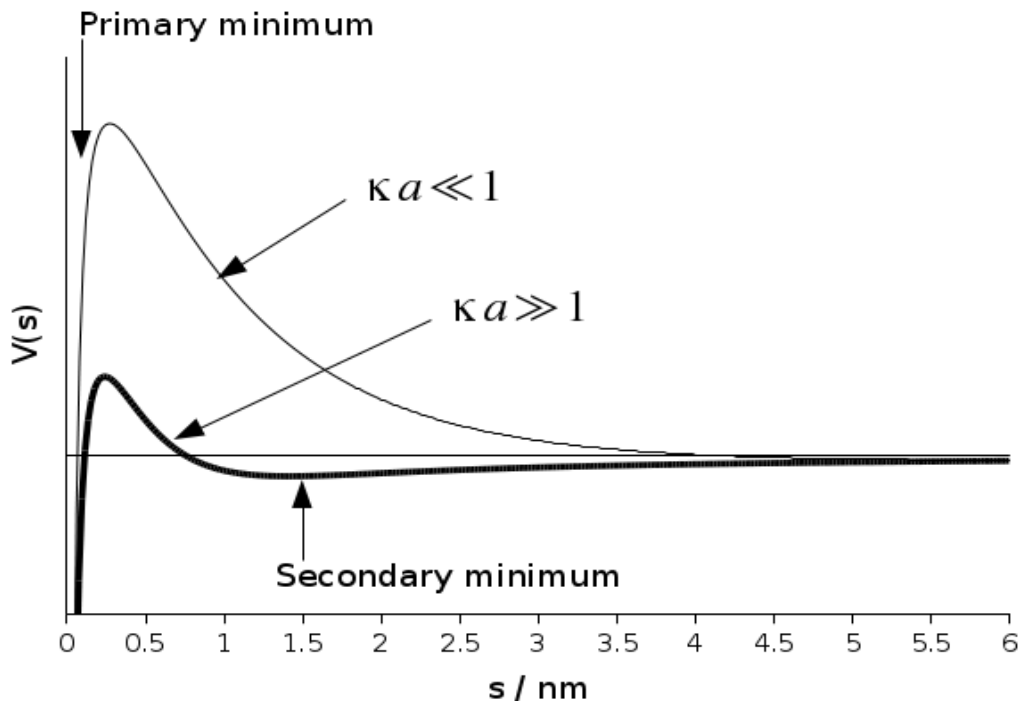


Figure 6.4. Interparticle interaction potential according to the DLVO theory for two identical spherical particles.

In summary, the stability of AgNP sols is favoured by high particle charges and low ionic strength media. In the absence of other effects, the dialysis of AgNP sols should result in lower ionic strength and favour stability of the dispersion. However, corrosion and other chemical processes can strongly affect the particle charge.

6.3.3 Dynamic light scattering (DLS)

As discussed in Chapter 2, dynamic light scattering measures the hydrodynamic size of the particles and not directly their physical sizes. This implies that the diameter measured by this technique may include the hydration layer for pure water AgNPs or the adsorbed anions in the aqueous NaCl and Na₂SO₄ preparations of AgNPs as well as any ligands bound to the particle surface during the preparation. In general, it is expected that DLS will estimate larger particle sizes^{194,195} than other size measurement techniques (AFM, SEM, XRD/Scherrer analysis) which are mainly sensitive to the metallic Ag core of the particles. However, this is not always the case because local heating effects and multiple scattering can cause DLS to underestimate the hydrodynamic diameter. While the method has advantages of simplicity, quick measurements as well as the ability to access a large quantity of particles^{194,196}, DLS may be ineffective in distinguishing between particles of varying sizes. In a mixture of small and large particles, the intensity of scattering by the small particles may be overwhelmed by that from the larger ones because scattered intensity depends on diameter¹⁹⁷ D as D^6 . It is also worth noting that DLS may suffer artefacts at low apparent hydrodynamic diameter because of impurities in the solutions or indeed any extraneous source of scattering.

There is a general increase in mean sizes of nanoparticles as measured by DLS before and after dialysis. While the increase in diameter from 31.1 nm to 34.2 nm may be regarded as marginal for pure water AgNPs, the difference is pronounced in the NaCl-AgNPs signifying the effect of the medium on the extent of aggregation. This increase of nanoparticle sizes as influenced by different media and exposure over a long period of time has been reported by other researchers⁹⁴ in the field. The DLS analysis data of pure water AgNPs before and after dialysis are shown in *figure 6.5* and *figure 6.7*.

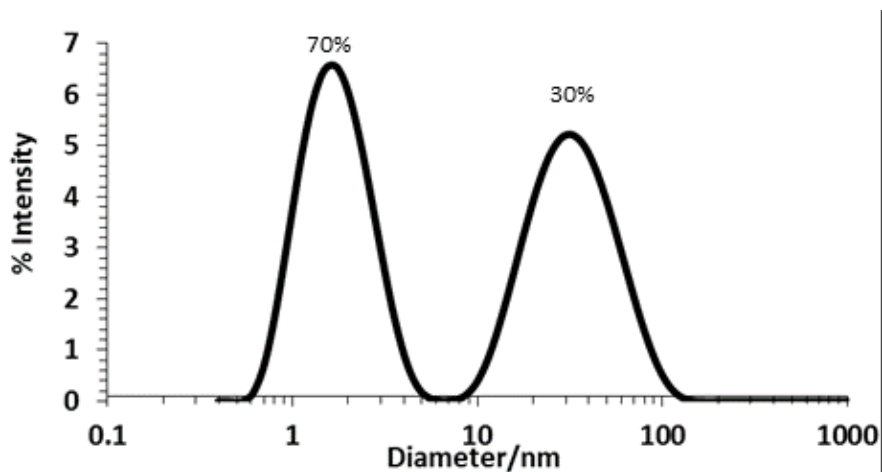


Figure 6.5. DLS analysis of pure water AgNPs before dialysis showing particles with a mean diameter of 31.1 nm and a PDI of 0.26. The peak for particles at size 1-10 nm is probably an artefact resulting from impurities or other extraneous scattering sources, while the lower intensity of 30% is for particles of sizes ranging from 10-100 nm.

Plots with multiple peaks indicate presence of both isolated and aggregate particles, the latter appearing at longer wavelengths. A clearer picture of this is presented in the analysis histograms of Figure 6.6, where PDI refers to polydispersity index (see equation 2.25).

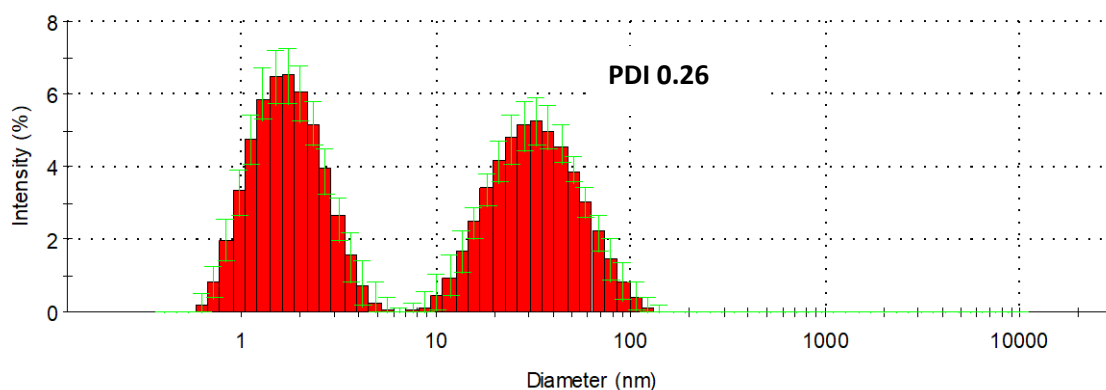


Figure 6.6. DLS analysis histogram of pure water AgNPs before dialysis showing the size ranges of the isolated and aggregate particles.

Similarly, the particle size distribution of the pure water nanoparticles after dialysis is as shown in figure 6.7.

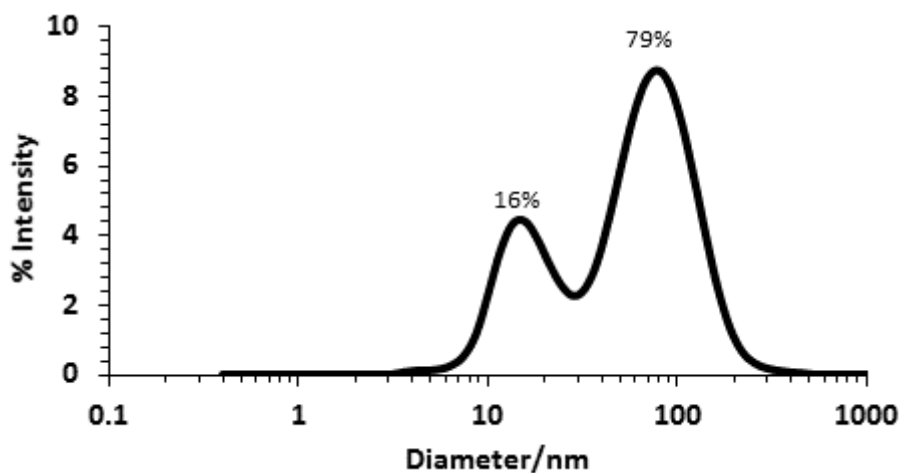


Figure 6.7. DLS analysis of pure water AgNPs after dialysis. They are more populated with particles about 100 nm in size with a light scattering intensity of 79%.

A histogram of the distribution is also presented in figure 6.8.

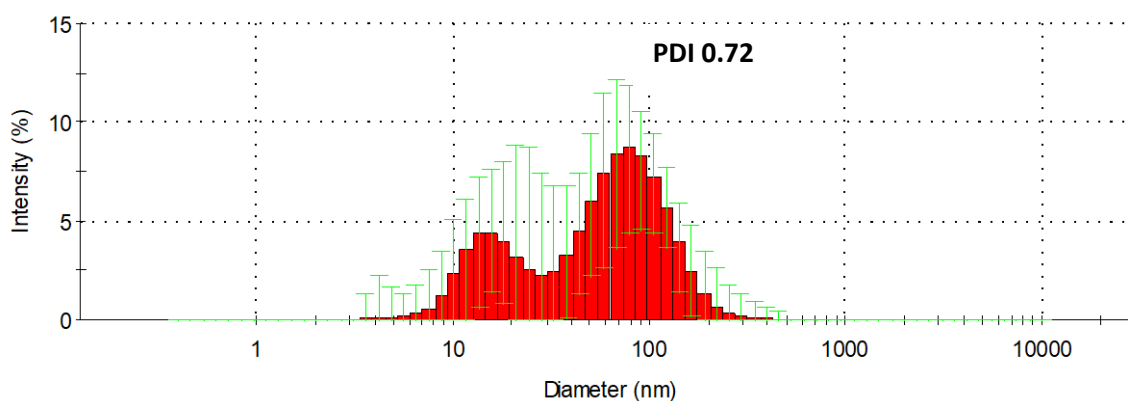


Figure 6.8. DLS analysis histogram of pure water AgNPs after dialysis with a PDI value of 0.72 indicating that the particles are highly polydisperse.

The increase in particle sizes in NaCl-AgNPs is more pronounced than what has been observed in pure water silver nanoparticles, the effect being due to the added ligand and this increases with concentration. Data for the silver nanoparticles infused with 10 mM NaCl are presented in figure 6.9.

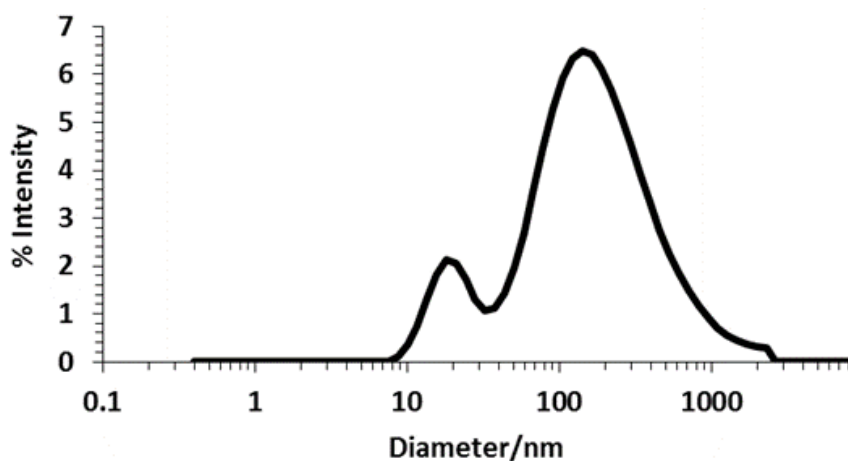


Figure 6.9. DLS analysis of 10 mM NaCl-AgNPs particles before dialysis with diameter of 102 nm and polydispersity index of 0.50.

Particles of size 100 nm and above are clearly in excess in this mixture, with a better picture of the scenario presented in figure 6.10.

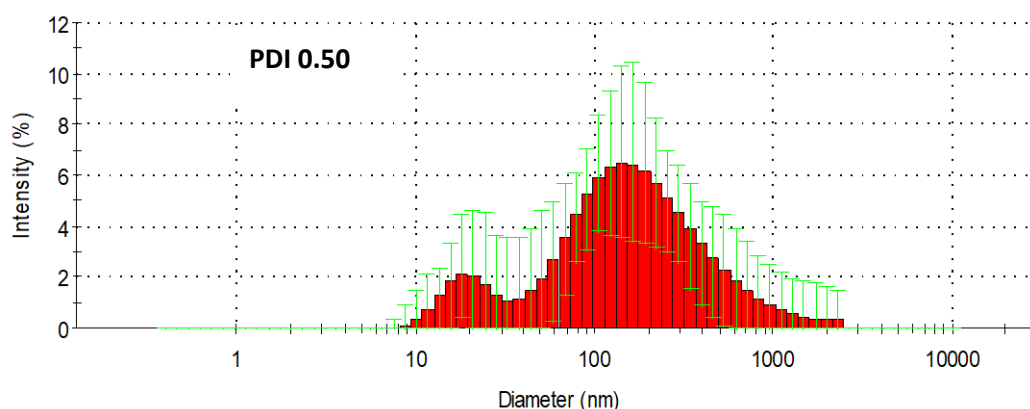


Figure 6.10. DLS analysis histogram of 10 mM NaCl-AgNPs before dialysis.

A summary of the size measurement data as obtained by DLS is presented in table 6.1.

	Pure water		10 mM NaCl		30 mM NaCl		50 mM NaCl	
	Before dialysis	After dialysis						
Mean diameter/nm	31.1	34.2	102	538	735	990	658	893
PDI	0.26	0.72	0.50	0.26	0.68	0.83	0.59	0.83

Table 6.1. Summary of DLS data on particle sizes for pure water and NaCl-AgNPs.

From the table, it can be observed that there is a general increase in polydispersity with increasing concentration of NaCl as well as aggregate sizes, and this trend has been reported elsewhere¹⁹⁸ with sizes of up to 700 nm. The data, especially size distributions (see *figure 6.9*) strongly suggests that the presence of aggregates is responsible for the apparent increase in mean particle diameter with dialysis.

6.3.4 Atomic force microscopy (AFM)

Alongside DLS analysis of particle size, AFM measurements of drop cast aliquots of AgNPs were also performed as an independent check because of the well-known limitations of DLS mentioned at the start of section 6.3.2. AFM measurements involved drop casting 2 μL of sample on Si wafer which had been cleaned with acid piranha solution (3:1 mixture of concentrated sulphuric acid and hydrogen peroxide), rinsed with nanopure water and dried with a stream of nitrogen gas. The aliquot was then left on the substrate to dry after which straightforward AFM images (tapping mode) were made to estimate the particle sizes from both height and diameter as described in *figure 6.11*.

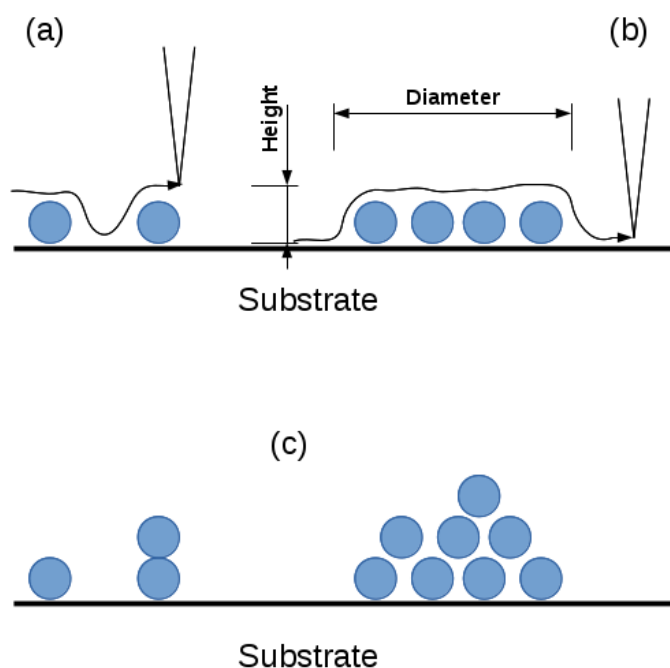


Figure 6.11. Schematic diagram of the AFM measurement of AgNPs. The blue circles represent individual AgNPs and the curves with arrows indicate the path of the AFM tip as it passes over the sample (ignoring the tapping motion for simplicity). (a) Samples comprising well-separated AgNPs give roughly the same particle size whether it is obtained from the height of the feature or its lateral dimension (denoted diameter). (b) If monolayer islands of AgNPs form on the surface, the feature height will roughly match the diameter from DLS, but the feature diameter will be much larger. (c) The formation of clusters of AgNPs is also possible and this will result in feature heights larger than individual particle diameters and possibly larger than DLS sizes.

As can be seen in *figure 6.11*, interpretation of the AFM images requires a consideration of the form in which the AgNPs lie on the surface. In general, we find much larger diameters of the features than heights, but the heights are in rough agreement with DLS – this is consistent with monolayer island formation as AgNPs aggregate during deposition in the manner of *figure 6.11 (b)*.

As earlier reported in chapter 2, imaging was done in the tapping mode and the images obtained therefrom were processed and analysed using Nanoscope™ software version 1.4. Apart from the standard flattening of the raw images in software to remove artefacts related to drift, all the images are presented as acquired.

The sizes of particles in terms of both height and diameter were observed to decrease after dialysis for both 10 mM and 50 mM NaCl-AgNPs. Sample AFM images of the 10 mM concentration of AgNPs before and after dialysis, together with their grayscale and some line profiles are shown in *figure 6.12*. The rest of the data on particle sizes is summarized in *table 6.2*.

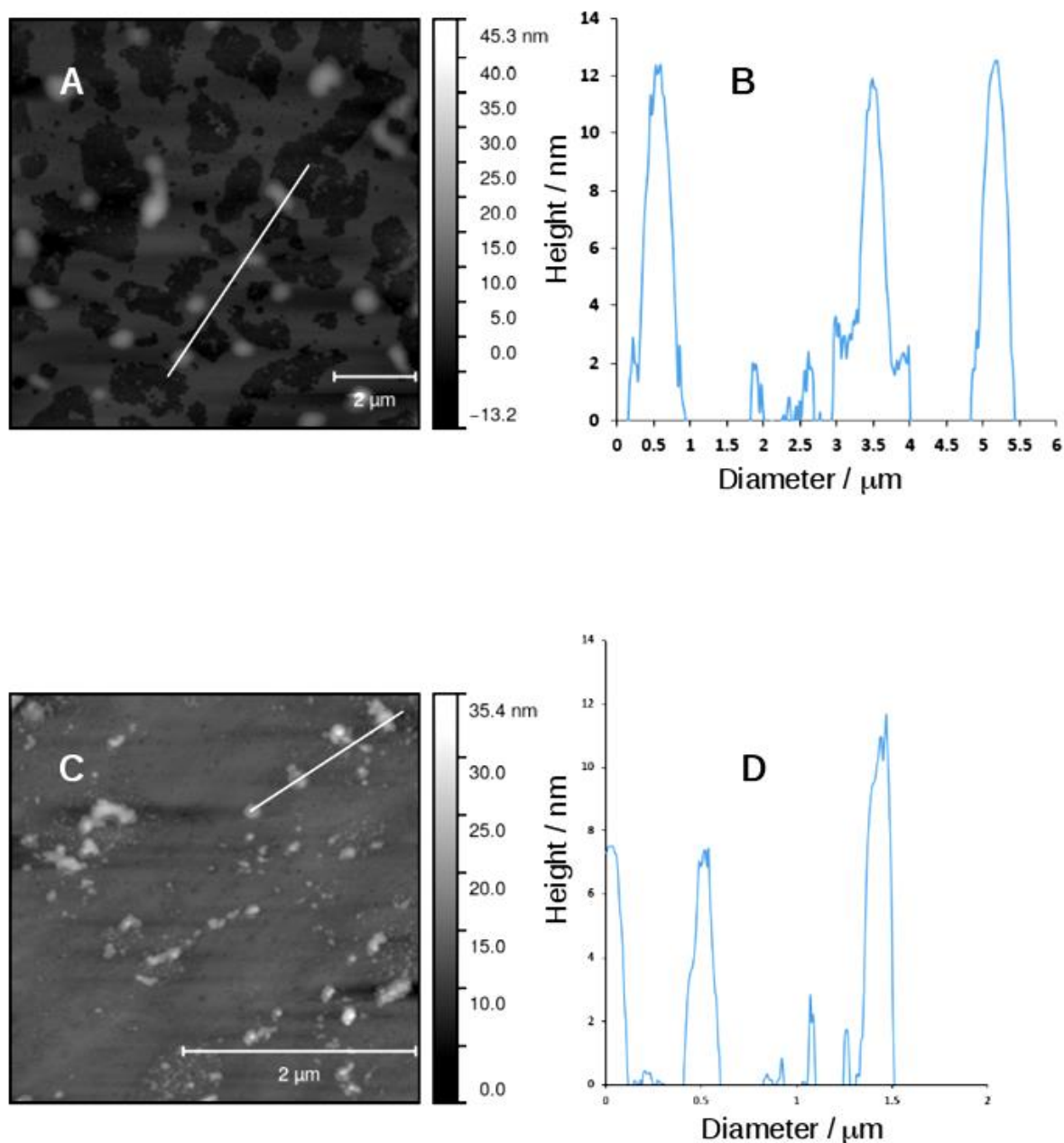


Figure 6.12. (A) AFM image of 10 mM NaCl-AgNPs before dialysis (B) the line profile of 03 particles along the white line in A (C) 10 mM NaCl-AgNPs after dialysis and (D) a line profile along the white line in (C). The scale bars are as indicated on the images. The sample aliquot was drop cast on Si wafer that had been cleaned with acidic piranha solution, thoroughly rinsed with nanopure water and dried with a stream of nitrogen gas.

Sample diameter histograms of the 10 mM NaCl-AgNPs are also presented in Figure 6.13 to give a clearer picture of the size distributions of the particles before and after dialysis.

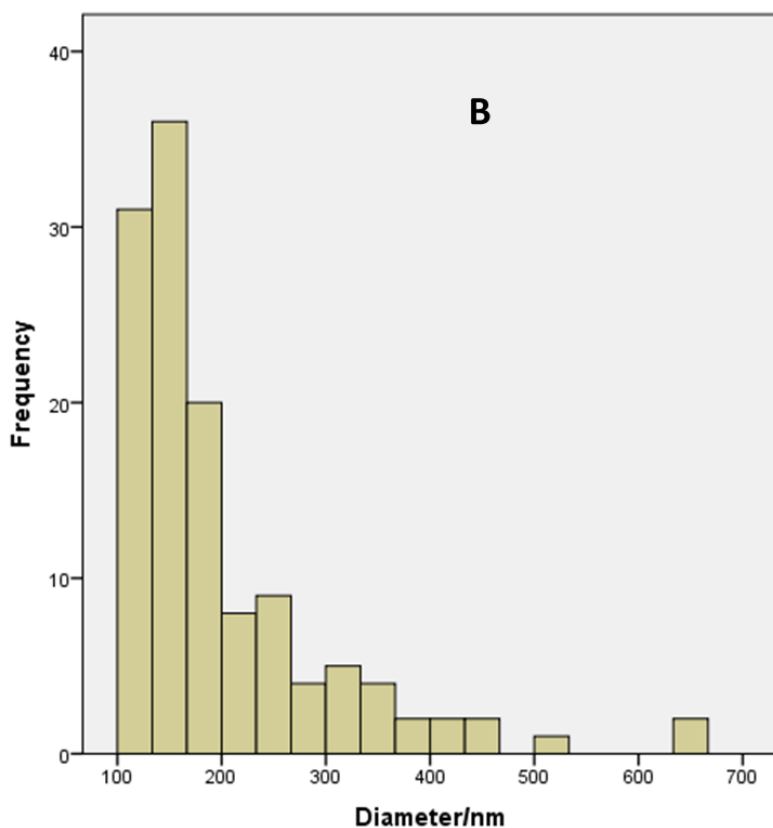
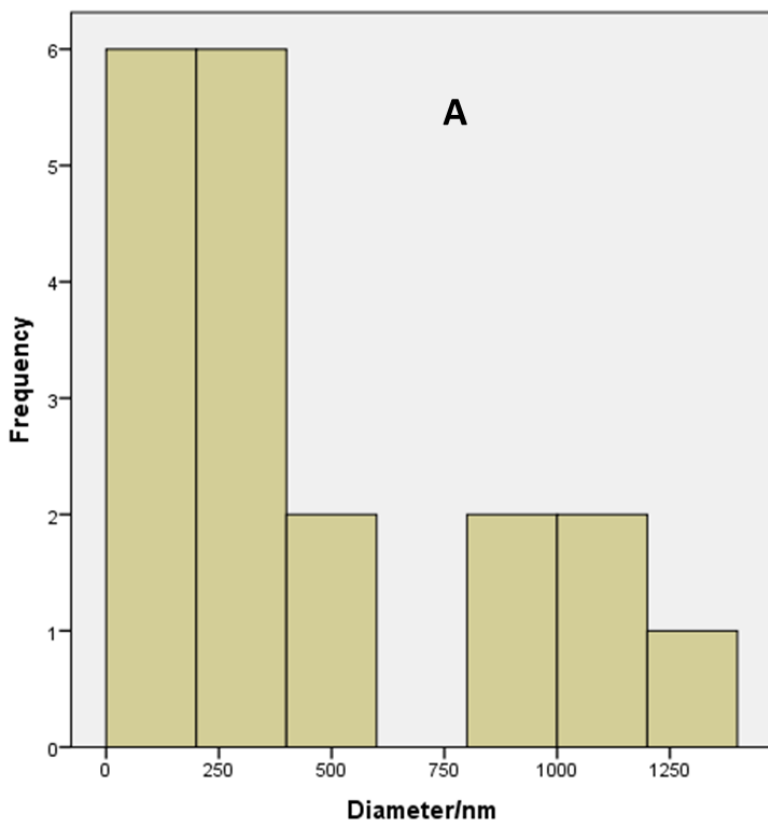


Figure 6.13. (A) Diameter histogram of 10 mM NaCl(aq)-AgNPs before dialysis showing 19 particles with a mean size of 451 nm and standard deviation of 385 nm. (B) Diameter histogram of 10 mM NaCl(aq)-AgNPs after dialysis showing 126 particles with a mean size of 199 nm and standard deviation of 102 nm.

The decrease in size is consistent with corrosion of the AgNPs. In spite of aggregation, nanoislands about 1 particle in height deposit on the AFM substrate of silicon wafer. The tip therefore recognizes the height of these islands as, on average, that of single particles.

An unusual behaviour was however observed with the 30 mM NaCl(aq)-AgNPs which showed increases in size after dialysis. Sample images of this concentration are also shown in the *figure 6.14* below.

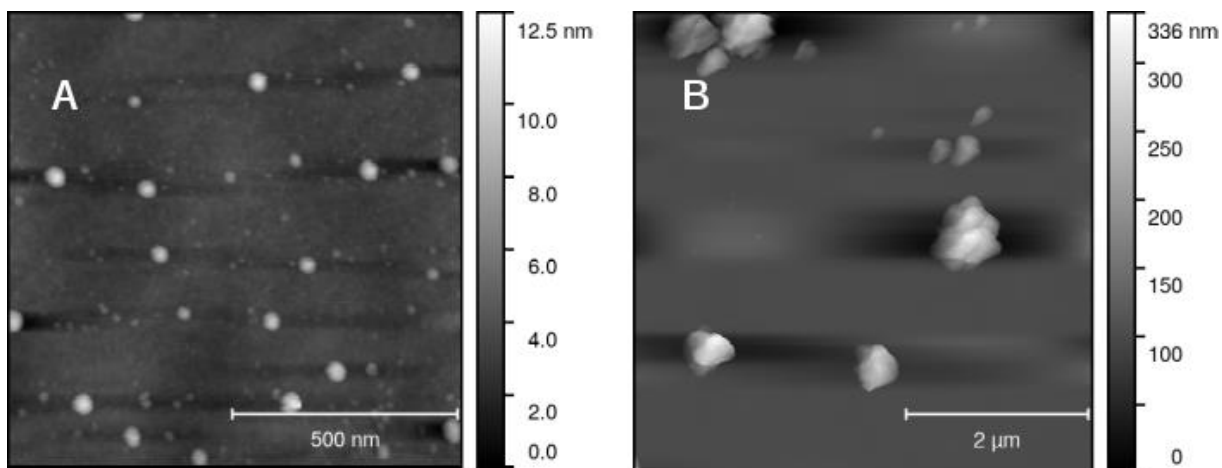


Figure 6.14. AFM images of 30 mM NaCl(aq)-AgNPs (A) showing single particles before dialysis and (B) aggregates after dialysis. The sample aliquot was drop cast on Si wafer that had been cleaned with acidic piranha solution, thoroughly rinsed with nanopure water and dried with a stream of nitrogen gas.

This may be due to the adsorption of AgCl on the surface of the AgNPs. However, owing to repulsive forces between Ag^+ as they go into solution, the sizes of the AgNPs decrease. *Figure 6.14(B)* clearly shows the presence of larger aggregates after drop casting on the Si substrate for AFM.

Height histograms of the 30 mM NaCl(aq)-AgNPs as they indicate apparent increase in sizes is presented in *figure 6.15*.

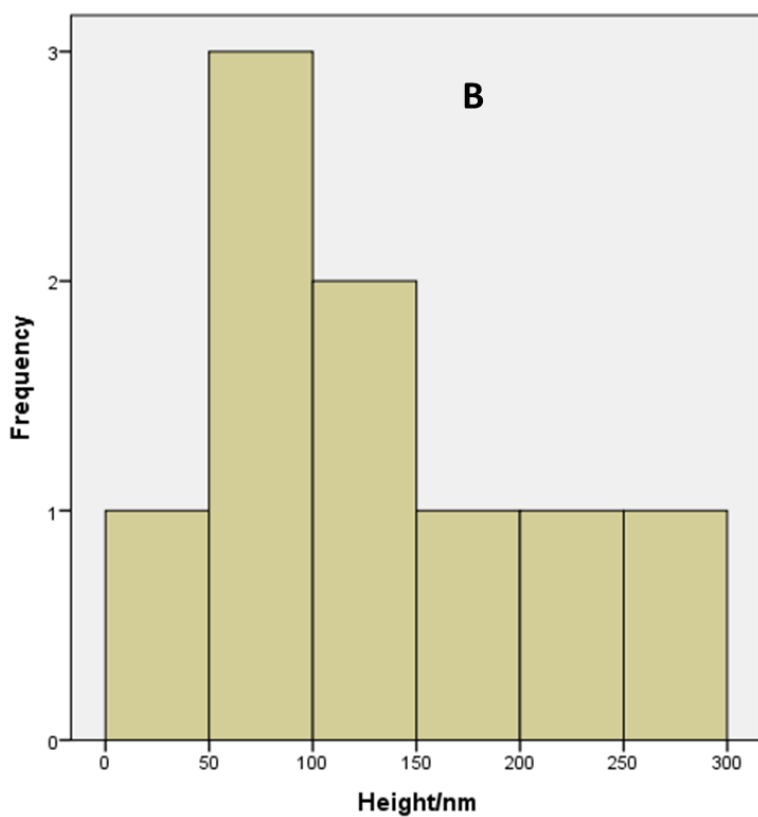
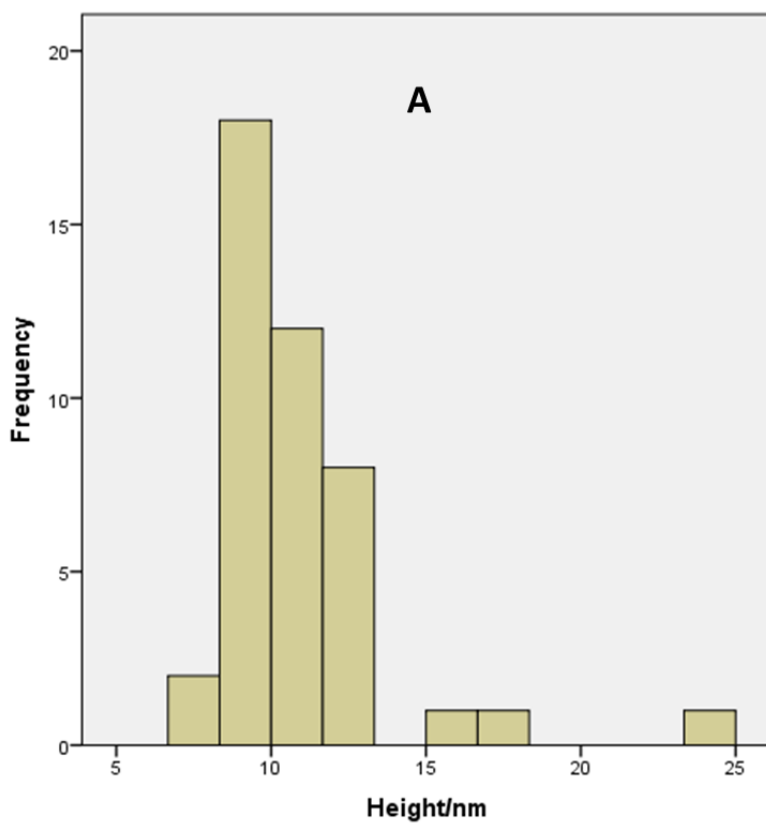


Figure 6.15. (A) Height histogram of 30 mM NaCl(aq)-AgNPs before dialysis showing 43 particles with a mean size 10.9 nm and a standard deviation of 2.7 nm. (B) Height histogram of 30 mM NaCl(aq)-AgNPs after dialysis showing 09 particles with mean size of 135 nm and a standard deviation of 81.7 nm.

A summary of results for AFM images of NaCl-AgNPs is presented in *table 6.2*

Concentration/mM		Image no.	Total count	Mean height/nm	SD (Ht)	Mean diameter/nm	SD (Dia)	Scan size/ μm	
10	Before dialysis	0.001	19	104	76.5	451	385	10 for all	
		0.002	53	80.4	57.8	283	193		
		0.003	21	15.4	9.00	553	199		
		0.004	81	54.6	21.9	334	195		
	After dialysis	0.001	126	17.1	12.9	199	102	10.0	
		0.002	96	7.83	3.73	85.9	56.6	3.50	
		0.004	55	27.7	31.4	210	134	10.8	
		0.013	56	11.3	4.93	67.5	21.9	3.0	
		0.014	53	12.6	3.19	71.3	17.4	3.3	
	30	Before dialysis	0.001	43	10.9	2.70	49.8	8.91	4.0
0.002			44	4.08	2.44	24.7	12.9	1.0	
0.003			93	8.81	0.84	48.4	4.23	4.0	
0.004			62	8.64	0.85	47.2	3.33	4.0	
After dialysis		0.003	12	14.3	3.91	143	56.0	10.0	
		0.004	9	135	81.7	290	205	5.0	
		0.004(a)	15	21.0	14.5	112	70.5	4.0	
		0.005(a)	13	12.6	9.23	90.1	48.9	4.5	
50		Before dialysis	0.001	33	13.9	3.50	89.1	16.4	4.0 for all
			0.002	28	14.8	3.67	77.9	18.1	
	0.003		33	15.3	1.87	89.8	10.7		
	0.005		16	13.6	7.43	77.81	28.6		
	After dialysis	0.001	6	9.82	3.28	78.8	13.8	4.0 for all	
		0.002	17	8.48	1.75	74.2	33.3		
		0.003	30	8.71	2.25	65.2	18.1		
		0.004	14	5.80	2.05	73.6	34.0		

Table 6.2. Summary of AFM data obtained for NaCl-AgNPs. SD is the standard deviation of the feature height (Ht) or of the feature lateral diameter (dia) in nm.

The $\text{Na}_2\text{SO}_4(\text{aq})$ -AgNPs also showed a general decrease in size, both in terms of height and diameter as was the case with $\text{NaCl}(\text{aq})$ -AgNPs. The particles of $\text{Na}_2\text{SO}_4(\text{aq})$ -AgNPs are however much larger than those of the $\text{NaCl}(\text{aq})$ -AgNPs. This could be due to adsorption of sulphate ions on the surface of the AgNPs. The solubility product value of 1.4×10^{-5} at 25°C as well as a standard reduction potential of 0.653 V for Ag_2SO_4 suggests that the $\text{Ag}(\text{I})$ ions have relatively low affinity for sulphate ions. This partly explains why a high concentration of Ag^+ ions were released upon dialysis of the $\text{Na}_2\text{SO}_4(\text{aq})$ -AgNPs.

The solubility product of AgCl is 1.8×10^{-10} at 25°C and with a relatively low electrode potential for Ag/AgCl of 0.222 V, the interaction between Ag^+ and Cl^- is much stronger.

Sample AFM images of the $\text{Na}_2\text{SO}_4(\text{aq})\text{-AgNPs}$ are shown in *figure 6.16*.

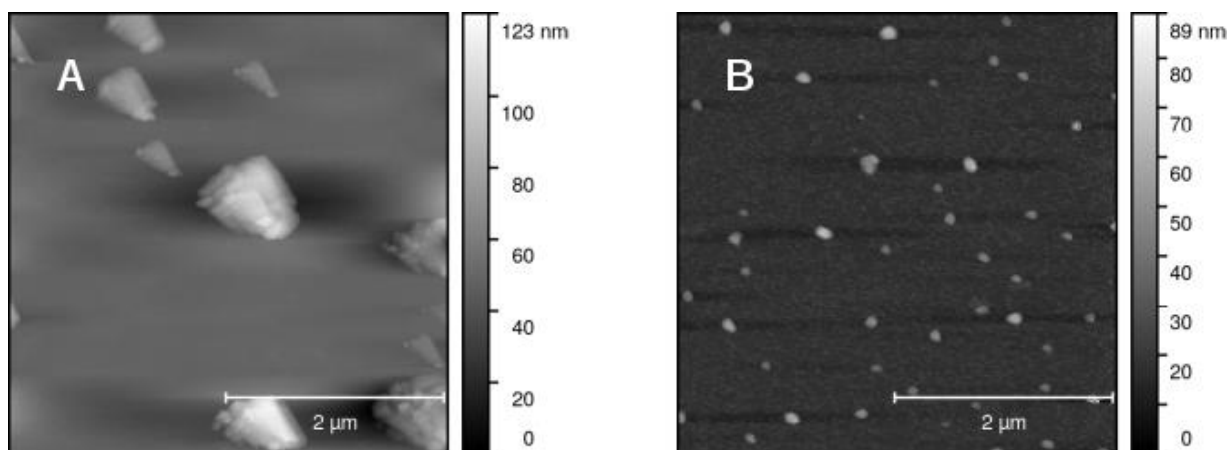


Figure 6.16. AFM images of 10 mM $\text{Na}_2\text{SO}_4(\text{aq})\text{-AgNPs}$ (A) before dialysis and (B) after dialysis; all with scan size of $4\ \mu\text{m}$ and scale bars as indicated on the images. The sample aliquot was drop cast on Si wafer that had been cleaned with acidic piranha solution, thoroughly rinsed with nanopure water and dried with a stream of nitrogen gas.

Diameter histograms of the 10 mM $\text{Na}_2\text{SO}_4(\text{aq})\text{-AgNPs}$ are also presented in *figure 6.17* to show the size distribution of the particles more clearly.

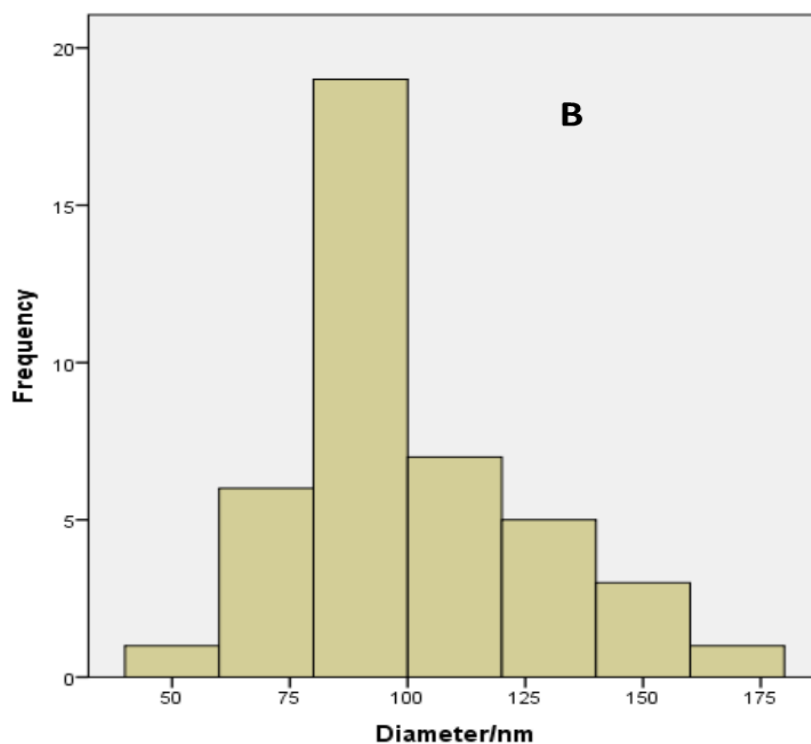
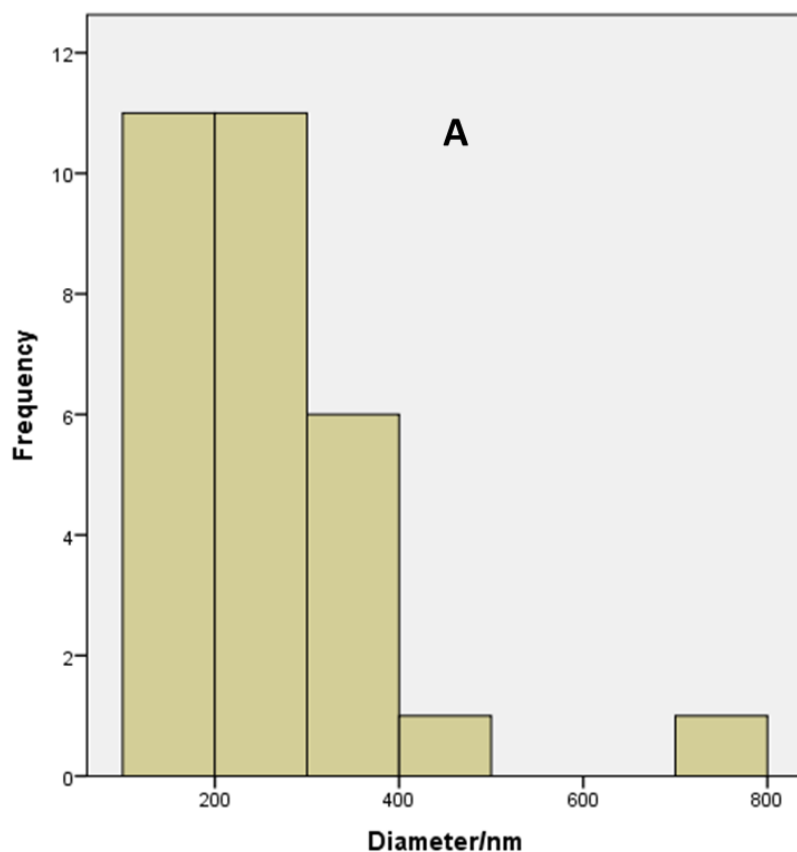


Figure 6.17. (A) Diameter histogram of 10 mM $\text{Na}_2\text{SO}_4(\text{aq})$ -AgNPs before dialysis showing 30 particles with a mean size of 254 nm and a standard deviation of 121 nm. (B) Diameter histogram of 10 mM $\text{Na}_2\text{SO}_4(\text{aq})$ -AgNPs after dialysis showing 42 particles with a mean size of 100 nm and a standard deviation of 25.1 nm.

A summary of AFM data obtained for Na₂SO₄(aq)-AgNPs is presented in *table 6.3*.

	Image no.	Total count	Mean height/nm	SD (Ht)	Mean diameter/nm	SD (Dia)	Scan size/μm
Before dialysis	0.002	30	93.1	32.2	254	121	4.0
	0.003	20	128	23.1	314	159	4.0
	0.005	20	66.8	28.7	552	385	10.0
After dialysis	0.002	44	31.2	9.2	93.5	22	4.0 for all
	0.003	53	37	16.3	87.7	17	
	0.004	42	36.8	13.9	100	25.1	
	0.005	55	58.2	21.8	81.3	19.5	

Table 6.3. Summary of AFM data for 10 mM Na₂SO₄(aq)-AgNPs. SD is the standard deviation of the feature height (Ht) or of the feature lateral diameter (Dia) in nm.

It is to be observed that in all cases of NaCl(aq)- and Na₂SO₄(aq)-AgNPs, the lateral diameters of the particles are larger than their heights. Although small differences between diameter and height could be attributed to tip dilation which brings about an extended diameter size¹⁹⁹⁻²⁰², the effects here are large and best understood in terms of aggregation of AgNPs on the Si substrates. The height is less influenced by tip or probe effects and related directly to the particle diameter in the case of island formation of AgNPs on the substrate.

A comparison of the DLS data of *figure 6.5 – figure 6.10* and the AFM images of *figure 6.11 – figure 6.17* leads to the following conclusions: the size of individual particles reduces during dialysis in most cases. The mean particle size obtained from DLS typically increases; however this reflects aggregation of the individual particles – evidenced by the bimodal size distribution in DLS and the observation of height decreases in AFM, where AFM heights of particle islands match approximately the individual particle diameters.

6.3.5 Anodic stripping voltammetry (ASV)

The amount of Ag(I) ions released from the nanoparticles through the dialysis membrane was monitored by stripping voltammetry at glassy carbon, with

Hg/Hg₂SO₄ as reference electrode for an accumulation time of 30 s. The accumulation time was increased to 300 s for dialysate fractions in which a stripping curve was not observable after 30 s of pre-concentration time. In such cases, the signal was scaled by a factor of 10 to take account of the change in deposition time.

Values of Ag(I) ion concentration were obtained using the baseline corrected calibration equation 6.5 obtained by standard addition measurements using AgNO₃(aq) standards.

$$Q_p = 0.00106[\text{Ag(I)}] - 0.00355 \quad (R^2 = 0.946) \quad (6.5)$$

Q_p is the integral of the stripping peak in μC and [Ag(I)] is the Ag(I) concentration in μM.

The calibration curve for this data is shown in *figure 6.18*.

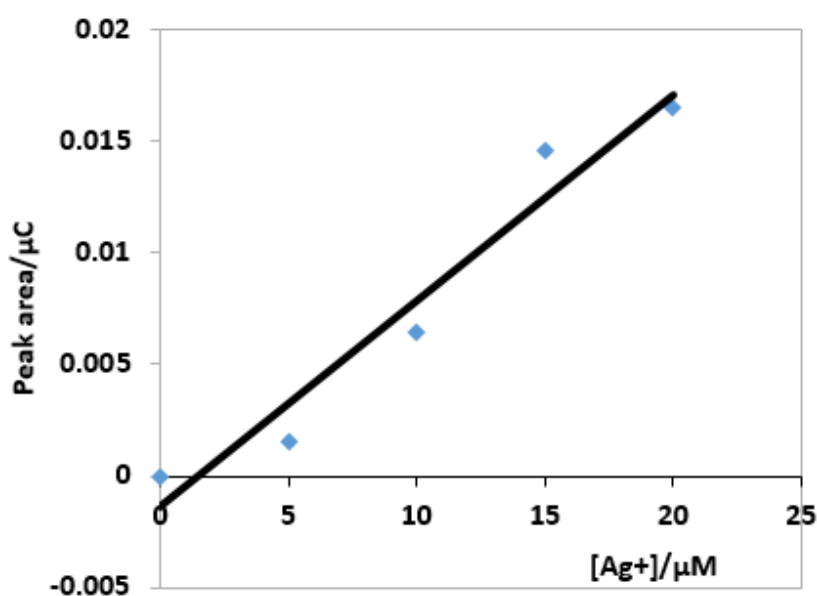


Figure 6.18. Baseline corrected calibration curve for stripping at AgNO₃(aq).

The result showed a substantial amount of 90 μM Ag(I) ions present in the initial nanoparticle preparation in the absence of any deliberately added electrolyte. After 73 h of dialysis, about 4 μM of Ag(I) ions could be detected. Almost the same concentration of Ag(I) was observed in experiments with deliberately added NaCl(aq), irrespective of the concentration of chloride ions present. The concentration of Ag(I) ions in the dialysate from the experiments with pure water and NaCl(aq)-AgNPs is presented in *figure 6.19*.

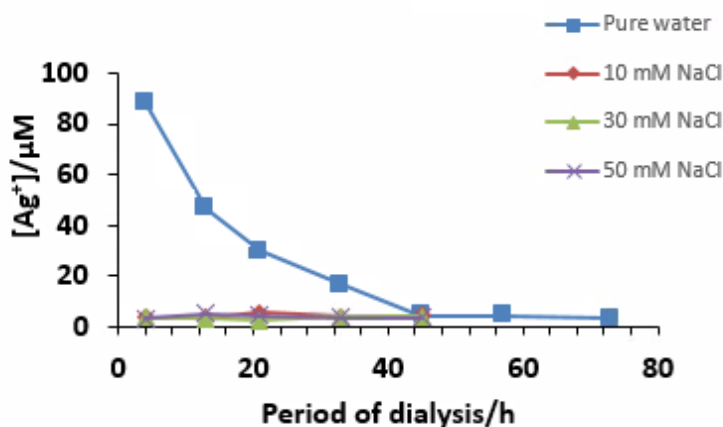


Figure 6.19. Variation of $[Ag(I)]$ with time of dialysis for four different sets of experiments to show the composition of the medium against which the sample was dialysed.

An example of anodic stripping voltammogram from the calibration set is shown in figure 6.20. A linear baseline was subtracted from the ASVs and the data integrated numerically on a spreadsheet.

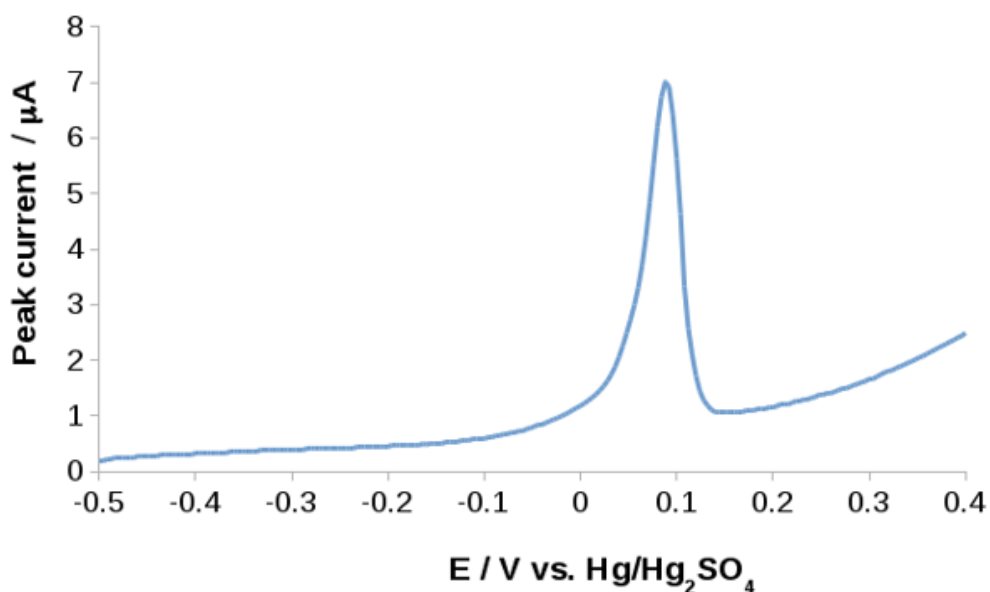


Figure 6.20. Anodic stripping voltammogram for $20 \mu M AgNO_3(aq)$ in $0.1 M NaNO_3(aq)$. The data is presented as was acquired, before baseline correction. The Ag stripping peak is observed just below $0.1 V$ and the scan rate was $1 V s^{-1}$.

Examples of stripping curves that were integrated to arrive at the data of figure 6.21 are shown below, for the 1st and 5th fractions of dialysates of 50 mM NaCl-AgNPs.

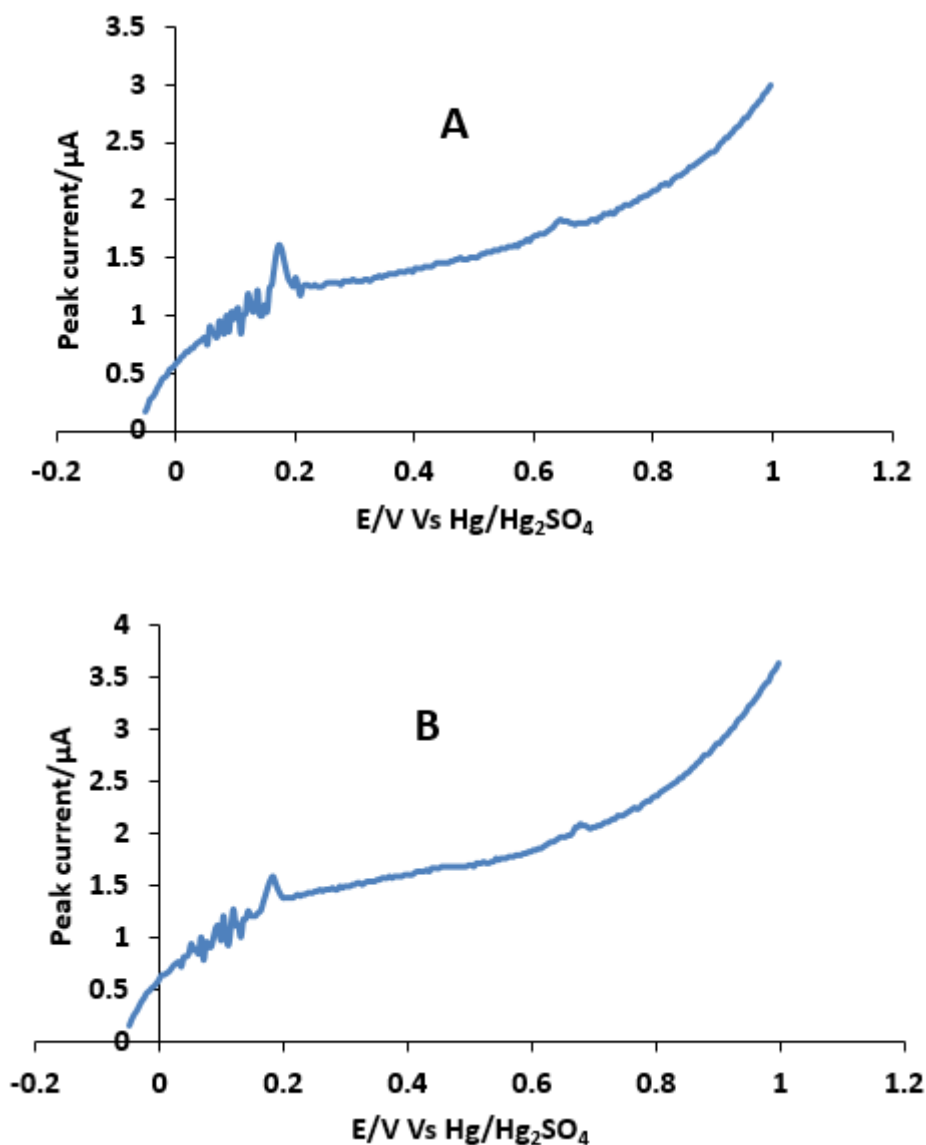


Figure 6.21. (A) Anodic stripping voltammogram for 1st fraction of 50 mM NaCl(aq)-AgNPs dialysate at glassy carbon. (B) Anodic stripping voltammogram for 5th fraction of 50 mM NaCl(aq)-AgNPs dialysate at glassy carbon. The data is presented as was acquired, before baseline correction. The Ag stripping peaks are observed just below 0.2 V and the scan rate was 1 V s^{-1} .

For $\text{Na}_2\text{SO}_4(\text{aq})\text{-AgNPs}$, only two fractions of dialysates yielded stripping peaks as none was noticed even at the extended deposition time of 300 s. Baseline correction data from these fractions gave Ag(I) ion concentrations of $61.8 \text{ }\mu\text{M}$ and $14.7 \text{ }\mu\text{M}$ for the 1st and 2nd fractions respectively.

Previous workers have used anodic stripping voltammetry to quantify Ag in NPs.²⁰³ Complications in the analysis due to aggregation of the AgNPs and effects of the capping ligand were reported. In the experiments described in this chapter we took a different approach and aimed to measure the free Ag(I) in solution produced by corrosion of AgNPs under ambient conditions in various aqueous electrolytes. To

avoid issues related to oxidation of AgNPs and unreacted material (citrate) we employed a dialysis technique in which the dialysate was analysed by anodic stripping voltammetry. The data of figure 6.17 shows that, perhaps surprisingly, the concentration of dissolved Ag(I) is of the same order in the presence or absence of chloride. It might have been expected that Cl⁻ would precipitate AgCl and therefore reduce the freely-dissolved Ag(I) concentration. In fact the data shows that at long durations, the concentrations of Ag(I) released are of the order of μM even in 50 mM NaCl(aq). The reduction in standard potential for Ag/Ag(I) in the presence of Cl⁻ appears to compensate approximately for the reduced solubility of Ag(I) in chloride media. This result is of relevance to the fate of AgNPs in marine environments

6.4 Conclusions

From the findings carried out on silver nanoparticles, the following conclusions can be made:

The surface plasmon resonance (SPR) of the AgNP sols was blue-shifted for pure water – AgNPs, suggesting corrosion and reduction in particle size. The SPR peak for Na₂SO₄ – AgNPs was red-shifted suggesting aggregation.

Taken together, AFM and DLS data show that the AgNPs aggregate during dialysis and that the mean particle size appears to increase because of this.

However, a more detailed analysis of the DLS and AFM data shows that the size of *individual* nanoparticles generally decreased with time of dialysis.

The dialysis experiment shows the steady release of micromolar [Ag(I)] in the presence of up to 50 mM NaCl(aq) because of corrosion of the AgNPs.

The concentration of chloride in a water sample has little influence on the release of Ag(I) from AgNPs.

Presence of sulphates does not exert significant influence on the release of Ag(I) ions from a product or substrate.

Chapter 7. Conclusions and Future Work.

The research work reported in this thesis is made up of two parts: the first part continues investigations with bismuth electrodes as possible replacements for mercury in electroanalyses because of their ease of preparation and relative the lack of toxicity of bismuth. The second part concerns the detection of Ag(I) ions released by corrosion of silver nanoparticles (AgNPs) in aqueous media, where anodic stripping voltammetry (ASV) at glassy carbon electrodes was used for the detection of Ag(I) ions released from AgNPs. Glassy carbon electrodes were preferred for this work as neither bismuth nor platinum electrodes were found to be suitable. Conclusions are therefore made on these two aspects separately.

7.1 Bismuth Electrodes.

Bismuth bulk electrodes (BiBEs) were used in this research to measure differential capacitance in aqueous and non-aqueous media as well as study the electroactivity of a variety of redox couples, as summarized below.

7.1.1 Capacitance measurements.

Electrochemical impedance spectroscopy (EIS) measurements showed that the potential dependence of the differential capacitance of Bi in aqueous electrolytes was complex. In particular a capacitance peak was observed near -0.6 V vs Ag/AgCl (1 M KCl) depending on the nature of the electrolytes (Cl^- , Br^-) and concentration. This peak was attributed to reduction of the anodic oxide formed at more positive potentials, but appears also to contain a contribution from adsorbed anions.

Ex-situ photoemission spectroscopy was used to provide direct evidence of the presence of a thin oxide film at bismuth electrodes and of the adsorption of halide anions at the oxide surface.

On the other hand, the low values of differential capacitance ($<20 \mu\text{F cm}^{-2}$) in the non-aqueous electrolyte of AN/ LiClO_4 is as a result of the relatively low dielectric constant of AN as well as the weak adsorption capacity of the ClO_4^- anion. This interface displays simple capacitance-potential curves that are approximately consistent with the Gouy-Chapman-Stern theory. However, the irregular variation of capacitance with concentration and frequency confirms that the bismuth and platinum

electrode surfaces are not ideal capacitors. These surfaces should therefore be seen to be behaving as constant phase elements (CPEs) or non-ideal capacitors.

Next, several redox couples were studied by cyclic voltammetry with a view to selecting one or more for detailed analysis of the electron transfer rates at Bi electrodes in aqueous electrolytes.

7.1.2 Anthraquinone-2-sulfonate (AQS)

The data showed good CVs within the cathodic potential range of -0.2 V to -1.0 V for all the concentrations of 2 mM to 10 mM investigated. In terms of the cathodic potential criterion therefore, AQS can be said to qualify to be used as a redox mediator. However, at higher scan rates evidence of adsorption on the bismuth electrodes was observed and AC voltammetry indicated the simple cyclic voltammogram hides a more complex reduction process.

Impedance spectra were also collected on this compound but the quality of the spectra was not good enough to be used for detailed kinetic studies and ruthenium hexaammine was the preferred choice.

7.1.3 Cobaltocenium

Cyclic voltammetry was used to study the $\text{CoCp}_2^+/\text{CoCp}_2$ couple in AN/TBAF₆. The peak current ratio was found to be far less than unity just as the potential peak separation was about 130 mV. From these findings therefore, the $\text{CoCp}_2^+/\text{CoCp}_2$ redox couple falls short of being recommended as a reference system at Bi based on the conditions for a one-electron transfer process. Bismuth electrodes were however used here successfully to confirm the quasi-reversible behaviour of cobaltocenium.

Estimates of standard rate constants (k^0) were made from electrochemical impedance spectroscopy (EIS) measurements but the apparent values of the rate constant varied with concentration. The highest value of $1.39 \times 10^{-3} \text{ cm s}^{-1}$ was observed for the 2 mM concentration and the lowest value of $2.59 \times 10^{-4} \text{ cm s}^{-1}$ for the 10 mM concentration. Therefore the potential dependence of the rate of electron transfer in this compound cannot be reliably measured at bismuth electrodes and the electron transfer process appears more complex than an outer sphere reaction. The

decrease in apparent rate constant with concentration suggests an electrode fouling effect due to adsorbed reaction products.

7.1.4 Methyl viologen

Although methyl viologen has been previously studied¹⁹ in acetonitrile, its electrochemical behavior in aqueous media was not satisfactory. Cyclic voltammetric data showed failure of the plot of peak current against square root of scan rate to meet the standard criterion of a straight line for freely diffusing molecules. The symmetric shape of the reduction peak and the dependence of the impedance spectroscopy on concentration suggest strong adsorption of the products at Bi. There were also obvious signs of dimerization of the monocation MV^+ as the product was observed to be irreversible and therefore electro-inactive.

7.1.5 Ruthenium(III) hexaammine²⁰⁴

The electrode kinetics of the reduction of $Ru(NH_3)_6^{3+}$ at polycrystalline Bi electrodes in aqueous solution have been analysed by impedance spectroscopy. The rates were much slower than at Pt electrodes because of the presence of a thin oxide film at potentials in the vicinity of the formal potential of the couple. Differential capacitance and ex-situ photoemission spectra provided evidence for the presence of the thin oxide layer, in the order of 1.5 nm on the Bi surface near the formal potential of -0.217 V vs Ag/AgCl/1 M KCl(aq). Despite the presence of this oxide, reproducible impedance spectra near the formal potential were obtained for Bi/ $Ru(NH_3)_6^{3+}$ that could be analysed using a Randles circuit modified to incorporate a constant phase element.

The value of standard rate constant corrected for diffuse layer effects was $1.47 \pm 0.44 \times 10^{-3} \text{ cm s}^{-1}$. Under the same conditions, impedance spectra for Pt/ $Ru(NH_3)_6^{3+}$ were reversible up to the highest frequencies (10^5 Hz) employed. The voltammetric behaviour of $Ru(NH_3)_6^{3+}$ at Bi is that of an uncomplicated outer-sphere electron transfer and impedance spectra were obtained over a range of dc potentials from -0.1 V to about -0.35 V and at electrolyte concentrations from 0.01 M KCl to 0.5 M KCl(aq).

The charge transfer resistances obtained from the impedance spectra were fitted by a new method in which the regression model allowed estimation of the transfer

coefficients at each dc potential without any a priori assumption about the potential dependence of the transfer coefficient. This procedure may be generally useful for heterogeneous electrode kinetics investigations, because precise values of transfer coefficient (uncertainty 1% or better) are obtained as long as the electrode remains immersed in the electrolyte during the experiment.

The measured transfer coefficients showed clear evidence of diffuse layer effects, but in addition an increase in transfer coefficient at the most negative potentials studied was observed and interpreted in terms of the reduction and thinning of the anodic oxide. Therefore in the reduction of $\text{Ru}(\text{NH}_3)_6^{3+}$ at Bi, the potential dependence of the transfer coefficient can be interpreted in terms of two factors: (i) the well-known diffuse layer contribution arising from the Frumkin correction and (ii) the thinning of the tunnelling barrier due to reduction of the anodic oxide at negative potentials.

7.2 Silver Nanoparticles

The importance of the study conducted on silver nanoparticles (AgNPs) relates to the fate of their release in the environment; AgNPs are now widely employed in many substrates for their antimicrobial activity. However, it is not clear what their eventual fate is nor how much Ag(I), the putative active agent is released. From our experimental findings, it is safe to conclude as follows:

The surface plasmon resonance (SPR) of the AgNP sols was blue-shifted for pure water – AgNPs, suggesting corrosion and reduction in particle size. The SPR peak for $\text{Na}_2\text{SO}_4(\text{aq})$ – AgNPs was red-shifted suggesting aggregation.

Taken together, AFM and DLS data show that the AgNPs aggregate during dialysis and that the mean particle size appears to increase because of this.

However, a more detailed analysis of the DLS and AFM data shows that the size of *individual* nanoparticles generally decreased with time of dialysis.

The dialysis experiment shows the steady release of micromolar [Ag(I)] in the presence of up to 50 mM NaCl(aq) because of corrosion of the AgNPs.

The concentration of chloride in a water sample has little influence on the release of Ag(I) from AgNPs.

Presence of sulphates does not exert significant influence on the release of Ag(I) ions from AgNPs.

7.3 Future Work

The search for a possible replacement for mercury electrodes in electrochemical studies has not been concluded, and in consideration of the environmentally benign nature of bismuth, investigations at this semi-metal electrode surface could still be carried out on the aforementioned redox couples; with a variation of the experimental conditions and analytical techniques.

There are other redox couples that have not been studied at bismuth and published in the literature. These could form virgin areas of research, with the hope to replacing mercury electrodes with their potential toxicity.

In Nigeria where I am expected to put the knowledge and skills acquired in this training into practice, water treatment and purification is still a major challenge. Future work in this regard will involve the application of silver nanoparticles in the treatment and purification of potable drinking water. Research will also be conducted to find the suitability of other metal nanoparticles in water treatment, with emphasis on cost and effects on the environment upon discharge.

References.

1. Economou, A. Bismuth-film electrodes: recent developments and potentialities for electroanalysis. *Trends in Analytical Chemistry* **24**(2005).
2. Scanvara, I., Prior, C., Hocevar, S.B. & Wang, J. A Decade with Bismuth Film Electrodes in Electroanalysis. *Electroanalysis* **22**, 1405-1420 (2010).
3. Jaimez, J.B., Joya, M.R. & Ortega, J.B. Bismuth electrodes, an alternative in stripping voltammetry. *Journa of Physics : Conference series* **466**, 1-4 (2013).
4. Wang, J., Lu, J., Kirgoz, U.A., Hocevar, S.B. & Ogorevc, B. Insights into the anodic stripping voltammetric behaviour of bismuth film electrodes. *Analytica Chimica Acta* **434**, 29-34 (2001).
5. Jothimuthu, P., Wilson, R. A.,Herren, J. Haynes, E. N.,Heineman, W. R., and Papautsky, I. Lab-on-chip sensor for detection of highly electronegative heavy metals by anodic stripping voltammetry. *Biomed Microdevices* **13**, 695-703 (2011).
6. Rehacek, V., Hotovy, I., Vojs, M. & Mika, F. Bismuth film electrodes for heavy metals determination. *Microsyst Technol* **14**, 491-498 (2008).
7. Wang, J. Stripping Analysis at Bismuth Electrodes: A Review. *Electroanalysis* **17**, 1341-1346 (2005).
8. Zou, Z., Jang, A.,Macknight, E., Wu, P., Do, J., Bishop, P. L., and Ahn, C. H. Environmentally friendly disposable sensors with microfabricated on-chip planar bismuth electrode for *in situ* heavy metal ions measurement. *Sensors and Actuators B: Chemical* **134**, 18-24 (2008).
9. Wang, J. & Lu, J. Bismuth film electrodes for adsorptive stripping voltammetry of trace nickel. *Electrochemistry Communications* **2**, 390-393 (2000).
10. Wang, J., Lu, J., Hocevar, S.B., Farias, P.A.M. & Ogorevc, B. Bismuth -coated carbon electrodes for anodic stripping voltammetry.pdf. *Analytical Chemistry*. **72**, 3218-3222 (2000).
11. Härk, E. & Lust, E. Electroreduction of Hexaamminecobalt(III) Cation on Bi(hkl) Electrodes from Weakly Acidified LiClO₄ Solutions. *Journal of The Electrochemical Society* **153**, 7 (2006).

12. Pauliukaitė, R., Hočevár, S.B., Ogorevc, B. & Wang, J. Characterization and Applications of a Bismuth Bulk Electrode. *Electroanalysis* **16**, 719-723 (2004).
13. Vaartnou, M. & Lust, E. Electrical double layer and adsorption of iodide ions at the Bi|acetonitrile interface. *J Solid State Electrochem*, 173-180 (2014).
14. Dal Borgo, S., Jovanovski, V., Pihlar, B. & Hocevar, S.B. Operation of bismuth film electrode in more acidic medium. *Electrochimica Acta* **155**, 196-200 (2015).
15. Hutton, E.A., Ogorevc, B., Hocevar, S. B., Weldon, F., Smith, M. R., and Wang, J. An introduction to bismuth film electrode for use in cathodic electrochemical detection. *Electrochemistry Communications* **3**, 707-711 (2001).
16. Sá, É.S., da Silva, P.S., Jost, C.L. & Spinelli, A. Electrochemical sensor based on bismuth-film electrode for voltammetric studies on vitamin B2 (riboflavin). *Sensors and Actuators B: Chemical* **209**, 423-430 (2015).
17. Serrano, N., Alberich, A., Diaz-Cruz, J.M., Arino, C. & Esteben, M. Coating methods, modifiers and applications of bismuth screen-printed electrodes. *Trends in Analytical Chemistry* **46**, 15-29 (2013).
18. Isaacson, R.T. & Williams, G.A. Alfvén-Wave Propagation in Solid-State Plasmas. III. Quantum Oscillations of the Fermi Surface of Bismuth. *Physical Review* **185**, 682-688 (1969).
19. Cook, S.K. & Horrocks, B.R. Heterogeneous Electron Transfer Rates for the Reduction of Viologen Derivatives at Platinum and Bismuth Electrodes in Acetonitrile. *ChemElectroChem* **3**, 1-13 (2016).
20. Smith, G.E., Baraff, G.A. & Rowell, J.M. Effective g Factor of Electrons and Holes in Bismuth. *Physical Review* **135**, A1118-A1124 (1964).
21. Lust, K., Vaartnou, M. & Lust, E. Adsorption of anions on bismuth single crystal plane electrodes from various solvents. *Journal of Electroanalytical Chemistry* **532**(2002).
22. Lust, K., Vaartnou, M. & Lust, E. Adsorption of halide anions on bismuth single crystal plane electrodes. *Electrochimica Acta* (2000).
23. Romann, T., Lust, K. & Lust, E. Adsorption of 1,6-hexanediol on Bi single crystal electrodes. *Electrochimica Acta* **52**(2007).

24. Romann, T. & Lust, E. Electrochemical properties of porous bismuth electrodes. *Electrochimica Acta* **55**, 5746-5752 (2010).
25. Vaartnou, M. & Lust, E. Adsorption of iodide ions on bismuth single crystal planes from solutions in ethanol. *Electrochimica Acta* **47**(2001).
26. Vaartnou, M. & Lust, E. Analysis of impedance spectra of the Bi single crystal planes in solutions of LiClO₄ in ethanol. *J. Electroanal. Chem.* **533**(2002).
27. Dehghanzade, M. & Alipour, E. Voltammetric determination of diazepam using a bismuth modified pencil graphite electrode. *Anal. Methods* **8**, 1995-2004 (2016).
28. Thomberg, T., Nerut, J., Jager, R., Moller, P., Lust, K and Lust, E. The kinetics of electroreduction of peroxodisulfate ions on single crystal cadmium and bismuth electrodes. *J. Electroanal. Chem.* **582**, 130-143 (2005).
29. Mirceski, V., Sebez, B., Jancovska, M., Ogorevc, B. & Hocevar, S.B. Mechanisms and kinetics of electrode processes at bismuth and antimony and bare glassy carbon surfaces under square-wave anodic stripping voltammetry. *Electrochimica Acta* **105**, 254-260 (2013).
30. Jäger, R., Hark, E., Moller, P., Nerut, J., Lust, K. and Lust, E. The kinetics of electroreduction of hexaamminecobalt(III) cation on Bi planes in aqueous HClO₄ solutions. *Journal of Electroanalytical Chemistry* **566**, 217-226 (2004).
31. Hutton, E. A., Hocevar, S. B., Mauko, L., Ogorevc, B. Bismuth film electrode for anodic stripping voltammetric determination of tin. *Analytica Chimica Acta* **580**, 244-250 (2006).
32. Sopha, H., Baldrianova, L., Tesarova, E., Grinciene, G., Weidlich, T., Svancara, I and Hocevar, S. B. A new type of bismuth electrode for electrochemical stripping analysis based on the ammonium tetrafluorobismuthate bulk-modified carbon paste. *Electroanalysis* **22**, 1489-1493 (2010).
33. Scanvara, I., Baldrianova, L., Tesarova, E., Hocevar, S. B., Elsucarry, S. A. A., Economou, A., Sotiropoulos, S., Ogorevc, B. and Vytras, K. Recent advances in anodic stripping voltammetry with Bismuth-modified carbon paste electrodes. *Electroanalysis* **18**, 177-185 (2006).

34. Hocevar, S.B., Ogorevc, B., Wang, J. & Pihlar, B. A study on operational parameters for advanced use of bismuth film electrode in anodic stripping voltammetry. *Electroanalysis* **14**, 1707-1712 (2002).
35. Krolicka, A. & Bobrowski, A. Bismuth film electrode for adsorptive stripping voltammetry-electrochemical and microscopic study. *Electrochemistry Communications* **6**, 99-104 (2004).
36. Sharifian, P. & Aliakbar, A. Determination of Se(IV) as a 5-nitropiazselenol complex by adsorptive stripping voltammetry at an *in situ* plated bismuth film electrode. *Analytical Methods* **7**, 4321-4327 (2015).
37. Castaneda, M.T., Perez, B., Pumera, M., Valle, M., d., Merkoci, A. and Alegret, S.. Sensitive stripping voltammetry of heavy metals by using a composite sensor based on a built-in bismuth precursor. *Analyst* **130**, 971-976 (2005).
38. Hocevar, S.B., Svancara, I., Vytras, K. & Ogorevc, B. Novel electrode for electrochemical stripping analysis based on carbon paste modified with bismuth powder. *Electrochimica Acta* **51**, 706-710 (2005).
39. Jang, A., Zou, Z., Macknight, E., Wu, P. M., Kim, I. S., Ahn, C. H. and Bishop, P. L. Development of a portable analyzer with polymer lab-on-chip (LOC) for continuous sampling and monitoring of Pb(II). *Water Science and Technology* **60**, 2889-2896 (2009).
40. Legeai, S., Soropogui, K., Cretinon, M., Vittori, O., Oliveira, A. H. D., Barbier, F. and Loustalot, M. F. G . Economic bismuth-film microsensor for anodic stripping analysis of trace metals using differential pulse voltammetry. *Anal Bioanal Chem* **383**, 839-847 (2005).
41. Rosolina, S.M., Carpenter, T.S. & Xue, Z. Bismuth- based disposable sensor for the detection of hydrogen sulfide gas. *Anal. Chem.* **88**, 1553-1558 (2016).
42. Wang, J. *Analytical Electrochemistry.*, (VCH Publishers., New York, 1994).
43. Brett, C.M. & Brett, A.M.O. *Electrochemistry. Principles, Methods and Applications.*, (Oxford University Press., New York, 1994).
44. Bard, A.J. & Faulkner, L.R. *Electrochemical Methods: Fundamentals and Applications.*, (John Wiley and Sons., New York, 2001).
45. Stern, O.Z. *Electrochem.* **30**(1924).

46. Grahame, D.C. *Chem. Rev.* **41**(1947).
47. Bockris, J.O.M., Devenathan, M.A.V. & Muller, K. *Proc. Roy. Soc.* **A274**(1963).
48. Rieger, P.H. *Electrochemistry*, (Chapman and Hall., New York, 1994).
49. IUPAC. IUPAC Compendium of Chemical Technology (2014).
50. Bogotsky, V.S. *Fundamentals of Electrochemistry*, (John Wiley and Sons, New York, 2006).
51. Delahay, P. *Double Layer and Electrode Kinetics*, (John Wiley and Sons, Inc., New York, 1965).
52. Marcus, R.A. Electron transfer reactions in chemistry. Theory and experiment. *Reviews of Modern Physics* **65**, 599-610 (1993).
53. Endicott, J.F. & Taube, H. Kinetics of some outer-sphere electron-transfer reactions. *J. Am. Chem. Soc.* **86**, 1686-1691 (1964).
54. Bard, A.J., Inzelt, G. & Scholz, F. *Electrochemical Dictionary*. (Springer., New York., 2012).
55. Marcus, R.A. On the theory of oxidation-reduction reactions involving electron transfer. V. Comparison and properties of electrochemical and chemical rate constants. *J Phys Chem* **67**, 853-857 (1963).
56. Souza, D.D., Codognoto, L., Machado, S.A.S. & Avaca, L.A. Electroanalytical Determination of the Herbicide Paraquat in Natural water and Commercial Tea Samples with Gold Electrodes Obtained from Recordable Compact Disc. *Electroanalysis*, 331-341 (2004).
57. Yoon, K.B. & Kochi, J.K. Observation of superoxide electron transfer with viologens by immobilization in zeolite. *J. Am. Chem. Soc.* **110**, 6586-6588 (1988).
58. Bockman, T.M. & Kochi, J.K. Isolation and Oxidation-Reduction of Methylviologen Cation Radicals. Novel Disproportionation in charge-Transfer Salts by X-ray Crystallography. *J. Org. Chem.* **55**, 4127-4135 (1990).
59. Walcarius, A. & Lamberts, L. Square wave voltammetric determination of paraquat and diquat in aqueous solution. *J. Electroanal. Chem.* **406**, 59-68 (1996).

60. Barroso-Fernandez, B., Lee-Alvarez, M.T., Seliskar, C.J. & Heineman, W.R. Electrochemical behaviour of methyl viologen at graphite electrodes modified with Nafion sol-gel composite. *Analytica Chimica Acta* **370**, 221-230 (1998).
61. Melo, L.C., Salazar-Banda, G. R., Machado, S. A. S., Lima-Neto, P. d., Souza, D. D. and Correia, A. N. A simple and sensitive detection of diquat herbicide using a dental amalgam electrode. A comparison using the chromatographic technique. *Talanta* **79**, 1216-1222 (2009).
62. Chang, H.C., Cheng, T.J. & Chen, R.J. EQCM Studies of Paraquat on Gold Electrode Modified with Electropolymerized Film. *Electroanalysis* **10**(1998).
63. Rueda, R.G.C. M., Alden, J. A. and Prieto, F. Impedance voltammetry of electro-dimerization mechanisms: Application to the reduction of the methyl viologen di-cation at mercury electrodes and aqueous solutions. *Journal of Electroanalytical Chemistry* **443**, 227-235 (1998).
64. Figueiredo-Filho, L.C.S.d., Santos, V. B. d., Janegitz, B. C., Guerreiro, T. B., Fatibello-Filho, O., Faria, R. C. and Marcolino-Junior, L. H. Differential Pulse Voltammetric Determination of Paraquat Using a Bismuth-Film Electrode. *Electroanalysis* **22**, 1260-1266 (2010).
65. Bechtold, T., Fitz-Binder, C. & Turcanu, A. Electrochemical characteristics and dyeing properties of selected 9,10-anthraquinones as mediators for the indirect cathodic reduction of dyes. *Dyes and Pigments* **87**, 194-203 (2010).
66. Bectold, T., Burtscher, E. & Turcanu, A. Anthraquinones as mediators for the indirect cathodic reduction of dispersed organic dyestuffs. *J. Electroanal. Chem.* **465**, 80-87 (1999).
67. Guidelli, R., Compton, R. G., Feliu, J. M., Gileadi, E., Lipkowski, J., Schmickler, W. and Trasatti, S. Definition of the transfer coefficient in electrochemistry (IUPAC Recommendations 2014). *Pure and Applied Chemistry* **86**(2014).
68. Fultz, M.L. & Durst, R.A. Mediator Compounds for the Electrochemical Study of Biological Redox systems: A Compilation. *Analytica Chimica Acta* **140**, 1-18 (1982).

69. Meckstroth, M.L., Norris, B.J. & Heineman, W.R. Mediator-titrants for Thin-Layer Spectroelectrochemical measurement of biocomponent U^o and n values. *Bioelectrochemistry and Bioenergetics* **8**, 63-70 (1981).
70. Bechtold, T. & Turcanu, A. Iron-complexes of bis(2-hydroxyethyl)-amino-compounds as mediators for the indirect reduction of dispersed vat dyes – Cyclic voltammetry and spectroelectrochemical experiments. *J. Electroanal. Chem.* **591**, 118-126 (2006).
71. Bailey, S.I. & Ritchie, I.M. A cyclic voltammetric study of the aqueous electrochemistry of some quinones. *Electrochimica Acta* **30**, 3-12 (1985).
72. Blackburn, R.S. & Harvey, A. Green Chemistry Methods in Sulfur Dyeing. Application of Various Reducing D-sugars and Analysis of Optimum Redox Potential. *Environmental Science and Technology*. **38**, 4034-4039 (2004).
73. Bechtold, T. & Turcanu, A. Electrochemical Vat Dyeing Combination of an Electrolyzer with a Dyeing Apparatus. *Journal of The Electrochemical Society* **149**, D7 (2002).
74. Bechtold, T., Burstcher, E., Gmeiner, D. & Bobleter, O. The redox-catalysed reduction of dispersed organic compounds. Investigations on the electrochemical reduction of insoluble organic compounds in aqueous solution. *J. Electroanal. Chem.* **306**, 169-183 (1991).
75. Gritzner, G. & Kuta, J. Recommendations on reporting electrode potentials in non-aqueous solvents. *Pure and Applied Chemistry* **56**, 461-466 (1984).
76. Stojanovic, R.S. & Bond, A.M. Examination of conditions under which the reduction of the cobaltocenium cation can be used as a standard voltammetric reference process in organic and aqueous solvents. *Anal. Chem.* **65**, 56-64 (1993).
77. Rogers, E.I., Silvester, D. S., Poole, D. L., Aldous, L., Hardcare, C. and Compton, R. G. Voltammetric characterization of the ferrocene-ferrocenium and cobaltocenium-cobaltocene redox couples in RTILs. *J. Phys. Chem. C* **112**, 2729-2735 (2008).
78. Lewandowski, A., Waligora, L. & Galinski, M. Electrochemical Behavior of Cobaltocene in Ionic Liquids. *J Solution Chem* **42**, 251-262 (2013).

79. Sukardi, K.S., Zhang, J., Burgar, I., Horne, D. M., Hollenkamp, F. A., MacFarlane, R. D. and Bond, M. A. Prospects for a widely applicable reference potential scale in ionic liquids based on ideal reversible reduction of the cobaltocenium cation. *Electrochemistry Communications* **10**, 250-254 (2008).
80. Waligora, L., Lewandowski, A. & Gritzner, G. Electrochemical studies of four organometallic redox couples as possible reference redox systems in 1-ethyl-3-methylimidazolium tetrafluoroborate. *Electrochimica Acta* **54**, 1414-1419 (2009).
81. Keeler, J. & Wothers, P. *Structure and Reactivity: An Integrated Approach*, (Oxford University Press, New York, 2008).
82. Ji, X., Chevallier, F.G., Clegg, A.D., Buzzeo, M.C. & Compton, R.G. The electrochemical reduction of aqueous hexamminecobalt(III): Studies of adsorption behaviour with fast scan voltammetry. *Journal of Electroanalytical Chemistry* **581**, 249-257 (2005).
83. Hromadova, M. & Fawcett, W.R. Studies of Double-Layer Effects at Single-Crystal Gold Electrodes. 1. The Reduction Kinetics of Hexaamminecobalt(III) Ion in Aqueous Solutions. *J Phys Chem A* **104**, 4356-4363 (2000).
84. Mech, K., Żabiński, P., Kowalik, R. & Fitzner, K. EQCM, SEC and voltammetric study of kinetics and mechanism of hexaamminecobalt(III) electro-reduction onto gold electrode. *Electrochimica Acta* **81**, 254-259 (2012).
85. Lincoln, S.F. Mechanistic Studies of Metal Aqua Ions: A Semi-Historical Perspective. *Helv. Chim. Acta* **88**, 23 (2005).
86. Bard, A. J. and Mirkin, M. V. Simple Analysis of Quasi-Reversible Steady-State Voltammograms. *Analytical Chemistry* **64**, 5 (1992).
87. Iwasita, T., Schmiskler, W. and Schultze J. W. The Influence of the Metal on the Kinetics of Outer- Sphere Redox Reactions. *Ber. Bunsenges. Phys. Chem.* **89**, 5 (1986).
88. Meyer, D.E., Curran, M.A. & Gonzalez, M.A. An examination of silver nanoparticles in socks using screening-level life cycle assessment. *Journal of Nanoparticle Research* **13**, 147-156 (2010).

89. Benn, M.T. & Westerhoff, P. Nanoparticle Silver Released into Water from Commercially Available Sock Fabrics. *Environ. Sci. Technol.* **42**, 4133-4139 (2008).
90. Wilkinson, L.J., White, R.J. & Chipman, J.K. Silver and nanoparticles of silver in wound dressings: a review of efficacy and safety. *J Wound Care* **20**, 543-549 (2011).
91. Maneerung, T., Tokura, S. & Rujiravanit, R. Impregnation of silver nanoparticles into bacterial cellulose for antimicrobial wound dressing. *Carbohydrate Polymers* **72**, 43-51 (2008).
92. Hebeish, A., El-Rafie, M.H., El-Sheikh, M.A., Seleem, A.A. & El-Naggar, M.E. Antimicrobial wound dressing and anti-inflammatory efficacy of silver nanoparticles. *Int J Biol Macromol* **65**, 509-515 (2014).
93. Udapudi, B., Naik, P., Savadatti, S.T., Sharma, R. & Balgi, S. Synthesis and characterization of silver nanoparticles. *International Journal of Pharmacy and Biological Sciences* **2**, 10-14 (2012).
94. Odzak, N., Kistler, D., Behra, R. & Sigg, L. Dissolution of metal and metal oxide nanoparticles in aqueous media. *Environmental Pollution* **191**, 132-138 (2014).
95. Mavani, K. & Shah, M. Synthesis of Silver Nanoparticles by using Sodium Borohydride as a Reducing Agent. *International Journal of Engineering Research and Technology* **2**(2013).
96. Sharma, V.K., Yngard, R.A. & Lin, Y. Silver nanoparticles: green synthesis and their antimicrobial activities. *Adv Colloid Interface Sci* **145**, 83-96 (2009).
97. Kaegi, R., Voegelin, A., Sinnet, B., Zuleeg, S., Hagendorfer, H., Burkhardt, M. and Siegrist, H. Behavior of metallic silver nanoparticles in a pilot wastewater treatment plant. *Environ Sci Technol* **45**, 3902-3908 (2011).
98. Dankovich, T.A. & Gray, D.G. Bactericidal paper impregnated with silver nanoparticles for point-of-use water treatment. *Environ Sci Technol* **45**, 1992-1998 (2011).

99. Kim, J.S., Kuk, E., Yu, K. N., Kim, J. H., Park, S. J., Lee, H. J., Kim, S. H., Park, Y. K., Park, Y. H., Hwang, C. Y., Kim, Y. K., Lee, Y. S., Jeong, D. H. and Cho, M. H. Antimicrobial effects of silver nanoparticles. *Nanomedicine* **3**, 95-101 (2007).
100. Suchomel, P., Kvittek, L., Panacek, A., Pucek, R., Hrbac, J., Vecerova, R. and Zboril, R. Comparative study of antimicrobial activity of AgBr and Ag nanoparticles (NPs). *Plos One*, 1-15 (2015).
101. Siller, L., Lemloh, M. L., Piticharoenphun, S., Mendis, B. G., Horrocks, B. R., Brummer, F. and Medakovic, D. Silver nanoparticle toxicity in sea urchin *Paracentrotus lividus*. *Environ Pollut* **178**, 498-502 (2013).
102. Li, X., Schirmer, K., Bernard, L., Sigg, L., Pillai, S. and Behra, R. Silver nanoparticle toxicity and association with the alga *Euglena gracilis*. *Environ. Sci.: Nano* **2**, 594-602 (2015).
103. Kittler, S., Greulich, C., Diendorf, J., Köller, M. & Epple, M. Toxicity of Silver Nanoparticles Increases during Storage Because of Slow Dissolution under Release of Silver Ions. *Chemistry of Materials* **22**, 4548-4554 (2010).
104. Tschulik, K., McAuley, C.B., Toh, H.S., Stuart, E.J.E. & Compton, R.G. Electrochemical studies of silver nanoparticles: a guide for experimentalists and a perspective. *Phys. Chem. Chem. Phys.* **16**, 616-623 (2014).
105. Liu, J., Yu, S., Yin, Y. & Chao, J. Methods for separation, identification, characterization and quantification of silver nanoparticles. *Trends in Analytical Chemistry* **33**, 95-106 (2012).
106. Fabrega, J., Luoma, S.N., Tyler, C.R., Galloway, T.S. & Lead, J.R. Silver nanoparticles: behaviour and effects in the aquatic environment. *Environ Int* **37**, 517-531 (2011).
107. Navarro, E., Piccapietra, F., Wagner, B., Marconi, F., Kaegi, R., Odzak, N., Sigg, L. and Behra, R. Toxicity of silver nanoparticles to chlamydomonas. *Environ. Sci. Technol.* **42**, 8959-8964 (2008).
108. Taylor, M.M.C., Kroll, A., Read, D. S., Svendsen, C., Crossley, A.. Toxic interactions of different silver forms with fresh water algae and cyanobacteria and their effects on mechanistic endpoints and the production of extracellular polymeric substances. *Environmental Science Nano* **3**, 396-408 (2016).

109. Beer, C., Foldbjerg, R., Hayashi, Y., Sutherland, D.S. & Autrup, H. Toxicity of silver nanoparticles - nanoparticle or silver ion? *Toxicol Lett* **208**, 286-292 (2012).
110. Piao, M.J., Kang, K. A., Lee, I. K., Kim, H. S., Kim, S., Choi, J. Y., Choi, J. and Hyun, J. W.. Silver nanoparticles induce oxidative cell damage in human liver cells through inhibition of reduced glutathione and induction of mitochondria-involved apoptosis. *Toxicol Lett* **201**, 92-100 (2011).
111. Hackenberg, S., Scherzed, A., Kessler, M., Hummel, S., Technau, A., Froelich, K., Ginzkey, C., Koehler, C., Hagen, R. and Kleinsasser, N. Silver nanoparticles: evaluation of DNA damage, toxicity and functional impairment in human mesenchymal stem cells. *Toxicol Lett* **201**, 27-33 (2011).
112. Chatterjee, N. & Walker, G.C. Mechanisms of DNA Damage, Repair, and Mutagenesis. *Environmental and Molecular Mutagenesis* **58**, 235-263 (2017).
113. Durán, N., Durán, M., de Jesus, M.B., Seabra, A.B., Fávaro, W.J., Nakazato, G. Silver nanoparticles: A new view on mechanistic aspects on antimicrobial activity. *Nanomedicine: Nanotechnology, Biology, and Medicine* **12**, 789–799 (2016).
114. Marambio-Jones, C. & Hoek, E.M.V. A review of the antibacterial effects of silver nanomaterials and potential implications for human health and the environment. *J Nanopart Res* **12**, 1531–1551 (2010).
115. Sinha, R.P. & Häder, D.-P. UV-induced DNA damage and repair: a review. *Photochem. Photobiol. Sci.*, **1**, 225–236 (2002).
116. Geranio, L., Heuberger, M. & Nowack, B. The Behaviour of silver nanotextiles during washing. *Environ. Sci. Technol.* **43**(2009).
117. Solomon, S.D., Bahadory, M., Jeyarajasingam, A.V., Rutkowsky, S.A. & Boritz, C. Synthesis and study of silver nanoparticles. *Journal of Chemical Education* **84**, 322-325 (2007).
118. Lee, P.C. & Meisel, D. Adsorption and surface-enhanced Raman of dyes on silver and gold sols. *Journal of Physical Chemistry* **86**, 3391-3395 (1982).
119. Kuyper, A.C. The Oxidation of Citric Acid. *J. Am. Chem. Soc.* **55**, 1722-1727 (1933).

120. Brownson, D.A.C. & Banks, C.E. *The Handbook of Graphene Electrochemistry*, (Springer, London, 2014).
121. Brillas, E., Garrido, J.A., Rodriguez, R.M. & Domenech, J. A Cyclic Voltammetry Experiment Using a Mercury Electrode. *Journal of Chemical Education* **64**, 189-191 (1987).
122. Kissinger, P.T. & Heineman, W.R. Cyclic Voltammetry. *Journal of Chemical Education* **60**, 702-706 (1983).
123. Evans, D.H., O'Connell, K.M., Peterson, R.A. & Kelly, M.J. Cyclic Voltammetry. *Journal of Chemical Education* **60**, 290-293 (1983).
124. Dickinson, E.J.F., Lim-Peterson, J.G., Rees, N.V. & Compton, R.G. How much supporting electrolyte is required to make a cyclic voltammetry experiment quantitatively "diffusional"? A theoretical and experimental investigation. *J Phys Chem C* **113**, 11157-11171 (2009).
125. Instruments, G. *Basics of Electrochemical Impedance Spectroscopy*, Vol. 2016 (2005).
126. Cogger, N.D. & Evans, N.J. *An Introduction to Electrochemical Impedance Measurement*. (1999).
127. Electronics, P. *XPS/ESCA*. Vol. 2017 (Chanhasen, 2017).
128. London, Q.M.U. *Photoelectron Spectroscopy*. Vol. 2016 (2013).
129. Naukim, A.V., Kraut-Vass, A., Gaarenstroom, S.W. & Powell, C.J. NIST X-ray photoelectron Spectroscopy Standard Reference Database 20. (ed. Material Measurement Laboratory, U.S.D.o.C.) (Measurement Services, Division of the National Institute of Standards and Technology, 2012).
130. Horiba. *Dynamic Light Scattering for Particle size Analysis*. [www.horiba.com/uk/scientific/products/.../dynamic light stattering](http://www.horiba.com/uk/scientific/products/.../dynamic%20light%20stattering). Accessed 01 May, 2016.
131. LS Instruments. *Dynamic Light Scattering: Measuring the Particle size Distribution*. www.lsinstruments.ch/technology/dynamic. Accessed 3rd February, 2017.

132. West University of St. Louis. Dynamic Light Scattering.
<http://www.nano.wustl.edu/doc/Instrument%20Manuals%20and%20Protocols/DLS%20Final>. Dynamic Light Scattering. in *Nano Research Facility*. Accessed 18th April, 2016.
133. Mai, W. Fundamental Theory of atomic Force Microscopy.
<http://www.nanoscience.gatech.edu/zlwang/research/afm>. Accessed 21 April, 2016.
134. Basics of Atomic Force Microscopy.,
<http://www.eng.utah.edu/lzang/images/lecture>. Accessed 02 May, 2016.
135. Shaw, D.J. *Introduction to Colloid and Surface Chemistry*, (Butterworth-Heinemann Ltd, London, 1992).
136. Kissinger, P.T. & Heineman, W.R. *Laboratory Techniques in Electroanalytical Chemistry.*, (Marcel Dekker Inc., New York, 1996).
137. Scholz, F.E. (ed.) *Electroanalytical Methods. Guide to Experiments and Applications.*, (Springer., New York., 2002).
138. McGilp, J.F., Weighton, P. & McGuire, E.J. The $N_{6,7}O_{4,5}O_{4,5}$ Auger spectra of thallium, lead and bismuth. *Journal of Physics C: Solid State Physics* **10**, 3445-3460 (1977).
139. Ley, L., Kowalczyk, S.P., McFeely, F.R., Pollak, R.A. & Shirley, D.A. X-Ray Photoemission from Zinc: Evidence for Extra-Atomic Relaxation via Semilocalized Excitons. *Physical Review B* **8**, 2392-2402 (1973).
140. Morgan, W.E., Wazer, J.R.V. & Stec, W.J. Inner-Orbital Photoelectron Spectroscopy of the Alkali Metal halides, Perchlorates, Phosphates and Pyrophosphates. *Journal of American Chemical Society* **95**, 751-755 (1973).
141. Attekum, P. M. Th M. van & Trooster., J.M. Bulk- and surface-plasmon-loss intensities in photoelectron, Auger, and electron-energy-loss spectra of Mg metal. *Physical Review B* **20**, 2335-2340 (1979).
142. Kumar, P.S.A., Mahamuni, S., Nigaveka, A.S. & Kulkarni, S.K. Reactivity and surface modification at a Bi/Bi₂Sr₂CaCu₂O₈ interface. *Physica C* **201**, 145-150 (1992).

143. Powell, C.J. Recommended Auger parameters for 42 elemental solids. *Journal of Electron Spectroscopy and Related Phenomena* **185**, 1-3 (2012).
144. Shalvoy, R. B., Fisher, G. B. & Stiles., P.J. Bond ionicity and structural stability of some average-valence-five materials studied by x-ray photoemission. *Physical Review B* **15**, 1680-1697 (1977).
145. Nyholm, R., Berndtsson, A. & Martensson, N. Core level binding energies for the elements Hf to Bi(Z= 72-83). *Journal of Physics C: Solid State Physics* **13**, L1091-L1096 (1980).
146. Dharmadhikari, V.S., Sainkar, S.R., Badrinarayan, S. & Goswami, A. Characterisation of Thin Films of Bismuth Oxide by X-Ray Photoelectron Spectroscopy. *Journal of Electron Spectroscopy and Related Phenomena*. **25**, 181-189 (1982).
147. Afsin, B. & Roberts, M.W. Formation of an oxy-chloride overlayer at a Bi(0001) surface. *Spectroscopy Letters* **1**(1994).
148. Nefedov, V.I. & Salyn, Y.V. A comparison of Different Spectrometers and Charge Corrections used in X-Ray Photoelectron Spectroscopy. *Journal of Electron Spectroscopy and Related Phenomena*. **10**(1977).
149. Debies, T.P. & Rabalais, J.W. X-Ray Photoelectron Spectra and Electronic Structure of Bi_2X_3 (X= O, S, Se, Te). *Chemical Physics*. **20**, 277-283 (1977).
150. Morgan, W.E., Stec, W.J. & Wazer, J.R.V. Inner-Orbital Binding-Energy Shifts of Antimony and Bismuth Compounds. *Inorganic Chemistry* **12**, 953-955 (1973).
151. Schuhl, Y., Baussart, S., Delobel, R., Brass, M. L., Leroy, J., Gengembre, L. G., and Grimblot, J. Study of Mixed-oxide Catalysts Containing Bismuth, Vanadium and Antimony. Preparation, Phase Composition, Spectroscopic Characterization and Catalytic Oxidation of Propene. *Journal of Chemical Society. Faraday Transaction I*. **79**, 2055-2069 (1983).
152. Tanuma, S., Powell, C.J. & Penn, D.R. Calculation of electron inelastic mean free paths (IMFPs) VII. Reliability of the TPP-2M IMFP predictive equation. *Surface and Interface Analysis* **35**, 268-275 (2003).

153. Tanuma, S., Powell, C.J. & Penn, D.R. Calculations of electron inelastic mean free paths. IX. Data for 41 elemental solids over the 50 eV to 30 keV range. *Surface and Interface Analysis* **43**, 689-713 (2011).
154. Williams, D.E. & Wright, G.A. Nucleation and growth of anodic oxide films on bismuth-1. Cyclic voltammetry. *Electrochimica Acta* **21**, 1009-1019 (1976).
155. Grubac, Z. & Metikos-Hukovic, M. Nucleation and growth of anodic oxide films on bismuth. *Electrochimica Acta* **43**, 3175-3181 (1998).
156. Kuchler, R., Steinke, L., Daou, R., Brando, M., Behnia, K. and Steglich, F. Thermodynamic Evidence for the Valley-dependent Density of States in Bulk Bismuth. *Nature Materials Letters*, 6 (2014).
157. Wren, A.G., Phillips, R.W. & Tolentino, L.U. Surface Reactions of Chlorine Molecules and Atoms with Water and Sulfuric Acid at Low Temperatures. *Journal of Colloid and Interface Science* **70**, 544-557 (1979).
158. Park, C. D., Choi, W. Y. & Kang., H. Ion and X-ray induced decomposition of alkali halates. A comparative study of the radiation induced reaction paths. *Radiation Effects and Defects in Solids* **115**, 65-72 (1990).
159. Kadono, K., Kinugawa, K. & Tanaka, H. X-ray photoelectron spectroscopy of ZnCl₂ based glasses. *Physics and chemistry of glasses* **35**, 59-64 (1994).
160. Kohiki, S., Ohmura, T. & Kusao, K. Appraisal of a New Charge Correction Method in X-Ray Photoelectron Spectroscopy. *Journal of Electron Spectroscopy and Related Phenomena*. **31**(1983).
161. Crist, B.V. KBr Crystal: Cleaved in Air. *Surface Science Spectra* **1**, 292 (1992).
162. Sharma, J. & Iqbal, Z. X-ray Photoelectron Spectroscopy of Brominated (SN)_x and S₄N₄. *Chemical Physics Letters*. **56**, 373-376 (1978).
163. Riddick, J.A., Bunger, W.B. & Sakano., T.K. *Organic Solvents: Physical Properties and Methods of Purification*, (Wiley-Interscience, New York, 1986).
164. Monk, P.M.S., Turner, C. & Akhtar, S.P. Electrochemical behaviour of methyl viologen in a matrix of paper. *Electrochimica Acta* **44**, 4817-4826 (1999).

165. Olmstead, M.L., Hamilton, R.G. & Nicholson, R.S. Theory of cyclic voltammetry for a dimerization reaction initiated electrochemically. *Analytical Chemistry*. **41**, 260-267 (1969).
166. Xiao, L., Wildgoose, G.G. & Compton, R.G. Investigating the voltammetric reduction of methylviologen at gold and carbon based electrode materials. Evidence for a surface bound adsorption mechanism leading to electrode 'protection' using multi-walled carbon nanotubes. *New Journal of Chemistry* **32**, 1628-1633 (2008).
167. Haque, M.A., Rahman, M.M. & Susan, M.A.B.H. Aqueous Electrochemistry of Anthraquinone and Its Correlation with Dissolved States of a Cationic Surfactant. *J Solution Chem* **40**, 861-875 (2011).
168. Lewandowski, A., Waligora, L. and Galinski, M. Electrochemical Behaviour of Cobaltocene in Ionic Liquids. *J Solution Chem* **42**, 251-262 (2013).
169. Tsierkezos, N.G. Electron transfer kinetics for the cobaltocene (+1/0) couple at platinum disk electrode in acetonitrile/dichloromethane binary solvent system. *Journal of Molecular Liquids* **138**, 1-8 (2008).
170. Chemistry, A. B. C. EIS Analyzer.
<http://www.abc.chemistry.bsu.by/vi/analyzer/program/program.htm>, Accessed on 26th June, 2017.
171. Schmickler, W. and Santos, E. *Interfacial Electrochemistry*, (Springer, Berlin, 2010).
172. Mohilner, D.M. Double-Layer Effects in the Kinetics of Heterogeneous Electron Exchange Reactions. *J Phys Chem* **73**, 2652-2662 (1969).
173. McAuley, C.B., Katelhon, E., Barnes, E. O., Compton, R. G., Laborda, E. & Molina, A. Recent Advances in Voltammetry. *ChemistryOpen* **4**, 224-260 (2015).
174. Gavaghan, D.J. & Feldberg, S.W. Extended electron transfer and the Frumkin correction. *Journal of Electroanalytical Chemistry* **491**, 103-110 (2000).
175. E. J. F. Dickinson, R.G.C. Influence of the diffuse double layer on steady-state voltammetry. *Journal of Electroanalytical Chemistry* **661**, 198-212 (2011).

176. White, R.J. & White, H.S. Electrochemistry in Nano-Wide Electrochemical Cells. *Langmuir* **24**, 2850-2855 (2008).
177. Liu, Y., He, R., Zhang, Q. & Chen, S. Theory of Electrochemistry for Nanometer-Sized Disk Electrodes. *J. Phys. Chem. C* **114**, 10812-10822 (2010).
178. Halford, J.H. & Hacker, H. Dielectric Properties of Bismuth Trioxide Thin Films. *Thin Solid Films* **4**, 265-279 (1969).
179. World Health Organization. Silver in drinking-water. Background document for development of WHO guidelines for drinking-water quality., Vol. 2, 2nd ed. (WHO, Geneva, 2003).
180. Sohn, E.K., Johari, S. A., Kim, T. G., Kim, J. K., Kim, E., Lee, J. H., Chung, Y. S. and Yu, I. J. Aquatic Toxicity Comparison of Silver Nanoparticles and Silver Nanowires. *Biomed Res Int* **2015**, 893049 (2015).
181. Aghari, S., Johari, S. A., Lee, J. H., Kim, Y. S., Jeon, Y. B., Choi, H. J., Moon, M. C. and Yu, I. J. Toxicity of various silver nanoparticles compared to silver ions in *Daphnia magna*. *Journal of Nanobiotechnology* **10**, 1-11 (2012).
182. Bratsch, S.G. Standard Electrode Potentials and Temperature Coefficients in Water at 298.15 K. *Journal of Physical Chemistry Reference Data* **18**, 1-21 (1989).
183. Ghosh, S.K. & Pal, T. Interparticle Coupling Effect on the Surface Plasmon Resonance of Gold Nanoparticles: From Theory to Applications. *Chemical Reviews* **107**, 4797-4862 (2007).
184. Hu, L., Hu, S., Guo, L., Tang, T. & Yang, M. Optical and electrochemical detection of biothiols based on aggregation of silver nanoparticles. *Analytical Methods* **8**, 4903-4907 (2016).
185. Khan, Z., Hussain, J.I., Kumar, S., Hashmi, A.A. & Malik, M.A. Silver Nanoparticles: Green Route, Stability and Effect of Additives. *Journal of Biomaterials and Nanobiotechnology* **02**, 390-399 (2011).

186. Shrivastava, K., Sahu, S., Patra, G.K., Jaiswal, N.K. & Shankar, R. Localized surface plasmon resonance of silver nanoparticles for selective colorimetric detection of chromium in surface water, industrial waste water and vegetable samples. *Analytical Methods* **8**, 2088-2096 (2016).
187. Ijaz Hussain, J., Kumar, S., Adil Hashmi, A. & Khan, Z. Silver Nanoparticles: Preparation, Characterization and Kinetics. *Advanced Materials Letters* **2**, 188-194 (2011).
188. Wang, H., Qiao, X., Chen, J. & Ding, S. Preparation of silver nanoparticles by chemical reduction method. *Colloids and Surfaces A: Physicochem. Eng. Aspects* **256**, 111-115 (2005).
189. Toh, H.S., Jurkschat, K. & Compton, R.G. The Influence of the Capping Agent on the Oxidation of Silver Nanoparticles: Nano-impacts versus Stripping Voltammetry. *Chemistry A European Journal*, 2998-3004 (2015).
190. Espinoza, M.G., Hinks, M.L., Mendoza, A.M., Pullman, D.P. & Peterson, K.I. Kinetics of Halide-Induced Decomposition and Aggregation of Silver Nanoparticles. *The Journal of Physical Chemistry C* **116**, 8305-8313 (2012).
191. Nanda, A. & Saravanan, M. Biosynthesis of silver nanoparticles from *staphylococcus aureus* and its ANTImicrobial activity against MRSA and MRSE. *Nanomedicine: Nanotechnology, Biology, and Medicine* **5**, 452-456 (2009).
192. Trefalt, G. & Borkovec, M. Overview of DLVO Theory. [http://www.colloid.ch/dlvo theory](http://www.colloid.ch/dlvo%20theory), accessed on 6th June, 2017.
193. Pinchuk, A.O. Size-Dependent Hamaker Constant for Silver Nanoparticles. *J. Phys. Chem. C* **116**, 20099-20102 (2012).
194. Fissan, H., Ristig, S., Kaminski, H., Asbach, C. & Epple, M. Comparison of different characterization methods for nanoparticle dispersions before and after aerosolization. *Analytical Methods* **6**, 7324-7334 (2014).
195. Cumberland, S.A. & Lead, J.R. Particle size distributions of silver nanoparticles at environmentally relevant conditions. *J Chromatogr A* **1216**, 9099-9105 (2009).

196. Tomaszewska, E., Soliwoda, K., Kadziola, K., Tkacz-Szczesna, B., Celichowski, G. Cichomski, M., Szmaja, W. and Grobelny, J. Detection Limits of DLS and UV-Vis Spectroscopy in Characterization of Polydisperse Nanoparticles Colloids. *Journal of Nanomaterials* **2013**, 1-10 (2013).
197. Shaw, R. Dynamic Light Scattering Training Achieving Reliable Nanoparticle Sizing. www.atascientific.com.au , accessed on 6th June 2017.(Malvern Instruments, 2017).
198. Pletikapic, G., Zutic, V., Vrcek, I.V. & Svetlicic, V. Atomic force microscopy characterization of silver nanoparticles interactions with marine diatom cells and extracellular polymeric substance. *Journal of Molecular Recognition* **25**, 309-317 (2012).
199. Klapetek, P., Valtr, M., Necas, D., Salyk, O. & Dzik, P. Atomic force microscopy analysis of nanoparticles in non-ideal conditions. *Nanoscale Research Letters* **6**, 1-9 (2011).
200. Wong, C., West, P.E., Oslon, K.S., Mecartney, M.L. & Starostina, N. Tip dilation and AFM capabilities in the characterization of nanoparticles. *JOM: Journal of Minerals, Metals and Materials Society* **59**, 12-16 (2007).
201. Alahmad, A. Preparation and Characterization of Silver Nanoparticles. *Internation Journal of ChemTech Research* **6**, 450-459 (2014).
202. Alahmad, A., Eleoui, M., Falah, A. & Alghorabi, I. Preparation of colloidal silver nanoparticles and structural characterization. *Physical Sciences Research International* **1**, 89-96 (2013).
203. Cloake, S.J., Toh, H. S., Lee, P. T., Salter, C., Johnston, C. and Compton, R. G. Anodic stripping voltammetry of silver nanoparticles: aggregation leads to incomplete stripping. *ChemistryOpen* **4**, 22-26 (2015).
204. Nomor, A.S. & Horrocks., B.R. Kinetics of Reduction of Ruthenium Hexaammine at Bismuth Electrodes in Aqueous Solution: Analysing the Potential Dependence of the Transfer Coefficient. *ChemElectroChem* **4**, 2943-2951 (2017).

APPENDIX I: Glossary of Abbreviations.

AAS	atomic absorption spectroscopy
AC	alternating current
ACS	American Chemical Society
ACV	alternating current voltammetry
AdSV	adsorptive stripping voltammetry
AFM	atomic force microscopy
AgNPs	silver nanoparticles
AN	acetonitrile
AQS	sodium anthraquinone-2-sulfonate
ASV	anodic stripping voltammetry
SWASV	square wave anodic stripping voltammetry
B.E	binding energy
BiBEs	bismuth bulk electrodes
BiFEs	bismuth film electrodes
CE	counter electrode
CPE	constant phase element
cps	count per second
CV	cyclic voltammetry
DLS	dynamic light scattering
DLVO	Derjaguin, Landau, Verwey and Overbeek (theory of)
DME	dropping mercury electrode
DNA	deoxyribonucleic acid
DOS	density of states
DPV	differential pulse voltammetry
ECM	electrocapillary maximum
EIS	electrochemical impedance spectroscopy
ESCA	electron spectroscopy for chemical analysis, another name for XPS
GC	glassy carbon (electrode)
HD	hexanediol
HMDE	hanging mercury drop electrode
HOMO	highest occupied molecular orbital
ICP-MS	inductively coupled plasma-mass spectroscopy

ID	internal diameter
IHP	inner Helmholtz plane
IMFP	inelastic mean free path
IUPAC	International Union of Pure and Applied Chemistry
K.E	kinetic energy
LUMO	lowest unoccupied molecular orbital
MIC	minimum inhibitory concentration
MV	methyl viologen
MWCO	molecular weight cut-off
NPs	nanoparticles
OD	outer diameter
OHP	outer Helmholtz plane
PCS	photon correlation spectroscopy, another name for DLS
PdI	polydispersity index
PZC	potential of zero charge
QELS	quasi-elastic light scattering, yet another name for DLS
RE	reference electrode
RTILs	room temperature ionic liquids
RuHex	ruthenium hexamine
SEM	scanning electron microscopy
SPR	surface Plasmon resonance
SSR	sum of squared residuals (residual sum of squares)
SWASV	square wave anodic stripping voltammetry
TBAPF ₆	tetrabutyl ammonium hexafluorophosphate
UV-Vis	ultraviolet-visible spectroscopy
WE	working electrode
XPS	X-ray photoelectron spectroscopy
XRD	X-ray diffraction (analysis)

APPENDIX II: Symbols.

A_H	Hamaker constant
C_d	differential capacitance of the double layer
C_O	concentration of oxidized species
$CoCp_2$	cobaltocene
$CoCp_2^+$	cobaltocenium cation
C_R	concentration of reduced species
ΔE_P or $ E_{pa} - E_{pc} $	peak potential separation
E_{pa}	anodic peak potential
E_{pc}	cathodic peak potential
E^o	formal potential
i_{pa}	anodic peak current
i_{pc}	cathodic peak current
k^o	standard rate constant
q^m	charge on metallic electrode
q^s	charge in solution
R_{CT}	charge transfer resistance
W	Warburg impedance
Z	impedance
Z' or ReZ	real part of impedance
Z'' or ImZ	imaginary part of impedance
α	charge transfer coefficient